INVESTIGATION OF FLUID DYNAMICS AND EMULSIFICATION IN SONOLATOR LIQUID WHISTLES

by

DAVID JONATHAN RYAN

A thesis submitted to the
University of Birmingham
for the degree of
DOCTOR OF ENGINEERING

Centre for Formulation Engineering
School of Chemical Engineering
College of Engineering and Physical Sciences
University of Birmingham
United Kingdom
February 2015

UNIVERSITY OF BIRMINGHAM

University of Birmingham Research Archive

e-theses repository

ABSTRACT

The Sonolator liquid whistle is an industrial inline mixer used to create complex multiphase mixtures which form components of high value added liquid products. Despite its wide use, this device's mechanism of operation is not well understood which has led to this combined experimental and computational study to elucidate key phenomena governing drop and jet break-up. The work has focused on single phase Particle Image Velocimetry (PIV) measurements of a model device to validate single phase Computational Fluid Dynamics (CFD) simulations to gain basic understanding of the flow fields which are responsible for the breakage behaviour, assuming dilute dispersions. Multiphase pilot plant experiments on a silicone oil-water-SLES emulsion have been used to characterise the droplet size reduction in a pilot scale Sonolator for both dilute and medium concentrations of the dispersed phase. An empirical model of droplet size was constructed based on pressure drop, dispersed phase viscosity and surfactant concentration. This empirical model was compared with the droplet breakage theories of Hinze, Walstra and Davies. Extra work mentioned in the appendices includes studies on cavitation in the Sonolator, with the cavitating flow conditions identified and the contribution to emulsification considered, and the usage of population balance methods to simulate droplet breakup in the environment indicated by CFD/PIV studies in order to investigate how the droplet size distributions measured in pilot plant studies came about.

DEDICATION

Dedicated to my wonderful wife Maggie (Nguyễn Thị Diệu Huyền)

who has supported me tremendously throughout this project,

also to my parents Patrick and Mary Ryan for everything,

and finally to my seventeen month old daughter Amy Hope Ryan

who I'm sure will enjoy reading an engineering thesis

when she comes of age.

ACKNOWLEDGEMENTS

TABLE OF CONTENTS

LIST OF FIGURES

LIST OF TABLES

Chapter 1   INTRODUCTION

1.1   Background

Consumers, businesses and industries worldwide purchase large quantities of manufactured fluids to satisfy widely varying needs within homes, workplaces, factories and industrial sites. Fluid production and consumption is important within many industries including: food, pharmaceuticals, home and personal care, oil and gas.

The types of fluids required can be simple fluids (water) or complex structured fluids (emulsions, surfactant or micellar solutions, particulate-laden fluids, etc). Manufacturing these complex structured fluids requires specialist techniques and processing stages which are studied within the academic and research communities of chemical engineering.

These techniques can be categorised as batch or continuous; both usually involve fluid mixing since the fluid manufacture may require any or all of: dissolving a component in fluid, mixing of miscible fluids, emulsification of immiscible fluids, introduction of surfactants, dispersion of solid particles within a fluid.

These requirements can be met through a wide variety of techniques or industrial devices, including: shaking, pipe flow, injection, stirring, colloid mills, ball or roller mills, homogenizers, liquid whistles, static mixers, electrical discharges, aerosols, foaming, boiling and condensation. All of these techniques involve subjecting the working fluid to external forces. The classification of these forces includes (but is not limited to) viscous, turbulent and cavitating forces (Walstra 1983).

In the present work the technique under consideration is subjecting a fluid to passage through a **Sonolator**, a device ex. Sonic Corp., USA. Sonolators are in the liquid whistle class of inline static mixers, containing an orifice which directs flow over

a vibrating blade. They are used within industry as a process step towards creating structured fluids which form components of high value added liquid products. They operate by introducing a multiphase fluid, typically containing oil, water and surfactant, at the Sonolator inlet. A large inlet pressure is supplied to create an appreciable flow through the small orifice, over the blade, past the back pressure valve and finally out of the Sonolator. Each of these components may have some effect on the structure of the end product; the typical effects are mixing and dispersed phase droplet size reduction.

The Sonolator was thought to operate by one or more of several potential modes. The manufacturer (Sonic 2011) stated that the Sonolator operated by utilising extreme pressure, shear forces, ultrasonic oscillations causing cavitation, and turbulence. Previously, Walstra (1983) had stated that liquid whistles (ultrasonic vibrating knives) could operate by cavitation or turbulence. Davies (1985) classified liquid whistles as a high intensity mixing device along with homogenizers and colloid mills, and suggests that Hinze's theory (1955) can be used to quantify the emulsification effect, where maximum drop size is related to the local specific turbulent energy dissipation rate, denoted ε.

Walstra (1983) also commented on the lack of experimental data: to date, published experiments now include usage to remove unwanted dissolved gas from a liquid (Clark *et al* 2001), usage to disinfect wastewater in conjunction with ozone (Chand *et al* 2007), investigations into the cavitation noise and its interpretation (Quan *et al* 2011). None of these papers included any flow analysis or application to emulsions.

To date there is still a dearth of available literature on the performance and operation of Sonolators and liquid whistles. Given the lack of literature, this research

project aimed to provide clarity regarding the mode (or modes) of operation of the Sonolator, and the novelty of this work on the Sonolator is to provide a broad theoretical and experimental understanding of the nature of the flow fields in the Sonolator and the emulsions it produces.

Research questions remain outstanding on the relationship between: inputs such as pressure drop, multiphase fluid mix used, back-pressure valve position; conditions inside the Sonolator such as pressure, velocity and turbulence fields; and the outputted structure of the final liquid product, which may be measured in terms of, for example, the average emulsion droplet size. This thesis is concerned with addressing these research questions through elucidating the flow fields inside the Sonolator, understanding how those flow fields might affect restructuring of the fluid, and conducting experiments to measure the change in structure of fluids when processed on the Sonolator.

1.2   Context, applications and business case

The Sonolator is used primarily for mixing or dispersion processes. Some typical industrial applications are presented in Table 1.1:

Table 1.1: Examples of industrial applications for liquid whistles.

Application	Description
Personal Care / Cosmetic liquids	US patents from Unilever (2004, 2008) describing a system incorporating a Sonolator in which many different product lines sharing certain characteristics could be created using Sonolator in a similar setup. Examples include shampoos, hair conditioners, shower gels, body washes, skin lotions, skin creams, deodorants (also see Sonic Mixing website, here referencing a 2014 download)
Food and Beverage	Sauces, purees, soup bases, beverage emulsions, dressings, fillings (Chem Info website 2009, Sonic Mixing website 2014).
Pharmaceutical	Ointments, creams, vaccines. Sonolator is a sanitary and hygienic process (Sonic Mixing website 2014).
Fine Chemicals	Silicones, resins, waxes, lubricants (Sonic Mixing website 2014). US patent from Wenger (2002) describing how to make high viscosity pastes with a meltable dispersed phase using a Sonolator.
General industrial uses	Degassing (Clark *et al* 2001), disinfection (Chand *et al* 2007), textile finish emulsions, silicone oil emulsions (Chem Info website 2009), deflocculation of paint and dispersion of pigments (PCI website 2004)

The sponsoring company, Unilever, desires to expand usage of the Sonolator across many product lines as part of a move towards continuous processing. Continuous processing is desirable since it eliminates many of the disadvantages of batch processing (typically stirred tank). These include: long times for loading, unloading and cleaning; space for tanks and storage; capital expenditure into land and equipment. Additional advantages of continuous processing are: potential for 24 hour processing, elimination of loading and unloading times, reduced cleaning and switch over times, lower floor space requirement. With continuous processing, more varied products and greater quantity of products can be created with the same capital expenditure, whilst creating lower levels of waste and providing enhanced environmental credentials.

In order to redesign existing product lines to be continuous, and design new product lines that are continuous, it is necessary to understand on what basis to choose a

particular inline processing device; in the case of the work presented in this thesis the aim is to understand where the Sonolator is either best for a specific job, or most cost-effective.

However, a major disadvantage of moving to continuous processes, using devices such as the Sonolator, is that they have fewer scientific studies published in the open literature, reflecting that they are less well understood compared to batch devices.

Hence the **business case** for Unilever to fund an EngD research programme to investigate the Sonolator's mixing performance, and to develop a much better knowledge and understanding of this particular continuous processing device, includes the following points:

- Increased confidence in scale-up of Sonolator processes from pilot scale to factory scale.

- Improved robustness of industrial scale semi-continuous processes.

- Provide insights to improve existing processes, reducing costs or improving quality.

- Provide insights to lead to new product opportunities.

Unilever's **confidence** in using the Sonolator at factory scale would be increased as a result of this EngD research project, since the interior workings of the Sonolator would no longer be a "black box" but a component subjecting fluids to a known range of conditions, e.g. turbulent stresses, helping analyse whether a particular scale-up relation is likely to hold, and to choose the best scale-up parameters.

The **robustness** of industrial semi-conti processes would improve since better knowledge about how the Sonolator works would reduce the frequency of errors, where the process output in practice does not match the designed output.

Insights to **improve existing processes** come about as the process is understood better; sponsoring this EngD project provides new information about what is really going on inside the Sonolator, hence process parameters can be better optimised to improve the end product, or unnecessary inputs (such as heat or electricity) minimised to improve efficiency and reduce cost.

Finally, knowledge gained about the Sonolator from this thesis, combined with experience in optimising processes using this knowledge, is likely to help operators to identify **new products** or other products which can be made at lower cost or higher quality using the Sonolator as part of the process. This should help provide valuable new product opportunities to Unilever.

In summary, this research will help elucidate the fundamentals of the Sonolator and how it structures a multiphase fluid, streamlining future research and development, in particular helping cut superfluous pilot plant scale experiments using the knowledge gained, and understanding how to incorporate the Sonolator into the factory scale. Some of these are direct outputs of this research programme; others are aided indirectly through the enhanced understanding. These benefits would be disseminated immediately to Unilever, the sponsoring company, and through publications to the wider research community as appropriate for research partly funded by the UK Engineering and Physical Sciences Research Council (EPSRC).

1.3   Design

Sonic Corp. introduced different generations of Sonolator device, which are described by different US patents (Sonic 1965, Sonic 1975). The patents cover the blade and the assembly of parts, and give a variety of uses such as emulsification and sanitary

uses in the food industries, as well as hypothesising regarding the benefits for the acoustic vibrations imparted by the blade.
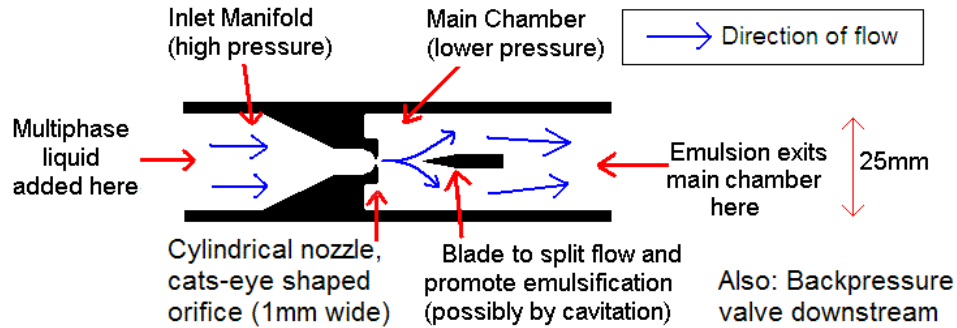
Figure 1.1: Schematic diagram of Sonolator.

(a) Orifice (3.87 mm^2 or 0.0060 in^2; hereafter denoted as "orifice type 0060" or just 0060).

(b) Main Chamber and Blade.

Figure 1.2: Model ACIP2 Sonolator – main components.

A schematic diagram of a typical Sonolator is given in Figure 1.1. From left to right: the multiphase fluid enters from the left; it is forced at high pressure through a cylindrical (Model A Sonolator) or almost-conical (Model ACIP2 Sonolator) nozzle containing a cats-eye shaped orifice (Figure 1.2a); a turbulent (high Reynolds number) jet emerges from the orifice and impinges on a blade (Figure 1.2b); flow is diverted above and below the blade and continues down the main chamber (Figure 1.2b). Finally the flow exits from the Sonolator past a conical back-pressure valve (not shown in schematic).

The Sonolator, being produced in the USA, used imperial units throughout in the design drawings and orifice sizings. In this thesis, each orifice has been denoted by a four digit (NNNN) type number, which corresponds to the following measurements given in inches squared (imperial) and millimetres squared (SI):

Table 1.2: Orifice size codes for each orifice size

Orifice size code	Orifice size (nominal manufacturer stated) in inches squared	Orifice size in millimetres squared	Pilot plant or factory scale?	Thesis chapters used in?
0025	0.0025	1.61	Pilot scale	Emulsification experiments (Model emulsion)
0037	0.0037	2.39	Pilot	PIV experiments (and CFD, and comparison)
0045	0.0045	2.90	Pilot	None
0060	0.0060	3.87	Pilot	Model emulsion
0080	0.0080	5.16	Pilot	Model emulsion
0110	0.0110	7.10	Pilot	PIV
0140	0.0140	9.03	Pilot	PIV and Model emulsion
0960	0.0960	61.94	Factory scale	None
2750	0.2750	177.42	Factory	None
3200	0.3200	206.45	Factory	None

1.4   Industrial operation

High-throughput Sonolators are used as a continuous processing stage in factories for mixing of fluids, emulsification of multiphase fluids and de-agglomeration of particulate fluids. Research and development is normally done at the pilot scale where flow volumes are more manageable than the factory scale. The geometry between pilot and factory scales varies little, except for the orifice, which is resized closely in line with the change in throughput.

Table 1.3: Typical flow parameters in the Sonolator at pilot and factory scales

Scale	Orifice size code	Orifice Area (mm^2)	Orifice Jet Velocity (m·s^{-1})	Mass Flow Rate (kg·s^{-1})	Discharge Coefficient	Pressure Drop (kPa)	Epsilon (W·kg^{-1})
Pilot	0060	3.90	30	0.12	0.79	720	120 000
Factory	2750	180.00	30	5.30	0.79	720	18 000

Table 1.3 gives typical flow parameters in the Sonolator at both pilot and factory scales. Between the two scales, the Sonolator geometry is generally unchanged, except for the orifice which is scaled up considerably.

In Table 1.3 scaling up has been done on constant pressure drop according to manufacturer instructions (Sonic 2011): note that orifice jet velocity was fixed in these example figures. It is possible also to scale up on constant epsilon. Understanding which variable to scale up on (pressure drop or epsilon) was one of the objectives of the present research.

Note also that: fluid density generally does not change much between scenarios and here was assumed constant at 997 kg·m^{-3} (water), discharge coefficient was found to be almost constant across a wide variety of flow rates and orifice sizes. The formula for pressure drop is given in Eq. (7.23) in a later chapter, and a typical choice of epsilon is given in Eq. (7.25).

1.5 Aims and Objectives

Previously the Sonolator was treated as a "black box" device; operators understood that it worked as a mixing/emulsification device, with some guesses possible as to what was happening inside the Sonolator, but no detailed understanding of how it worked. Therefore, the overall aim of the work presented in this thesis is **to**

provide a detailed understanding of what happens inside the Sonolator during normal usage in terms of the flow fields therein and the typical outputs of emulsification. The specific objectives of this research to achieve this aim are thus to:

1) Characterise the flow fields inside the Sonolator, including pressures, velocities and turbulence intensities.

2) Understand the emulsification performance of the Sonolator and provide models predicting droplet size distribution as a function of the processing conditions.

3) Understand how these distributions change as a function of orifice size.

4) Understand which physical phenomena are controlling the emulsification process in the Sonolator, including droplet breakage regime, cavitation, orifice size, blade or backpressure valve.

5) Achieve a predictive ability for emulsification in new Sonolator-like geometries.

1.6   Thesis Outline

This thesis consists of several chapters contributing towards the aims listed above:

- Chapter 1 provides background on the Sonolator, liquid whistles, their design and industrial uses, as well as providing context and objectives for this thesis.

- Chapter 2 describes PIV experiments undertaken to obtain reliable experimental data (in 2D cross-section) about the flow fields inside the Sonolator, to start Aim 1 above.

- Chapter 3 describes CFD simulations carried out on the same geometries as the PIV experiments in order to obtain fully 3D flow field data (continuing Aim 1).

- Chapter 4 describes the comparison between PIV and CFD and the validation of CFD modelling for the Sonolator (completing Aim 1 above).

- Chapter 5 describes emulsification experiments on a pilot plant Sonolator and presentations of the droplet size distribution data (towards Aims 2 and 3 above).

- Chapter 6 discusses the development of correlations for the droplet size distributions obtained from pilot plant experiments, and the comparison of these to theoretical models and experimental data in the literature (towards Aims 2, 3, 4, 5 above)

- Chapter 7 summarizes the findings of these topics of research, including a discussion on scale-up (Aim 5) and discusses further work carrying on from this research.

Other research which was included in the appendices:

- Appendix 1 describes experiments into visual and audio cavitation measurements on the PIV perspex section of the Sonolator (towards Aim 4).

- Appendix 2 gives preliminary methodology for development of population balance equations describing droplet breakage in the Sonolator, to match the emulsification results and according to the turbulence profiles obtained from CFD and PIV (Aims 4 and 5 above).

1.7   Publications and presentations

Findings from this EngD research programme have been disseminated to Unilever Research & Development, University of Birmingham and various national conferences through several PowerPoint presentations and research posters.

In addition, key findings have been published in two international conference papers. These papers are included as appendices to this thesis; please see Appendix 12 and Appendix 13.

- Ryan, D., Simmons, M. and Baker, M. (2011). "Modelling Multiphase Jet Flows for High Velocity Emulsification", *Proceedings of ASME-JSME-KSME Joint Fluids Engineering Conference*, 24-29 July 2011, Hamamatsu, Japan, Paper number AJK2011-03023.

- Ryan, D., Simmons, M. and Baker, M. (2013). "Investigating Dispersion and Emulsification Processes using a Sonolator Liquid Whistle", *Proceedings of 8th International Conference on Multiphase Flow*, 26-31 May 2013, Jeju, Korea.

1.8   Nomenclature & Abbreviations

Greek Symbols

ε Epsilon; local specific turbulent energy dissipation rate (W·kg^{-1})

Abbreviations

EngD   Engineering Doctorate (UK)

EPSRC   Engineering & Physical Sciences Research Council (UK funding body)

PIV   Particle Image Velocimetry – experiments to determine flow velocities

CFD   Computational Fluid Dynamics – simulations to determine flow fields

1.9   References

- Chand, R., Bremner, D. H., Namkung, K. C., Collier, P. J., Gogate, P. R., (2007). "Water disinfection using the novel approach of ozone and a liquid whistle reactor". *Biochemical Engineering Journal*, **35(3)**, 357-364.

- Chem Info website (2009). http://www.chem.info/product-releases/2009/08/what-sonolator downloaded 12th Sept 2014.

- Clark, A., Dewhurst. R. J., Payne, P. A., Ellwood, C., (2001). "Degassing a liquid stream using an ultrasonic whistle", *IEEE Ultrasonics Symposium Proceedings. eds. Yuhas, D. E., Schneider, S. C., Vols 1 and 2 of Ultrasonics Symposium*, 579-582.

Chapter 1 INTRODUCTION

- Davies, J. T., (1985). "Drop Sizes of Emulsions Related to Turbulent Energy Dissipation Rates", *Chem. Eng. Sci.*, **40(5)**, 839-842.

- Hinze, J. O., (1955). "Fundamentals of the Hydrodynamic Mechanism of Splitting in Dispersion Processes", *AIChE. Journal*, **1(3)**, 295.

- PCI website (2004). http://www.pcimag.com/articles/sonolator-system downloaded 12th Sept 2014.

- Quan, K., Avvaru, B., Pandit, A. B., (2010). "Measurement and interpretation of cavitation noise in a hybrid hydrodynamic cavitating device" *AIChE Journal*, In Print.

- Sonic Corp., (1965). "Methods and Apparatus for Producing Acoustic Vibrations in Fluids", US Patent 3176964.

- Sonic Corp., (1975). "Apparatus for Producing Acoustic Vibrations in Liquids", US Patent 3926413.

- Sonic Corp (2011). "*Sonolator Operating and Instruction Manual*", http://www.sonicmixing.com/Manuals/Sonolator_System_Manual.pdf, downloaded on 27th July 2013.

- Sonic Mixing website (2014). http://www.sonicmixing.com downloaded 12th Sept 2014.

- Unilever PLC, (2004). "Sonolator Mixing Process for Personal Care", World Intellectual Property Organisation, Patent WO 2004/054693.

- Unilever PLC, (2008). "Process for Manufacture of Personal Care Products Utilising a Concentrate Water Phase", US Patent 7351749.

- Walstra, P., (1983). "Formation of emulsions", *Encyclopedia of Emulsion Technology*, Volume **1**, Becher, P., (Ed.), Marcel Dekker, New York, USA.

- Wenger Manufacturing Inc., (2002). "Method and apparatus for the production of high viscosity paste products with added components", US Patent 6386748.

Chapter 2   PIV EXPERIMENTS ON A LABORATORY SONOLATOR

2.1   Abstract

Particle image velocimetry experiments were carried out on a laboratory scale Sonolator, an inline mixer in the liquid whistle category. A Perspex main chamber was used for laser transparency downstream of the Sonolator orifice. Multiple flow rates and orifices were investigated. Comparisons were made with the blade in and out. Large time series of image pairs were collected and cross-correlated to yield time-averaged velocity fields in the two symmetry planes of the Sonolator. Evidence of unsteady flow-field behaviour was seen in the time series of photographs. Circular eddy patterns in the velocity vector field which were due to turbulence were seen at all flow rates investigated. Highly reflective patches in the photographs due to cavitation were seen at high flow rates. Turbulence fields were approximated using an isotropic assumption and a sub-grid scale model. Sources of error were identified across different laser planes, blade configurations, orifice sizes and flow rates, with subsets of reliable velocity measurements identified.

2.2   Introduction

As described in the introduction, a Sonolator can be used to produce emulsions and structured fluids. The critical working parts of the Sonolator include the inlet manifold, an orifice shaped like a cat's eye, the main chamber and blade, outlet and a backpressure valve.

Understanding the flow in the main chamber downstream of the orifice is important for understanding the mechanism or mechanisms behind how emulsions and structured fluids are formed yet there are a paucity of data in the open literature with regard to experimental results to describe the particular flow fields involved. This chapter describes work carried out to obtain the flow fields within the Sonolator device for a single phase flow to obtain velocity fields inside the Sonolator using PIV along the two symmetry planes given by the Sonolator axis together with the long and short axes of the orifice respectively. These data are important for understanding the distribution of energy dissipation in the main chamber and thus give insight into the possible break-up mechanisms for drops in two phase emulsions.

2.3   Literature Review

This literature review includes a brief overview of the flow measurement methods available, a discussion of how PIV in particular has been used in other research to gain data on flow fields inside devices, and the methods and equipment needed to gain quantitative data accurately.

Although to date PIV analysis of the Sonolator has not been published by other authors, a subset of findings from this research were presented at ICMF 2013 conference, see Appendix 13 for a copy of the paper (Ryan, Simmons and Baker 2013).

2.3.1   Experimental methods available

An experimental method was sought to measure the velocity and turbulence fields within the Sonolator directly, which would aid in understanding where droplet break-up might occur. Some available measurement techniques including: pitot tubes, HWA (hot-wire anemometry), LDA (Laser Doppler Anemometry), simple imaging, PTV (Particle Tracking Velocimetry), PIV (Particle Image Velocimetry) and LSV (Laser Speckle Velocimetry) (Mavros 2001, Khan 2005).

Methods for measuring flow fields could be categorised into those which measure components of velocity at a single point (pitot tube, HWA, LDA) and those which measure the whole flow field, or some velocity components at some different positions in the flow field for example imaging, PTV, PIV, LSV which are all optical based techniques.

Single point techniques have the advantage of very good temporal resolution, however have the disadvantage of not giving direct information about spatial gradients. Studying the turbulence field in the Sonolator which affects droplet breakup requires knowledge about spatial gradients in velocity. Although information could be derived using Taylor's frozen turbulence hypothesis (1938) it has been found to not always be true in highly turbulent flows (Kresta & Wood 1993). Accordingly, single point techniques were not considered further here.

Whole flow field, or multi-point measurement techniques provide flow information across a wide range of spatial positions at a single point in time. They are typically harder to repeat rapidly than single point measurement techniques, e.g. LDA repetition rates are of order 10 kHz, PIV of order 10 Hz. However, recent advances in

acquisition rates and hardware storage (as of 2014) mean that temporal resolution is increasing.

All of the multi-point methods require optical access which means that the region of flow be transparent as must be the surrounding flow geometry; this usually means making a replica device in a transparent material such as poly methyl methacrylate (PMMA) or glass. They also require the flow to be seeded with small neutrally buoyant particles which faithfully follow the flow and also scatter light. Simple imaging records photographic snapshots of these particles, and multiple pictures or video imaging allow qualitative information to be obtained regarding flow patterns.

To obtain quantitative information, computer analysis of the images becomes necessary. PTV, PIV and LSV are variations on the same technique, and require low (less than 5 particles per interrogation area or IA), medium (5 to 25 particles per IA) and high (more than 25 particles per IA) concentrations of seeding respectively, according to Keane & Adrian (1991). For all three methods, illumination is provided by a laser sheet perpendicular to the camera, hence the flow field is only measured in a plane. In addition, two illuminations very close to each other in time are provided, and the image recorded on one, or preferably two frame exposures. In the latter case, quantitative information regarding the flow is provided by how the seeding particles move between frames (Buchhave 1992, Mavros 2001, Khan 2005).

In PTV the seeding particles are at low enough concentration to track individual particles. This yields a velocity vector for each particle. In PIV the seeding particles are at a medium concentration, so by splitting the image into small regions called interrogation areas (IAs) the local velocity can be deduced through cross-correlation techniques (described below). In LSV the same technique applies, but the particles often

overlap due to their high concentration. This reduces the effectiveness of cross-correlation. For this reason PIV is currently the preferred technique over LSV.

PIV was chosen as the measurement technique for investigating the Sonolator. This was because it promised high spatial resolution data (up to 50 measurements per millimetre) on velocities and their gradients in the Sonolator, suitable for deriving turbulence information from, and it was a reliable and well-tested technique as evidenced by the large number of experimental studies using PIV, some of which are discussed below.

2.3.2   Existing PIV experimental investigations

PIV has been in widespread usage for over two decades to get accurate experimental data concerning flow fields inside fluid domains. PIV has been used both at macro-scale and micro-scale; confined and open flows; aqueous and non-aqueous flows. To give some idea of the breadth of PIV application, a selection of experiments are mentioned: environmental flows include turbulent thermal convection (Xia, Sun and Zhou 2003) and beach swash zones (Cowen *et al* 2003); biological interest includes flow analysis around aquatic animals (Stamhuis and Videler 1995), a heart valve (Jun *et al* 2014) and a vessel phantom with elastic wall (Qian, Niu and Wong 2014); generic flows include turbulent structure in a channel (Liu *et al* 1991), eddy structures in a turbulent boundary layer (Carlier and Stanislas 2005) and backward-facing step flow (Kostas, Soria and Chong 2002); reacting flow includes turbulent nonpremixed flames (Carter, Donbar and Driscoll 1998); micro-PIV includes electro-osmosis-driven microchannel flows (Kim, Beskok and Kihm 2002); mechanical flow includes turbomachinery (Wernet 2000), Wind Turbine (Tescione *et al* 2013). PIV is therefore a well-established technique with recognised scientific merit.

The Sonolator has a confined turbulent flow; experiments are now reviewed of this flow type. Experiments involving PIV for turbulent flow in a microchannel see Blonski and Kowalewski (2007); for mixing at a T-junction see Pan and Meng (2001); for a high-pressure homogenizer see Innings and Tragardh (2005). Numerous experiments have been carried out for PIV on a stirred tank: pitched-blade turbine and gas-liquid flow (Khopkar *et al* 2003), comparison of up-pumping and down-pumping variants on a pitched-blade turbine (Aubin *et al* 2004), Rushton turbine with unbaffled tank and eccentric shaft (Montante, Bakker, Paglianti and Magelli 2006), bubbly Rushton turbine (Montante, Horn and Paglianti 2008), miniature vessel with aerated Rushton turbine (Chung, Simmons and Barigou 2009), two phase dispersions (Laurenzi *et al* 2009), angle resolved Rushton turbine (Gabriele, Nienow and Simmons 2009), partially filled tanks with surface air entrainment (Motamedvaziri and Armenante 2012), turbulence modification using particulate flows in a pitched blade turbine (Gabriele, Tsoligkas, Kings and Simmons 2011). Given that the Sonolator has larger geometry than a microchannel, lower pressure conditions than a high-pressure homogenizer and (with a transparent section downstream of the orifice) offers similar optical access to a stirred tank, it was therefore expected that PIV was a suitable experimental technique for investigating turbulent flow in the Sonolator.

2.3.3   Overview of the PIV experimental technique

Particle Image Velocimetry (PIV) is a technique which allows collection of multiple velocity vectors instantaneously in space through image analysis of the flow. The hardware components required include: a flow field seeded with particles, a transparent section housing the part of the flow of interest, a laser to illuminate a plane

in the flow, a camera to record images of this plane in the flow and a synchroniser to link the components of the system together.
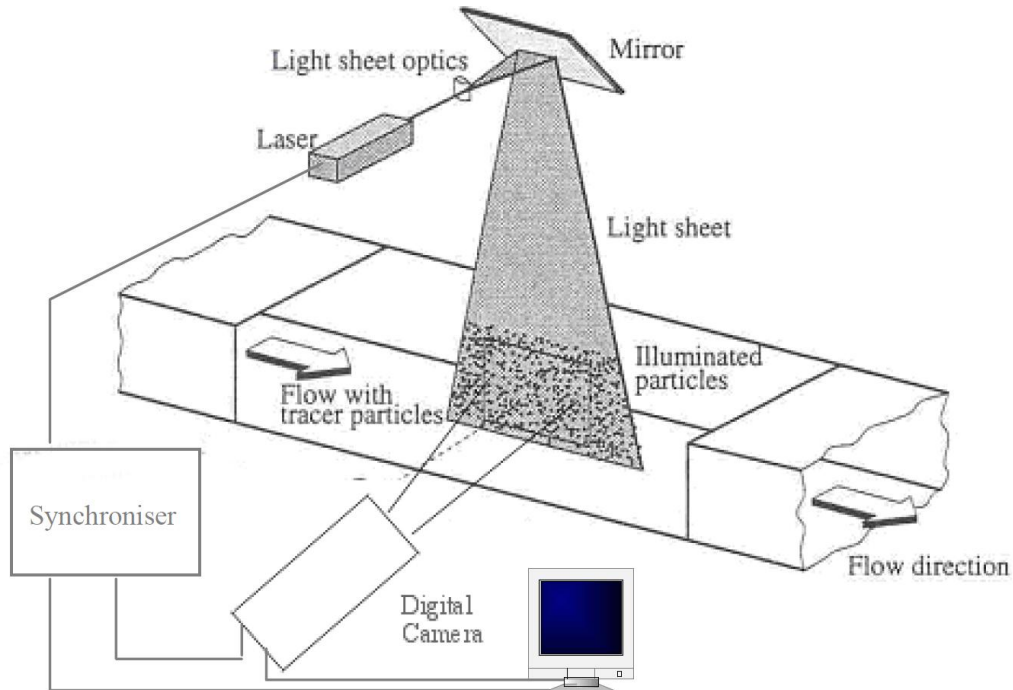
Figure 2.1: PIV experimental setup (figure reproduced from Raffel *et al* 1998)

Figure 2.1 shows a diagram of a typical experimental setup. Most PIV systems are controlled from a PC equipped with appropriate software to analyse the images produced and turn them into sets of velocity vectors representing measurements of the underlying flow field. Recent advances in PIV have become possible due to modern data processing power and automation of the image analysis task.

2.3.3.1 Seeding particles in flow

For PIV to work correctly, each region of the overall image ought to contain around 15 seeding particles (Keane and Adrian 1991) which fill the flow (see Figure 2.2 for an experimental photo from this work). Melling (1997) discusses some properties these particles must have, which include: being small enough to accurately follow the

flow, scattering enough light to show up on the image, being in high enough concentration to give reliable PIV measurements of velocity. They also ought to be neutrally buoyant, chemically inert; not abrasive, toxic, volatile, corrosive or soluble in the flow medium.
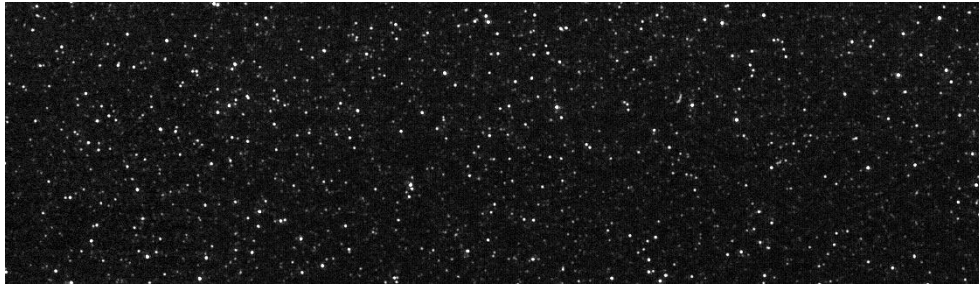
Figure 2.2: Example of a seeded PIV image

There is a trade off between following the flow and reflecting light: smaller particles follow the flow better, but larger particles reflect more light. Care must therefore be taken to select an optimal size of particle which is small enough to follow the flow accurately but large enough to reflect sufficient light to form bright spots of around 1 or 2 pixels on the measurement image.

Some materials which generally meet the requirements for PIV seeding particles include: glass particles (spherical, hollow), alumina, titanium dioxide, silver, polypropylene. Particle sizes generally used in PIV range from a micron to a few hundred microns (Khan 2005). The suitability of the particle size can be checked by calculating its Stokes number (Stk) defined in Eq. (2.2), see section 2.4.4.

2.3.3.2 Laser and focusing arrangement

Illumination of the image plane in PIV has multiple restrictions. Firstly, two illuminations are necessary in close succession to gain the two image exposures for correlation; the maximum time delay between exposures is optimally calculated as the

time taken for the fastest particles in the flow to travel a quarter of an IA (Keane and Adrian 1991). Secondly, each illumination must be at least an order of magnitude shorter than this duration to prevent blurring of the images. Typically, both durations are measured in microseconds.

Providing these speeds of illumination requires either spark illumination or a laser, the latter being superior when considering the added requirement of illuminating only a plane of interest. Continuous and pulsed lasers exist; for PIV the pulsed laser is superior since the continuous laser would require a shutter arrangement to control the exposure time (Khan 2005).

Types of pulsed laser include Ruby, Copper vapour and Nd:YAG. The Ruby laser type is single pulse with a low repetition rate, making it not suitable for PIV. Copper vapour lasers can have high repetition rates, however this form of laser is too expensive to be economical for PIV. Nd:YAG lasers are both low-recovery time and relatively economical, making them the first choice for PIV (Khan 2005). Their illumination time of between 4 and 9 nanoseconds is sufficiently short to prevent blurring of the particle images. The recovery time allows typically 5 to 10 illuminations a second, each giving a separate measurement. Although this is still too slow for twin-pulse PIV, by building two lasers into one head the requirement of twin pulses only microseconds apart can be met.

The laser must be shone onto the flow field as a sheet of light. To achieve this, a cylindrical lens is first used to diverge the laser beam into a sheet, and then a spherical lens to focus this sheet on the flow field of interest. It is important that the sheet thicknesses are less than 1 mm (Khan 2005) which is narrow enough to concentrate the light brightly enough on individual particles in the plane for them to form bright spots

on the image, narrow enough to avoid illuminating particles too far back or forwards which would appear out of focus in the image, but wide enough to make it likely that enough particles are illuminated to show up in the required concentration on the final image. The brightness of the laser can be adjusted to ensure that individual particles show up as bright spots on the final image well above background light levels.

2.3.3.3   CCD camera

PIV has been made possible by the advent of modern digital cameras, as well as digital processing. Charged Coupled Device (CCD) cameras are often used in PIV work. They turn photons of light into electric current to create digital images. Each CCD contains many picture elements or pixels (Raffel *et al* 1998). Recent advances in Complementary Metal–Oxide–Semiconductor (CMOS) camera technology have allowed faster frame rates to be achieved (Dantec 2014).

Two types of camera are used for PIV: those which record single exposures and download the image before the next image can be acquired; and frame-straddling cameras which can acquire two images before download, enabling the time between each image to be considerably reduced which makes them highly suitable for PIV (Khan 2005). The advantages of frame-straddling cameras will be shown below.

2.3.3.4   Synchroniser

For frame-straddling cameras, the laser and camera must be synchronised in order for the two laser pulses to be timed to fall during the two exposures of the camera. A dedicated device is used for this purpose: the synchroniser. It synchronises the following events:

- Camera: start of exposure of first image

- Laser: first pulse (duration 4-9 ns)

- Camera: change from first exposure to second exposure

- Laser: second pulse (duration 4-9 ns)

- Camera: end exposure, download images from CCD, await start of next exposure.

Typically the two laser pulses are very close to the time the camera switches between exposures. This minimises the laser pulse gap and allow fast velocities to be accurately captured by the PIV technique (Khan 2005). The whole cycle of events occurs with multiple pairs of images acquired per second, typically with frequency of 5 Hz to 50 Hz, i.e. slow enough to be within the specifications of both camera and pulsed laser, but fast enough to gain reasonable temporal resolution.

2.3.3.5 Image Analysis

Once images of the seeding particles in the flow are obtained, various techniques exist to analyse these images to extract velocities within the flow. For a low number of seeding particles it is possible to track individual particles and deduce point velocities (this is the PTV method). For larger number of seeding particles (e.g. the density shown in Figure 2.2) this is not possible, however the techniques of auto-correlation (1 frame) and cross-correlation (2 frames) are both possible. When both laser illuminations are on a single image, auto-correlation of small squares within the frame can be used to deduce the movement of particles, however this technique makes it impossible to detect zero velocities and direction of motion (Raffel *et al* 1998) since the original and final positions of the particles are not known since they are on the same image.

It is preferable to record each laser illumination onto a separate camera exposure using a frame-straddling camera. Velocity magnitude and direction can then be deduced using cross-correlation between the two frames. Small portions of each frame (denoted

"interrogation areas", abbreviated to IA) are cross-correlated, normally squares with sides of length 8, 16, 32 or 64 pixels. The measurements can be interpolated, i.e. for IA of length 32 pixels, velocity vectors can be produced via cross-correlation in a grid every 16 pixels. Although the highest theoretical velocity recordable is derived from a particle travelling up to a whole IA between laser pulses, Keane and Adrian (1991) recommend that particles travel no more than a quarter of an IA between laser pulses, this is so that most of the particles being cross-correlated stay in the relevant IA between exposures. The laser pulse delay should therefore be chosen short enough to ensure particles travel less than quarter of an IA between pulses.

Another reason to make the laser pulse delay short is to minimise the distance particles travel out-of-plane; if their out-of-plane velocity component is non-zero (e.g. from turbulence) this component cannot be measured by 2D PIV and will result in worse cross-correlation due to particles entering and leaving the measured plane perpendicularly, giving less accurate velocity readings overall (Keane & Adrian 1991).

$$R(x_0, y_0) = \int \int I(x,y) I'(x + x_0, y + y_0) \, dx \, dy \qquad \text{Eq. (2.1)}$$

(References: Keane & Adrian 1991, Khan 2005)

The cross-correlation function is given in Eq. (2.1). The light intensities I and I' correspond to pixel brightnesses in the IAs from the first and second frames obtained from the camera. The function R is constructed as a function of the displacement x_0, y_0 between these two IAs. The velocity vector is derived from the displacement (x_0, y_0) which maximises the double integral R, combined with the known laser pulse delay. Since only one velocity vector is produced per calculation, it is necessary that velocities are roughly constant within the whole of an IA. Usually a Fast Fourier Transform (FFT)

technique is used to solve for (x_0, y_0) since this speeds up the calculation of R considerably.

2.3.4 Limitations of the PIV experimental technique

The measured flow often has small scale velocity structures, e.g. turbulent eddies. However, PIV is limited in spatial resolution to half an interrogation area, with the velocities constructed at each point effectively an average over an interrogation area; Sheng, Meng and Fox (2000) note how the velocities are low-pass filtered by this length scale. The temporal resolution is likewise limited to the maximum of the frequency at which a dual laser pulse can be generated and the frequency of a (double) image exposure on the camera. Given these restrictions in length and time scales, some information about small scale features (e.g. the smallest turbulent eddies) will be lost.

In addition, for the 2D PIV methodology reviewed above the velocity data obtained exists only in a plane; additionally only components of the velocity vector field which are coplanar are measured; this is 2 out of 3 velocity components for a 2D slice of the 3D flow. In situations where either a 3rd component of velocity is desired or a "thick" region that is fully 3D is investigated, extra techniques such as stereoscopic PIV would be required.

2.3.5 Summary of literature reviewed

Experimental methods able to measure flow velocities were reviewed. PIV was able to measure planar velocities inside complex geometries simultaneously across a 2D grid; other techniques (e.g. LDV) only return velocities at one point at a time. PIV had widespread use in many scientific disciplines to gather experimental measurements of flow fields. PIV required a transparent section to be made of the flow geometry, a laser,

camera and synchroniser to gain the images, and large amounts of computation to carry out the image analysis and extract the velocity field. Its main benefit was to make available a 2D flow field with reasonable spatial resolution. PIV was expected to be able to measure Sonolator velocities, given the alteration of an original Sonolator unit to have a transparent viewing window.

2.4   Materials and Methods for PIV experiments

The specific equipment and methods are described below which have been used to investigate a Sonolator using PIV.

2.4.1   Dimensions and positioning of all equipment used

The Sonolator used was a "Model A Sonolator" by Sonic Corporation, Cincinnati, USA, equipped with "Seepex progressive cavity pumps" rated to $0.17\,\mathrm{kg \cdot s^{-1}}$ ($10\,\mathrm{kg \cdot min^{-1}}$). The Sonolator upstream and downstream of the orifice, as received, was made entirely out of steel. In order to use the PIV technique, a plane of visible light had to be able to enter the flow field and to be observed perpendicularly. This required a redesign of the main chamber of the Sonolator to manufacture it out of a transparent material.
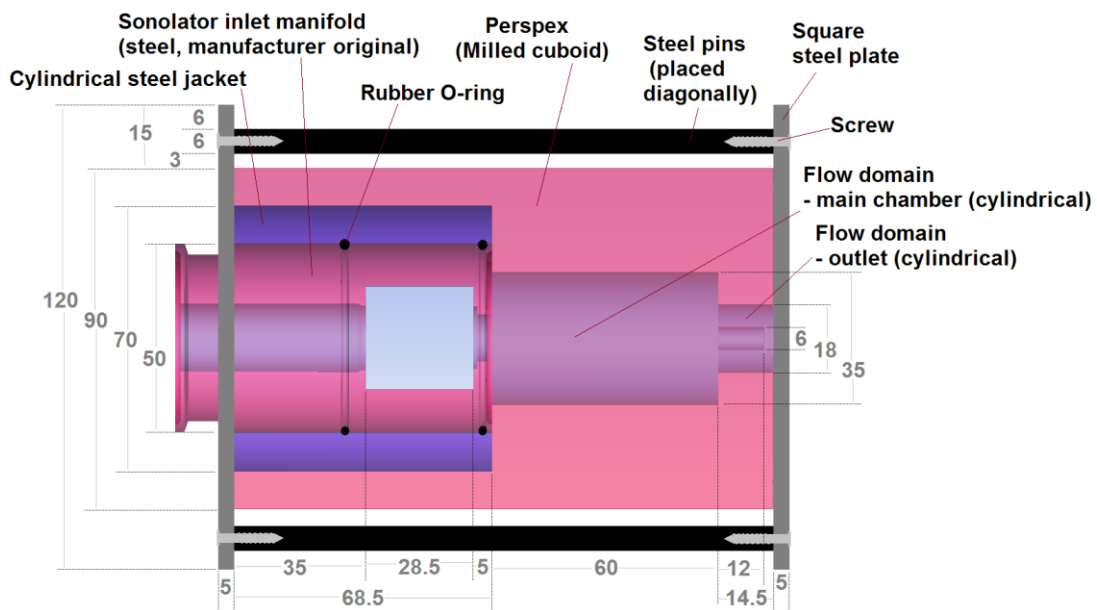
Figure 2.3: Cross-section of Sonolator assembly, ZY plane. All dimensions in millimetres unless otherwise stated.

The inlet manifold from a manufacturer original Sonolator (steel, cylindrical) was retained from the Sonolator rig. Figure 2.3 shows the design for placing the inlet manifold inside a steel jacket (for pressure tightness), which was sealed inside a Perspex cuboid which had been milled out to have the same flow geometry as the original Sonolator rig. This apparatus was held together with a frame comprising of two square steel plates, four steel pins (placed diagonally so as not to impede laser and camera access) and eight screws. When this apparatus was sealed, using silicone grease between the parts, it was capable of operating under the same inlet pressure as the original Sonolator, 1000 kPa.
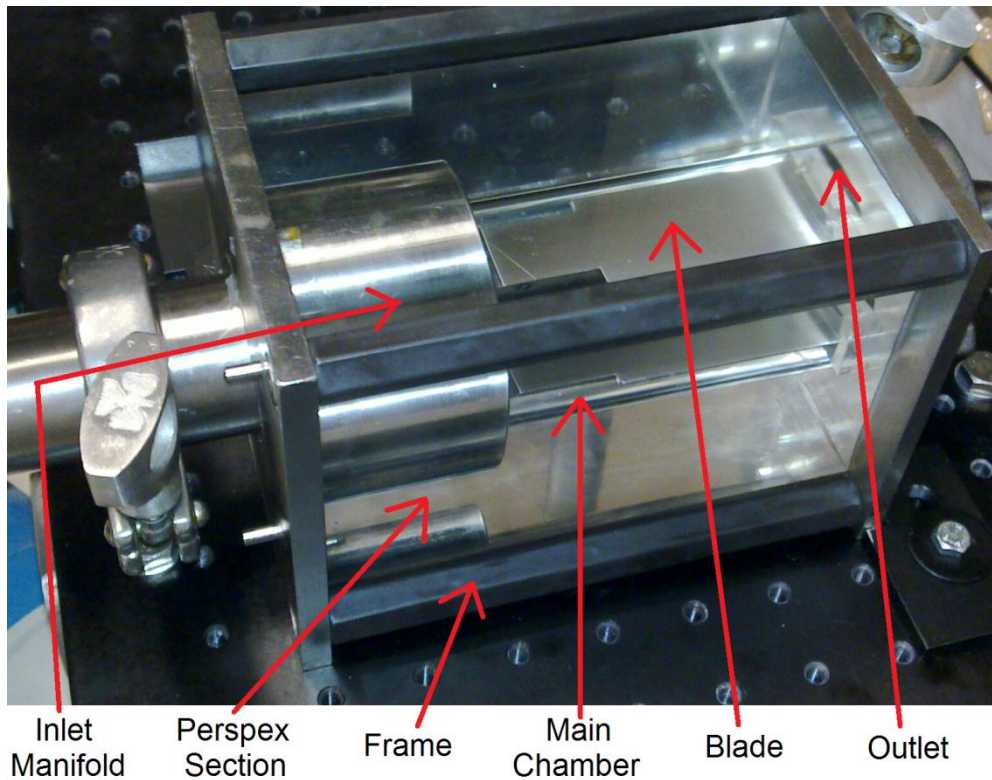
Figure 2.4: Photograph of experimental Perspex Sonolator rig

Figure 2.4 shows the assembled Sonolator experimental rig, including the blade which was made out of steel and slotted into a milled cavity near the outlet. Note that the inlet manifold and orifice are obscured in this photograph by the cylindrical steel jacket on the left.
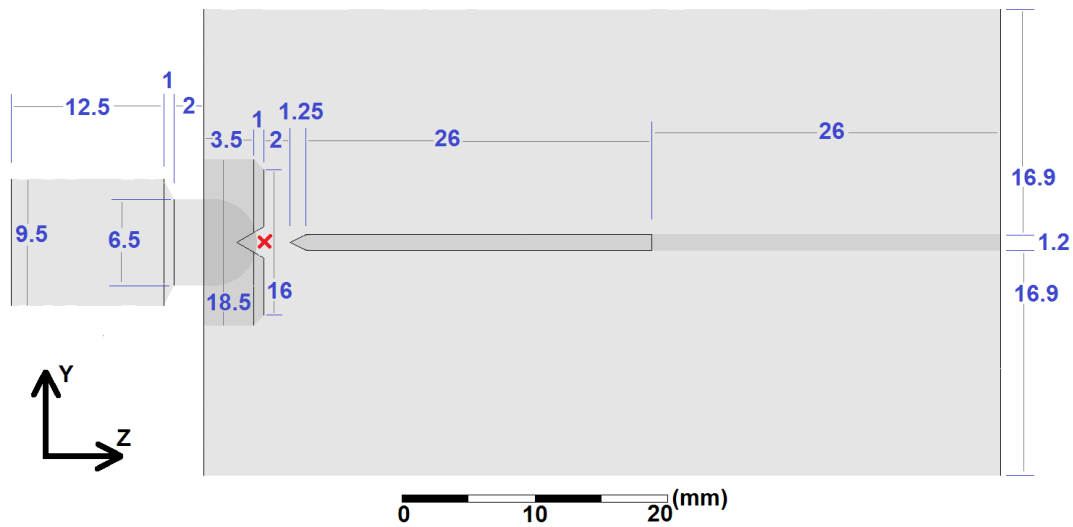
Figure 2.5: Sonolator flow domain, ZY plane, 0110 orifice, blade in. Red X is position of origin $(x,y,z)=(0,0,0)$

Figure 2.5 shows the flow domain along the plane containing y and z axes (denoted ZY). The flow domain was bounded by the steel inlet (far left) and Perspex (middle and right) . The blade (when present) was positioned 2 mm downstream of the orifice. In all following work, the geometrical origin was taken to be at the front and centre of the nozzle, illustrated by a red cross.

This ZY plane was used for PIV with both blade in and blade out. The ZY plane cut the orifice through its short axis.
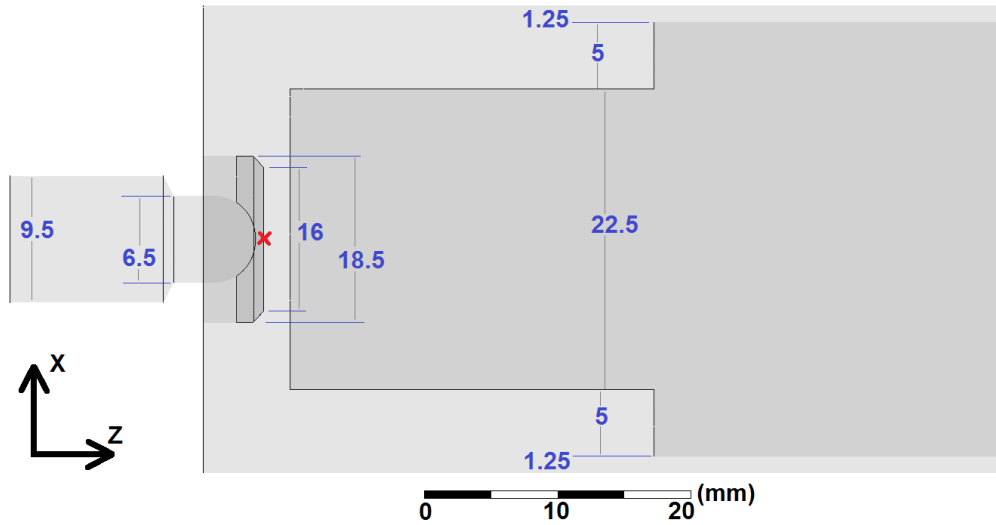
Figure 2.6: Sonolator flow domain, ZX plane (0110 orifice, blade in).

Figure 2.6 shows a different cross-section of the flow domain through the ZX plane. The blade occupies much of this plane (dark grey, on right) and so PIV could only be carried out in ZX plane when the blade was removed. The ZX plane cut the orifice through its long direction.
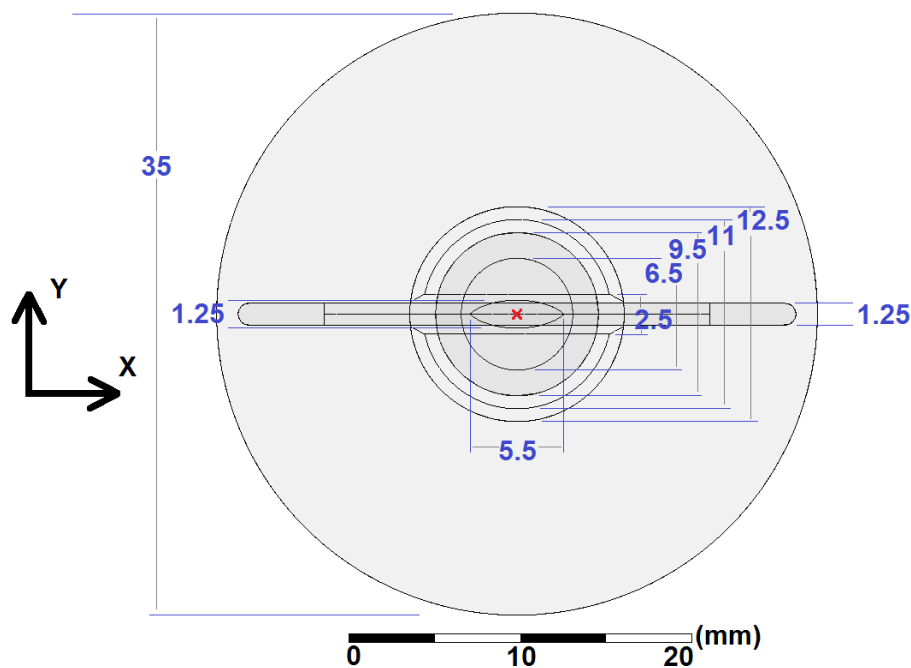
Figure 2.7: Sonolator projection onto XY plane (0110 orifice, blade in).

Figure 2.7 shows a projection of the flow geometry onto the XY plane in which the shape of the orifice (0110 orifice illustrated) can be ascertained, along with the relative position of the blade. Two cylindrical flow domains are seen in the projection: main chamber (large, light grey) and inlet (small, dark grey).
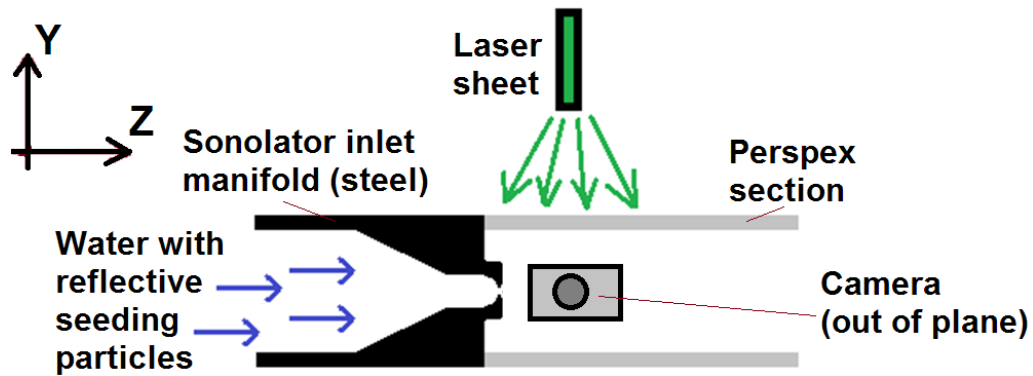
Figure 2.8: Schematic ZY diagram of overall PIV setup
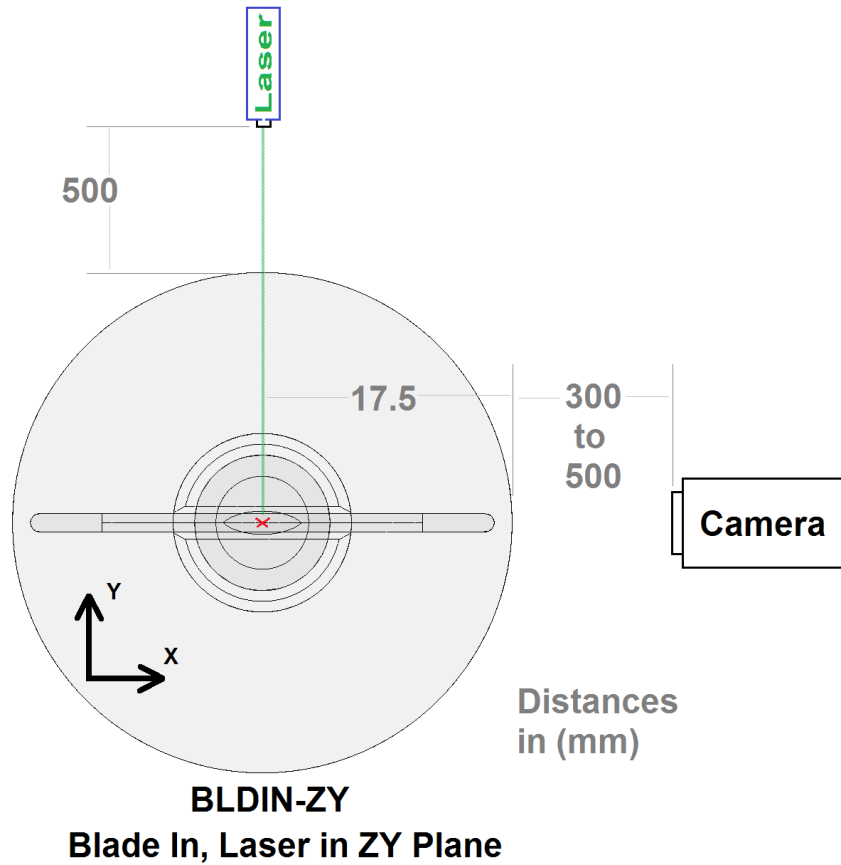
Figure 2.9: Diagram in XY plane showing camera position and projected position of laser sheet. Measurements in millimetres (not to scale). Blade in setup (BLDIN-ZY).
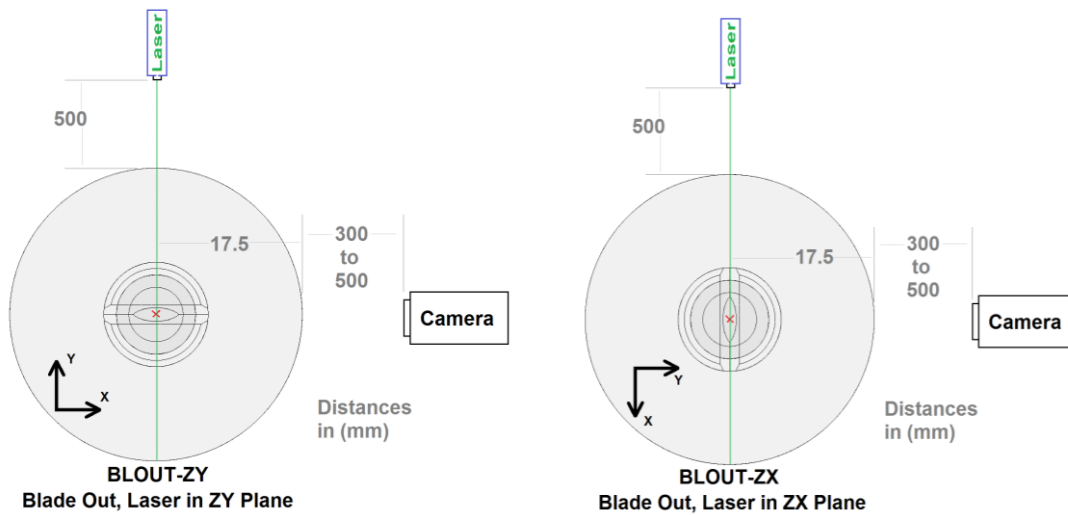
Figure 2.10: Diagrams in XY plane showing camera and laser sheet positions for two orientations of blade out setup.

Figure 2.8 above shows a schematic of the overall PIV experimental setup. Figure 2.9 shows detailed positioning information for the blade-in setup used. Figure 2.10 shows the same information for the blade-out setups, for which there were two distinct orientations.

2.4.2   Details of construction for Sonolator Perspex test section

The steel inlet manifold which housed the Sonolator orifice was removed from the assembly, and a new transparent Perspex section was constructed downstream of the orifice. This stayed as close to the original main chamber geometry as possible: the orifice size and main chamber diameter were identical; the front edges of the blade were also the same; however the rear of the blade had been elongated in order to increase optical access. (This change would not have been thought to affect industrial performance since the mixing / emulsification due to the Sonolator was thought to originate from turbulence generated at the orifice and the front edges of the blade, not from the rear surfaces of the blade.) The Perspex section thus allowed the flow downstream from the orifice to be photographed using a laser and camera combination. Figure 2.8 above has a schematic diagram for this experimental setup with blade out.

The Perspex section was a Perspex cuboid with two cylindrical cavities milled out of it. The cylindrical inlet manifold from the Model A Sonolator, wrapped in a steel jacket with rubber O-rings to seal it, fitted tightly into the larger diameter cavity on the left (Figure 2.4) of diameter 70 mm. The smaller diameter cavity on the right of diameter 35 mm acted as the main chamber of the Sonolator after the orifice; this was the same size as the original geometry.

An optional blade (visible in Figure 2.4) was installed in the main chamber so that PIV experiments with both blade in and blade out could be carried out. The front of the blade geometry was the same as that of a Model A Sonolator. The blade edge was positioned 2 mm downstream from the front of the nozzle in order to be positioned in the fastest region of the orifice jet, as per the original Sonolator. The blade was sprayed with black paint (subsequent to photograph in Figure 2.4) in order to minimise laser reflection.

The downstream portion of the blade was redesigned so as to have an unobstructed field of view of the area above it for at least 30 mm downstream of the front of the blade. This gave the advantage of increased visibility for PIV measurements, but made it more difficult to position the blade exactly in line with the orifice, and also made the blade less stiff, however this alteration was thought necessary in order to obtain sufficient PIV measurements across the whole main chamber.

All of these components were held together by a frame, and fixed to an optical breadboard so that the PIV laser and camera could be trained upon them accurately.

2.4.3 PIV equipment: laser, camera, synchroniser and workstation

The PIV equipment was supplied by TSI Inc. (USA) to University of Birmingham and had been previously used successfully to obtain PIV measurements of other systems – see Gabriele *et al* (2011), Gabriele *et al* (2009), Hall *et al* (2005a, 2005b).

The 2-D PIV measurements were performed using a TSI PIV system (TSI Inc, Shoreview, MN., USA) comprised of a 532 nm Nd-Yag 50 millijoule per pulse dual-head laser (New Wave Solo III, ex. New Wave Research, Fremont, CA., USA) pulsing at 7 Hz, synchronized to a single TSI Powerview 4MP (2048×2048 px^2) 12 bit grayscale frame-straddling CCD camera using a synchronizer (TSI 610035) attached to

a Dell Precision 620 workstation. The PIV system was controlled using TSI Insight 4G software, which stored the PIV images and carried out the cross-correlation described below which extracted the velocity vectors of the flow from the data.

2.4.4 Working fluid with seeding particles

The working fluid for PIV experiments was mains water at ambient temperature and pressure. Recorded temperatures were not outside of the range 22°C to 27°C. The working fluid was stored in a tank of volume 60 litres and recirculated through the experimental apparatus.

Seeding particles were added to the working fluid for PIV imaging. The particles chosen for this study were 10 μm silver coated hollow glass spheres which were neutrally buoyant in water. They were found to give good reflectivity under the laser sheet, being clearly visible on the image with only around 0.5 g being necessary to seed 60 litres of water. Examples of the seeded images are given in Figure 2.2 (an example of the clarity obtained) and Figure 2.11 where the nozzle is visible for scale.
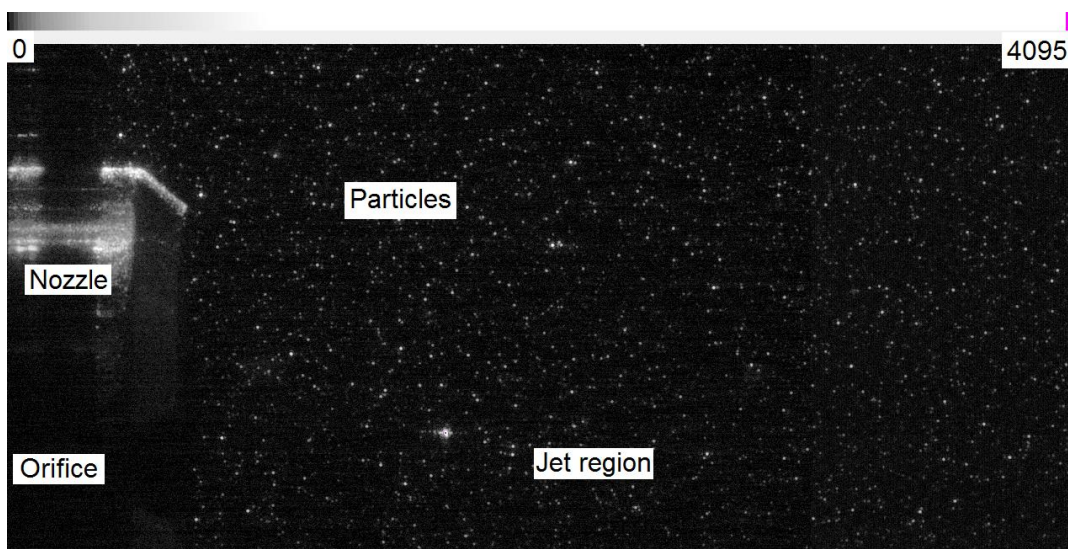
Figure 2.11: Typical seeded PIV image before onset of cavitation.

The relaxation time had to be small for the particles to follow the flow faithfully. This was checked by calculating the Stokes number (Stk) at the orifice, using the typical local flow velocity (U), typical obstacle size (L), particle relaxation time (τ), the jet velocity and the orifice gap distance, see Eq. (2.2) and Eq. (2.3) for equations and Appendix 4 for calculations (note that as the length scale decreases towards that of turbulence, this relaxation time becomes less relevant since the particles are pulled in all directions by turbulent eddies). The Stokes number was always much less than unity. This indicated that the particles followed the flow faithfully.

$$Stk = \frac{\tau U}{L} \qquad \text{Eq. (2.2)}$$

$$\tau = \frac{(\rho_{\mathrm{p}} - \rho_{\mathrm{c}})d^2}{18\mu_{\mathrm{c}}} \qquad \text{Eq. (2.3)}$$

(Reference: Brennen 2005)

Gas bubbles were present in the flow at higher mass flow rates. This was because the orifice caused cavitation and de-gassing of dissolved air. For more discussion of under which conditions cavitation and de-gassing occurred in the Sonolator, as well as methods for measuring these, see Appendix 1. An experiment is described below which compared PIV results with gas bubbles to those from seeding particles, to check that no significant differences could be found.

2.4.5 Positioning of the laser and camera

The laser was mounted on a proprietary fixed platform which allowed it to be aimed directly downwards perpendicularly onto the Perspex section. The camera was mounted on a computer-controlled traverse which allowed full three-dimensional motion; the image could be centred on any part of the flow, zoomed in or out, and the lens could be focused to a specific depth, all as required by the specific PIV experiment.

Figure 2.9 and Figure 2.10 above show the relative positions of the laser, Sonolator and camera; note these diagrams are not to scale, but distances in millimetres are indicated.

The laser had a cylindrical lens and focusing system which allowed it to produce a narrow sheet of green light of width 1 mm. It was positioned 500 mm vertically above the centreline of the Perspex section for best focus. The laser was aimed vertically downwards to bisect the Sonolator Perspex section along a symmetry plane. The Sonolator had two symmetry planes; these are both illustrated above in Figure 2.10 where in plan (XY) view the green laser line describes each symmetry plane (XZ, YZ) in turn.

The camera was positioned perpendicular to the laser sheet in all cases, in order to record the reflections of the seeding particles with as undistorted an image as possible. Distances from camera to Perspex were between 300 mm and 500 mm. The flow area recorded in the images always included the orifice and the area directly after it, up to a distance of around 35 mm downstream from the orifice. This was where turbulence was highest and droplets were thought most likely to break. By zooming in upon this area, maximum fidelity in the measurements was ensured.

2.4.6   Choice of experimental parameters

Several experimental parameters were available to vary: PIV measurement plane, blade in or out, orifice size, mass flow rate, particle seeding density, delay between laser pulses. First these options will be explained in detail, then a summary table of actual experimental choices will be given in Table 2.1.

Two different planes were used for PIV measurement, corresponding to the two symmetry planes of the Sonolator geometry; these planes were denoted ZY and ZX as follows: the ZY plane aligned with the Sonolator axis and the short direction of the

orifice (and blade if present), the ZX plane aligned with the Sonolator axis and the long direction of the orifice (and blade if present).

The blade was removable; PIV experiments were denoted BLDIN if the blade was in, and BLOUT if the blade was out.

To represent the entire geometric choice, the blade choice and PIV measurement plane choice were concatenated to give four options (for each orifice and flow rate): BLOUT-ZY, BLOUT-ZX, BLDIN-ZY, BLDIN-ZX. However, the BLDIN-ZX setup was not used since the laser plane was almost entirely blocked by the blade and no useful PIV results could be obtained. Hence the three setups investigated were: BLOUT-ZY, BLOUT-ZX, BLDIN-ZY.

Three orifice sizes were used: 0037, 0110 and 0140 (see Table 1.2 for complete list of size codes; those quoted here vary between 0.0037 in^2 (2.39 mm^2) and 0.014 in^2 (9.03 mm^2). These orifice sizes represented those typical for Sonolator pilot plants.

Mass flow rate was varied between low, medium and high flow rates (exact values given below in Table 2.1). The flow rates were slightly different between different orifice sizes, due to pump and pressure drop limitations.

Table 2.1: Summary of PIV experimental setups. List for each orifice size and flow rate category of: mass flow rate (M), superficial velocity (u_{orif}) at the orifice, Reynolds numbers (Re) at the inlet, orifice and main chamber.

Orifice size code	Low Flow Rate	Medium Flow Rate	High Flow Rate
0037	$M = 0.036$ kg·s^{-1} $u_{orif} = 15.2$ m·s^{-1} Re$_{inlet}$ = 4200 Re$_{orif}$ = 26 500 Re$_{MC}$ = 1500	(PIV not carried out)	$M = 0.091$ kg·s^{-1} $u_{orif} = 38.4$ m·s^{-1} Re$_{inlet}$ = 10 500 Re$_{orif}$ = 66 700 Re$_{MC}$ = 3700
0110	$M = 0.046$ kg·s^{-1} $u_{orif} = 6.5$ m·s^{-1} Re$_{inlet}$ = 5300 Re$_{orif}$ = 19 600 Re$_{MC}$ = 1900	$M = 0.092$ kg·s^{-1} $u_{orif} = 12.9$ m·s^{-1} Re$_{inlet}$ = 10 500 Re$_{orif}$ = 38 800 Re$_{MC}$ = 3800	$M = 0.182$ kg·s^{-1} $u_{orif} = 25.8$ m·s^{-1} Re$_{inlet}$ = 20 900 Re$_{orif}$ = 77 200 Re$_{MC}$ = 7500
0140	$M = 0.047$ kg·s^{-1} $u_{orif} = 5.2$ m·s^{-1} Re$_{inlet}$ = 5400 Re$_{orif}$ = 17 500 Re$_{MC}$ = 1900	$M = 0.092$ kg·s^{-1} $u_{orif} = 10.2$ m·s^{-1} Re$_{inlet}$ = 10 500 Re$_{orif}$ = 34 500 Re$_{MC}$ = 3800	$M = 0.182$ kg·s^{-1} $u_{orif} = 20.3$ m·s^{-1} Re$_{inlet}$ = 21 000 Re$_{orif}$ = 68 500 Re$_{MC}$ = 7500

A summary table of all PIV experimental setups used is given above in Table 2.1. This table allows easy description of each experimental case, e.g. as 0110 orifice, medium flow rate. Note that each of these eight experiments was carried out for all three geometric choices BLOUT-ZY, BLOUT-ZX, BLDIN-ZY, giving 24 experiments in total.

The final two experimental options were seeding particle density and laser pulse delay. Values were set for these using knowledge gained from preliminary runs and the analysis of their images, as follows.

Cross-correlation (described later) was used to extract velocity vectors from the PIV images. This cross-correlation occurred between square interrogation area (IAs). Although different IA sizes were investigated, their size was later fixed at 32 pixels per

side. There were two requirements for the seeding particles: firstly that 5 to 25 of them were present in each IA, and secondly that they moved not more than one quarter of an IA between the two laser pulses (Keane & Adrian 1991).

The following technique was used to get the correct concentration of seeding particles at both high and low flow rates. Seeding particles could be added but not taken out. At high flow rates small bubbles were always present (see Appendix 1 on cavitation). Hence the high flow rate required less seeding than the low flow rate. By carrying out the high flow rate experiment first with fewer seeding particles, and then adding seeding particles for the lower flow rate, each flow rate could have the optimum seeding density.

Each experiment set (high flow rate, then medium, then low; other parameters fixed) started with a high mass flow rate; a small quantity of seeding particles were allowed to circulate to all parts of the working fluid. When captured images showed that the distribution of seeding particles was within 5 to 25 per IA, and evenly spread, the concentration of seeding particles was judged correct and the PIV images were captured. This was repeated for lower mass flow rates where higher quantities of seeding particles were added. Hence at a lower mass flow rate there were no bubbles (so a single source of laser reflections) and the correct seeding density. (Section 2.4.11 below shows that these bubbles followed the flow accurately, as did the seeding particles.)

In order to ensure that the particles always travelled less than one quarter of an IA, the maximum flow velocity was calculated for each PIV parameter set. An example calculation would be: orifice 0110 had area 7.10 mm^2 (see Table 1.2); if the mass flow rate was set at 0.083 kg$\cdot$s^{-1} then since water density was 997 kg$\cdot$m^{-3} then volumetric

flow rate was $8.36 \cdot 10^{-5}$ m^3·s^{-1}. The jet velocity was volumetric flow rate divided by orifice area (see Eq. (7.22) below) which evaluated to 11.8 m·s^{-1}. Given this maximum flow velocity, the time taken to travel 8 px was calculated in the following way: the image resolution was calculated as 17 μm·px^{-1} since a PIV image width of 2048 px corresponded to 35 mm measured on the experimental rig. Hence 8 px corresponded to 136 μm. Then 136 μm divided by 11.8 m·s^{-1} gave 11.5 μs as the time taken. Hence the laser pulse delay should be less than 11 μs to obtain accurate PIV results for this example. In the same way, the laser pulse delay was always set to an appropriately small value. (Note that to avoid rounding errors all decimal places were retained in intermediate calculations.) The minimum delay possible on the equipment used was 5 μs which managed to capture almost all velocities accurately in every system.

2.4.7   Experimental procedure to produce PIV images

The Insight 4G software was used to record 500 image pairs in sequence for each individual experiment. The camera allowed image pairs to be recorded at a frequency of 7 Hz. Each image pair consisted of two separate exposures of the CCD element of the camera.
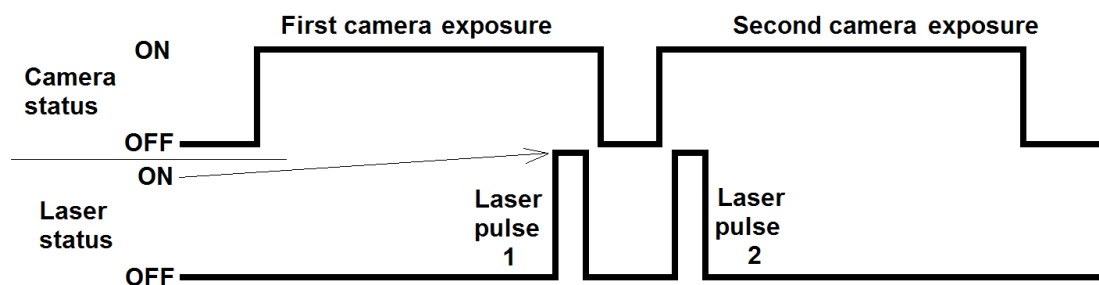
Figure 2.12: Timing diagram of sequence of camera exposures and laser
pulses (horizontal time axis not to scale)

Figure 2.12 shows the sequence of events for capturing an individual PIV image pair: two separate camera exposures were made, and two laser pulses were fired so that

the entirety of each laser pulse fitted within different camera exposures. The first camera exposure was 500 μs long, the second camera exposure was 49 500 μs. Each of these frame lengths produced images of particles of the same brightness since the only source of illumination was the laser, having minimised background light. Preliminary experiments found that the gap between camera exposures was 5 μs long, therefore this was the minimum laser pulse gap which could be achieved on the equipment.

The laser pulses were equally spaced either side of the change in camera exposure. Image pairs from each experiment were visually examined to show that single particle images showed up on each frame, with small movements between the two frames; this established for each experiment that the sequence shown in Figure 2.12 had been carried out correctly.
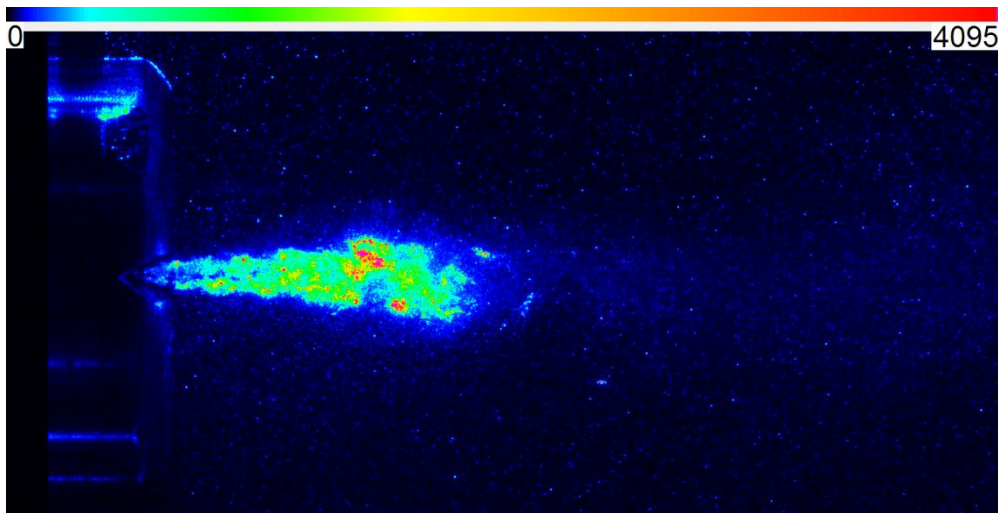
Figure 2.13: Seeded PIV image of Sonolator in BLOUT-ZY setup.
Pseudocolour scale is provided, representing 0 to 4095 (12-bit) greyscale.
Cavitation seen as bright region.

Recording all the image pairs took a time duration of around 70 s to 140 s for each experiment. The result was a set of raw TIFF image files to be processed in Insight 4G to obtain velocity vectors. An example image is shown in Figure 2.13 where a pseudocolour scale has been used to highlight features of the flow which are of different

light intensities. The background is black, particles are dark blue, and the high intensity region contains cavitation. The nozzle and orifice are visible on the left to give scale.

2.4.8   Removal of bad pixels

The camera used had 12 dead pixels across the whole 2048×2048 px^2 CCD. These interfered with cross-correlation since they were permanently set to maximum intensity; since the dead pixel was stationary, it caused an unphysical zero vector to register in every IA with a dead pixel.

MATLAB processing of the TIFF image files was used to locate these dead pixels and to remove them by setting them to minimum intensity, black. This was done for all images using a mask constructed from the 12 dead pixels. Most dead pixels were spread out over many IAs, and the effect of zeroing a single pixel in an 1024 pixel IA was judged to be very small, since most pixels were near 0 (black) anyway, which was the background colour due to low background light intensity.

The result was that the velocity vectors produced in IAs with dead pixels removed became similar to the velocity vectors of the surrounding IAs, as expected. This indicated that the error removal procedure had succeeded. The code used to remove dead pixels is in Appendix 9.

2.4.9   PIV image cross-correlation to give instantaneous flow fields

Previously a set of 500 image pairs in TIFF format had been captured. Insight 4G was used to process these into vector files, comma separated files suitable for external processing, using the following technique.

Each TIFF image was 2048×2048 px^2. The IA size was 32×32 px^2. The IAs were formed every 16 px in both directions giving a "Nyquist" grid. This gave a maximum

number of 127 by 127 velocity vector measurements (the 128th was not used since its IA would lack 16 pixels on at least one side). In practice only the portion of the image representing a flow field was processed, and the rest was removed by a mask, so only a fraction of the 127^2 potential velocity vectors were obtained.

Given an IA of size $32{\times}32$ px^2, a cropped image of that size was available from both the first and the second images in the image pair. These images were in greyscale; light areas mostly corresponded to particles in the flow, and dark areas corresponded to empty areas. The particles moved slightly (up to 8 px) between the two cropped images. This slight movement was detectable by cross-correlating the two images from the IA and resulted in a 2D vector with maximum magnitude ±8 px in each component. The "Fast Fourier Transform" cross-correlation option was used in Insight 4G to perform this cross-correlation.
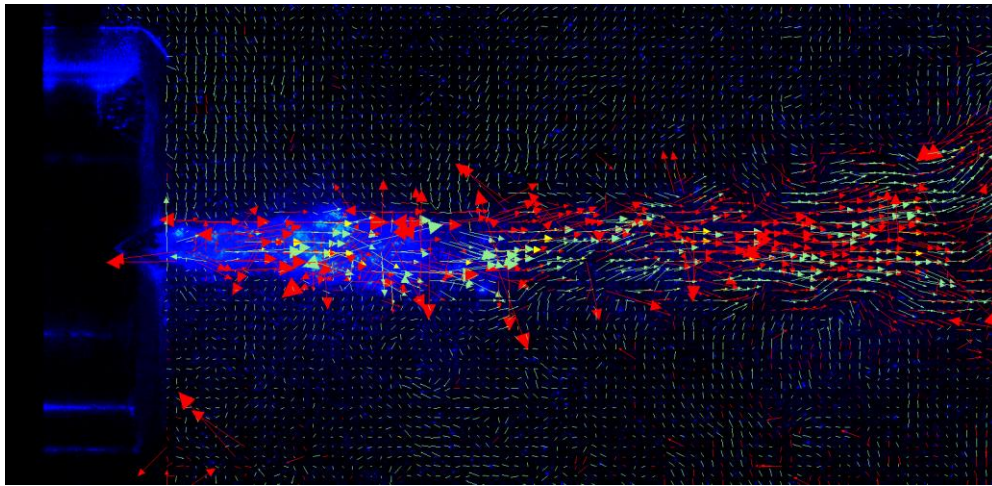
Figure 2.14: PIV image with velocity vectors from FFT cross-correlation superimposed. Green vectors are valid, red are invalid, yellow are valid after post-processing. Flow features in and around the jet are visible.

2D vectors were thus provided for all IAs (several thousand) and for all 500 image pairs. The cross-correlation was generally quite accurate, but occasionally an unphysical vector resulted, see the velocity vectors in Figure 2.14 superimposed on a PIV image.

The vectors which have been marked as unphysical (invalid) were those where the displacement was more than 8 px in any direction; these were marked as invalid during the processing stage. Subsequently, the 2D pixel displacement vector set was turned into a velocity vector set by multiplying by the image resolution (calculated earlier as 17 μm·px^{-1}, from a 35 mm length occupying 2048 px) and dividing by the laser pulse delay (in μs, varied between experiments).

The vectors were post-processed using a Universal Median Test on a 5×5 grid of interrogation areas. Vectors which failed the median test were replaced either by a secondary cross-correlation peak if available, or the local median velocity value given suitable numbers of valid vectors in the 24 surrounding IA cells. Using this method, around 2% to 5% of invalid vectors were able to be replaced with post-processed vectors.

(Note on IA size: IAs were always square, and previously three different sizes with side 16 px, 32 px and 64 px had been tried. Analysis showed that the IAs with the 32 px side gave the most physically realistic results. This IA size was subsequently used exclusively.)

Given IAs of 32 px square, a Nyquist grid giving velocity measurements every 16 px, and the image resolution of 17 μm·px^{-1}: velocity measurements were thus obtained every 270 μm, which was a spatial resolution of around 4 velocity measurements per millimetre.

The set of velocity measurements for each image pair, after filtering, was exported from Insight 4G as a plain-text vector file with columns for z and y components of position in the laser plane (ZY setup) and w and v components of velocity; 500 such

files were generated for each PIV experiment, each vector file representing an instantaneous velocity field measurement for the Sonolator.

2.4.10 Processing of instantaneous flows to give average flow field

A large number of vector files were necessary in order for the time-averaged velocity fields to converge; later (in section 2.5.4) it is demonstrated that 500 vector files were more than sufficient. To obtain the averaged velocity field in the Sonolator, all vector files for a particular experimental condition were analysed using MATLAB; the script used is given in Appendix 10.

The MATLAB script included the following stages: trimming the vector files so they only contained valid vectors in the selected region of interest (done via filtering on the validation code exported with the vector data), changing z and y coordinates (in mm) to an integer grid (denoted Z, Y), calculating mean velocity and turbulent statistics at each integer grid location (see below), saving all these to file.

To create the integer grid the set of z and y positions were extracted where at least one valid (w, v) velocity measurement was recorded. These were sorted and allocated grid references Z and Y using natural numbers (1, 2, etc.). The advantage of this was to be able to search via a natural number pair (Z, Y) for all velocities at a particular location. In general between 200 and 450 valid vectors were found at each such location. The time-averaged velocity vector at a location was defined to be the average of the valid velocity vectors at that location.

The following equations for k, ε_{de} and ε_{sgs} are derived in Appendix 3. They represent turbulent kinetic energy (k) and two variants of local specific turbulent energy dissipation rate (ε; derived from Direct Evaluation from the defining equation, or using a model for Sub-Grid Scale eddies):

$$k = \frac{3}{4}(\tilde{v} + \tilde{w})$$

Eq. (2.4)

(Reference: Gabriele, Nienow and Simmons 2009)

$$\varepsilon_{de} = \upsilon_C \left[2\overline{\left(\frac{\partial w'}{\partial z}\right)^2} + 2\overline{\left(\frac{\partial v'}{\partial y}\right)^2} + 3\overline{\left(\frac{\partial w'}{\partial y}\right)^2} + 3\overline{\left(\frac{\partial v'}{\partial z}\right)^2} + 2\overline{\frac{\partial w'}{\partial y} \cdot \frac{\partial v'}{\partial z}} \right]$$

Eq. (2.5)

(υ_c is the continuous phase kinematic viscosity, the prime ' represents a variable minus its time-averaged value)

$$\varepsilon_{sgs} = (C_S \Delta)^2 \left[4\overline{\left(\frac{\partial w'}{\partial z}\right)^2} + 4\overline{\left(\frac{\partial v'}{\partial y}\right)^2} + 2\overline{\left(\frac{\partial w'}{\partial y}\right)^2} + 2\overline{\left(\frac{\partial v'}{\partial z}\right)^2} \right]^{3/2}$$

Eq. (2.6)

(C_s is the Smagorinsky constant, estimated at 0.17, and Δ is the grid scale which was approximately 0.27 mm.)

The two epsilon calculations ε_{de} and ε_{sgs} represented different properties: ε_{de} represented a calculation of ε based on eddies larger than the grid scale Δ, which was expected to be too small since it did not take into account the energy bearing eddies of scale between l_e and Δ (the "sub-grid" scales); ε_{sgs} represented an estimate of the true value of ε given a model for how much extra energy was contained in the sub-grid scales. Which was more suitable out of these two epsilon calculations, given the limitations of each, will be considered when comparing PIV to CFD in Chapter 4.

2.4.11 Comparison of gas bubble seeding to particle seeding

The PIV technique required seeding particles to be present in the flow, in order to reflect the laser light into the camera and allow images of the flow to be captured. One important attribute of the seeding particles was to follow the underlying flow accurately; this is quantified by the Stokes number, which is calculated in Appendix 4 for two choices of seeding particle. This appendix concluded that the silver seeding

particles used followed the flow closely, that gas bubbles present at high flow rates also followed the flow, and that to ensure a constant density of bubbles and particles to start at a high flow rate with only gas bubbles, and as flow rate was decreased, to add seeding particles as the gas bubbles decreased in density.

2.5   Results and Discussion

PIV results were obtained for a variety of orifices, flow rates, and both blade in and blade out. Results are first discussed for the middle size orifice for a medium flow rate and blade out; discussion is then widened to other flow conditions and geometries.

2.5.1   PIV velocity component distributions at selected points

PIV was carried out on a laboratory Sonolator with BLOUT-ZY setup, orifice size code 0110, and medium mass flow rate. (This was: blade out, ZY orientation of laser plane as per Figure 2.8, orifice size 0.011 in^2 or 7.10 mm^2 as given in Table 1.2, mass flow rate of 0.092 kg·s^{-1} as given in Table 2.1). Orifice superficial velocity was calculated as 12.9 m·s^{-1} and 500 image pairs were taken. The w and v components of velocity (in z and y directions respectively) were measured by cross-correlation at many points in (z, y) coordinates.
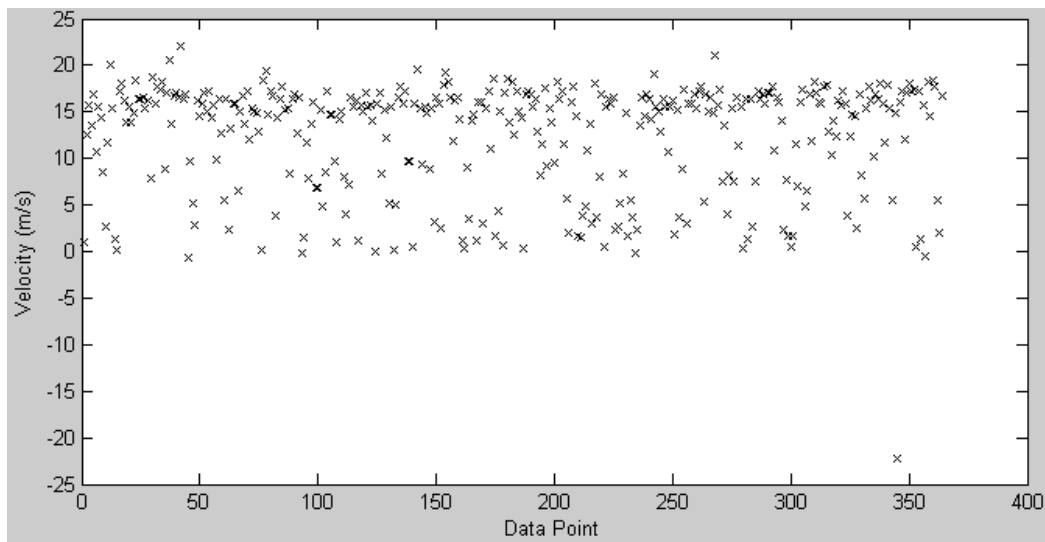
Figure 2.15: Time series of axial velocity (w) component 1 mm downstream from the orifice, blade-out setup; this is (z, y) = (1, 0) mm.

In Figure 2.15 the axial velocity (w) component measured 1 mm downstream of the orifice is given as a time series; this was located in the middle of the fast jet from the

orifice. Here 364 of the 500 vectors were valid, hence this number of data points were given. Most of the measurements were near to 15 m·s^{-1}, with 70% of the measurements in the range 10 m·s^{-1} to 20 m·s^{-1}. The remainder of the measurements were mostly in the range 0 m·s^{-1} to 10 m·s^{-1}. Only occasional scatter was outside the range 0 m·s^{-1} to 20 m·s^{-1}.
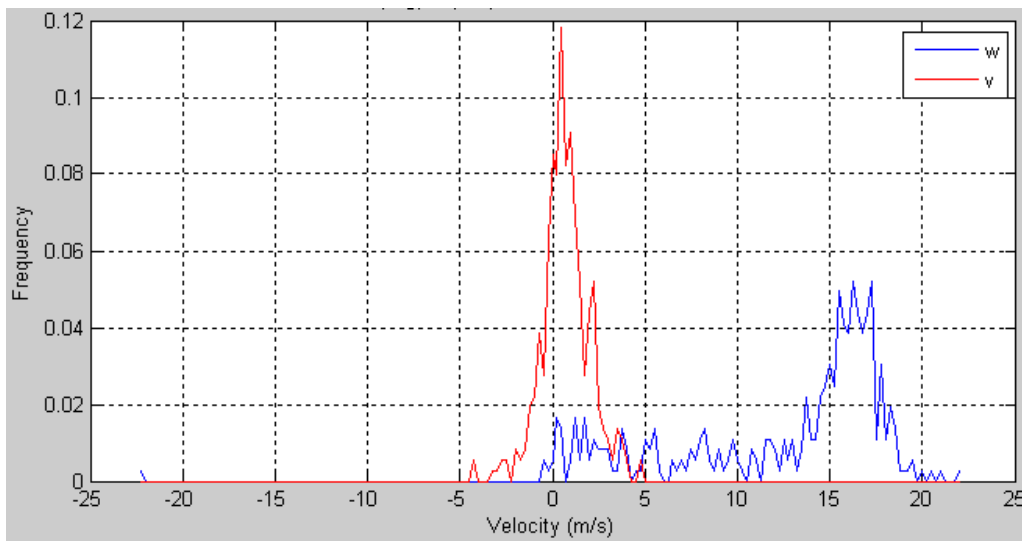
Figure 2.16: Velocity distributions in ZY plane 1 mm downstream from the orifice for both *w* and *v* velocity components, blade-out setup. Velocities grouped to nearest 0.25 m·s^{-1}.

In Figure 2.16 the distributions of each velocity component (*w*, *v*) are given 1 mm downstream from the orifice. The perpendicular component (*v*) was seen to be approximately normal and centred very close to 0 m·s^{-1}, with most measurements between -2.5 m·s^{-1} and +4 m·s^{-1}. The axial component (*w*) had a clear peak between 13 m·s^{-1} and 19 m·s^{-1} which agreed well with the superficial velocity of 12.9 m·s^{-1} since at the vena contracta the maximum flow velocity would be greater than the orifice superficial velocity. There was also a small amount of uniformly distributed noise from 0 m·s^{-1} to 23 m·s^{-1}, which may be explained as follows: in turbulent regions the particles move in all directions, including perpendicular to the laser sheet; particles

exiting or entering perpendicularly would introduce noise into PIV measurements which are based on cross-correlations from images of particles expected to be moving within the laser plane only.

The mean value of these measurements for w was 12.3 m·s^{-1}. The difference between the mean and the peak value (of 16 m·s^{-1}) was since the noise was equally distributed over 0 m·s^{-1} to 20 m·s^{-1}, and thus depressed the mean measurement slightly. This mean value still compared well with the orifice superficial velocity of 12.9 m·s^{-1}. In areas of lower velocity there was both less noise and a smaller range of noise making mean velocity component values approximately equal to peak values. Hence in general the peak PIV velocity in each component was measured using the mean value for that component.
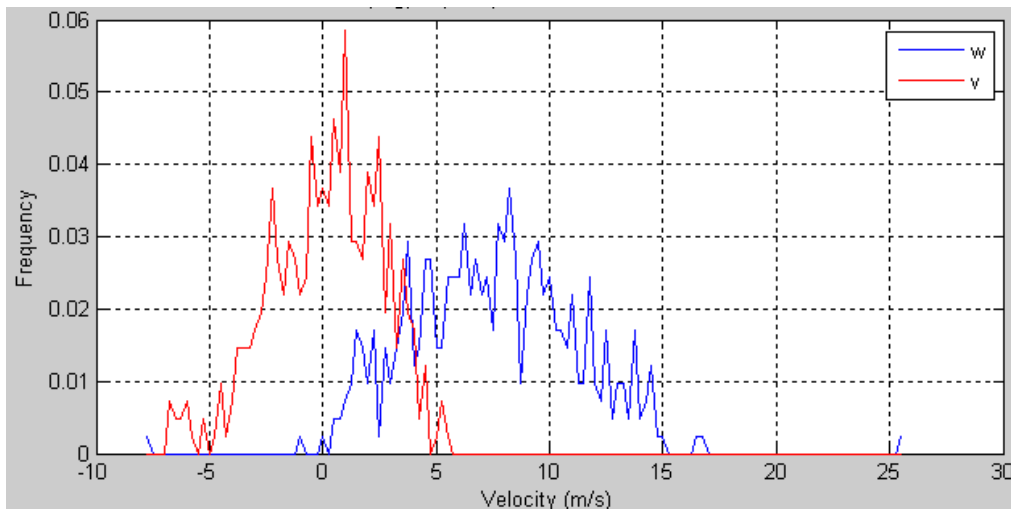
Figure 2.17: Velocity distributions 10 mm downstream from orifice for w and v components, blade-out setup.

In Figure 2.17 the w and v velocity distributions 10 mm downstream of the orifice are given. The number of valid measurements was now 410 out of 500. Again the perpendicular component (v) had zero average value; this time most values between -5 m·s^{-1} to +5 m·s^{-1} which was a wider range, thought to be due to turbulence.

The axial velocity component (w) had a single peak between 0 m·s^{-1} and 15 m·s^{-1}, with a peak value at around 8 m·s^{-1}, agreeing well with the mean value of 7.5 m·s^{-1} obtained from these data. Two outliers were still present, but were insignificant compared to the 408 remaining measurements. This time the noise could not be distinguished from the wide peak. Hence this peak represented a reliable PIV measurement. Generally it was found that as velocities reduced away from the orifice, the distributions became cleaner and the peak measurements coincided well with the mean values, hence the PIV measurements were more reliable in lower velocity regions.

2.5.2 Type of time dependent behaviour

Some types of measurement are static in time, but it was clear from Figure 2.15 that w component velocity measurements were varying in time due to the turbulence in the flow. The source of this time-variation was investigated, and several different sources were suggested. It was thought that the time-dependent measurement could be decomposed into a sum over all these sources:

- Time independent part of flow

- Macro-instability in flow

- Periodic variation in flow

- Turbulent variation in flow

- Measurement error from PIV technique

The relative contribution of each of these sources were considered in turn.

The flow after the orifice was seen to oscillate when observed through the test section; at higher speeds cavitation (Appendix 1) was present making the periodic oscillation visible; at lower speeds periodicity was also observed through PIV measurements (e.g. see Figure 2.22 later). Hence the time-dependent flow in the

74

Sonolator had a periodic element of a particular frequency corresponding to the oscillating jet coming from the orifice.

Macro-instabilities are defined as variations in the transient behaviour which are much slower than the periodic behaviour (Khan 2005) and have the effect of making the time-averaged behaviour look as though it is varying slowly. On the other hand, turbulent variation is of higher frequency than the periodic behaviour and tends to be noisy (i.e. a wide frequency spread). Finally, the measurement error is an extra noise factor added to everything else; it can be ignored as long as it is small compared to the measurement. The measurement error (noise in Figure 2.16, Figure 2.17) was small enough to ignore this term in the current work.
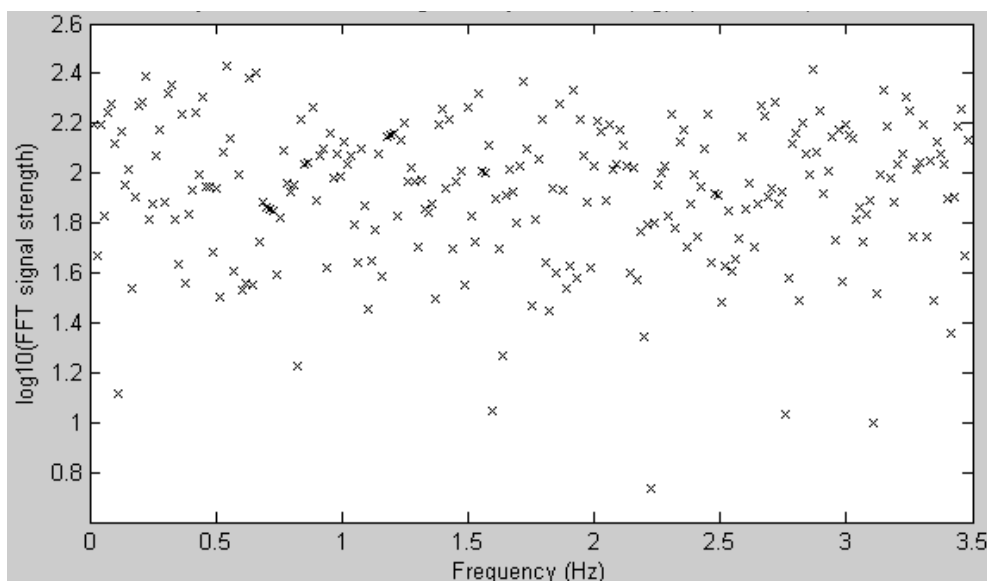
Figure 2.18: Scatter plot of FFT of time series.

In order to determine what type of time-varying behaviour was present in the time series given in Figure 2.15 for *w* data 1 mm after the orifice, the FFT of this data was taken (Figure 2.18). Note that invalid data points were replaced with the mean of the valid vectors to ensure correct timing of all data. The original PIV measurements were at a rate of 7 Hz, so this FFT measured 500 frequencies equally spaced between 0 Hz

and 7 Hz. Due to frequency cross-over (which occurs at half the sample rate), the maximum unique measurement was at 3.5 Hz (the Nyquist frequency).

Within the frequency range of 0 Hz to 3.5 Hz there was no large peak at any individual frequency. Hence the FFT showed noise, which was compatible with the hypothesis that the time variation was turbulent in origin. However, since fast jet oscillation had already been visually observed, the oscillation frequency must have been greater than 3.5 Hz, so not distinguishable from turbulence in these measurements. But more positively, macro-instabilities could almost certainly be ruled out since they would have low frequencies in the range measured in the FFT; the lack of sharp peaks indicated no macro-instabilities were present.

The conclusion from this was that the velocity measurement was the sum of three components: a time-averaged value, a periodic value, and a turbulent value. Since the period could not be found from the data set (due to the low sampling frequency of 7 Hz), the periodic and turbulent values could not be separated and are hereafter analysed together. Later on, to aid the comparison between CFD and PIV, this same approach will be taken to analyse the CFD data. Note however that the failure to separate out the periodic flow increases the apparent values of turbulent kinetic energy and dissipation rates.

2.5.3   Independence of consecutive measurements

A large number of independent measurements were required in order to obtain a meaningful time-average. In the worst case scenario, if all 500 measurements were taken very quickly they would all be roughly equal, be highly correlated with each other, and fail to give a meaningful time-average. However, these measurements were

taken at a relatively low frequency of 7 Hz. Analysis was carried out to check if consecutive measurements were independent.
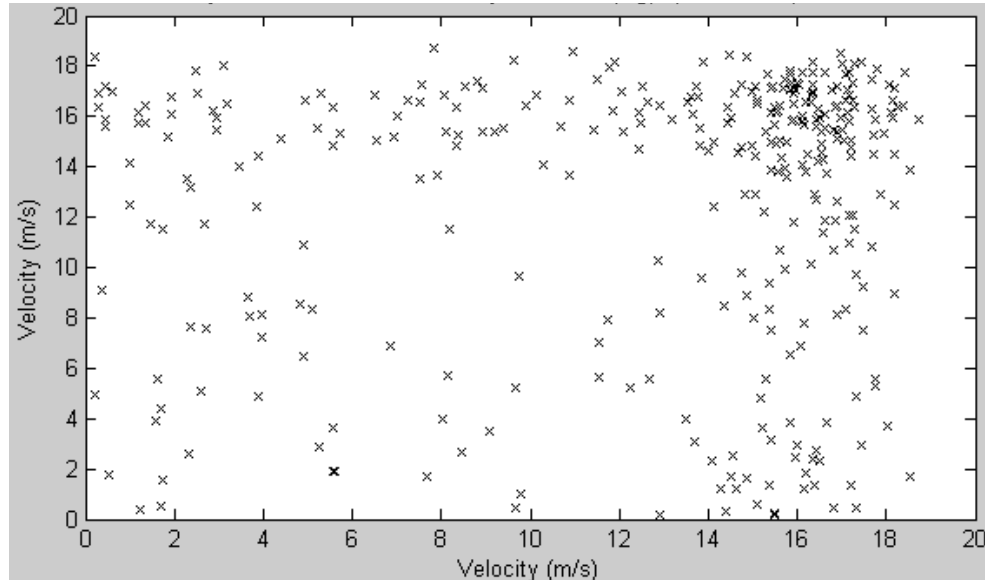
Figure 2.19: Scatter plot of consecutive *w* components 1 mm after the orifice.
Outliers have been removed.

In Figure 2.19 consecutive velocity measurements were plotted against each other on a scatter diagram. If these data were not independent the shape of the data would cluster around either positive or negative diagonal lines (commonly denoted "*y = x*" and "*y = -x*" respectively). In fact, by examining the velocity region 0 m·s^{-1} to 20 m·s^{-1} the overall data pattern was found to be rectangular, and hence uncorrelated. Similarly, taking the subset in the region 13 m·s^{-1} to 19 m·s^{-1} no clustering was found, hence these data from the peak velocity region were also uncorrelated. This indicated that consecutive velocity measurements were independent, and that the 500 measurements taken represented a wide range of transient flow patterns suitable for a time-average.

2.5.4   Statistical convergence of PIV measurements at selected points

A time-averaged *w* component of velocity was obtained for the data in Figure 2.15; the value was 12.3 m·s^{-1}. To show that this averaged value had converged after

measurements from 500 image pairs had been taken, time-averages were constructed from 1, 2, 3, …, 499, 500 image pairs, and the series of averages plotted against number of points used. This process was also carried out for a function of TKE ($k^{1/2}$) calculated from variances of one or both velocity components w and v.
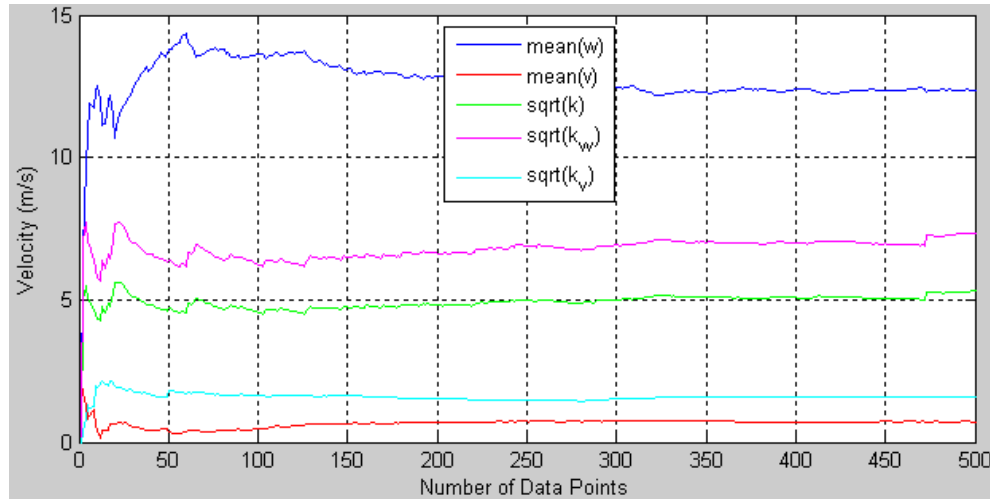
Figure 2.20: Velocity and TKE convergence 1 mm downstream of orifice.

In Figure 2.20 the convergence of velocity components and TKE calculations is shown after between 1 and 500 image pairs, for data 1 mm after the orifice. All data series were found to converge to an accuracy of ±5% of the final value well before the end of 500 image pairs, and in fact as few as 200 frames were seen to give suitable accuracy in these variables. (Note that by taking square roots of k, all units were in m·s^{-1} so could be plotted on the same axes, in fact k was linearly related to standard deviation of velocity components.)

These graphs also shed light on the isotropy of the turbulence 1 mm after the orifice. Turbulent kinetic energy (k) by definition is equal to 0.5 times the sum of variances of u, v and w components of velocity; however u was not available from 2D PIV in the BLOUT-ZY setup. Using an isotropic assumption, k was estimated to be 0.75

times the variance of w and v velocity components, e.g. Eq. (2.4), and k_w (from w alone) was estimated to be 1.5 times the variance of w; similarly for k_v.

If the flow was isotropic then $k = k_w = k_v$; conversely in Figure 2.20 the fact that each version of k converged to different values showed that the turbulence was not completely isotropic just after the orifice.
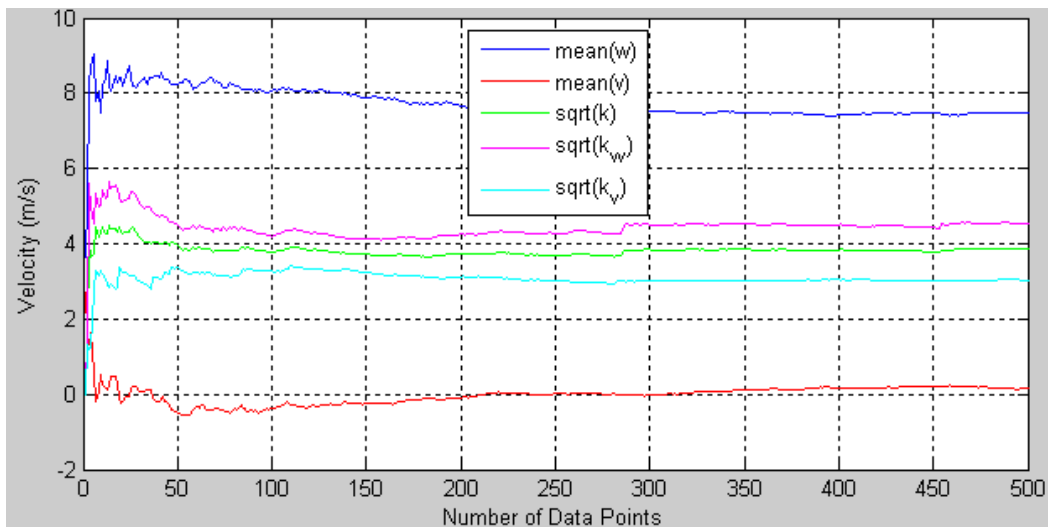
Figure 2.21: Velocity and TKE convergence 10 mm after the orifice.

The same comparison was made in Figure 2.21 for convergence of velocity and TKE values 10 mm after the orifice. Again, velocities and TKE values were found to converge well before 500 data points were averaged. This time the three versions of k were found to be similar, showing that there was greater turbulence isotropy further from the orifice.

By considering convergence at other points too, generally it was found that turbulence was only non-isotropic close to the orifice, and that far from the orifice $k_w = k_v$ and that the isotropic assumption held.

2.5.5   PIV instantaneous velocity fields

For the 500 sets of PIV vectors, two typical sets are illustrated below. Note that the orifice was at $(z, y) = (0, 0)$:
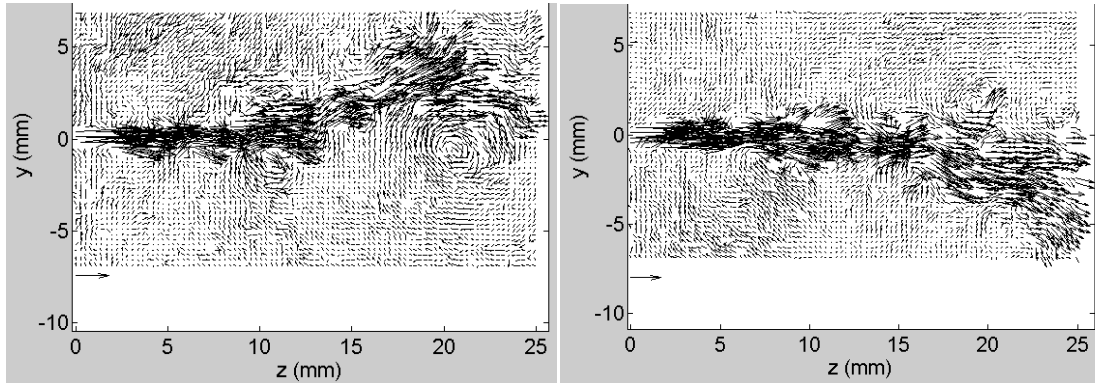
Figure 2.22: Vector plots of instantaneous flow in BLOUT setup, ZY plane, 0110 orifice, 0.092 kg·s^{-1}. Two different times illustrated at 24.6 s (left) and 38.4 s (right). Scale vector shown at bottom is 10 m·s^{-1}.

In Figure 2.22 the instantaneous velocity field in the 2D laser plane was plotted for two distinct times. These were chosen to illustrate a mode of oscillation of the jet. The main features of the flow were: a jet emanating from the orifice, a relatively quiet region surrounding the jet, unsteady behaviour as shown by changes between the two frames, turbulence as evidenced by local random velocity gradients and small velocity eddies of all scales.

2.5.6   PIV time-averaged velocity fields

Given 500 sets of PIV vectors similar to those illustrated in the previous section, time-averaging was carried out at every (z, y) coordinate for all valid vectors at that coordinate, typically 350 to 450 in number. A time-averaged set of velocity vectors was thus obtained.
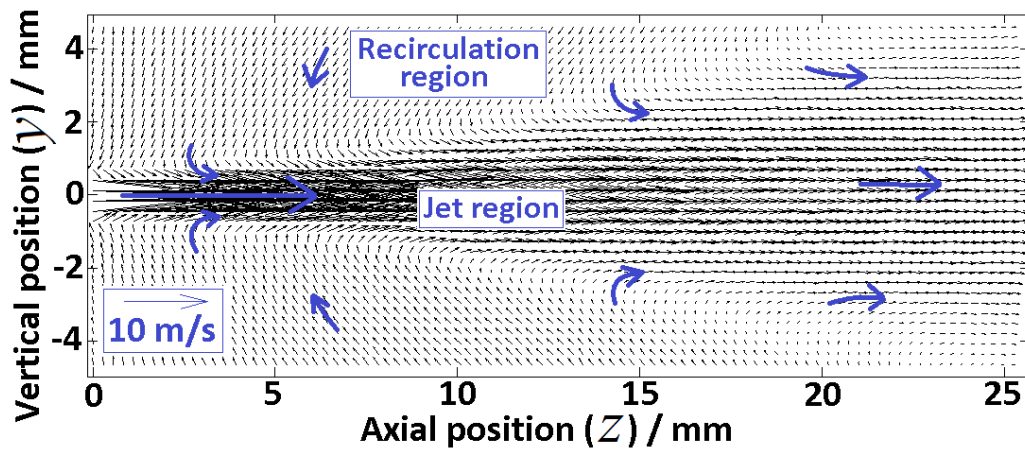
Figure 2.23: Vector plot of time-averaged flow (BLOUT-ZY, 0110 orifice, 0.092 kg·s^{-1}).

The time-averaged vector plot in Figure 2.23 was seen to be symmetrical about the Sonolator axis (z axis), even though the individual vector fields (Figure 2.22) were asymmetric. The time-averaged plot has been enhanced by displaying with bold vectors some local flow patterns, which reveal the two main regions of flow: the jet and the recirculation. The recirculation was much more clearly visible on Figure 2.23 than in the snapshots in Figure 2.22, and showed that fluid was pulled in towards the orifice by the fast moving jet.
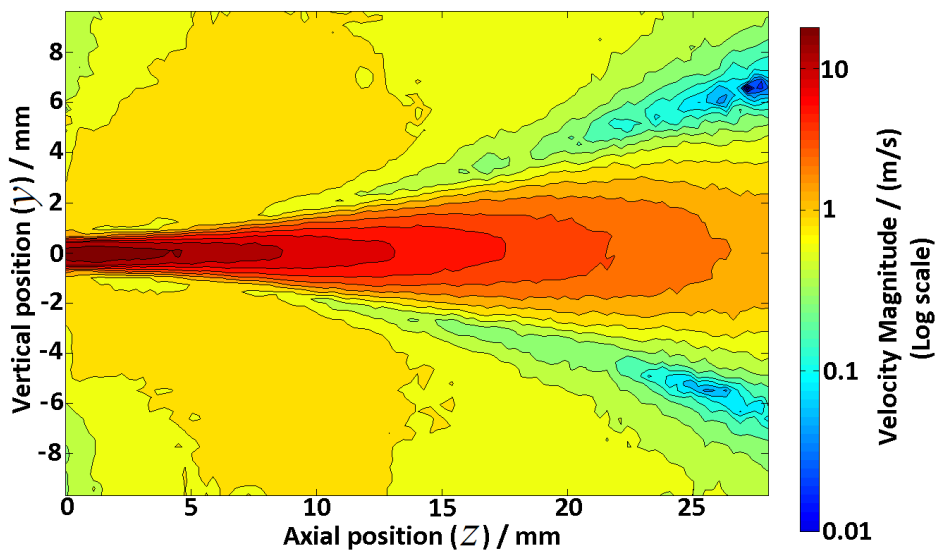
Figure 2.24: Contour plot of velocity magnitudes.

A contour plot was created (Figure 2.24) of the magnitudes of the time-averaged velocity vectors from Figure 2.23. This clearly distinguished the jet and recirculation regions, and showed that the peak jet velocity was above 10 m·s^{-1}, and that the average recirculation velocity above and below the orifice was of the order of 1 m·s^{-1}. This recirculation velocity was an order of magnitude greater than the main chamber superficial velocity of 0.1 m·s^{-1} (the main chamber diameter was 35 mm). Since the colour bands were on a logarithmic scale and in the jet these bands were equally spaced, velocity magnitude in the jet was seen to decrease at an exponential rate in the region plotted.

In addition, calculations showed that the averaged jet in Figure 2.24 (and Figure 2.23) widened at around 9°, although from the snapshots in Figure 2.22 the actual jet was narrower than this; the difference was attributed to the blurring effect of the process of averaging the vector fields.

2.5.7   Cavitation, particle speed and limitations of PIV accuracy

Not all PIV experiments were equally accurate in every spatial location. Two velocity-related issues reduced PIV accuracy: presence of cavitation, and inability to reduce the laser pulse separation below 5 µs, in addition laser alignment issues were apparent in the BLOUT-ZX setup, and blade alignment in BLDIN-ZY. The cavitation is highlighted in the following set of figures, which also includes important flow statistics.

0037 BLOUT-ZY
0.0363 kg·s⁻¹
15.2 m·s⁻¹
8 μs, 7.1 px
ΔP = 172.4 kPa

0037 BLOUT-ZY
0.0913 kg·s⁻¹
38.4 m·s⁻¹
5 μs, 11.2 px
ΔP = 1094.0 kPa

0110 BLOUT-ZY
0.0463 kg·s⁻¹
6.5 m·s⁻¹
7 μs, 2.6 px
ΔP = 34.5 kPa

0110 BLOUT-ZY
0.0917 kg·s⁻¹
12.9 m·s⁻¹
5 μs, 3.7 px
ΔP = 137.9 kPa

0110 BLOUT-ZY
0.1822 kg·s⁻¹
25.8 m·s⁻¹
5 μs, 7.4 px
ΔP = 540.1 kPa

0140 BLOUT-ZY
0.0467 kg·s⁻¹
5.2 m·s⁻¹
15 μs, 4.6 px
ΔP = 20.7 kPa

0140 BLOUT-ZY
0.0918 kg·s⁻¹
10.2 m·s⁻¹
7 μs, 4.3 px
ΔP = 82.7 kPa

0140 BLOUT-ZY
0.1825 kg·s⁻¹
20.3 m·s⁻¹
5 μs, 6.1 px
ΔP = 326.4 kPa

Figure 2.25: PIV images (pseudocolour scale) with some cavitation. Statistics
for orifice size code, geometry, mass flow rate, orifice superficial velocity,
laser pulse separation, number of pixels moved by a particle travelling at
orifice superficial velocity, pressure drop across the Sonolator. Vertical
height of images is 14 mm.

Figure 2.25 shows PIV images for the eight main combinations of orifice size and
flow rate investigated. Images are for BLOUT-ZY setup only, however the statistics are
valid for the corresponding BLOUT-ZX and BLDIN-ZY setups too. The pseudocolour
scale used here has black or dark blue for background pixels, and light blue to green and
red colours for particle pixels.

For each orifice size cavitation was present at the highest flow rate and not at the lower flow rates. Cavitation was seen as non-circular regions of continuous green or red pixels, since cavitation scattered laser light efficiently in all directions, including into the camera. Cavitation after the orifice was high for 0037 orifice at $0.092\,\mathrm{kg\cdot s^{-1}}$, medium for 0110 orifice at $0.182\,\mathrm{kg\cdot s^{-1}}$, and only in isolated regions showing up as bright specks larger than a particle for 0140 orifice at $0.182\,\mathrm{kg\cdot s^{-1}}$.

The cavitation interfered with PIV cross-correlation due to the lack of point particles in cavitation regions. This measurement inaccuracy was confined to where cavitation occurred, which was in the region directly after the orifice.

Another reason why PIV measurements were inaccurate in some regions was due to fast local velocities. The minimum laser pulse separation available on the equipment was 5 µs. The maximum number of pixels a particle was allowed to travel to obtain a valid velocity vector was 8 px (a quarter of an IA). In Figure 2.25 statistics are given for both the laser pulse separation and the number of pixels travelled when travelling at the orifice superficial velocity. In cases where this travel distance was 6.1 px or less PIV gave good measurements, but for 7.1 px or greater PIV accuracy was not good. This may be because in the latter case turbulence randomly pushes local travel distances over 8 px, invalidating some vectors at random.

Note − laser pulse separations could have been reduced further in Figure 2.25 for experiments with 0037 orifice, to gain some additional accuracy at the orifice, however experimental time was not available to repeat these experiments, so they remain as further work.

An additional source of inaccuracy which affected the BLOUT-ZX setup much more than the BLOUT-ZY setup was sensitivity to laser sheet alignment. In the

experimental rig used, fine adjustments to the laser sheet position were achieved by tightening screws on the laser mount. The lack of a computer controlled traverse for the laser (as well as the camera) meant that laser sheet accuracy (of a sheet 1 mm thick) was around ±0.25mm perpendicular to the target. For BLOUT-ZY setup this was sufficient accuracy since the laser sheet was aimed at the plane through the centre of the long axis of the orifice, a large target. For BLOUT-ZX setup the target was the orifice short axis, less than 2 mm in length, making the error bounds of laser sheet position comparable with the size of the target and giving unreliable positioning and velocity data. Further work ought to use a computer controlled traverse for the laser in order to achieve greater positioning accuracy.

For BLDIN-ZY setup the front of the blade ought to be positioned exactly in front of the long axis of the cats-eye shaped orifice, as per the industrial Sonolator. However, the blade had been redesigned as a single long thin piece of metal, to allow PIV measurements directly above the blade. It was anchored to a fixed support at the end of the main chamber, with very limited range of repositioning. Due to this design it was not possible to reposition it any more accurately than approximately ±0.5 mm from the centreline. Hence, the blade was not exactly in line with the orifice, in addition its small oscillations would be of a different size to the much stiffer blade in the industrial Sonolator. These gave limitations in the accuracy of the PIV measurements at the front of the blade, if these were compared to hypothetical PIV measurements from the original industrial system (unobtainable due to being made from steel).

Hence due to these three potential or actual sources of inaccuracy, PIV measurements near the orifice were sometimes adversely affected, however well away from the orifice the measurements were thought to be accurate. At the orifice the

measurements were thought to be accurate for geometry BLOUT-ZY, using orifice 0110 at low and medium flow rates or using orifice 0140 at low to high flow rates. For geometry BLDIN-ZY most corresponding measurements were thought accurate except for just downstream of the blade edge, due to blade positioning error.

2.5.8   PIV velocity graphs

Graphs were created of the velocity magnitude along a line of interest within the flow field. The line was either in the axial direction (z) or in a cross-sectional direction (y or x; only y used due to BLOUT-ZX laser plane alignment issues). Various orifices and flow rates were investigated, for both blade out (BLOUT) and in (BLDIN).

2.5.8.1   Velocity magnitude along Sonolator axis

Velocity magnitudes were compared along the Sonolator axis with the blade out, for different orifices and flow rates. The Sonolator produces a jet directly after the orifice, along the Sonolator axis. The highest velocity magnitude along this axis should therefore be slightly larger than the orifice superficial velocity, due to the presence of a vena contracta where the recirculating flow squeezes the jet and increases its velocity slightly.
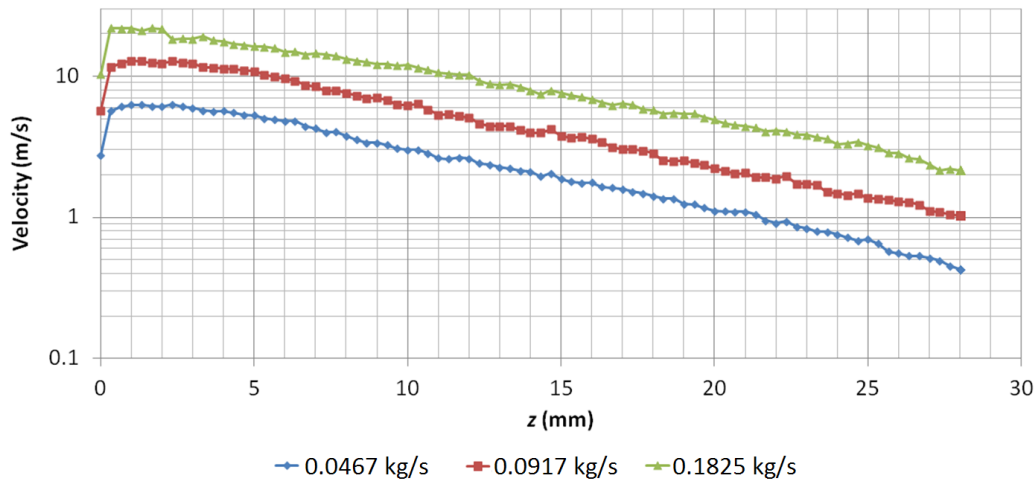
Figure 2.26: Graph of Velocity Magnitude along the Sonolator axis for
orifice size 0140, geometry BLOUT-ZY; low, medium and high mass flow
rates given; orifice superficial velocities 5.2 m·s^{-1}, 10.2 m·s^{-1}, 20.3 m·s^{-1}
respectively; main chamber superficial velocities 0.05 m·s^{-1}, 0.1 m·s^{-1},
0.2 m·s^{-1} respectively.

For the 0140 orifice the peak velocities were obtained 1 mm to 2 mm after the

orifice and were slightly larger than the orifice superficial velocity in each case, see

Figure 2.26. In addition, velocity decayed exponentially in each case (note that the

velocity axis is plotted on a logarithmic scale); the decay rate was constant, with

velocity halving every 7 mm downstream of the orifice. By the end of the measurement

each velocity was still well above its main chamber superficial velocity. The mass flow

rates were in approximate ratio 1:2:4, and the velocities scaled in the same ratios.

Therefore, PIV measurements were deemed realistic for orifice 0140, and thought to be

accurate.
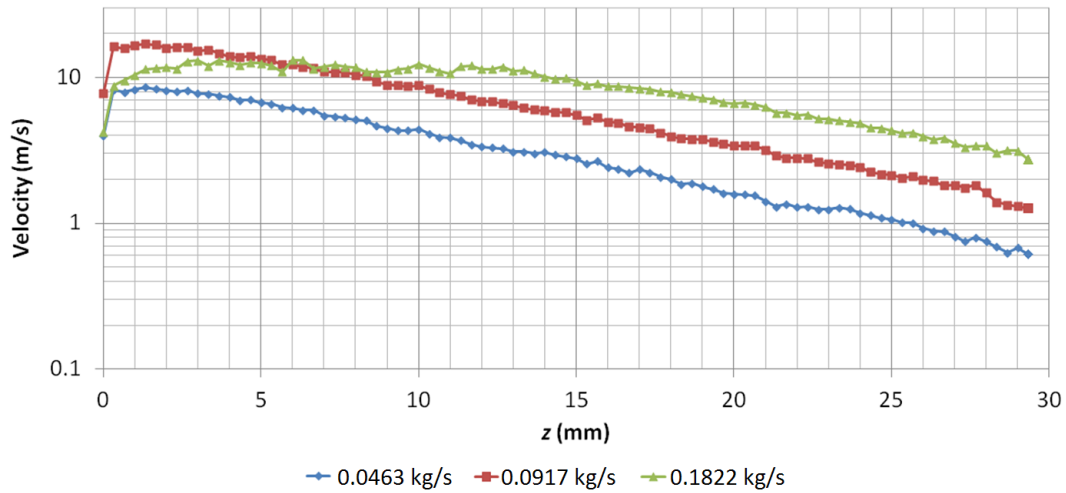
Figure 2.27: Velocity magnitude on the Sonolator axis: 0110, BLOUT-ZY; low, medium and high mass flow rates given; orifice superficial velocities 6.5 m·s^{-1}, 12.9 m·s^{-1}, 25.8 m·s^{-1} respectively; main chamber superficial velocities 0.05 m·s^{-1}, 0.1 m·s^{-1}, 0.2 m·s^{-1} respectively.

For the 0110 orifice three flow rates are illustrated in Figure 2.27. For the two lower flow rates the peak velocities and velocity profiles had similar features to those described previously for the 0140 orifice. For the highest flow rate, downstream of 15 mm the velocity profile was as expected; however before 15 mm it was different to expectations; there was a velocity plateau (circa 12 m·s^{-1}) from 2 mm to 15 mm; this was well below the orifice superficial velocity of 25.8 m·s^{-1}. Hence the PIV measurement in this case was unphysically small. Investigation of individual PIV images (see Figure 2.25 centre-right) showed a cavitation region present where measurements were thought to be inaccurate. Hence this gave evidence that large cavitation regions adversely affected accuracy of PIV measurements.

In addition, looking back at Figure 2.26 for the high flow rate the velocity profile near the orifice looked slightly diminished, and comparing with Figure 2.25 (bottom-right), it seemed that even small regions of cavitation which were larger in extent than particle size could adversely affect PIV accuracy.
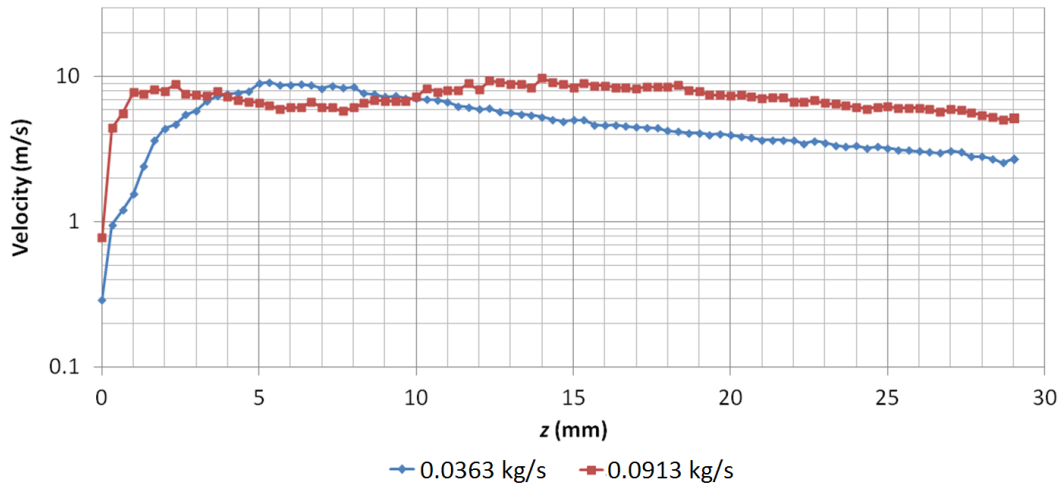
Figure 2.28: Velocity magnitude on the Sonolator axis: 0037, BLOUT-ZY;
low and high mass flow rates given; orifice superficial velocities 15.2 m·s^{-1},
38.4 m·s^{-1} respectively; main chamber superficial velocities 0.04 m·s^{-1},
0.1 m·s^{-1} respectively.

For orifice 0037 two flow rates were plotted in the same way, see Figure 2.28. In
neither case was the orifice superficial velocity reached, so in both cases unphysical
behaviour was found, indicating inaccuracy of the PIV technique.

The PIV images were examined, and for the higher flow rate (Figure 2.25
top-right) a large amount of cavitation was shown over much of the flow field. However
the lower flow rate had a different problem: a particle would move 7.1 px between laser
pulses at orifice superficial velocity (Figure 2.25 top-left). Since turbulence and the
vena contracta could together increase particle travel above 8 px in the 500 PIV frames,
a large number of higher-velocity vectors would become invalidated, leaving only low
velocity vectors and a time-averaged measurement which was too small, explaining the
inaccuracy for the low flow rate near the orifice. However, for 0037 far from the orifice
(20 mm to 25 mm) the scaling between the velocity profiles was reasonable.
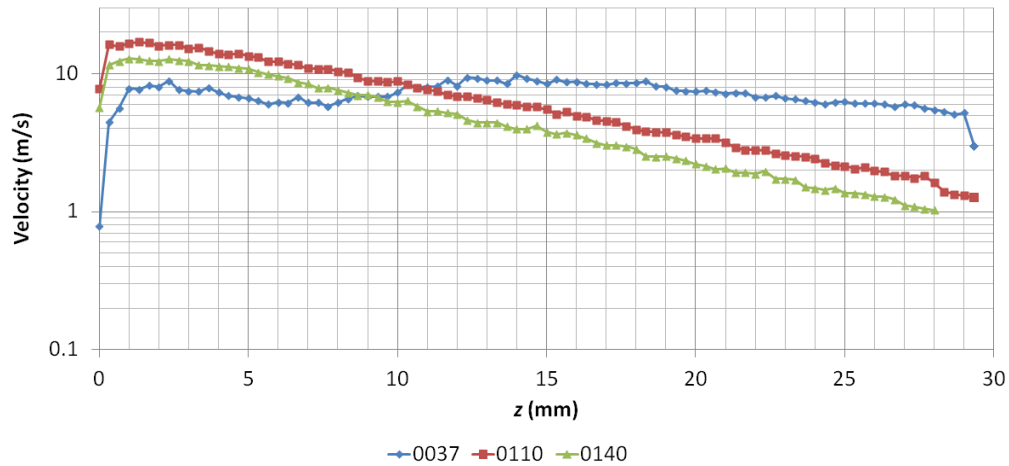
Figure 2.29: Velocity magnitude on the Sonolator axis for three orifice sizes
0037, 0110 and 0140; BLOUT-ZY, 0.092 kg·s^{-1}; orifice superficial velocities
38.4 m·s^{-1}, 12.9 m·s^{-1}, 10.2 m·s^{-1} respectively; main chamber superficial
velocity 0.1 m·s^{-1}.

In Figure 2.29 the velocity values shown for orifices 0110 and 0140 were as expected and obeyed the characteristics shown before, however the curve for orifice size 0037 (with cavitation in Figure 2.25 top-right) was unphysical near the orifice. Away from the orifice (20 mm) the velocity measurements were physical, since for the three orifices the three curves were in the correct order.

Overall, the graphs of velocity magnitude vs axial distance, for various flow rates and orifices, revealed characteristic behaviour for accurate PIV measurements, and all exceptions were found to be due to limitations or inaccuracies in the PIV measurement technique.

2.5.8.2   Velocity magnitude in jet cross-section

Velocity magnitudes were compared in a short line in the y direction, a short line cutting across the flattened jet flow cross-section in the thin direction, at various distances (z) from the orifice.
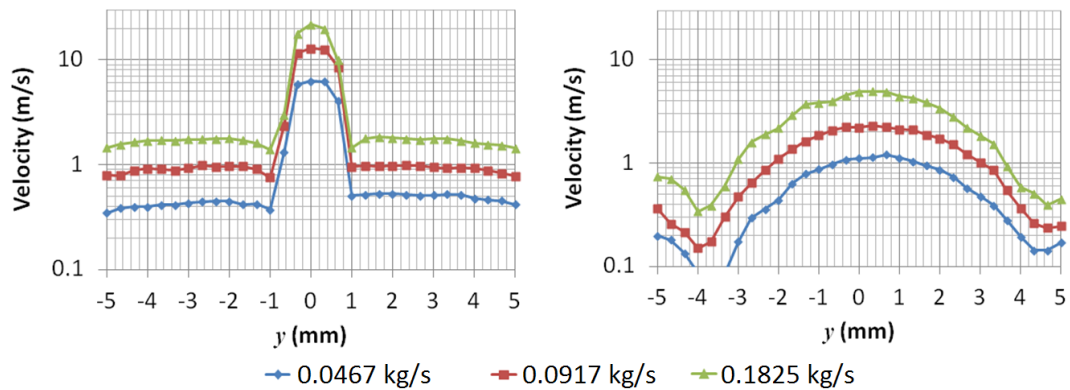
Figure 2.30: Velocity magnitude 1 mm (left) and 20 mm (right) after the orifice on a line in the *y* direction (aligned with short direction of orifice). Orifice type **0140**; BLOUT-ZY, three flow rates illustrated with orifice superficial velocities 5.2 m·s⁻¹, 10.2 m·s⁻¹, 20.3 m·s⁻¹ respectively; main chamber superficial velocities 0.05 m·s⁻¹, 0.1 m·s⁻¹, 0.2 m·s⁻¹ respectively.

For the 0140 orifice, velocity magnitude along a line in the *y* direction was plotted for three flow rates at 1 mm (Figure 2.30, left) and 20 mm (Figure 2.30, right) downstream from the orifice. As expected for a flattened jet, in all cases the peak in velocity magnitudes was sharp near to the orifice (left), and smoothed out with lower magnitude further downstream (right). The peak velocity was seen in the centre in all cases. A scaling pattern was seen: the flow rates were in the ratio 1:2:4, and the scaling between the curves was 1:2:4 everywhere except for the highest flow rate close to the orifice, where cavitation slightly suppressed the PIV reading as noted above.
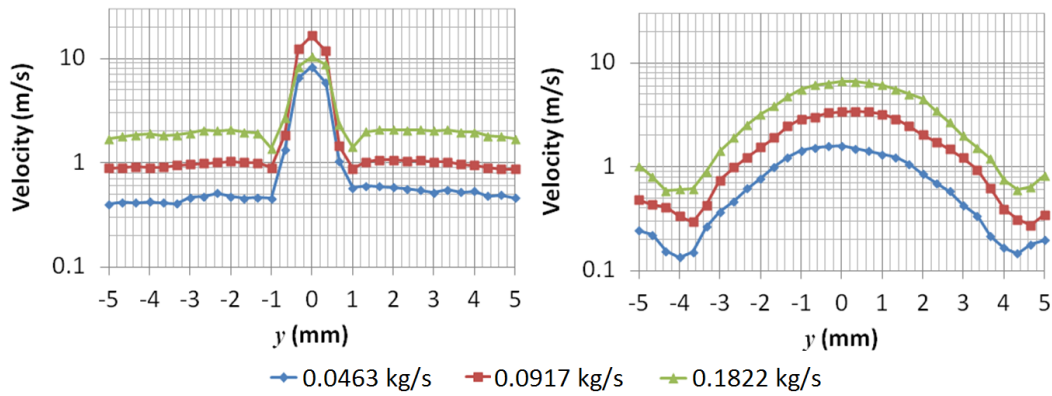
Figure 2.31: Velocity magnitude 1 mm (left) and 20 mm (right) after the orifice on a line in the *y* direction. Orifice type **0110**; BLOUT-ZY, three flow rates illustrated with orifice superficial velocities 6.5 m·s⁻¹, 12.9 m·s⁻¹, 25.8 m·s⁻¹ respectively; main chamber superficial velocities 0.05 m·s⁻¹, 0.1 m·s⁻¹, 0.2 m·s⁻¹ respectively.

Similar analysis was carried out for the 0110 orifice (Figure 2.31) with generally the same results found. The scaling seen was again 1:2:4 everywhere except near to the orifice for the highest flow rate; a larger amount of velocity suppression for the PIV readings for 0110 orifices was found than for the 0140 orifice; this was due to more cavitation for the 0110 orifice.
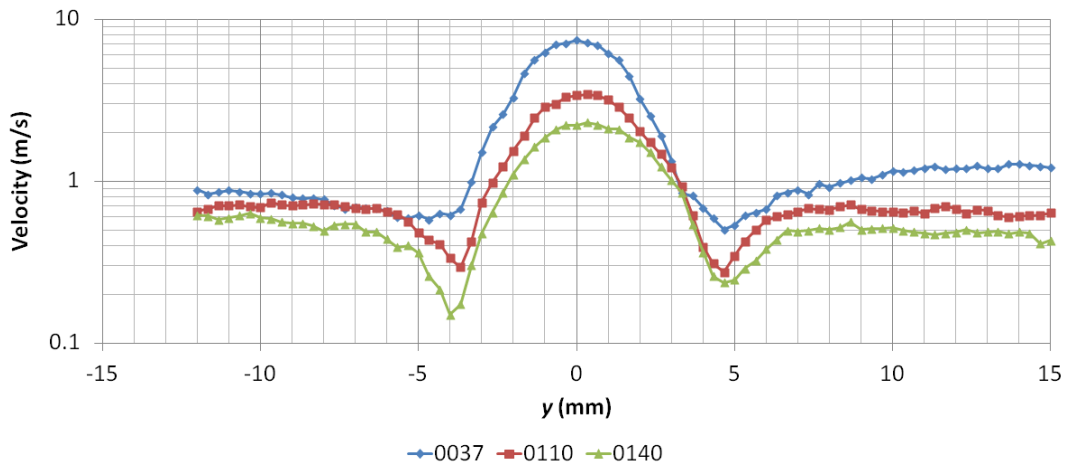
Figure 2.32: Velocity magnitude 20 mm after the orifice on a line in the *y* direction. Orifice types 0037, 0110, 0140 illustrated; BLOUT-ZY, 0.092 kg·s⁻¹; orifice superficial velocities 38.4 m·s⁻¹, 12.9 m·s⁻¹, 10.2 m·s⁻¹ respectively; main chamber superficial velocity 0.1 m·s⁻¹.

92

For the 0037 orifice a similar comparison of velocity magnitudes in cross-section for different flow rates was less meaningful due to the amount of measurement inaccuracy close to the orifice due to cavitation and long laser pulse gap.

However, far from the orifice a comparison of velocity magnitudes in cross-section for the same flow rates and for different orifice sizes was carried out (Figure 2.32). Peak velocity magnitudes were in increasing order for decreasing orifice size, which indicated that far from the orifice the 0037 results were of the right order of magnitude.

2.5.8.3 PIV comparisons with Blade In

With the blade in it was not possible to obtain velocity measurements on the Sonolator axis since the blade covered this region up, however measurements could be obtained in various cross-sections in the *y* direction.
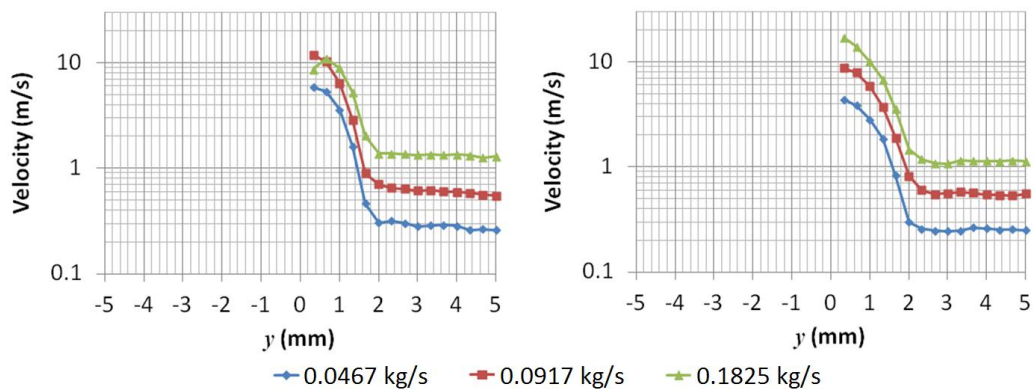
Figure 2.33: Velocity magnitude 5 mm (left) and 10 mm (right) after the orifice on a line in the *y* direction (aligned with short direction of orifice). Orifice type **0140**; BLDIN-ZY, three flow rates illustrated with orifice superficial velocities 5.2 m·s^{-1}, 10.2 m·s^{-1}, 20.3 m·s^{-1} respectively; main chamber superficial velocities 0.05 m·s^{-1}, 0.1 m·s^{-1}, 0.2 m·s^{-1} respectively.

For the 0140 orifice, velocity magnitudes were obtained on a line in the *y* direction, 5 mm and 10 mm from the orifice, for three different flow rates (Figure 2.33). The scaling relationship was good between these results everywhere except for the

highest flow rate next to the blade. This was due to cavitation as seen in Figure 2.34. The blade blocked out half of the PIV measurements, however the remaining half looked similar to the blade out measurements (e.g. Figure 2.30, although these were at different z coordinates). The boundary layer velocity gradient next to the blade was too thin to be captured, so the effect of the blade seen was merely to truncate the flow field.
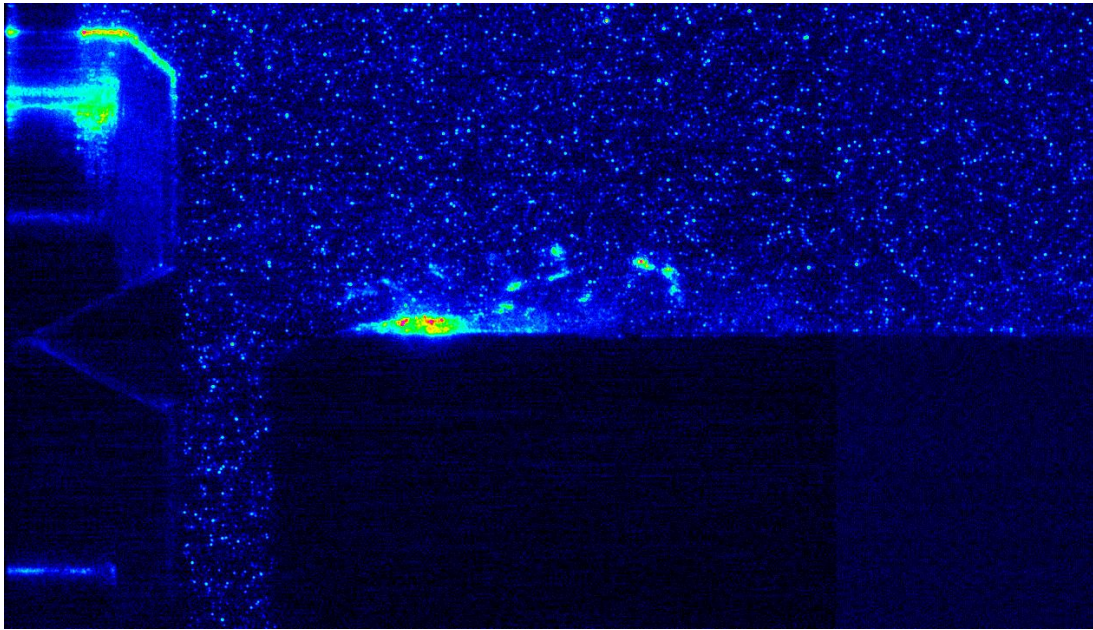
Figure 2.34: PIV image for 0140 BLDIN-ZY 0.182 kg·s^{-1}.

Figure 2.34 shows a typical PIV image for the Sonolator, blade in, above the onset of cavitation. Cavitation was seen next to the blade, behind the sharp edge. Although the blade was not necessary to create cavitation, it did seem to make the onset of cavitation slightly sooner (c.f. Figure 2.25 bottom-right).

The limitation in blade alignment accuracy can be seen in Figure 2.34. All possible care was taken when installing the blade within the Perspex section in order to position the edge of the blade in line with the orifice. The front of the 0140 orifice is 2.25 mm wide for comparison; here the sharp edge of the front of the blade is slightly below the centreline given by the orifice, the typical accuracy from such observations

was ±0.5 mm. As for the effect of blade-positioning accuracy upon the results, this is better examined later on during PIV-CFD comparison, since in CFD the blade edge was always exactly central.

2.5.8.4   Other PIV velocity comparisons

A comparison was also made between 0140 BLDIN-ZY and 0140 BLOUT-ZY (not illustrated, for brevity). Similar velocity magnitudes were found at 1 mm, 5 mm and 10 mm downstream from the orifice, in particular the cross-sectional velocities at 1 mm in the jet were very close. At 20 mm downstream from the orifice the velocity magnitude was higher for BLDIN setup; this was probably due to the fact that the blade guided the jet and so a coherent velocity structure was maintained for longer in the BLDIN setup; conversely in the BLOUT setup each result was the average of 500 individual results, in which the jet pointed in different directions; this lack of coherence meant that the jet dissipated sooner after the orifice.

A comparison between different flow rates was also carried out for BLDIN setup for 0110 and 0037 orifices. It has not been illustrated here since the observations were in line with what was observed for the 0140 BLDIN setup given above. The BLDIN data will be presented further in Chapter 4 as part of the PIV / CFD comparison.

2.5.9   Turbulence statistics at various flow rates

Turbulent kinetic energy (TKE, k) and local specific turbulent energy dissipation rate (epsilon, ε) were also estimated; k is given in Eq. (2.4), and the two estimates for ε are given in Eq. (2.5) for ε_{de} and Eq. (2.6) for ε_{sgs}. These were compared on the axial line for 0140 BLOUT-ZY setup for three different mass flow rates; the largest orifice size was used since its data was previously found to be the most accurate.
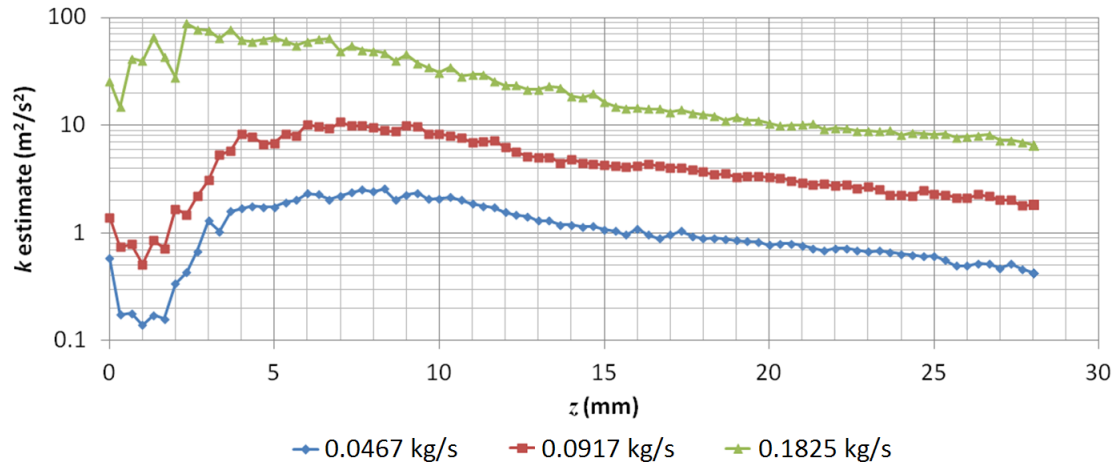
Figure 2.35: Graph of k estimate for 0140 BLOUT-ZY for three different
mass flow rates.

The mass flow rates were in the ratio 1:2:4. Dimensional considerations showed that the corresponding k measurements (Figure 2.35) should be in the ratio 1:4:16, which are the squares of the previous ratios. This is since k is proportional to a sum of variances of components of velocity, and each variance is the square of a standard deviation with units of velocity, see Eq. (2.4). These ratios of 1:4:16 were observed further away from the orifice after around 10 mm. Nearer the orifice, the two lower flow rates maintained 1:4 ratio, with a reduction in k at 1 mm and peak at around 8 mm, but the highest flow rate had different behaviour, with k peaking at around 3 mm. Due to the lack of proportionality, the measurements for high flow rate were suspect. An explanation could be that since a little cavitation was known to occur at this high flow rate, this allowed low velocity vectors to be erroneously generated, which would provide a larger variance in velocity component and erroneously high k values. Hence it was thought that the k values for the two lower mass flow rates were accurate, but those for the high flow rate were only accurate away from the orifice. The comparison with CFD (later) was necessary to shed more light on this.
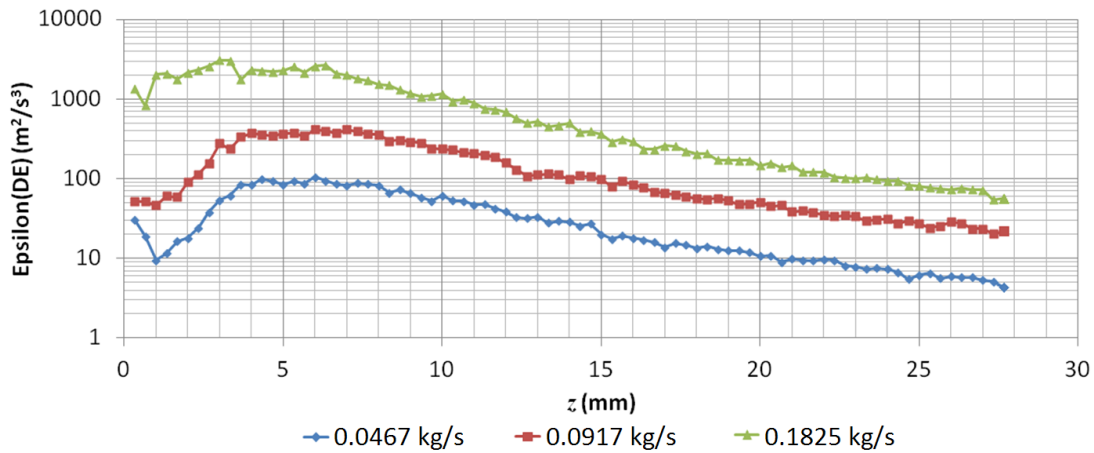
Figure 2.36: Graph of ε_{de} estimate for 0140 BLOUT-ZY for three different mass flow rates.

The variable ε_{de} in Figure 2.36 was derived from local gradients in the PIV velocity field, and based on the definition of the turbulent stresses in the fluid. For the medium flow rate, ε_{de} peaked at $400\ \mathrm{W\cdot kg^{-1}}$ (unit equivalent to $\mathrm{m^2\cdot s^{-3}}$). This is almost certainly an underestimate since ε should contain energy from all length scales, and the PIV grid scale (280 µm) was much coarser than the Kolmogorov length scale (<10 µm) where most of the energy dissipation occurs. In addition, the scaling between the three flow rates (1:2:4 ratio) far from the orifice was approximately 4 for the two lower flow rates, and 3 for the higher flow rate, giving ε_{de} scaling as 1:4:12. This was not close to 1:8:64 which was the expected scaling based on epsilon derived from a velocity variable and a fixed geometric length scale. This discrepancy indicated that these PIV measurements did not give an accurate ε_{de}.
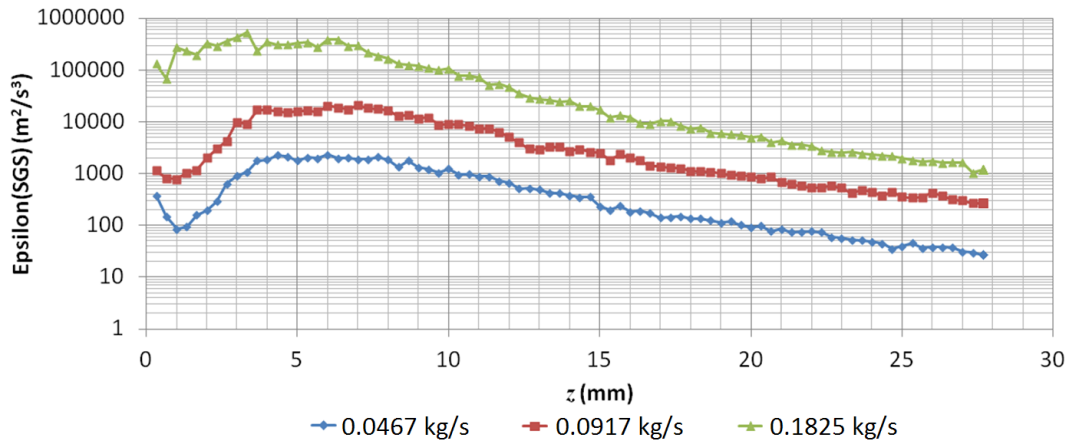
Figure 2.37: Graph of ε_{sgs} for 0140 BLOUT-ZY for three different mass flow rates.

The variable ε_{sgs} in Figure 2.37 was likewise derived from velocity gradients, however it contained an adjustment for sub-grid scale eddies; ε_{sgs} peaked at 20 000 W·kg^{-1} (20 000 m^2·s^{-3}) for the medium flow rate, which was 50 times the magnitude of ε_{de}. This SGS model therefore indicated that much of the turbulent energy was dissipated at scales below the PIV grid length which were not captured by ε_{de}.

The scaling between ε_{sgs} for the two lowest flow rates away from the orifice was approximately 1:8 (e.g. see Figure 2.37 at $z = 20$ mm) and the ratio for the higher flow rate was closer to 5 or 6. This gave scaling ratios of 1:8:40 or 1:8:48. The lower ratio is in line with the dimensional reasoning which gives epsilon proportional to flow rate cubed, for a fixed geometric length scale. Hence it was anticipated that ε_{sgs} was more accurate than ε_{de}.

An approximate calculation for ε for the medium flow rate was as follows: the pressure drop for the medium flow rate was 82.7 kPa, the volumetric flow rate was 9.205×10^{-5} m^3·s^{-1}, hence the total power dissipated was the product of these, which was 7.613 W. Assuming that this was all dissipated over a cuboid region around the jet of 20 mm in the x direction (from ZX plane data), 10 mm in the y direction (e.g. Figure

2.30 and Figure 2.32), and 20 mm in the z direction (e.g. ε values reduce by an order of magnitude from peak in Figure 2.36 and Figure 2.37), this gave a cuboid of volume 4×10^{-6} m^3, which at the density of water was 0.004 kg. An estimated value for ε was therefore 1903 W·kg^{-1}. Since this ought to underestimate the peak value of ε, ε_{sgs} seemed more reliable since its peak value was 20 000 W·kg^{-1}, rather than the 400 W·kg^{-1} of ε_{de}.

Overall a more detailed examination of k and ε will be given later in the comparison with CFD, since in CFD the two variables are available both directly as modelled variables and indirectly as derived from velocity gradients, similar to in this work.

2.6   Conclusions

PIV experiments have been carried out on a Model A Sonolator with Perspex main chamber and optional blade, in order to determine the velocity fields for different orifices and flow rates. Cavitation was found in the Sonolator as evidenced by photographic images showing regions of high reflectivity. The cavitation occurred downstream of and directly behind the sharp edges of the orifice (and the blade edges if the blade was present).

The Sonolator contains highly turbulent flow in the orifice jet as shown by velocity component distributions having a broad peak characteristic of chaotic variation, instead of a narrow peak characteristic of a single velocity. The number of PIV image pairs necessary for reliable time-averaged velocity measurements was 200 or more, with enough delay between consecutive velocity measurements so that they are independent. The orifice jet moved randomly up and down in the blade-out setup, but followed the blade if present. The averaged flow fields in all cases was symmetric in x and y coordinates, corresponding to the two reflective symmetries of the Sonolator geometry.

The main sources of error in PIV measurements were: particles travelling more than a fifth of an interrogation area (6.5 px of 32 px) between laser pulses, local cavitation giving non-circular reflections which could not cross-correlate correctly, difficulty in positioning the laser sheet centrally on the geometry, and difficulty positioning the blade directly downstream of the orifice. When the above sources of error were eliminated, the remaining velocity measurements were found to be reliable. Turbulent measurements (k, ε) were estimates only and had extra sources of unreliability, such as inability to separate periodic from turbulent unsteady components of velocity, and the coarse PIV grid scale.

2.7   Nomenclature & Abbreviations

Symbol   **Description**

C_S Smagorinsky Constant from SGS model, approximately 0.17

d Diameter of droplet or particle

f   General function

k   Turbulent Kinetic Energy (TKE)

I, I' Image intensity functions for first and second PIV frame

L Characteristic length scale

ΔP Pressure drop over Sonolator

R Cross-correlation function

u, v, w Components of velocity in the x, y, z directions respectively

U Characteristic velocity scale of fluid, droplet or particle

$\underline{v}$ Velocity vector (u, v, w)

x, y, z Spatial coordinates with orifice at origin (mm)

X, Y, Z Grid coordinates (processing stage in MATLAB)

<overbar>   Form a time-average of a quantity over all data points through time

Subscripts

0   reference point (e.g. x_0)

c   Continuous phase

d   Dispersed or particle phase

de   Direct Evaluation, a type of calculation of ε

pop   Population, e.g. for variance, as opposed to "sample"

sgs   Sub-Grid Scale, a type of calculation of ε

v, w   Associated with v, w components of velocity, e.g. for k

Greek Symbols

∂ Partial derivative

ε Epsilon, local specific turbulent energy dissipation rate (units $W \cdot kg^{-1}$)

μ Dynamic viscosity

υ_c Continuous phase kinematic viscosity (units $m^2 \cdot s^{-1}$)

ρ Density

τ Characteristic time scale, particle relaxation time

Δ Delta, distance between PIV measurements (approximately 0.27 mm)

Σ Sum

Dimensionless Groups

Stk   Stokes Number

Abbreviations

px   pixel, from "picture element", the unit of distance in a digital image.

var   Variance; sum of squares of (each data point minus the time-average).

2D   Two-dimensional

BLDIN   Blade in experiment

BLOUT   Blade out experiment

CCD   Charge coupled device

CFD   Computational fluid dynamics

D   Size of data set of valid velocity vectors for a given spatial location.

FFT   Fast Fourier transform

HWA   Hot-wire anemometry

IA   Interrogation Area

LDA   Laser Doppler Anemometry

LSV   Laser Speckle Velocimetry

MATLAB "Matrix Laboratory" software for processing matrix based data

PIV   Particle Image Velocimetry

PTV   Particle Tracking Velocimetry

TIFF   Image file format; "Tagged Image File Format"

TKE   Turbulent Kinetic Energy

ZX   Laser plane aligned with Sonolator axis and long diameter of orifice

ZY   Laser plane aligned with Sonolator axis and short diameter of orifice

2.8 Acknowledgements

2.9 References

- Aubin, J., Le Sauze, N., Bertrand, J., Fletcher, D.F., Xuereb, C., (2004). "PIV measurements of flow in an aerated tank stirred by a down- and an up-pumping axial flow impeller". *Exp. Therm. Fluid. Sci.*, **28**, 447-456.

- Blonski, S., Kowalewski, T.A., (2007). "PIV analysis of turbulent flow in a micro-channel", *J. Theor. App. Mech.*, **45(3)**, 489-503.

- Brennen, C.E., (2005). "Fundamentals of multiphase flow", *Cambridge Univ. Press*, ISBN 9780521848046.

- Buchhave, P., (1992). "Particle Image Velocimetry – Status and Trends", *Exp. Therm. Fluid. Sci.*, **5**, 586-604.

- Carlier, J., Stanislas, M., (2005). "Experimental study of eddy structures in a turbulent boundary layer using particle image velocimetry", *J. Fluid. Mech.*, **535**, 143-188.

- Carter, C.D., Donbar, J.M., Driscoll, J.F., (1998). "Simultaneous CH planar laser-induced fluorescence and particle imaging velocimetry in turbulent nonpremixed flames", *App. Phy. B - Lasers and Optics*, **66(1)**, 129-132.

- Chung, K.H.K., Simmons, M.J.H., Barigou, M., (2009). "Local gas and liquid phase velocity measurement in a miniature stirred vessel using PIV combined with a new image processing algorithm", *Exp. Therm. Fluid. Sci.*, **33**, 743-753.

- Cowen, E.A., Sou, I.M., Liu, P.L.F., *et al*, (2003). "Particle image velocimetry measurements within a laboratory-generated swash zone", *J. Eng. Mech. ASCE*, **129(10)**, 1119-1129.

- Dantec website (2014). http://www.dantecdynamics.com/time-resolved-piv   for CMOS sensor cameras, downloaded 1ˢᵗ March 2014.

- Dieter, J., Bremeyer, R., Hering, F., (1994). "Flow Measurements Close To The Free Air/Sea Interface", *Proceedings to the Seventh International Symposium on Applications of Laser Techniques to Fluid Mechanics*.

- Gabriele, A., Nienow, A. W., Simmons, M. J. H., (2009). "Use of angle-resolved PIV to estimate local specific energy dissipation rates for up- and down-pumping pitched blade agitators in a stirred tank.", article plus later erratum, *Chem. Eng. Sci.*, **64**, 126–143.

- Gabriele, A., Tsoligkas, A. N., Kings, I. N., Simmons M. J. H., (2011). "Use of PIV to measure turbulence modulation in a high throughput stirred vessel with the

addition of high Stokes number particles for both up- and down-pumping configurations", *Chem. Eng. Sci.*, **66**, 5862-5874.

- Hall, J. F., Barigou, M., Simmons, M. J. H., Stitt, E. H., (2005a). "Comparative study of different mixing strategies in small high throughput experimentation reactors", *Chem. Eng. Sci.*, **60**, 2355–2368.

- Hall, J. F., Barigou, M., Simmons, M. J. H., Stitt, E. H., (2005b). "A PIV study of hydrodynamics in gas-liquid high throughput experimentation (HTE) reactors with eccentric impeller configurations", *Chem. Eng. Sci.*, **60**, 6403–6413.

- Innings, F., Tragardh, C., (2005). "Visualization of the drop deformation and break-up process in a high pressure homogenizer", *Chem. Eng. Tech.*, **28(8)**, 828-891.

- Jun, B.H., Saikrishnan, N., Arjunon, S., *et al* (2014). "Effect of hinge gap width of a St. Jude medical bileaflet mechanical heart valve on blood damage potential – an in vitro micro particle image velocimetry study", *Journal of Biomechanical Engineering*, **136(9)**, 091008.

- Keane, R. D., Adrian, R. J., (1991). "Optimization of particle image velocimeters: II Multiple pulsed systems", *Meas. Sci. Tech.*, **2**, 963-974.

- Khan, F.R., (2005). "*Investigation of turbulent flows and instabilities in a stirred vessel using Particle Image Velocimetry*", Ph.D.Thesis, Loughborough University.

- Khopkar, A.R., Aubin, J., Xuereb, C., Le Sauze, N., Bertrand, J., Ranade, V.V., (2003). "Gas-Liquid Flow Generated by a Pitched-Blade Turbine: Particle Image Velocimetry Measurements and Computational Fluid Dynamics Simulations", *Ind. Eng. Chem. Res.*, **42**, 5318-5332.

- Kim, M.J., Beskok, A., Kihm, K.D., (2002). "Electro-osmosis-driven micro-channel flows: A comparative study of microscopic particle image velocimetry measurements and numerical simulations", *Exps. in Fluids*, **33(1)**, 170-180.

- Kostas, J., Soria, J., Chong, M.S., (2002). "Particle image velocimetry measurements of a backward-facing step flow", *Exps. in Fluids*, **33(6)**, 838-853.

- Kresta, S. M., Wood, P. E., (1993). "The Flow Field produced by a Pitched Blade Turbine: Characterization of the Turbulence and Estimation of the Dissipation Rate", *Chem. Eng. Sci.*, **48(10)**, 1761-1774.

- Liu, Z.C., Landreth, C.C., Adrian, R.J., et al, (1991). "High Resolution Measurement of Turbulent Structure in a Channel with Particle Image Velocimetry", *Exps. in Fluids*, **10(6)**, 301-312.

- Mavros, P., (2001). "Flow Visualization in Stirred Vessels: A Review of Experimental Techniques", *Trans. IChemE.*, **79**, Part A.

- Melling, A., (1997). "Tracer particles and seeding for particle image velocimetry", *Meas. Sci. Tech.*, **8**, 1406-1416.

- Montante, G., Bakker, A., Paglianti, A., Magelli, F., (2006). "Effect of the shaft eccentricity on the hydrodynamics of unbaffled stirred tanks", *Chem. Eng. Sci.*, **61**, 2807-2814.

- Motamedvaziri, S., Armenante, P.M., (2012). "Flow regimes and surface air entrainment in partially filled stirred vessels for different fill ratios", *Chem. Eng. Sci.*, **81**, 231-250.

- Pan, G., Meng, H., (2001). "Experimental study of turbulent mixing in a tee mixer using PIV and PLIF", *AIChE Journal*, **47(12)**, 2653-2665.

- Qian, M., Niu, L., Wong, K.K.L., *et al* (2014). "Pulsatile flow characterization in a vessel phantom with elastic wall using ultrasonic particle image velocimetry technique: the impact of vessel stiffness on flow dynamics", *IEEE transactions on bio-medical engineering*, **61(9)**, 2444-2450.

- Raffel, M., Willert, C., Kompenhans, J., (1998). "*Particle Image Velocimetry - a practical guide*", Springer-Verlag, Berlin, Heidelberg.

- Ryan, D., Simmons, M. and Baker, M. (2013). "Investigating Dispersion and Emulsification Processes using a Sonolator Liquid Whistle", *Proceedings of 8th International Conference on Multiphase Flow*, 26-31 May 2013, Jeju, Korea.

- Sheng, J., Meng, H., Fox, R. O., (2000). "A large eddy PIV method for turbulence dissipation rate estimation", *Chem. Eng. Sci.*, **55**, 4423-4434.

- Stamhuis, E.J., Videler, J.J., (1995). "Quantitative Flow Analysis around Aquatic Animals using Laser Sheet Particle Image Velocimetry", *J. Exp. Biology*, **198(2)**, 283-294.

- Taylor, G. O., (1938). "The spectrum of turbulence", *Proceedings of the Royal Society of London, Series A, Mathematical and Physical Sciences*, **164(919)**, 476-490.

- Tescione, G., Ragni, D., He, C., Simão Ferreira, C.J., van Bussel, G.J.W., (2014). "Near wake flow analysis of a vertical axis wind turbine by stereoscopic particle image velocimetry", *Renewable Energy*, **70**, 47-61.

- Tropea, C., Yarin, A., Foss J, (eds.), (2007). "*Springer Handbook of Experimental Fluid Mechanics*", **1**, Springer, ISBN 978-3-540-25141-5.

- Wernet, M.P., (2000). "Development of digital particle imaging velocimetry for use in turbomachinery", *Exps. in Fluids*, **28(2)**, 97-115.

- Xia, K.Q., Sun, C., Zhou, S.Q., (2003). "Particle image velocimetry measurement of the velocity field in turbulent thermal convection", *Phy. Rev. E*, **68(6)**, Article 066303.

Chapter 3   CFD SIMULATIONS

3.1   Abstract

Single phase transient Computational Fluid Dynamics (CFD) simulations are presented for turbulent flow inside a Sonolator, an industrial static mixer. The methodology is given for obtaining high quality, converged, mesh-independent results. The transient and time-averaged pressure, velocity and turbulence fields were obtained throughout the fluid domain for industrially-relevant mass flow rates for three nozzle orifice sizes and with the blade present or absent. Scaling rules for these variables as a function of the different flow rates are discussed. Transient and time-averaged flow features are discussed and related to the blade-in and blade-out geometries. The research carried out describes a power balance within the Sonolator, the effect of the blade, the time decay of turbulence fields after the orifice, and characterisation of recirculation zones present.

3.2   Introduction

Particle Image Velocimetry (PIV) experimentation has already been completed for the Sonolator liquid whistle as described in Chapter 2. Since PIV experiments are costly in terms of both equipment and experimentation time, it was desired to have the ability to replace experiments with simulations to enable investigation of a wider range of flow fields and emulsification conditions in the Sonolator. This ability would be granted by designing and carrying out Computational Fluid Dynamics (CFD) simulations of the Sonolator.

CFD simulations rely on solving the Navier-Stokes equations using numerical methods. Unlike PIV, the flow field solutions produced by CFD require validation since they rely on discretisation of the fundamental equations and the use of models for the turbulence. In some cases, errors can be introduced by both of these assumptions. Hence validation would ideally show the errors to be small for the CFD application in question.

In this chapter the CFD methods and results are described. In the next chapter (Chapter 4) a suitable subset of these CFD results are validated against PIV results (as reported in Chapter 2).

In order to carry out CFD simulations, various technical challenges had to be solved, including: selection of suitable software, specification of the geometry, setup of the flow domain, initial conditions and boundary conditions. Once the results were obtained, a multitude of post-processing options were available; suitable analysis options for the Sonolator are discussed relevant to the industrial context of emulsification.

3.3   Literature Review for CFD

Although to date CFD simulations of the Sonolator have not been published by other authors, a subset of findings from this research were presented at ICMF 2013 conference, see Appendix 13 for a copy of the paper (Ryan, Simmons and Baker 2013); hence this literature review concentrates on techniques for simulating the Sonolator using CFD.

Determination of the motion of fluids, given suitable initial and boundary conditions, is a well known problem within physics; the general solution can be found by solving the Navier-Stokes equations (*abbrev.* NSE; see Navier 1822, Batchelor 1967, Acheson 1990; also see Eq. (3.1) below) which describe conservation of momentum for the system in question, along with other suitable conservation equations such as for mass (continuity equation, see Eq. (3.2) below) or energy (typically used when temperature variations also exist).

These equations constrain the motion of a fluid domain existing within a four dimensional continuum consisting of one dimension of time and three dimensions of space. Since the mathematics of continuums is intractable, consisting of an infinite number of infinitesimal domains, in practice the spatial domain of a fluid problem is divided into a finite mesh, with finite time steps used to divide the time continuum. Hence, computational fluid dynamics (CFD) is concerned with simulating finite approximations to the NSE, using a finite mesh and finite time steps, see Patankar (1980), Anderson (1995) or Wendt (2008) for detailed expositions of CFD methods. In this chapter these approximations are studied and used in simulations, with Chapter 4 validating the simulation results using PIV experimental data.

$$\frac{\partial \underline{v}}{\partial t} + (\underline{v} \cdot \nabla)\underline{v} = -\nabla p + \nu \nabla^2 \underline{v} + \underline{f}(\underline{x}, t) \qquad \text{Eq. (3.1)}$$

General Navier-Stokes equations for a fluid existing in space (x) and time (*t*) with velocity vector field (v), pressure scalar field (*p*), kinematic viscosity (*v*) and external forces (f); del (∇) is the gradient or differential operator.

$$\nabla \cdot \underline{v} = 0 \qquad \text{Eq. (3.2)}$$

Continuity equation for an incompressible fluid

Using a finite mesh, common methods for solving the NSE include the Finite Difference Method (FDM), the Finite Volume Method (FVM) and the Finite Element Method (FEM).

FDM recasts the NSE from differential equations into difference equations. These are then solved across the finite mesh. The main limitation of this technique is that fluid dynamics problems must conserve mass, and FDM does not inherently conserve mass; the approximations used in the discretisation can cause cumulative errors in the mass of fluid in the system. Hence FDM, although of historical interest, is rarely used today for CFD. For further reading regarding FDM methods see Lomax, Pulliam and Zingg (2001).

FVM converts the NSE into volume integrals for each mesh cell, and surface integrals for the flux between the cells. Since fluid lost by one mesh cell must be gained by another mesh cell, the FVM conserves mass. This, along with the large literature on validation of turbulence models for FVM, gives confidence that FVM is a good choice for CFD. See Eymard, Gallouet and Herbin (2003) for further reading.

FEM converts the NSE into a series of interconnected "elements", one for each mesh cell. Each element provides a local approximation of the flow, and at the boundary the elements are joined so as to minimise the error between mesh cells. The local

approximations themselves can be first order (linear), second order (quadratic), or higher order; the error minimisation process ensures as smooth a transition between mesh elements as possible. For CFD purposes, although FEM is attractive due to developing smoother solutions with less elements (mesh cells), the turbulence literature for FEM is much less developed, giving less confidence that in highly turbulent flows FEM will give correct results. See Donea and Huerta (2003) for further reading.

Hence, for this study, the choice was taken to consider **finite volume methods** (FVM) only. A general equation describing the FVM method on a mesh consisting of many adjoining cells is given in Eq. (3.3) below. For any conserved quantity Θ, e.g. mass in a cell volume dV, or a momentum component; the flux θ over the cell's surfaces dA must together obey the given equation. Using this method, FVM approximates NSE in a given mesh comprising of a finite number of cells. Moreover, since the surface flux lost by one cell must be gained by the adjoining cell, all conservation equations can be adhered to.

$$\frac{\partial}{\partial t} \iiint \theta \, dV + \iint \theta \, dA = 0 \qquad \text{Eq. (3.3)}$$

Conservation equation in FVM for conserved variable Θ with surface flux θ. Note that both Θ and θ are in the conservative form (quantity per unit volume) to ensure continuity.

FVM solvers generally solve these equations using an iterative method to converge upon a numerical solution. In CFD, when numerical solvers are built using methods such as FVM, the general result is known as a Direct Numerical Simulation (DNS). For low Reynolds number flows (low velocities) convergence is usually good and a steady state solution is typically found for a non-moving flow geometry and constant boundary conditions (e.g. fixed mass flow rate at an inlet surface). However, for the same flow geometry, and with the only change an increase in Reynolds number

(and mass flow rate), turbulence is found to start at a finite Reynolds number, e.g. between 2300 and 4000 for pipe flow (Holman 2002). Turbulence is inherently unsteady (Taylor 1938), has eddies as a characteristic flow feature, and tends to transmit energy from eddies at large length scales to those at small length scales (Kolmogorov 1941) which are subsequently dissipated by viscosity. Hence DNS simulations for high Reynolds number must be both transient and have a very large number of mesh cells to resolve all of the small-scale features of turbulence. With realistic industrial geometries and Reynolds numbers, these simulations quickly become computationally intractable; although research continues to increase Reynolds numbers in DNS, see Lee, Malaya and Moser (2013) for a recent DNS with Reynolds number of only 5200 which required 242 billion degrees of freedom to be simulated.

The practical solution used to make CFD simulations tractable is, instead of DNS, to apply a **turbulence model** (Wilcox 1998) to approximate the effects of turbulent eddies below a certain length scale. This allows the number of mesh cells to be much smaller whilst producing simulation results that are broadly in line with observations of physical phenomena.

However, it is important to note that since no turbulence model has a proven general validity for all flows, and since all turbulence models involve approximation of the effect of turbulence, it is normal to **validate** all or part of the results of such CFD simulations against experimental data. In the present work, this will be carried out in Chapter 4.

Some common types of turbulence model listed by Wilcox (1988) include, in increasing order of computational cost: Reynolds-averaged Navier Stokes (RANS), Reynolds Stress Model (RSM) and Large Eddy Simulation (LES); DNS costs more than

all of these. In RANS and RSM the flow velocity is separated into time-averaged and unsteady components; the unsteady components combine in the non-linear convection term in the NSE to give apparent stresses commonly denoted as "Reynolds Stresses". These new terms are also transported phenomena, hence turbulence models increase the number of transported variables to be solved for in the flow domain.

The specific turbulence model specifies how these unknown stresses are calculated. In RANS an isotropic assumption is made on the Reynolds stresses, reducing the number of unknown variables typically to one or two, e.g. for the k-ε model (Jones and Launder 1972) the additional transported variables correspond to the turbulent kinetic energy (k) and the turbulent energy dissipation (ε); for the k-ω model (Wilcox 1988, 1998) the transported variables are k and turbulent frequency (ω). For RSM which does not use an isotropic assumption the full number of turbulent stresses (normally six) are modelled as transported variables, which increases computational cost. Moreover this approach does not always increase accuracy since the choice of model for these additional six variables can be less obvious, nor as well founded in literature, than for the simpler models employing only k, ε or ω. Finally, for LES the effect of the turbulent scales smaller than the mesh scale are given by a sub-grid model, using a low-pass filter on the NSE. This has been found to be the most accurate turbulence model for CFD, short of a full DNS. However it is computationally very expensive, especially near wall boundaries; full LES tends to be used in applications such as aeronautics where most of the flow volume is free stream.

The common RANS approaches of k-ε and k-ω also have characteristic advantages and disadvantages. The k-ε model has been validated for a wide range of applications, from large-scale (environmental) to small scale (industrial machinery), and

is thus very popular today. It is relatively accurate in the free stream and in recirculating flows and planar shear layers, however the $k\text{-}\omega$ model is superior in boundary layers with an adverse pressure gradient where flow separation occurs, this is very common in turbulent applications (Wilcox 1988). Hence each model has its strengths and weaknesses; generally speaking, $k\text{-}\varepsilon$ tends to be more accurate in the free stream, whereas $k\text{-}\omega$ tends to be more accurate near walls.

To improve on these limitations, Menter (1993, 1994) introduced the Baseline (BSL) and Shear Stress Transport (SST) variants of the $k\text{-}\omega$ turbulence model. Each of these used a blend of $k\text{-}\omega$ near the wall and $k\text{-}\varepsilon$ away from the wall, hence each turbulence model being used in the locations where its application is most suitable. Menter compared these four models across multiple type of simulation and concluded that the SST model possessed the strengths of each model whilst minimising the weaknesses of each. This was achieved by using a suitable blending function between the two models.

Other researchers also recommended the SST model; recent comparisons include: Meslem, Bode, Croitoru and Nastase (2014); Freeman and Roy (2014). Meslem *et al* (2014) considered steady-state jet flow from a cross shaped orifice and compared PIV experimental data to seven different turbulence models including $k\text{-}\varepsilon$, $k\text{-}\omega$, SST $k\text{-}\omega$ and Reynolds Stress Models (RSM). The SST $k\text{-}\omega$ model was found to predict best overall, including in areas such as the flow field near the jet and the velocity profile at the vena contracta, both relevant to the Sonolator. For a different application in aerodynamics, Freeman and Roy (2014) compared Spalart-Allmaras (S-A), $k\text{-}\varepsilon$, $k\text{-}\omega$ and SST $k\text{-}\omega$ models. The S-A and SST $k\text{-}\omega$ models were found to have less error, when compared to

a known solution, than the other models. So overall the **SST** model was recommended for steady-state CFD simulations.

The RANS models listed previously are suitable for steady-state simulations, however PIV experimentation on the Sonolator had confirmed that the flow field was time-dependent. For unsteady flow, Egorov and Menter (2007) compiled a list of turbulence modelling options including: unsteady RANS (URANS), large eddy simulation (LES), detached eddy simulation (DES) and introduced scale adaptive simulations (SAS), the latter of which was fully specified in later publications (Menter and Egorov 2010; Egorov, Menter, Lechner and Cokljat 2010). URANS was described as unphysical under some circumstances; LES as too computationally expensive, DES as a computationally less expensive blend of LES and RANS, and SAS as a more optimised version of DES which eliminated the dependence of the RANS mode on the grid spacing. The SAS model presented included an SST element, hence the full name of Menter's recommended model was **SST-SAS**. In the later publication (Egorov *et al* 2010), this model was demonstrated in engineering applications including: chemical mixers, turbine blades, gas turbine cavities, car mirrors and combustion chambers.

Industrial applications investigated by other authors include: a jet flow and cooling problem from aeronautics (Duda, Menter, Hansen and Esteve 2011); a Kaplan turbine (Jošt, Škerlavaj and Lipej 2012) and an agitated vessel with eccentric impeller (Domanski, Karcz and Bitenc 2014). In Duda *et al* (2011), SST-SAS was applied to a cooling jet in an irregular chamber found in the front of an aircraft wing. The model was found capable of resolving the local turbulent scales well and reproducing with good accuracy the fluctuating fields and temperature fields found from experiments. In Jošt, Škerlavaj and Lipej (2012), several steady-state and transient models were used to

predict the flow around a Kaplan turbine. The steady-state models gave good agreement with experiments for small blade angles, however for large blade angles SST-SAS was required to get good agreement. In Domanski *et al* (2014) an agitated vessel with eccentrically located impeller was investigated using SST-SAS turbulence modelling, with the data compared to *k-ε* simulations and PIV experiments. Out of the two turbulence models SST-SAS gave more realistic flow behaviour and better agreement with experiment.

Table 3.1: Summary of turbulence options

Turbulence Model	Strengths	Weaknesses
None (DNS)	Exact	Computationally intractable
RANS *k-ε*	Free Stream	Wall Treatment
RANS *k-ω*	Wall Treatment	Free Stream
RANS SST	Strengths of both *k-ε* and *k-ω*	Does not model transient eddies or non-isotropic turbulence
RSM	Non-isotropic turbulence allowed	Constants in model less well understood than for RANS sims.
LES	Large eddies modelled in detail	Still computationally expensive
DES	Less expensive than LES	Dependence on grid spacing
SST-SAS	SST model with LES eddies added and grid dependence eliminated	Judged best for Sonolator simulations, selected for this thesis.

The overall findings of this literature review are thus that CFD modelling of the Sonolator would best be carried out with a finite volume method (FVM) flow solver using the SST-SAS turbulence model to simulate the small scale turbulence not covered by the mesh discretisation used. A summary of the turbulence models discussed and the reasons for selection of SST-SAS is given above in Table 3.1.

3.4   Materials and Methods for CFD simulations

Computational Fluid Dynamics (CFD) simulations were designed, carried out and analysed using various computer programs. The main stages are delineated below, which included geometry creating and meshing, simulation setup and processing, results post-processing. ANSYS products were used for the setup, post-processing and 2D/3D visualisation, and Excel for the 1D post-processing into line graphs.

3.4.1   Design of Sonolator Geometry in CFD

The existing PIV experiments had water entering the Sonolator at the inlet, flowing through the narrow orifice, into the main chamber and out of the exit. The geometry used in CFD was designed to have exactly the same dimensions as this PIV work, in order to validate the CFD against these experimental results. This was achieved by consulting technical drawings for the construction of the Model A Sonolator (kindly provided by Rob Brakeman of Sonic Corp.), and checked against manual measurements and photographs of all relevant Sonolator components, taken at Unilever Research & Development, Port Sunlight, and of dismantled Model A Sonolator apparatus.

Preliminary steady state analysis (Ryan, Simmons and Baker 2011) had modelled the whole geometry using a one-quarter model with symmetry boundary conditions. This would only work for steady-state analysis, so for this work no simplifications due to Sonolator symmetry were used; the whole Sonolator flow domain was included in the geometric model.

3.4.2   Computer geometry creation (ANSYS ICEM)

ANSYS ICEM was used to enter the 3D geometric design into the computer. Points were entered by co-ordinate, joined to make lines and curves for the interior

edges of the Sonolator, areas created to model the inner walls of the Sonolator which bounded the fluid flow. Figure 3.1 shows geometry for 0110 orifice, blade in:
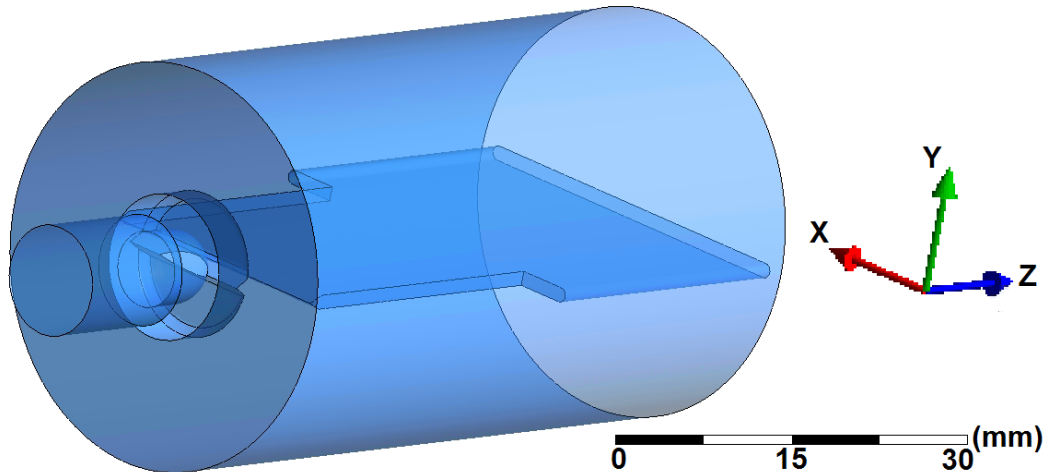
Figure 3.1: Geometry used for simulations of 0110 orifice, blade in. Axes X, Y, Z align with: long orifice direction, short orifice direction and Sonolator main axis respectively.

Six different geometries were created to explore all the permutations of two blade choices and three orifice sizes, as set out in the next two paragraphs for blade and orifice respectively.

The two blade choices were denoted BLOUT for blade out, and BLDIN for blade in. The blade design was the same as the earlier PIV work; the front of the blade had the same shape as the original Sonolator unit, and the rear of the blade had been elongated to give increased visual access. (This was not expected to cause industrial performance to deviate from the original; the turbulence originating from the orifice and possibly from the sharp front edge of the blade was thought to cause the Sonolator's industrial performance; the rear of the blade was not thought to do so.)

The three orifice size choices are referred to in this chapter by the orifice size codes 0037, 0110 and 0140. A full explanation of these codes is given in Table 1.2, and

they represented orifice sizes of between 0.0037 in^2 and 0.014 in^2 in imperial units, or 2.39 mm^2 to 9.03 mm^2 in SI units.

Sonolator orifices are manufactured by Sonic Corp., each from a steel cylinder, by axially milling out a hemispherical cavity at the end of a cylindrical cavity, and from the other end of the steel cylinder making two planar cuts at 60° to intersect the hemispherical cavity and create a cats-eye shaped orifice. The geometry in ANSYS ICEM was created using these geometric specifications, and resulted in orifice shapes very close to the original shape.

3.4.3 Meshing the geometry (ANSYS ICEM)

CFD required the continuous geometric flow domain to be modelled by a finite number of mesh cells. ANSYS ICEM had software to mesh the geometry, with some user choices required about the large-scale structure of the mesh. Two of the meshes used are given below in Figure 3.2 and Figure 3.3, and then the mesh construction is discussed.
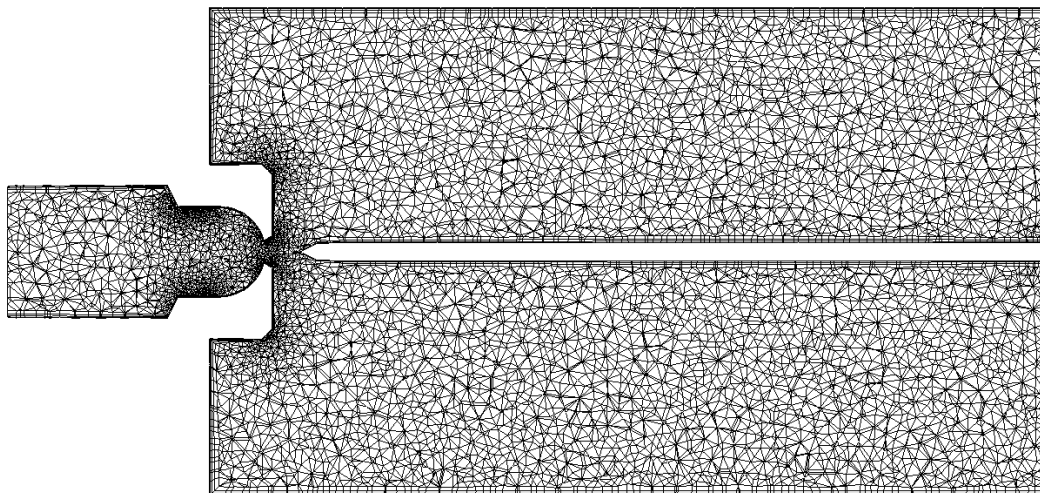
Figure 3.2: Section in ZY plane through the Delaunay Mesh with prism layers used for 0110 orifice, Blade In.

0   0.015   0.03   (m)

0.0075   0.0225
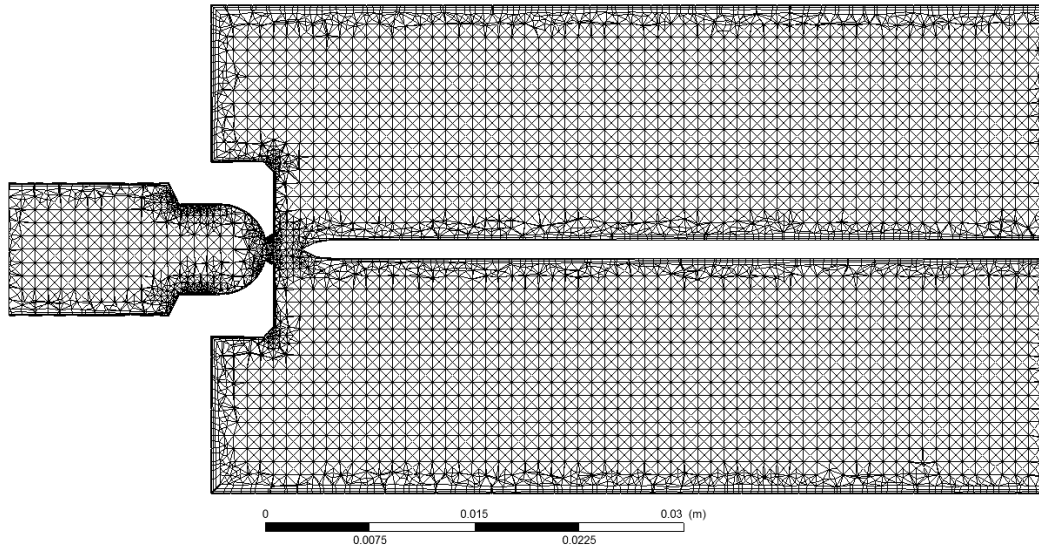
Figure 3.3: Section in ZY plane through the Octree Mesh with prism layers
used for 0110 orifice, Blade In.

Unstructured tetrahedral meshes were used; the construction methods in ICEM for these were found to be more reliable than for structured or unstructured hexahedral (cubic) meshes, which failed to give good hexahedral mesh cells near the sharp internal angles near the orifice and blade geometry. Two unstructured tetrahedral mesh creation methods were available: Delaunay and Octree. Delaunay was based on the 3D analogue of planar Delaunay triangulation methods; Octree was based on creating a cubic mesh, splitting individual cubes into tetrahedral, then mapping these to any adjacent surfaces and clipping the resulting tetrahedral mesh appropriately. Both Delaunay and Octree methods were used to generate unstructured tetrahedral meshes, and the results from both are compared in the results below. By using both unrelated meshes throughout the results, mesh independence is indicated wherever the results upon them agree.

Both methods allowed the mesh fineness (reciprocal of coarseness) to be globally specified and increased further near fine details in surface geometry where velocity gradients would be high. Mesh fineness could be varied in ANSYS ICEM through integer powers of 2; this allowed creation of meshes of three increasing levels of

122

fineness (global length scales in ratio 4:2:1) allowing assessment of mesh scale independence. These finenesses were chosen to be fine enough to capture flow through an orifice of width approximately 1 mm, but not too fine to require excessive memory or computational resources. For the whole range of simulations, ANSYS reported the total number of nodes as being in the range 50 k to 1.5 M, and the number of elements in the range 200 k to 7 M (k representing a thousand, M for a million).

Prism layers were always added to the exterior of the mesh where it was adjacent to the walls of the fluid domain, to make sure that near-wall flow was modelled correctly due to the large velocity gradients found there. Prism layers achieved this by having a small constant thickness perpendicular to the wall, compared to the large lateral area. In this way, the cells lined up with the wall gradients and allowed them to be resolved in their sharpest direction of change.

The general sequence of mesh creation using Delaunay or Octree methods, given a Sonolator geometry, was: create triangular surface mesh, smooth mesh (these two steps Delaunay only), create tetrahedral volume mesh, smooth mesh, create prism mesh with up to 4 layers (fewer layers did not sufficiently resolve the boundary flow; more layers caused mesh problems around sharp corners near the orifice) with height ratio of 1.75 between layers, smooth mesh (this smoothing stage was the most difficult to obtain good quality mesh cells from, and was split into multiple stages increasing mesh quality bit-by-bit), export to a completed mesh file.

In summary, for each geometry up to 6 different meshes were used in the results below, representing 3 finenesses of mesh and 2 styles (Delaunay, Octree) of tetrahedral mesh construction. Multiple meshes were used to establish the level of mesh independence of the underlying flow fields obtained.

3.4.4   Simulation Setup (ANSYS CFX-Pre)

ANSYS CFX-Pre was used to set up the simulations, which had many aspects discussed individually below.

3.4.4.1   Simulation physics

For the simulation physics of the fluid flow, the following assumptions were made: single phase water under ambient (25°C, 1 atm) conditions, incompressible Navier-Stokes equations for pressure and 3D velocity fields, no temperature modelling or heat transfer. Density and dynamic viscosity were set as at 997 kg·m^{-3} (Lide 1990) and 9×10^{-4} Pa·s (Al-Shemmeri 2012) respectively.

3.4.4.2   Choice of Steady State or Transient Simulations

Both steady state and transient simulations were carried out in preliminary work, see Ryan *et al* (2011) for some preliminary steady state analysis. Transient simulation results only have been presented here, since these, plus the PIV work, demonstrated that the flow field was unstable and oscillating in all cases investigated, explaining why previous steady state work failed to converge beyond a certain point. The time-averages obtained from transient simulations were more symmetric than the steady state solutions, indicating transient results were more representative since a symmetric geometry with symmetric flow conditions (as here) ought to have a symmetric solution. Finally, the PIV results were obtained from time-averaging 500 PIV frames, hence time-averaging CFD time steps was an appropriate technique to use bearing in mind the two data sets would be compared (below, in Chapter 4).

3.4.4.3   Simulation Fluid – Single or Multiphase Flow

Industrially the Sonolator is often used to structure multiphase fluids and emulsions. In the case where an emulsion is dilute (e.g. mouthwash with approximately 1% dispersed oil phase in continuous aqueous phase) a good approximation to the multiphase flow can be made by single phase water simulations assuming both phases behave as a single homogeneous continuum (Whalley 1996). Moreover, simulations of multiphase flows contain extra modelling assumptions, especially about the nature of the interfaces or the local droplet size distributions.

Disadvantages of using these multiphase simulations include: less well established suitability of models used compared to single phase; low accuracy of interface tracking; approximations necessary to modelling droplet size distributions changing through space and time by convection and droplet breakage; computational overhead of increasing the accuracy of any of these factors. For these reasons, single phase CFD modelling was chosen as a suitable starting point for investigating the Sonolator and a launch point for modelling the forces as the fluid traverses the orifice, and understanding how they may break droplets and form emulsions. Note: Further work on multiphase simulations of the Sonolator ought to be continued, for application to industrial cases where inhomogeneous flow of the different phases has been demonstrated.

3.4.4.4   Turbulence Modelling

Reynolds number calculations showed that $\text{Re} > 17\,000$ at the orifice for typical industrial flow rates, see Table 3.2 below on simulation setup. Direct numerical simulations (DNS) were therefore not tractable, hence RANS and LES turbulence models were considered. In the literature review the SST model was found to combine

the best aspects of two RANS models, *k-ω* and *k-ε.*, so the SST model would have been a good choice for steady-state simulations.

However the Sonolator required transient simulations due to the unsteady flow regime. The literature review showed that the SST-SAS model was suitable for modelling turbulence in such flows, combining some eddy simulations from the LES model with SST to efficiently model turbulence in the remainder of the flow. The SST-SAS model in ANSYS software had good convergence and robust performance. Hence the SST-SAS model was chosen for modelling turbulence in the Sonolator.

3.4.4.5   Simulation threading: serial and parallel setups

ANSYS CFX-Pre and CFX-Solver allowed simulations to be run serially on one core on a processor, or in various distributed modes across multiple cores on a processor, or across multiple processors and cores. Initial simulations were carried out serially, subsequently 4 core simulations in parallel on a workstation, and up to 2 processors with 16 cores each were used in parallel on a cluster computer at University of Birmingham. No differences were noted in the final results, other than the speed at which they were obtained. Simulations were therefore set up to run in parallel on as many processors and cores as were available at the starting time of each simulation.

3.4.4.6   Arithmetic precision – Single or Double

Simulation positions and velocities were generally floating point real numbers. ANSYS CFX-Pre and CFX-Solver allowed either single precision or double precision floating point numbers to be used throughout a given simulation. Selecting double precision did not seem to significantly increase simulation accuracy, as discussed below, but required double the storage capacity. For this reason, simulations were carried out with single precision arithmetic.

3.4.4.7   Courant number

Simulations presented here are transient, so an appropriate choice of time step had to be made. Too low a time step and the simulation will be computationally expensive; too high and accuracy may be lost.

The Courant number (C) is the ratio of local velocity magnitude to mesh length divided by time step. The Courant-Friedrichs-Lewy condition for explicit methods for solving differential equations states that the Courant number must be below 1 for a simulation to be sufficiently accurate. Since Courant number is proportional to time step, values of C below 1 mean the time step is small enough to resolve the transient detail correctly. When the time step is increased, so that $C > 1$, explicit methods cannot be used and implicit methods must be used instead.

The ANSYS solver was set to use implicit methods which allowed values of $C > 1$. An "Adaptive Time Step" option was used to vary the time step to make the Courant number not exceed some maximum value C_{max}. Simulations were carried out with C_{max} in the range 10 to 500. At 300 or above the simulation sometimes terminated prematurely due to instability, but with $C_{max} \leq 200$ the simulation was found to always run to completion, see Appendix 5 where it is shown that the choice of C_{max} within this range did not significantly affect simulation results.

3.4.4.8   Initial Conditions

Each transient simulation was carried out in two stages:

- Initialise the simulation with zero velocity and pressure everywhere. Continue time steps until the residuals converge to be suitably small, typically 10^{-5}. (These residuals represented root mean square discretisation errors in the solutions found to the Navier-Stokes equations discretised on a mesh, and should be minimised for an

accurate discrete solution to the continuous flow problem which was being modelled.)

- At this stage a good approximate solution to the Navier-Stokes equations had been obtained at a point in time.

- Stop the simulation and restart it with initialisation on the results set from the first stage.

This allowed all time steps in the final results set to have residuals converged to as low a value as possible, for greatest accuracy.

3.4.4.9   Convergence of coefficient loops

At each time step it was necessary to iterate to converge the residuals to a low level. Each iteration was called a "coefficient loop". Between 1 and 10 coefficient loops were used to try to reduce all residuals of velocity, mass and turbulence variables below 10^{-4}. In almost all simulations this was achieved almost every time step within 10 coefficient loops. In all cases the residuals could be converged below 0.0003 so the discretisation error was suitably low.

A global conservation target of 0.3% across the whole flow domain was also set, ensuring that mass and momentum conservation across the domain would not deviate by more than 3 parts in 1,000, with coefficient loops continuing until this occurred, up to a limit of 10 loops. Comparisons of mass flow at the inlet with those at the nozzle orifice verified that these quantities were indeed conserved. This number 0.3% was chosen because it was low enough to give accuracy, but high enough not to require excessive coefficient loops to achieve. In general, the targets for residuals were set pragmatically in order to balance accuracy and computational tractability.

3.4.4.10 Simulation time, Transient Results and Backup

Simulation time was taken to be long enough for any oscillation seen in the flow to occur at least 20 to 40 times, but short enough for the computation to be tractable – one second of simulation time took between 6 and 24 hours to obtain on 16 cores on the cluster computer. Good transient averages (indicated by velocity field symmetry where the underlying flow field was symmetric) were found after 20 oscillations had completed. Typically, 60 oscillations would complete in 40 000 time steps. The transient averages were updated by CFX-Solver every time step, hence the final transient averages took all the time steps into account.

In addition, transient flow field data was exported to a results file approximately every 20-100 time steps (depending on flow rate), allowing reconstruction of transient flow behaviour, e.g. for a video (Appendix 14). Finally, backups of the transient results were taken every 20 time steps to allow simulations to be restarted without need for a final results file; two reasons for this were occasional simulation instabilities, but more often running out of time on the cluster computer and the job terminating early.

3.4.4.11 Boundary Conditions and Mass Flow Rates

Boundary conditions were required for all time steps on the 2D boundaries of the 3D flow field. The geometry where boundary conditions were required, and the type of boundary condition set, included:

- Smooth non-slip stationary wall condition on inlet wall, orifice wall, main chamber wall. The blade (when present) was also modelled with this condition; modelling the small vibrations of the blade was left for further work.

- Mass flow rate fixed at inlet, see below.

- Outlet: pressure was held at 0 Pa (relative to the reference pressure of 101 325 Pa, or 1 atm) with entrainment option available in ANSYS CFX-Pre which suitably controlled the dynamic pressures caused by mass entering and exiting the outlet, conserving mass and momentum fields.

$$\text{Re} = \frac{Q}{A}\frac{D_H}{\nu} \qquad\qquad \text{Eq. (3.4)}$$

$$D_H = \frac{4A}{p} \qquad\qquad \text{Eq. (3.5)}$$

High, medium and low mass flow rates were chosen at the inlet to match the rates carried out in PIV experiments. Reynolds numbers at inlet, orifice and main chamber were calculated using Eq. (3.4) for Reynolds number (Re) and Eq. (3.5) for hydraulic diameter (D_H); Q was volumetric flow rate, ν was fluid kinematic viscosity, A was area and p perimeter at the location specified. The area and perimeter were directly available in ANSYS ICEM as calculations from the CFD geometry. The flow rates and Reynolds numbers are given in Table 3.2 (which are the same conditions as previously summarised for PIV in Table 2.1):

Table 3.2: List for each orifice and flow rate category of: mass flow rate (*M*; given in 2 different units), superficial velocity (u_{orif}) at the orifice, Reynolds numbers (Re) at the inlet, orifice and main chamber.

Orifice type	Low Flow Rate	Medium Flow Rate	High Flow Rate
0037 (BLDIN and BLOUT)	$M = 0.036$ kg·s^{-1} $u_{orif} = 15.2$ m·s^{-1} Re$_{inlet}$ = 4200 Re$_{orif}$ = 26 500 Re$_{MC}$ = 1500	(CFD not carried out)	$M = 0.091$ kg·s^{-1} $u_{orif} = 38.4$ m·s^{-1} Re$_{inlet}$ = 10 500 Re$_{orif}$ = 66 700 Re$_{MC}$ = 3700
0110 (BLDIN and BLOUT)	$M = 0.046$ kg·s^{-1} $u_{orif} = 6.5$ m·s^{-1} Re$_{inlet}$ = 5300 Re$_{orif}$ = 19 600 Re$_{MC}$ = 1900	$M = 0.092$ kg·s^{-1} $u_{orif} = 12.9$ m·s^{-1} Re$_{inlet}$ = 10 500 Re$_{orif}$ = 38 800 Re$_{MC}$ = 3800	$M = 0.182$ kg·s^{-1} $u_{orif} = 25.8$ m·s^{-1} Re$_{inlet}$ = 20 900 Re$_{orif}$ = 77 200 Re$_{MC}$ = 7500
0140 (BLDIN and BLOUT)	$M = 0.047$ kg·s^{-1} $u_{orif} = 5.2$ m·s^{-1} Re$_{inlet}$ = 5400 Re$_{orif}$ = 17 500 Re$_{MC}$ = 1900	$M = 0.092$ kg·s^{-1} $u_{orif} = 10.2$ m·s^{-1} Re$_{inlet}$ = 10 500 Re$_{orif}$ = 34 500 Re$_{MC}$ = 3800	$M = 0.182$ kg·s^{-1} $u_{orif} = 20.3$ m·s^{-1} Re$_{inlet}$ = 21 000 Re$_{orif}$ = 68 500 Re$_{MC}$ = 7500

Turbulence boundary conditions also had to be specified at the inlet and outlet. A medium turbulence input of 5% of mean flow velocity was chosen at the inlet, to represent a flow with medium turbulence already present entering from the inlet pipe; note that this level was much lower than the turbulence present after the orifice. A "Zero Gradient" option was chosen at the outlet to ensure turbulence levels were conserved in any recirculation zones at the outlet.

3.4.4.12   Solver Control

ANSYS CFX-Solver had various options for solving of the discretised Navier-Stokes equations. The following options were chosen:

- Transient Scheme – "Second Order Backward Euler".

- Advection Scheme – "High Resolution" which was second order.

- Turbulence Numerics – first order.

Using second order implicit solving for time steps and spatial gradients meant that good accuracy was maintained and that numerical diffusion of quantities were minimised. The reason that turbulence quantities were solved with only first order methods was because the turbulence quantities were approximate models of the underlying turbulent eddies, so numerical diffusion was not important to prevent, in addition it made the simulations more stable.

3.4.4.13   Monitor Points

ANSYS CFX-Solver provided monitor points such as residuals automatically. Other monitor points were added in CFX-Pre; for example, total pressure drop, velocity magnitude and turbulence levels at three points near the orifice jet, amongst others. As the simulation was processed these monitor points revealed the levels of the variables as the simulation progresses, and showed oscillations in them through time.

3.4.4.14   Run Definition

When the CFX-Pre simulation definition was finished as set out above, it was saved to a definition file for running in ANSYS CFX-Solver.

3.4.5   Running the simulations (ANSYS CFX-Solver)

ANSYS CFX-Solver was used to run the simulation definition files along with suitable initial conditions representing an existing converged simulation. Some simulations were run on the workstation with monitor points available to monitor simulation progress. Later simulations, when simulation technique had become stable, were run on a cluster computer (BlueBEAR at University of Birmingham) which allowed results to be gathered much faster due to the high level of parallel processing available.

When the simulation had reached its pre-determined end point (simulation time elapsed, alternatively being stopped by the user) a results file was generated which was processed, along with the transient results, in ANSYS CFD-Post.

3.4.6 Post-processing the simulations (ANSYS CFD-Post, Excel)

ANSYS CFD-Post was used to view the results of simulations, and carry out the following tasks as required: interrogate velocity, pressure or turbulence variables anywhere in the 3D flow domain and at any point in simulation time, plot these quantities along a line in 3D space, view these variables graphically along a plane through or a surface within the flow domain, produce contour or vector plots, and export flow variables to CSV file for external processing, e.g. comparison in Excel to PIV work (see Chapter 4).

3.4.6.1 Obtaining transient averaged files

From PIV work, time-averaged flow fields had been obtained. Consequently, time averaged flow fields were required from CFD for a meaningful comparison to be made.

ANSYS CFX software allowed transient averages to be calculated for all flow variables. For a specific variable, at each point in space, the average was kept by maintaining the sum of the variable, and the count of snapshots of the variable, and constructing a transient average by dividing the sum by the count. In this way averaged flow fields were constructed.

3.4.7 Experiments to ensure simulation accuracy

Several preliminary experiments were done to check that CFD simulations were working correctly and to fine-tune the methodology used. These are presented in Appendix 5. Conclusions included:

- Simulation duration and number of time steps were high enough to ensure statistical convergence of flow quantities such as local velocities

- Suitable Courant numbers were used

- Single precision arithmetic was sufficient

- Mesh independence was ascertained; both Octree and Delaunay meshes were used

- Boundary layers were checked

- Global conservation of mass was checked

3.4.8   Types of simulation analysis available in 0, 1, 2 and 3 dimensions

Data from the CFD simulations consisted of field values across discrete mesh points, with available fields including: velocity (three components), pressure (dynamic/static), turbulence (ε, k). These values were analysed across points, lines, planes and the flow domain (D = 0, 1, 2, 3; where D is dimensionality of analysis region). Suitable presentations of these results included:

- 0D: Values of velocity, pressure or turbulence variables at a point; also global values, e.g. pressure drop across the whole Sonolator.

- 1D: Graphs of variation of values on a line segment (c.f. Figure 3.9 below), line averages.

- 2D: Contour or vector plots of values on a plane in the flow region; also average flow values over a surface (ΔP was measured by difference of two such measurements on inlet and outlet).

- 3D: Isosurface and streamline plots, volume averages.

In the remainder of this chapter on CFD results, 2D and 3D presentations will be given of specific flow fields. In the next chapter on CFD/PIV comparison, mainly 1D

graphs over line segments will be used to compare experiment to simulation, and experiments of different flow rates. (0D results were found to be less useful since 2D or 3D averages gave measurements with less variation or error.)

3.5   Results and Discussion

3.5.1   Relationship of flow rate, measured orifice velocity and pressure drop

Earlier in Table 3.2 orifice superficial velocities were given. They are now compared to simulation results in Table 3.3 below. Six simulations were available for 0110 orifice at low, medium and high flow rate, and for blade in and out. For each simulation, time series were available for measured orifice velocity and Sonolator pressure drop. In all cases these time series were approximately constant, so a single point was sampled from these series as representative. In all cases the medium density Octree mesh results were used, since mesh independence had already been demonstrated.

$$u_{\text{orif}} = \frac{Q}{A} = \frac{M}{\rho A} \qquad\qquad \text{Eq. (3.6)}$$

Orifice superficial velocity was calculated using Eq. (3.6) from volumetric flow rate (Q) and orifice area (A); alternatively mass flow rate (M) and fluid density (ρ) could be used. Table 3.3 below contains results for the following quantities: mass flow rate (M), pressure drop across the Sonolator from inlet to outlet (ΔP), orifice superficial velocity (u_{orif}), measured Sonolator velocity magnitude (u_{meas}) calculated in CFD-Solver from an area-average of velocity magnitude on the internal orifice surface. This surface was the intersection between the hemispherical cavity inside the nozzle, with the two cuts made into the nozzle.

Table 3.3: CFD results for three flow rates, 0110 orifice, blade in and out:

Geometry	Low Flow Rate	Medium Flow Rate	High Flow Rate
0110 orifice Blade out	$M = 0.046$ kg·s^{-1} $u_{orif} = 6.5$ m·s^{-1} $u_{meas} = 5.78$ m·s^{-1} $\Delta P = 32.1$ kPa	$M = 0.092$ kg·s^{-1} $u_{orif} = 12.9$ m·s^{-1} $u_{meas} = 11.40$ m·s^{-1} $\Delta P = 125.7$ kPa	$M = 0.182$ kg·s^{-1} $u_{orif} = 25.8$ m·s^{-1} $u_{meas} = 22.69$ m·s^{-1} $\Delta P = 496.3$ kPa
0110 orifice Blade in	$M = 0.047$ kg·s^{-1} $u_{orif} = 6.5$ m·s^{-1} $u_{meas} = 5.77$ m·s^{-1} $\Delta P = 32.3$ kPa	$M = 0.092$ kg·s^{-1} $u_{orif} = 12.9$ m·s^{-1} $u_{meas} = 11.41$ m·s^{-1} $\Delta P = 125.6$ kPa	$M = 0.182$ kg·s^{-1} $u_{orif} = 25.8$ m·s^{-1} $u_{meas} = 22.64$ m·s^{-1} $\Delta P = 492.1$ kPa

On comparison in Table 3.3, the blade in and blade out cases for the measured variables u_{meas} and ΔP are almost identical. In Figure 3.4 below the blade out cases are non-dimensionalised by dividing out their units, and plotted together on a log-log graph:
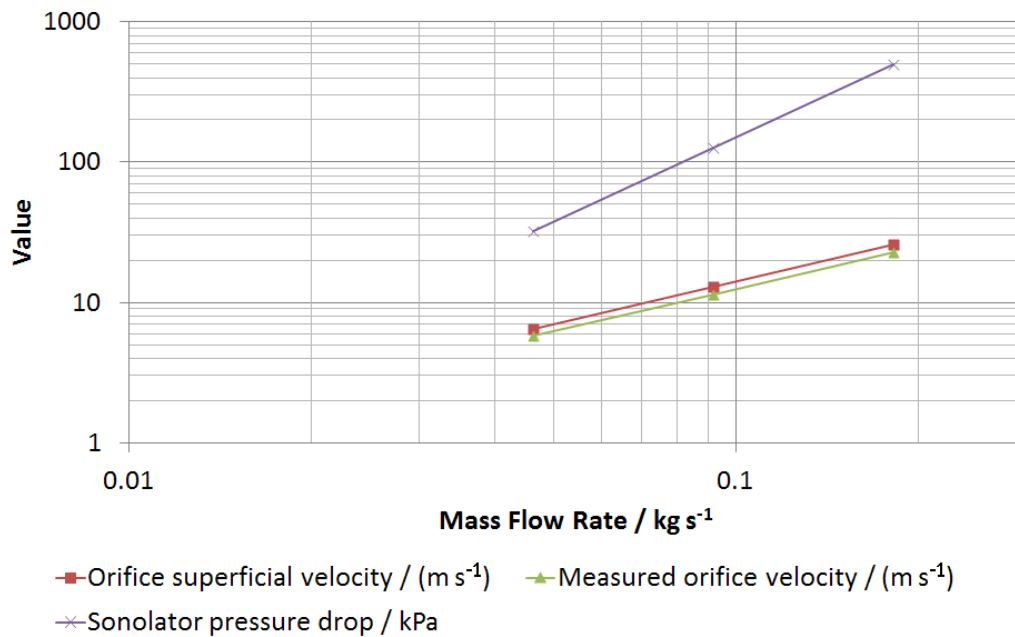
Figure 3.4: Graph of flow variables against mass flow rate, for 0110 orifice, blade out

Orifice superficial velocity (u_{orif}) and measured orifice velocity (u_{meas}) were both proportional to mass flow rate, since the slope on the log-log graph was calculated to be almost exactly 1. Sonolator pressure drop (ΔP) was proportional to the square of mass

flow rate (slope = 2). For each series, the correlation of the flow variable and mass flow rate was very high, indicating that the power laws given above hold strongly within the flow rates investigated. This was also found in preliminary steady state analysis (Ryan *et al* 2011).

3.5.2   Scaling of velocity, static pressure, *k* and *ε* fields with mass flow rate
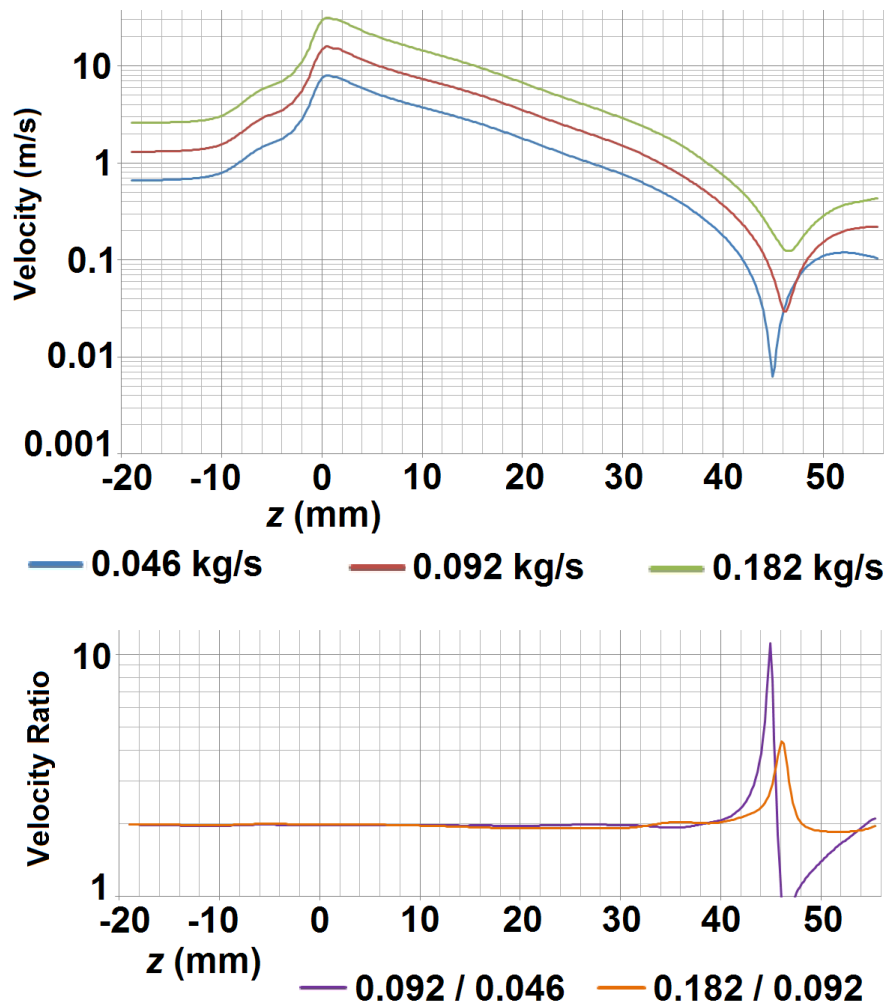
Figure 3.5: Graph of time-averaged velocity magnitude along the Sonolator axis for three flow rates, along with ratios of consecutive series. 0110 orifice, blade out

In Figure 3.5 velocity magnitude along the Sonolator axis was plotted for three mass flow rates, a ratio of 2 between consecutive flow rates. The series were evenly

spaced on the log-scale graph (upper figure), showing scaling rules applied. When the ratios between consecutive series were plotted (lower figure) they were almost exactly constant at a value of 2, ignoring zero magnitude velocities after $z = 40$ mm. This provides good evidence that the overall velocity magnitude field was closely proportional to mass flow rate.
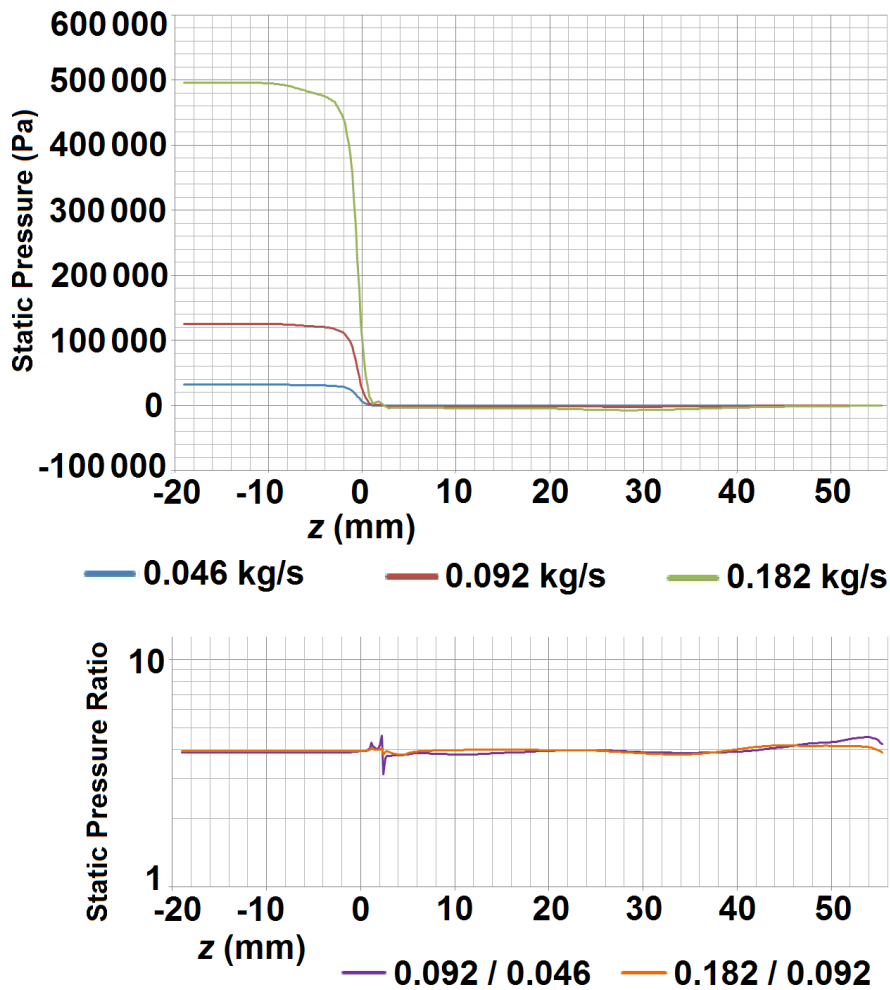
Figure 3.6: Graph of time-averaged static pressure (linear scale) along the Sonolator axis for three flow rates, along with ratios of consecutive series. 0110 orifice, blade out

In Figure 3.6 static pressure had to be plotted on a linear vertical axis since it became slightly negative in places, being measured relative to zero reference pressure at outlet. Nonetheless, the spacing between pressure plots (upper) showed evidence for

scaling rules; the ratios (lower) were near a constant value of 4. This was good evidence that the static pressure field scaled according to the **square** of mass flow rate.
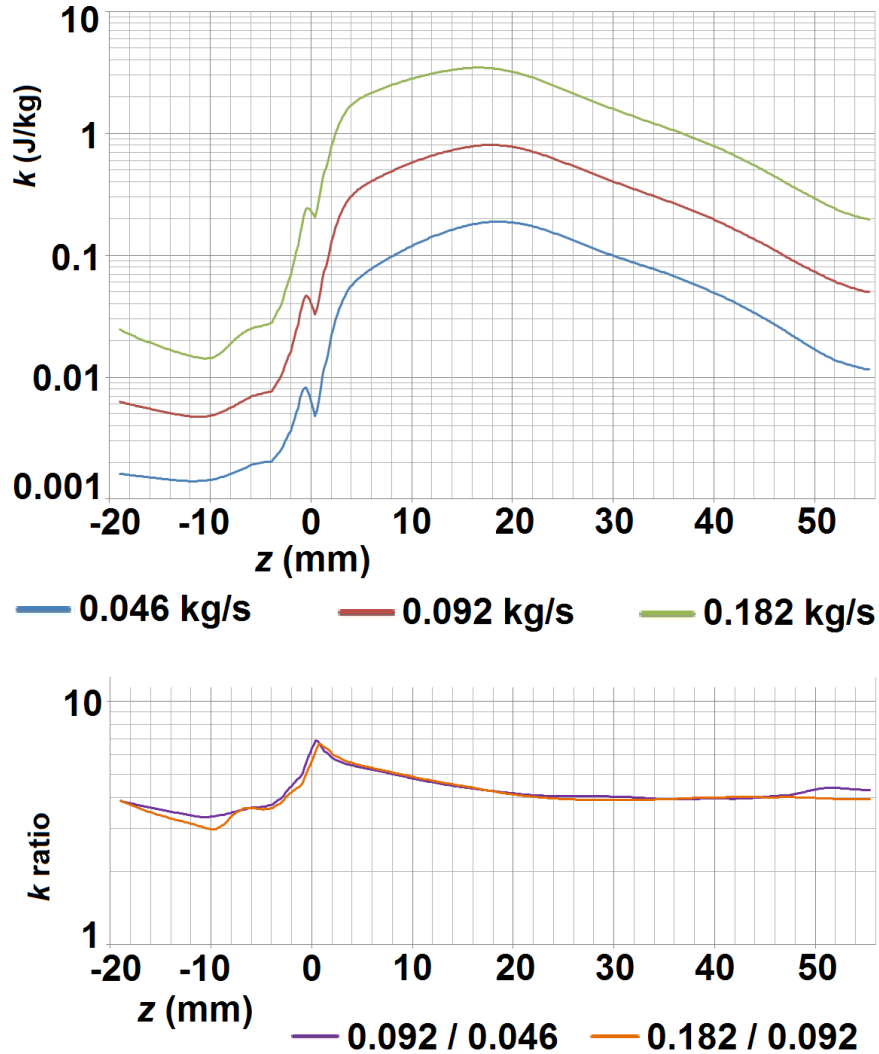
Figure 3.7: Graph of time-averaged k (TKE) along the Sonolator axis for three flow rates, along with ratios of consecutive series. 0110 orifice, blade out

In Figure 3.7 the same analysis was carried out for k, turbulent kinetic energy, an output of the simulation's SST-SAS turbulence model. The graphs of k for three flow rates (upper) showed what looked like a good scaling relation. However, on examining the ratios in more detail (lower) the scaling was not exactly constant at 4, as expected, varying upwards at the orifice ($z = 0$ mm) and downwards in the inlet region

($z < 0$ mm). Nonetheless in the dissipation region of the jet (z between 20 mm and 50 mm) k ratios were almost exactly 4, giving k proportional to **flow rate squared** in that region.
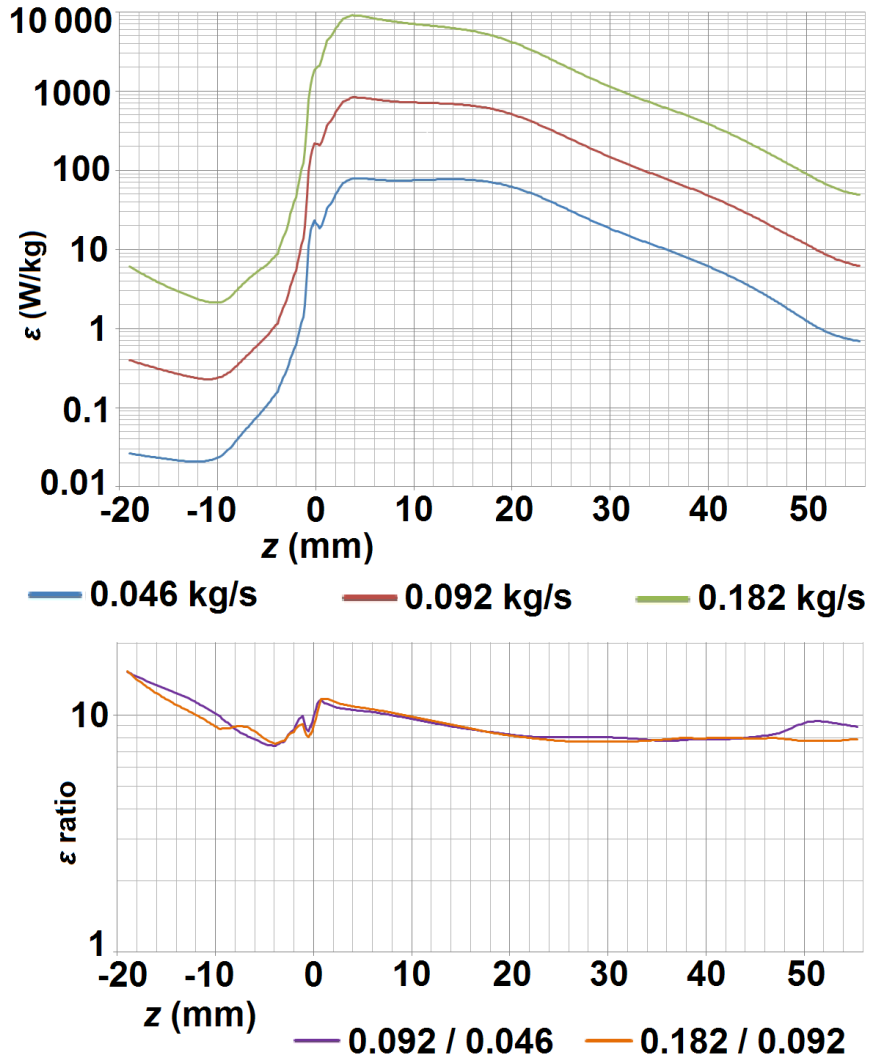
Figure 3.8: Graph of time-averaged ε (turbulent dissipation rate) along the Sonolator axis for three flow rates, along with ratios of consecutive series. 0110 orifice, blade out

Similarly to k, in Figure 3.8 ε plots (upper) looked as though they had good scaling relations. However, when examining their ratios (lower) in the jet dissipation region a near-constant value of 8 was obtained, but variation was found at the inlet and

orifice. Nonetheless, in the jet dissipation region ε therefore scaled by the **cube** of mass flow rate.

The overall evidence was that: velocity magnitude was proportional everywhere almost exactly to flow rate; static pressure to flow rate squared; k to flow rate squared in the jet dissipation region; ε to flow rate cubed in the same region. Additionally, components of velocity scaled according to flow rate, and dynamic pressure to flow rate squared (not illustrated here). All these scaling relations based on flow rate would be expected from dimensional analysis of a fixed geometry, and acts to sense-check the Sonolator results at this point in the analysis.

With these scaling relations, by understanding one flow rate well across the whole Sonolator it would be possible to scale up or scale down to other flow rates, with good accuracy in the jet dissipation region. The rest of the results section below therefore concentrates on one particular flow rate (the medium flow rate, 0.092 kg·s^{-1}).

3.5.3   Pressure drop and discharge coefficient

Using ANSYS CFD-Post a pressure profile was constructed along the Sonolator axis for the middle orifice and flow rate simulation:
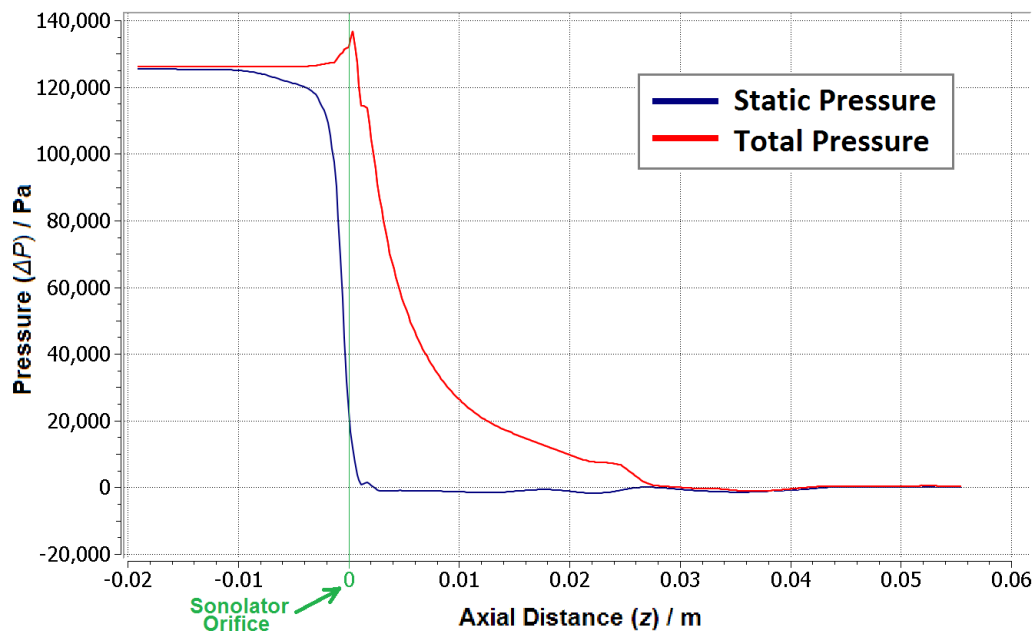
Figure 3.9: Graph of Pressure (both total and static) vs distance along the Sonolator axis; 0110 orifice, blade out, medium flow rate (0.092 kg·s^{-1}).

In Figure 3.9 pressure profiles are displayed for both total and static pressure measurements for a blade out case. Far from the orifice the two pressure measurements agreed, since flow rates were slow. The inlet-to-outlet pressure drop can be read from the graph in both cases as around 125 kPa (c.f. Table 3.3). The static pressure drop from 125 kPa to 0 kPa occurred almost entirely within a few millimetres of the orifice. The total pressure was greater than the static pressure in areas of faster flow; firstly at the orifice, but also in the orifice jet; both these regions were visible in the graph as areas of raised total pressure.
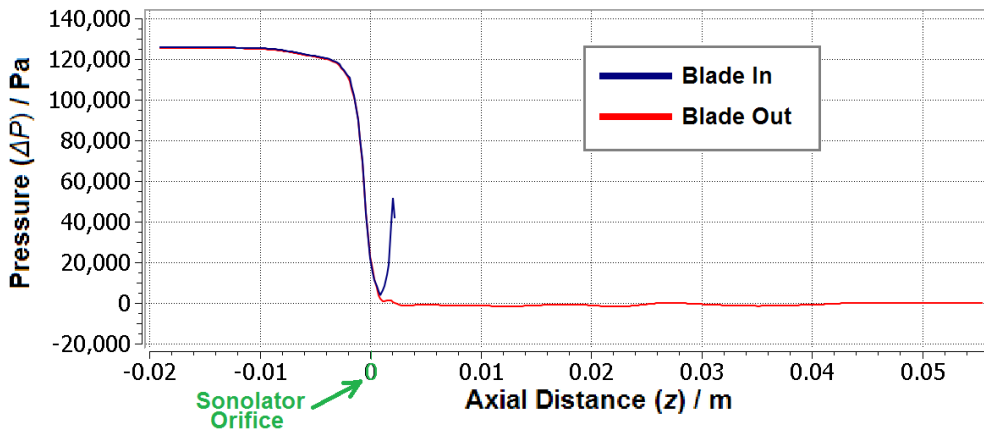
Figure 3.10: Graph of Static Pressure vs distance along the Sonolator axis, for
both blade-in and blade-out cases; 0110 orifice, medium flow rate
$(0.092 \text{ kg} \cdot \text{s}^{-1})$.

The blade-in case was compared to the blade-out case along the Sonolator axis in

Figure 3.10. Static pressures were the same at the inlet and orifice, but the blade-in case

had a spike in pressure just before the blade, due to the rapid deflection of fluid at the

sharp blade edge. (After the start of the blade at 2 mm the axis was no longer in the flow

domain for the blade-in case, hence no further readings could be obtained.)

The behaviour of pressure inside the Sonolator was dominated by the effect of the

orifice, and the blade had only a local and minor effect on pressure. This indicated that

pressure models for orifices would be applicable to Sonolators.

$$C_\mathrm{D} = \frac{Q}{A}\sqrt{\frac{\rho}{2\Delta P}}$$
Eq. (3.7)

(Reference: Perry and Green 1998)

One such model was Discharge Coefficient (C_D) in Eq. (3.7) which was the ratio

between the actual discharge achieved at the orifice to the theoretical maximum

discharge. (Perry's equation is simplified here due to main chamber area being much

larger than nozzle orifice area, giving a factor of approximately unity to remove.) For

144

the 0110 orifice size at medium flow rate: $A = 7.10$ mm^2, $Q = 9.23 \times 10^{-5}$ m^3 s^{-1}, fluid density (ρ) was 997 kg m^{-3}, pressure drop (ΔP) was 125.7 kPa; giving discharge coefficient (C_D) of 0.82 showing the Sonolator achieved near the theoretical maximum discharge. (This result holds for both blade-in and blade-out since the pressure drops were virtually identical in both cases.) Perry (1998) gave a range of 0.4 to 0.8 for orifice plate discharge coefficients; an explanation of how the Sonolator exceeded this range slightly could be that the tapered inlet gave better flow efficiency over a pure orifice plate perpendicular to the flow. Discharge coefficients were also calculated at the lower and higher flow rates given in Table 3.3, and in preliminary work had been calculated over a larger range of flow rates; in all cases comparable discharge coefficients were obtained due to the almost exact proportionality between pressure drop and flow rate squared. Moreover, the manufacturer (Sonic 2011) gave $C_D = 0.79$ for the Sonolator which is in agreement (within the expected tolerances) with the value given here. Hence to calculate pressure drop in the Sonolator it could be assumed that the discharge coefficient is a fixed number in the range 0.79 to 0.82, for flow rates comparable with those given here.

3.5.4 Pressures inside the Sonolator
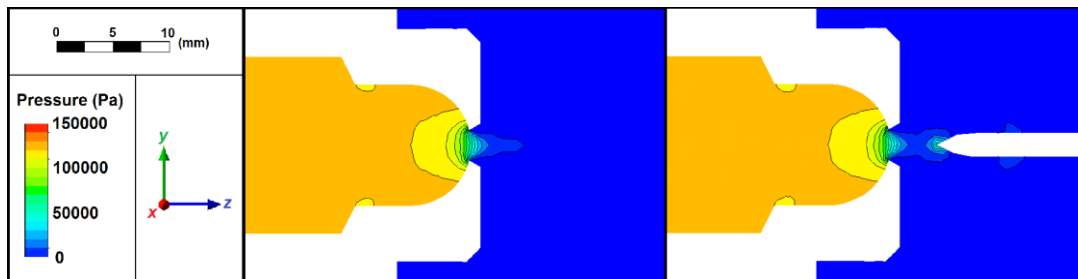
Figure 3.11: Contour plot of static pressure fields (time-averaged) for blade-out (left) and blade-in (right), in the ZY plane (cutting the orifice in the thin direction); 0110 orifice, medium flow rate (0.092 kg·s^{-1})

In Figure 3.11 time-averaged static pressure fields are given as contour plots for blade-out and blade-in cases. Comparing these fields: both exhibited top/bottom symmetry (indicating that the transient pressure field had converged to a stable time-averaged pressure field), high pressure (of around 125 kPa) at the inlet, low pressure (0 kPa) at the outlet, a sharp drop in pressure across the orifice, contours indicating that the pressure drop was concentrated at the orifice. Differences were introduced by the blade; the front of the blade caused a small local increase in pressure as expected by an impediment to the fast flowing jet from the orifice.
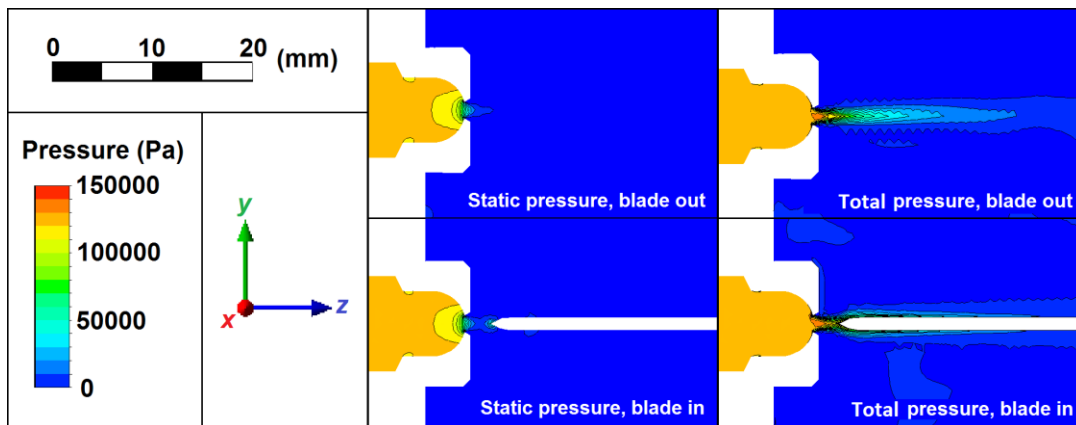
Figure 3.12: Contour plot of total and static pressure fields (**transient**; at final simulation time) for both blade in and blade out, in the ZY plane (cutting the orifice in the thin direction); 0110 orifice, medium flow rate (0.092 kg·s^{-1})

In Figure 3.12 transient pressure fields at the final simulation time are illustrated by contour plot. The 2×2 grid of four cases includes: static pressure (left), total pressure (right); blade-out (top) and blade-in (bottom). The view has been zoomed out slightly from Figure 3.11 in order to view the region after the orifice. In all four cases the inlet pressure was around 125 kPa, the outlet pressure was around 0 kPa, and the pressure drop was seen almost entirely across the orifice. Comparing total pressure to static pressure: the greatest variation was seen in the fast flowing region after the orifice

denoted the "orifice jet". Comparing blade-in to blade-out cases, the orifice jet was split by the presence of the jet and thereafter the split jet followed the blade closely, this is the Coandă effect (Tritton 1977). These results confirmed that the blade has minimal effect upon the pressure drop inside the Sonolator, however it does alter the flow patterns therein. Finally, the total pressure field more than 15 mm downstream from the orifice, in blade-out case, showed that the orifice jet started to oscillate, a phenomenon observed elsewhere and commonly denoted as a "von Kármán vortex sheet" (Kármán 1963).

Contour plots of pressure were also examined in other planes (ZX, XY); these confirmed that the time-averaged pressure fields had the same rectangular symmetry as the Sonolator itself, and that the bulk of the pressure drop was directly due to the orifice.

3.5.5 Transient velocities inside the Sonolator – study in ZY plane
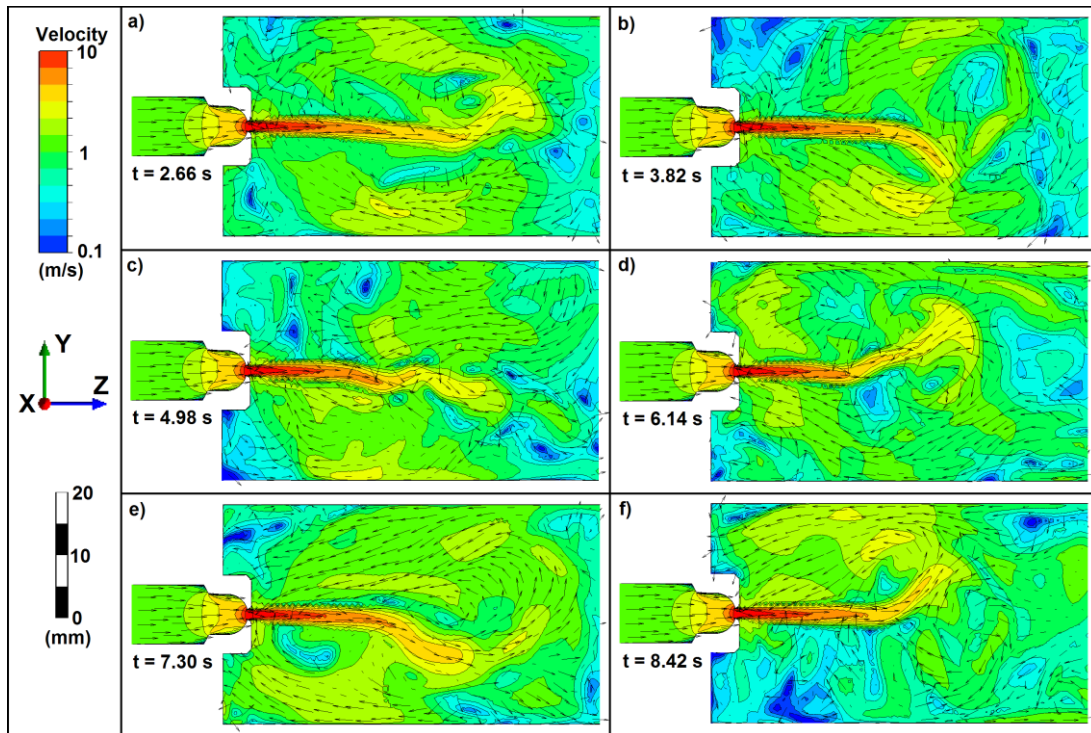
Figure 3.13: Contour plots in the ZY plane of velocity magnitude at six different times during the simulation. Vectors showing direction of flow (not magnitude) are superimposed. Blade-out case, 0110 orifice, medium flow rate (0.092 kg·s^{-1})

In Figure 3.13 six contour plots of the transient flow in the ZY plane of the blade-out Sonolator are given, with superimposed directional vectors. Common features of the transient snapshots were: the general flow pattern before the orifice, the jet just after the orifice where peak velocities were attained, termination of the jet around 30 mm to 40 mm downstream of the orifice. Most frames also showed eddies (blue region) where the velocity magnitude had a minimum due to the flow rotating around it. Differences between frames included: jet direction at the end could go up or down, the jet could be straight or bent by eddies (vortices as described by von Kármán, 1963), the recirculation patterns in the surrounding region were irregular; these features corresponded well with those expected in a region full of turbulent eddies.
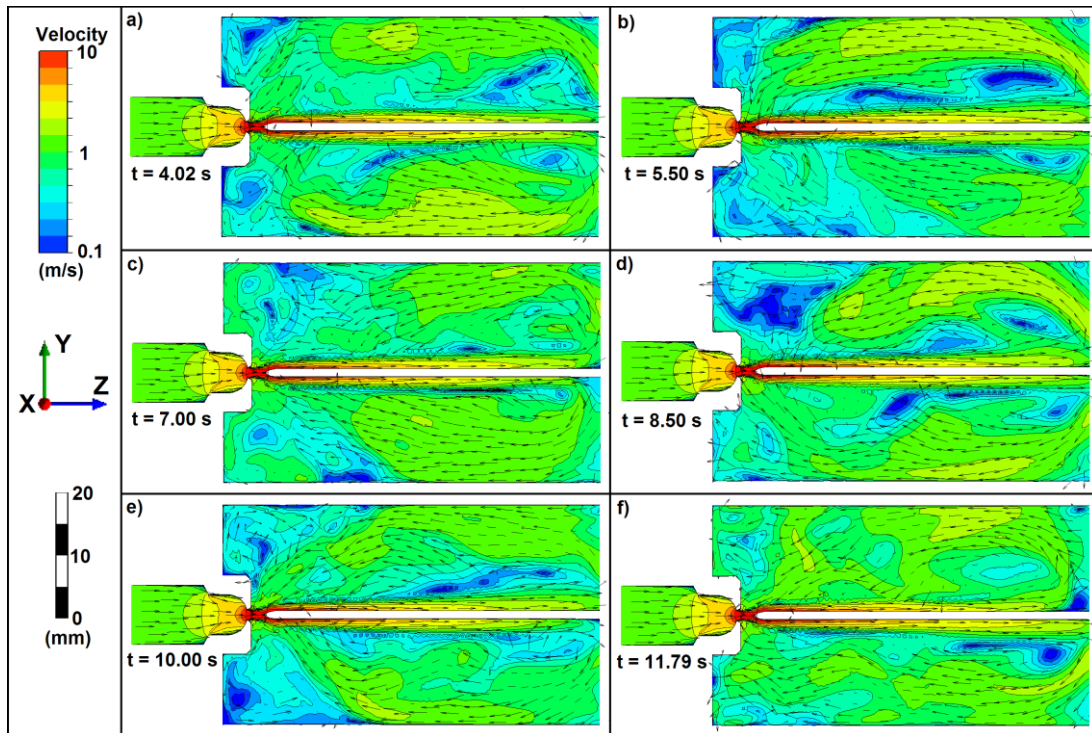
Figure 3.14: Contour plots in the ZY plane of velocity magnitude at six different times during the simulation. Vectors showing direction (but not magnitude) are superimposed. Blade-in case, 0110 orifice, medium flow rate (0.092 kg·s^{-1})

In Figure 3.14 the blade-in case was examined in the same way (see Figure 3.13 for blade-out case). Common features of all frames were, as before, the medium velocities in the inlet region and high velocities in the jet after the orifice. This time the orifice jet was split in all cases by the blade and followed the blade along the length of the blade. Unsteady behaviour was limited to recirculation areas above and below the blade, where at any point in time the recirculation was highly variable. Eddies were also seen in this area, indicating turbulence. The transient flow did not have the top/bottom symmetry of the Sonolator geometry, since turbulence had broken this symmetry.

Comparing Figure 3.14 (blade-in) to Figure 3.13 (blade-out): the effect of the blade was seen to be splitting the jet and directing the flow along the blade edge, lengthening the eventual size of the jet regions. It also constrained each recirculation

pattern to take up half the volume, and caused independent operation of upper and lower regions. The blade did not introduce significantly higher velocities anywhere.

3.5.6 Time-averaged velocities inside the Sonolator
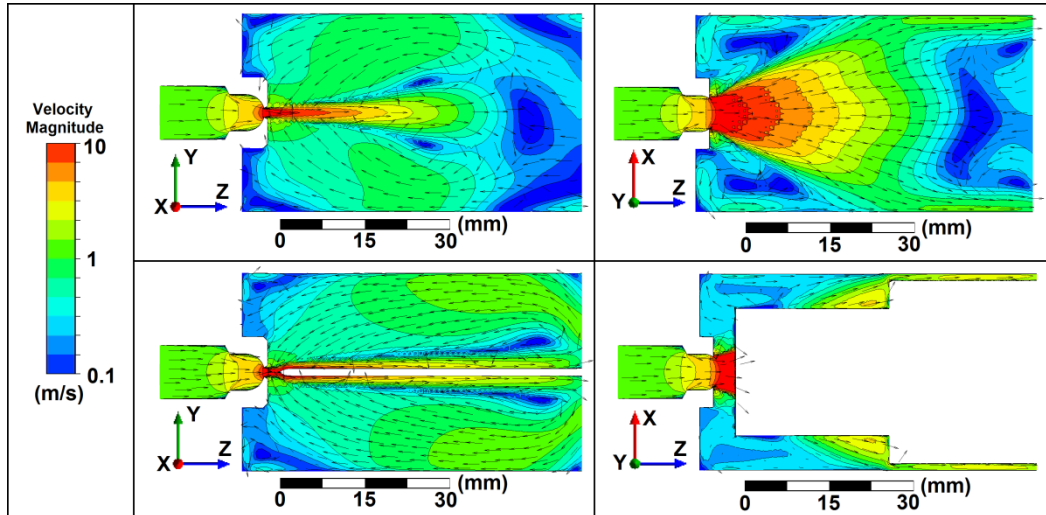
Figure 3.15: Contour plots in ZY (left) and ZX (right) planes of
time-averaged velocity magnitude for blade-out (upper) and blade-in (lower)
cases (2×2 grid). Vectors showing direction (but not magnitude) are
superimposed. 0110 orifice, medium flow rate (0.092 kg·s^{-1})

In Figure 3.15 the time-averaged velocities are shown; these velocities were built up over thousands of time frames from transient frames such as those shown in Figure 3.13 and Figure 3.14, in which the flow was not symmetric under vertical reflection and contained many small features such as eddies, seen as low velocity regions. The time-averaged velocities did have (approximate) vertical symmetry demonstrating a good level of convergence of the simulation results, and no low (average) velocity regions appearing on one side only. In the ZY plane (through thin direction of orifice) the outward jet and returning recirculation were seen clearly. In the ZX plane the jet's wide direction was displayed, and the jet widened rapidly moving away from the orifice. For blade-out case many areas of low velocity (blue) were identified, including above, below and after the jet (ZY), and to the left and right (ZX). For blade-in case the

jet was split, and following the blade the jet regions were longer, moving the low velocity regions above and below the jet further downstream. The other three low velocity regions were not seen, and the blade hindered visualisation of much of the flow in the ZX case, since those parts of the plane were not in the flow domain.
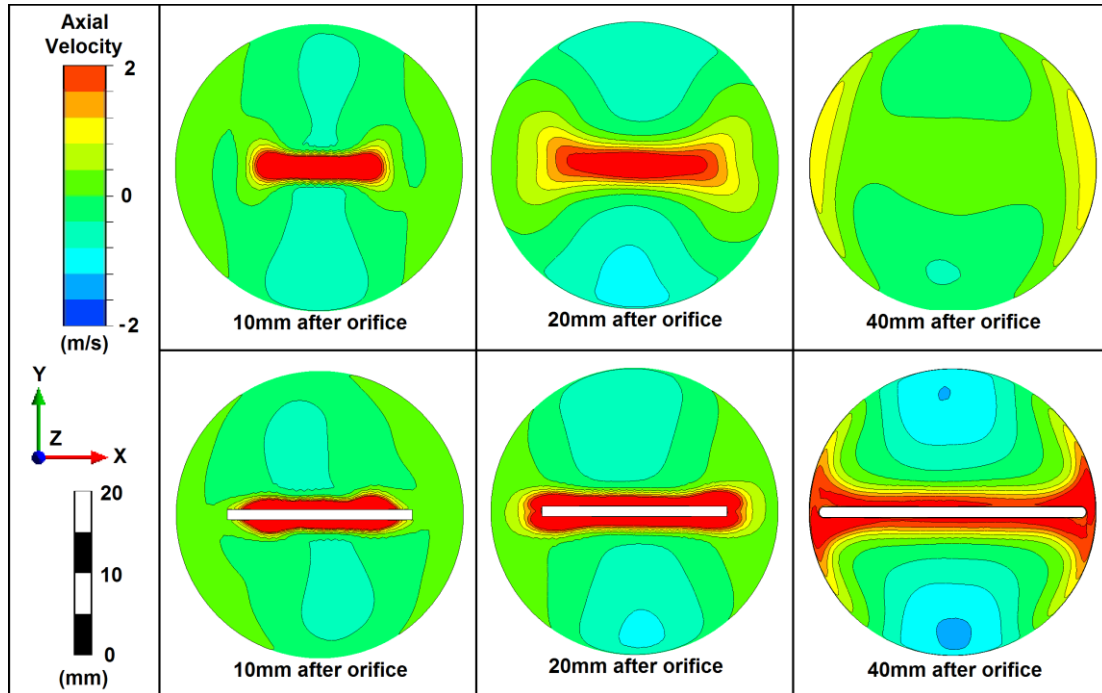
Figure 3.16: Contour plots in the XY plane of time-averaged axial velocity
(+ve downstream) at 10 mm, 20 mm and 40 mm after the orifice, for
blade-out and blade-in simulations. 0110 orifice, medium flow rate
(0.092 kg·s^{-1})

In order to find out the shape of the jet within the Sonolator, flow cross-sections were taken at 10 mm, 20 mm and 40 mm after the orifice for both blade-out and blade-in cases (Figure 3.16). The variable displayed was **axial velocity**, which was the velocity component in the z (downstream) direction. For blade out, the jet was seen to start off approximately rectangular (red area of velocities above 2 m·s^{-1}) and the sides of the jet formed lobes and eventually spread out along the wall. By 40 mm the jet had dissipated giving no more red area. However, for blade-in at 10 mm the jet cross-section was nearly the same shape, although more rounded than rectangular. However at 20 mm

the jet was seen to flatten along the blade, with a flat profile along the blade and part of the wall region at 40 mm. The differences between blade-in and blade-out cases could have been caused by stronger recirculation patterns in blade-in case, due to the more restrictive geometry, pressing the flow against the blade.

The transient and time-averaged velocity fields inside the Sonolator were both found to be complex and fully three-dimensional. Streamline plots are used below to illustrate the 3D nature of the time-averaged velocity pattern, with vector plots along planes of interest to further illustrate flow patterns.
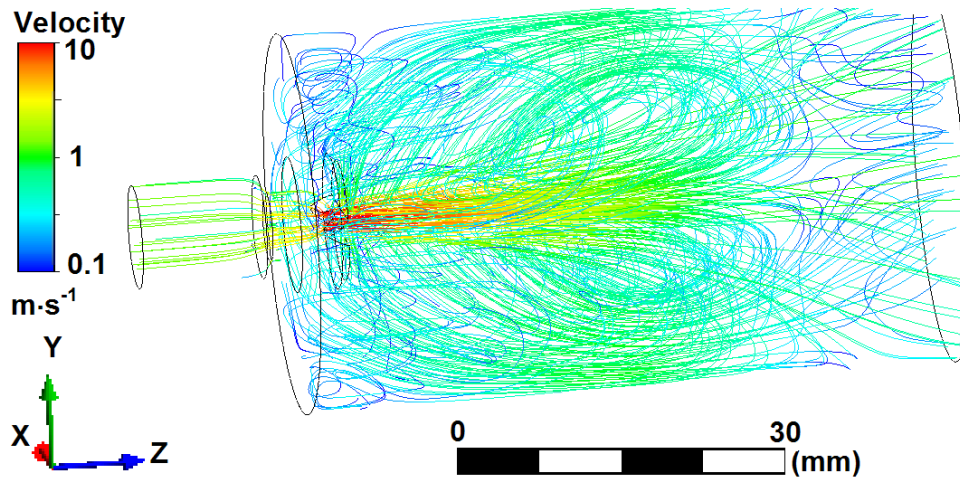
Figure 3.17: Streamline plot of time-averaged velocities with a slightly isometric view, for blade-out case, 0110 orifice, medium flow rate $(0.092 \text{ kg} \cdot \text{s}^{-1})$
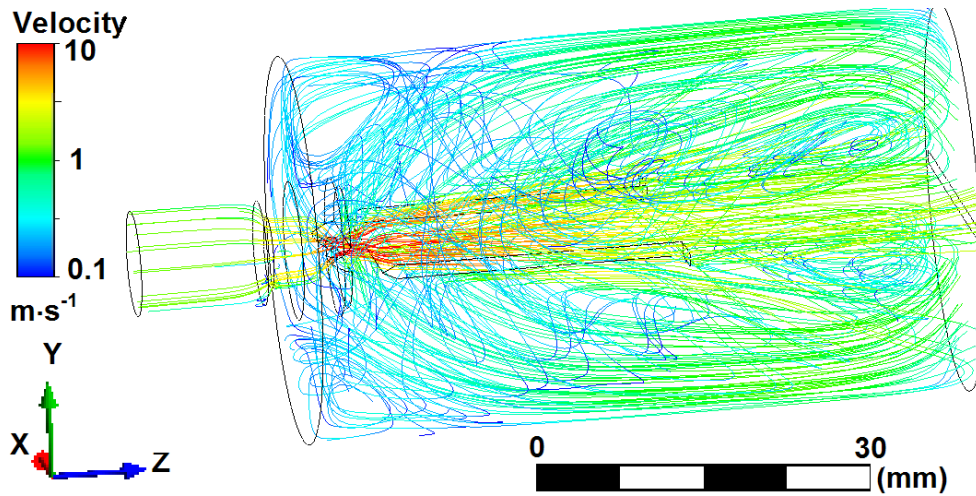
Figure 3.18: Streamline plot of time-averaged velocities with a slightly
isometric view, for blade-in case, 0110 orifice, medium flow rate
(0.092 kg·s^{-1})

Streamline plots are given for blade-out (Figure 3.17) and blade-in (Figure 3.18)
cases. Similarities included: an orifice jet region being visible, with the highest
velocities (red) were found directly downstream of the orifice. Differences include that
both the jet and recirculation regions were visibly longer for blade-in than for blade-out.
The same flow patterns were evident at higher or lower volumetric flow rates within an
order of magnitude (not illustrated here).
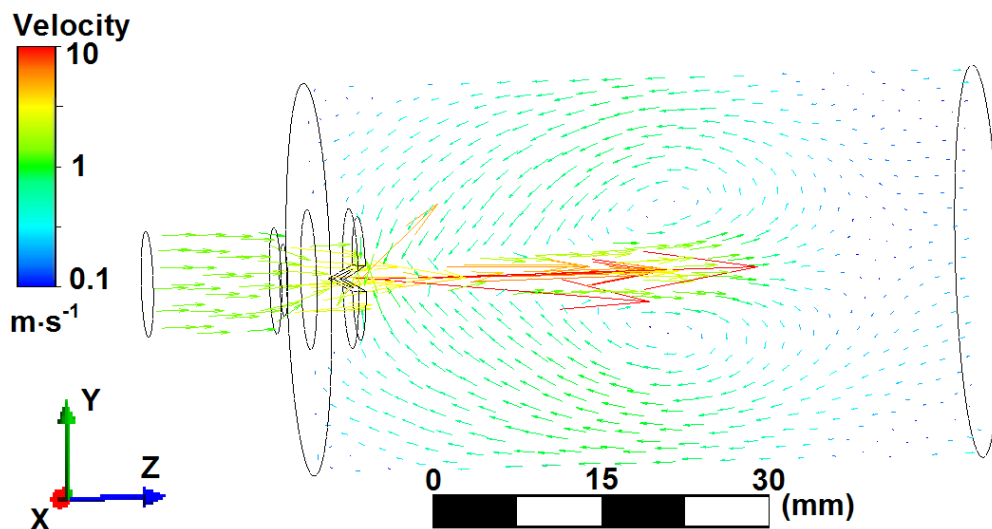
Figure 3.19: Vector plot of time-averaged velocities in the ZY plane for
blade-out case, 0110 orifice, medium flow rate (0.092 kg·s^{-1})

153
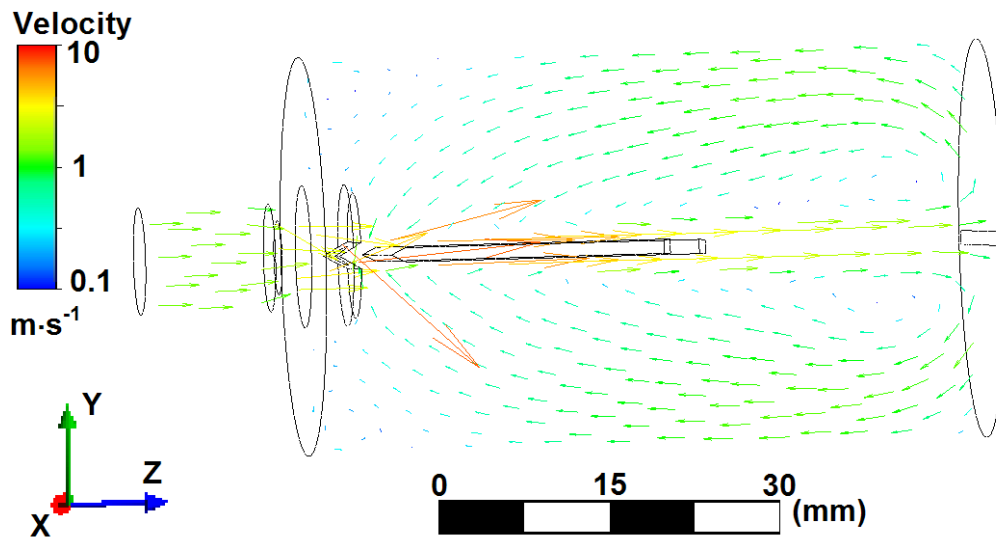
Figure 3.20: Vector plot of time-averaged velocities in the ZY plane for
blade-in case, 0110 orifice, medium flow rate (0.092 kg·s^{-1})

Vector plots for the velocity in the vertical (ZY) plane are given for blade-out (Figure 3.19) and blade-in (Figure 3.20) cases (note that each arrow is valid only at the point it starts from, e.g. the long red arrows are valid at their origin near the orifice). Here it can be seen that the recirculation region is longer in the blade-in case due to the flow following the blade. Interestingly, in both cases the whole plane, minus the jet region, was in the recirculation region, with velocity directions back towards the orifice.
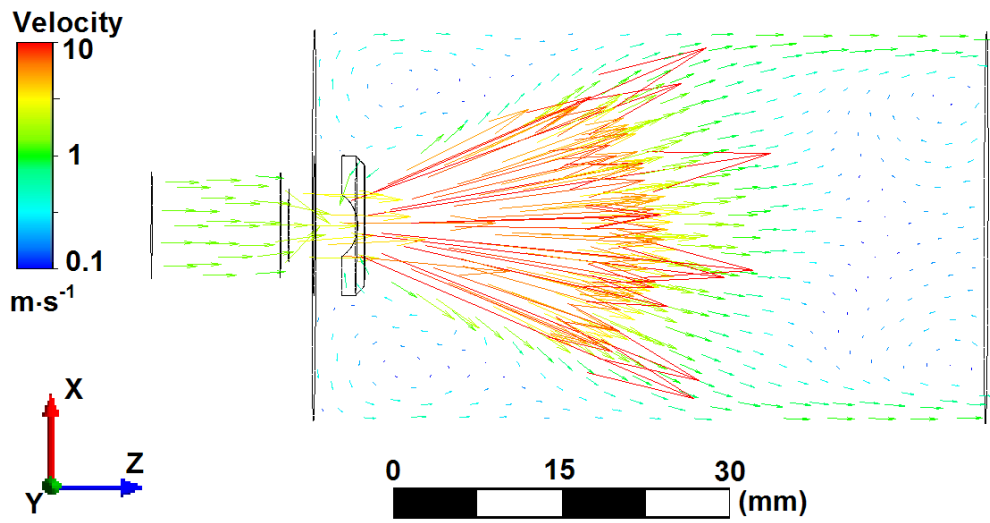
Figure 3.21: Vector plot of time-averaged velocities in the ZX plane for blade-out case, 0110 orifice, medium flow rate (0.092 kg·s^{-1})
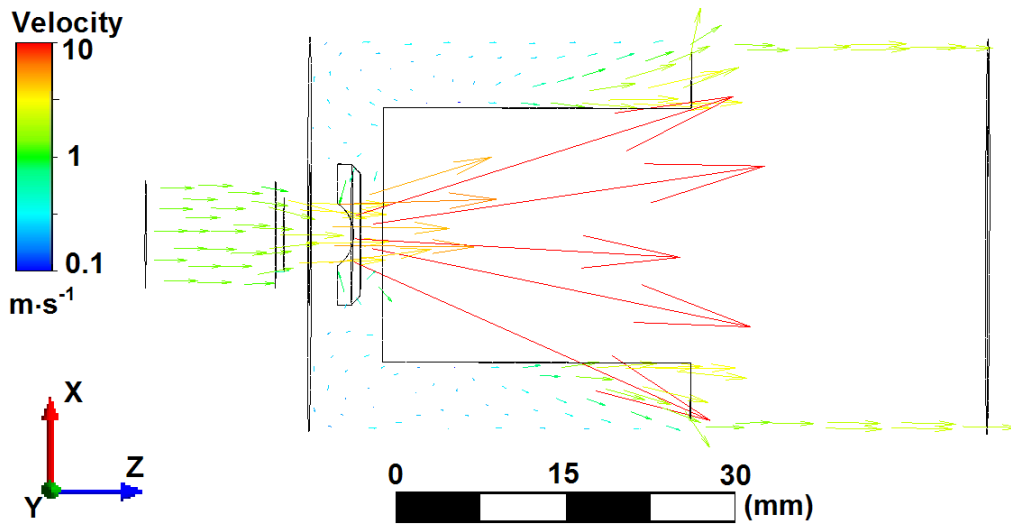
Figure 3.22: Vector plot of time-averaged velocities in the ZX plane for blade-in case, 0110 orifice, medium flow rate (0.092 kg·s^{-1})

Vector plots for the velocity in the horizontal (ZX) plane are given for blade-out (Figure 3.21) and blade-in (Figure 3.22) cases. In both cases the flow near the wall was seen to be in the direction of the outlet due to the widening of the jet and that the majority of fluid exited the Sonolator near this plane, however for blade-in case the

obstruction caused by the blade caused a large gap in the blade-in vector plot where the fluid was pushed out-of-plane.

3.5.7 Turbulence fields (k, ε) inside the Sonolator

Within the CFD simulations two turbulence variables were available as outputs of the SST-SAS turbulence model; k and ε; k was turbulent kinetic energy (TKE on graphs), ε was local specific turbulent energy dissipation rate (Epsilon). Both were available as fields across three dimensions of space inside the flow domain, and one dimension of time from simulation start to end times. For each of these transient fields, a 3D time-averaged field was also available. In the section below a transient frame of each field is given, and then a comparison of different time-averaged frames; each result a 2D contour plot.
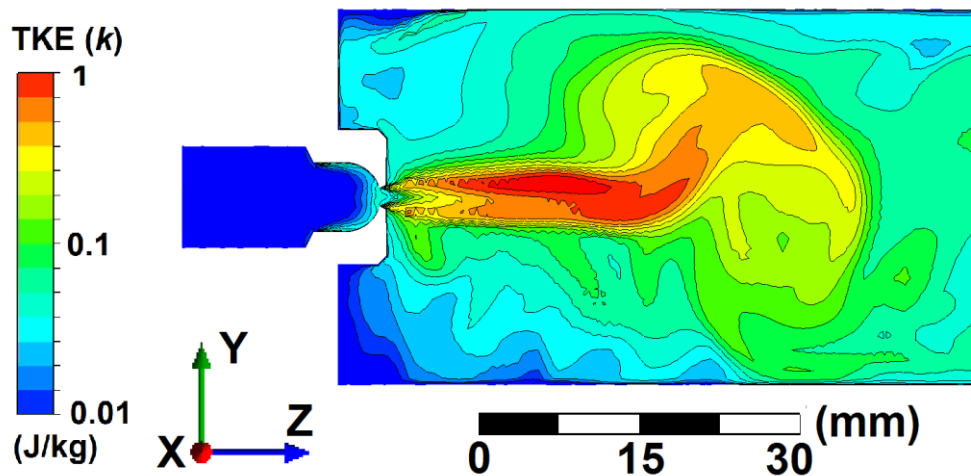
Figure 3.23: Contour plot of **transient** turbulent kinetic energy (k) in J kg^{-1} for blade-out, ZY plane, 0110 orifice, medium flow rate (0.092 kg·s^{-1}). Final time-step at 8.4 s illustrated.

In Figure 3.23 the orifice jet was shown by the k (TKE) contours to be initially straight but disrupted by eddies further downstream from the orifice. Typical values were 1 J kg^{-1} in the region with highest k, which was approximately 20 mm downstream

from the orifice; velocity magnitude peaked around 2 mm downstream, so k peaked later than velocity.
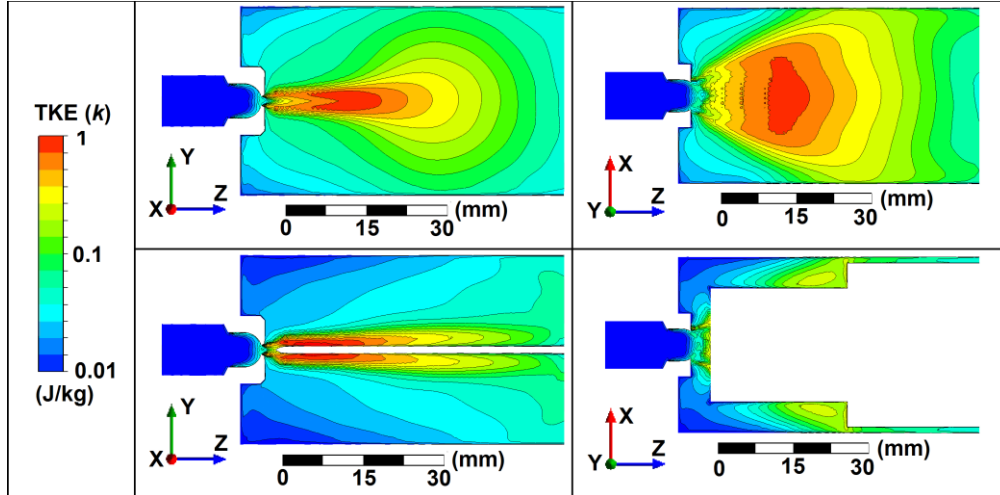
Figure 3.24: Contour plot of time-averaged turbulent kinetic energy (k) in J·kg^{-1} for four cases in a 2×2 grid: top, blade-out; bottom, blade-in; left, ZY plane; right, ZX plane. All data from 0110 orifice, medium flow rate (0.092 kg·s^{-1})

In Figure 3.24 the time-averaged k field was seen to be symmetric in both y and x directions, which was the same rectangular symmetry as the Sonolator. The degree of symmetry was greater for k than for velocity magnitude (c.f. Figure 3.15 above), which could have been because velocity was directional but turbulence was not. The peak value of order 1 J kg^{-1} was seen for both blade-in and blade-out cases, however the blade-out peak value was further downstream (at 20 mm) than that of the blade-in case (at 10 mm). The effect of the blade flow, as visualised by the k contours, was seen to be: splitting the flow, inducing an earlier peak k (but not a higher peak k), giving the flow a boundary to follow which narrowed the fast region of the flow which experienced higher turbulent k values.
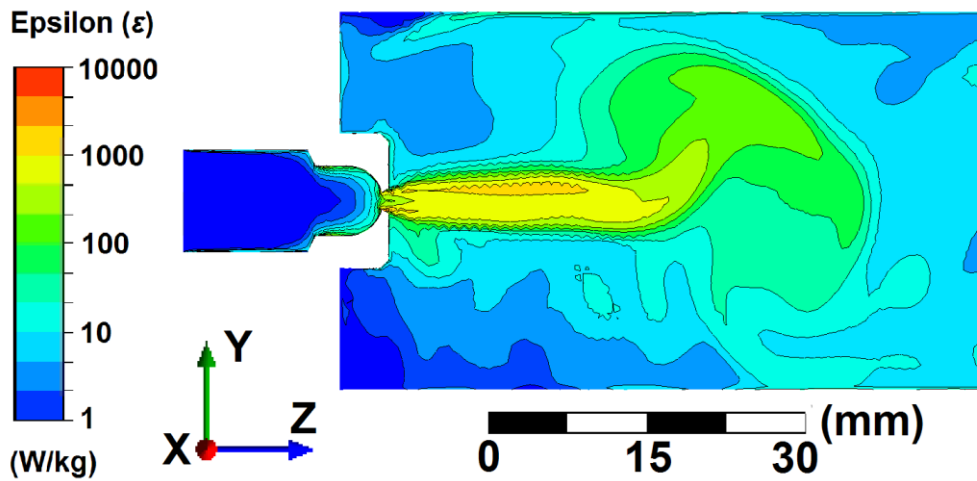
Figure 3.25: Contour plot of **transient** turbulent energy dissipation (ε) in
W kg^{-1} for blade-out, ZY plane, 0110 orifice, medium flow rate
(0.092 kg·s^{-1}). Final time-step at 8.4 s illustrated.

In Figure 3.25 (for transient ε) the time step was the same as for Figure 3.23 (illustrating transient k) and the contour patterns of these showed similar patterns of k and ε downstream of the orifice, up to scaling. Peak ε values of around 1000 W kg^{-1} were found.
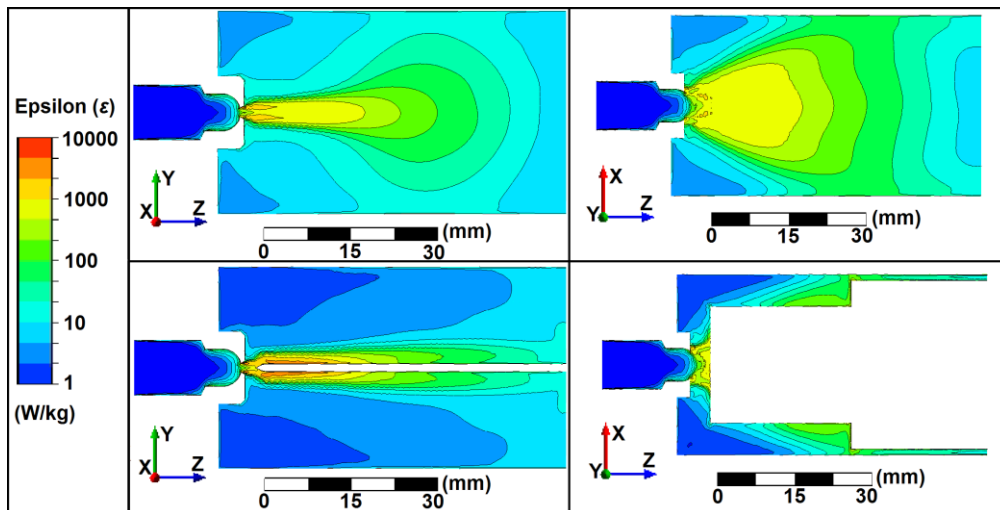
Figure 3.26: Contour plot of time-averaged turbulence energy dissipation (ε)
in W·kg^{-1} for four cases in a 2×2 grid: top, blade-out; bottom, blade-in; left,
ZY plane; right, ZX plane. All data from 0110 orifice, medium flow rate
(0.092 kg·s^{-1})

Similarly, in Figure 3.26 showing time-averaged ε for blade-in and blade-out flows in the ZY and ZX planes, the contour plots had a similar shape to those for k. One difference was that ε peaked on the jet boundary and just after the orifice; k peaked around 20 mm after the orifice (blade-out). In order to better distinguish the patterns of velocity, k and ε; a non-dimensionalised line graph of the different variables along the Sonolator axis was used:
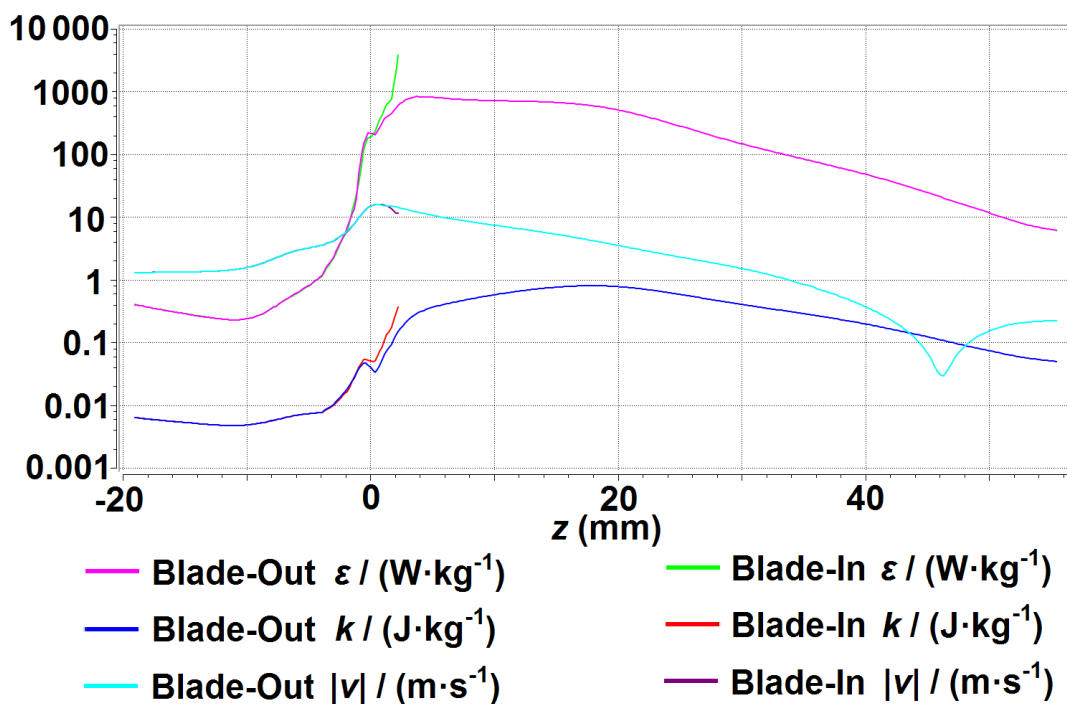
Figure 3.27: Graph of time-averaged variables (ε, k, |v| velocity magnitude) non-dimensionalised by dividing by their units, along the Sonolator axis ($x = y = 0$). 0110 orifice, medium flow rate (0.092 kg·s^{-1})

In Figure 3.27 non-dimensionalised ε and k were plotted for comparison, along with |v| (velocity magnitude). The blade-in cases followed the blade-out cases almost exactly before the orifice, and then diverged sharply at the front of the blade ($z = 2$ mm). For blade-out cases, the slight differences in shape of each variable could now be distinguished. The peak of each variable was at: 2 mm (|v|), 4 mm to 16 mm (ε) and 18 mm (k). After their respective peaks, each variable reduced on the graph in

approximately a straight line (ignoring the stagnation point in $|v|$ at 46 mm); since the graph was log-linear, this indicated exponential decay of magnitude of each variable. Given the two pieces of information: i) the location of the peak value, ii) the exponential decrease thereafter; using these a model for the value of each time-averaged variable along the Sonolator axis could be made.
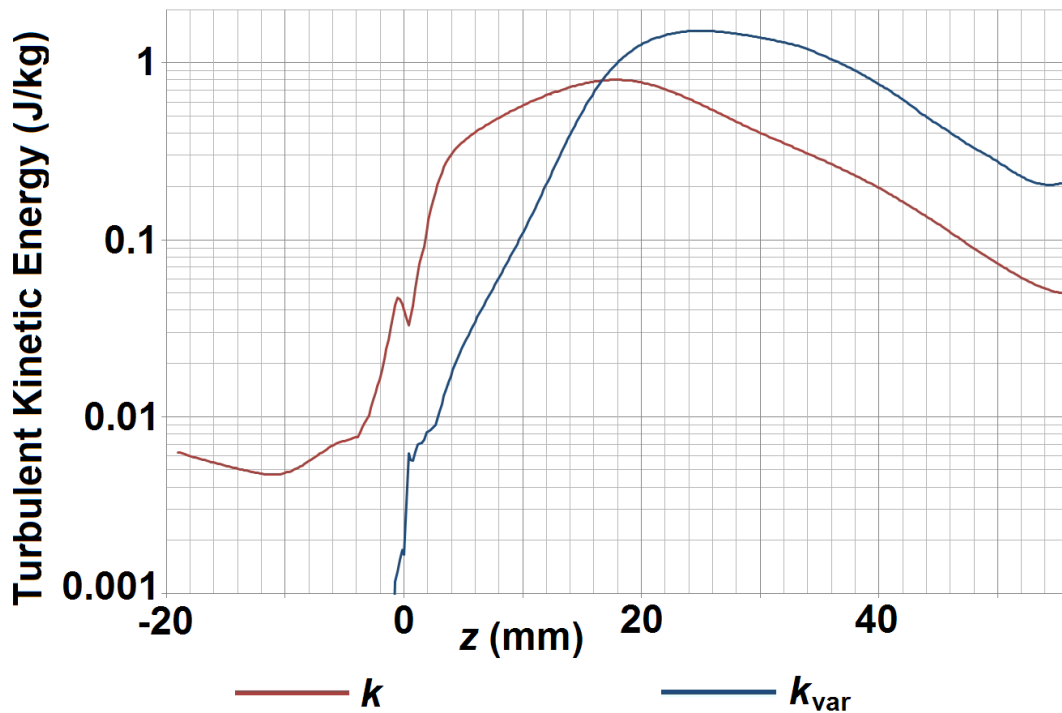
Figure 3.28: Graph along the Sonolator axis comparing: time-averaged k with TKE derived from variance of velocity (k_{var}). Blade-out, 0110 orifice, medium flow rate (0.092 kg·s^{-1})

$$k_{var} = \frac{1}{2}\mathrm{var}(\underline{v})$$ Eq. (3.8)

In Figure 3.28 two different versions of k are compared; in red the same k as previously shown (Figure 3.27) which was a transported variable outputted from the SST-SAS turbulence model; in blue k_{var} defined in Eq. (3.8) which was half the variance of velocity. (This definition had been used in previous PIV work to calculate k from experimental data, and would be used again in the CFD / PIV comparison later.)

Observations from this comparison: regarding peak values, k peaked at $0.8\ \mathrm{J \cdot kg^{-1}}$ at $z = 18$ mm, whereas k_{var} peaked at a higher value $1.5\ \mathrm{J \cdot kg^{-1}}$ further downstream at 25 mm. Within the inlet region and directly after the orifice k had the higher value, but after $z = 17$ mm k_{var} had the higher value. Both variables tailed off approximately exponentially after $z = 30$ mm, with k_{var} around 4 times the magnitude of k.

One reason for $k > k_{var}$ at the inlet was that k was derived from the SST-SAS turbulence model, which introduced medium turbulence (5%) at the inlet as a realistic boundary condition for a fast pipe flow, whereas the flow was nearly steady-state with very low velocity variance.

One reason why $k_{var} > k$ after 20 mm was that in this region the jet oscillated up and down (c.f. Figure 3.13) giving a large contribution to $\mathrm{var}(\underline{v})$, but true turbulence was aperiodic. Further work would include isolating periodic components and recalculating k_{var} after deducting them.

A final reason for differences between these two variables was that k was modelling the intensity of sub-grid eddies, however k_{var} was calculated from on-grid velocities. Nonetheless, since the time step was small, the local time series of velocity would be similar to the local sub-grid spatial profile of velocity (assuming local velocity $\gg$ eddy velocities, as per Taylor's frozen turbulence hypothesis). Hence k_{var} may have included some sub-grid velocity variation, depending on how well Taylor's hypothesis held.

Overall, k and k_{var} in the region of interest (the high turbulence region approximately 10 mm to 40 mm downstream of the orifice) were of the same order of magnitude, but should not be expected to exactly agree when the limitations held which

were listed above. Further work would be needed to verify which version of *k* was better for any specific application.

3.5.8 Power balance within the Sonolator

$$E_{\text{in}} = Q \cdot \Delta P \qquad \text{Eq. (3.9)}$$

Within the Sonolator, the total power input (E_{in}) given by Eq. (3.9) was the product of the volumetric flow rate (9.189×10^{-5} m^3·s^{-1} for blade in and out cases, 0110 orifice, medium flow rate) and the pressure drop (125 700 Pa for same conditions), giving a total power dissipation of 11.55 W.

$$E_{\text{vol}} = \iiint_V \rho \, \varepsilon \, dV \qquad \text{Eq. (3.10)}$$

$$E_{\text{out}} = \iint_S \rho \, \varepsilon \, w \, dS \qquad \text{Eq. (3.11)}$$

$$E_{\text{out+}} = \iint_S \rho \, \varepsilon \, \max(w, 0) \, dS \qquad \text{Eq. (3.12)}$$

$$R = \frac{E_{\text{vol}} + E_{\text{out}}}{E_{\text{in}}} \qquad \text{Eq. (3.13)}$$

$$R_+ = \frac{E_{\text{vol}} + E_{\text{out+}}}{E_{\text{in}}} \qquad \text{Eq. (3.14)}$$

The calculation *R* given in Eq. (3.13) compared the measured dissipation to the power input E_{in} to find the percentage of power input accounted for. The measured dissipation consisted of two terms: E_{vol} given in Eq. (3.10) which was a volume integral of ε over the whole flow domain V, and E_{out} given in Eq. (3.11) which was a surface integral measuring the amount of turbulent dissipation leaving the Sonolator through the outlet surface (this surface had unit normal of (0,0,1) so perpendicular velocity $\underline{v}\cdot\underline{n} = w$ at the Sonolator outlet).

Table 3.4 below gives values for R, E_{vol} and E_{out} for four different simulations with the same E_{in} of 11.55 W. Note that the integrals were formed over transient ε and $\underline{v}$ values from the final time frame for each simulation, since the surface integral term would be incorrect if taken over a product of two time-averaged values. Note also that $E_{\mathrm{out+}}$ and R_+ in Eq. (3.12) and Eq. (3.14) respectively were provided for comparison to E_{out} and R since it was unclear whether only outgoing fluid ($w \geq 0$ m·s^{-1}) or all fluid (all values of w) were the right parts of the outlet surface to integrate over.

Table 3.4: Power balance variables for medium flow rate, 0110 orifice.

Blade	Mesh Type	Mesh Density	E_{vol} (W)	E_{out} (W)	$E_{\mathrm{out+}}$ (W)	R	R_+
In	Octree	Med	1.962	3.893	5.824	50.7%	67.4%
Out	Delaunay	Med	1.949	7.622	8.959	82.9%	94.4%
Out	Octree	Med	2.524	2.340	3.464	42.1%	51.8%
Out	Octree	High	4.538	2.201	3.372	58.3%	68.5%

In Table 3.4 above the values for R were seen to be between 42.1% and 82.9%; those for R_+ were between 51.8% and 94.4%. Some observations include: none of the percentages were above 100% so they were all in a physically believable range; Delaunay mesh had better power balance (closer to 100%) than Octree mesh; blade in case had better power balance than blade out, higher resolution mesh had better power balance than medium resolution; using only the outgoing fluid (R_+) gave a better power balance than for all fluid at the outlet (R). Based on these investigations it would be recommended to calculate a power balance for the Sonolator based on high resolution Delaunay meshes with the blade in and using only the outgoing fluid; a good power balance of 94.4% was achieved this way. Limitations include: only tested for one flow

rate and one orifice, only calculated at one timeframe; further work ought to expand the work to more cases.

3.5.9   Effect of Blade

The blade-in and blade-out Sonolator cases were compared to identify specific blade effects. Previously it had been seen that velocity patterns before the blade were almost identical, but after the blade the jet was guided by the blade and recirculation patterns were strengthened and elongated. Pressure drop was almost identical with or without the blade; this indicated that total power dissipation was the same in the two cases. Large effects had not yet been seen for turbulent k and ε. The two figures below investigate ε in more depth for blade-out and blade-in.
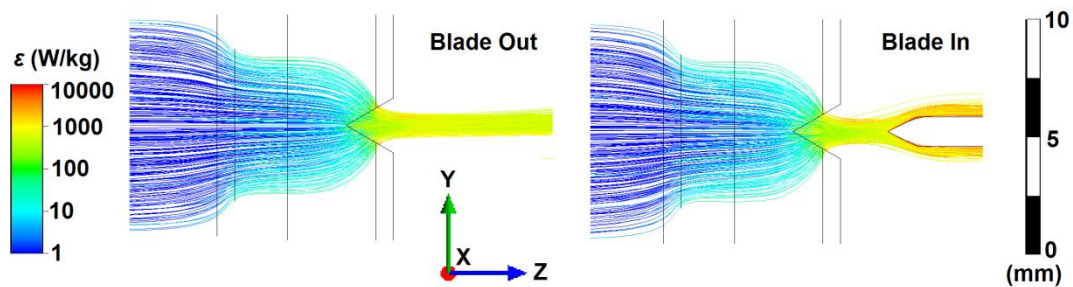
Figure 3.29: Streamline plot of time-averaged velocity in ZY plane (using 500 streamlines originating at inlet), coloured by magnitude of time-averaged ε. 0110 orifice, medium flow rate (0.092 kg·s^{-1})

In Figure 3.29 each streamline followed the time-averaged velocity vectors, and a ZY projection of ε magnitude was plotted on a colour scale. The diversion of flow around the blade was seen clearly. In the blade-in case the colouration was more orange than yellow around the blade, hinting at higher values of ε there. These were illustrated in more detail below, using a smaller subset of streamlines enabling counting of individual streamlines:
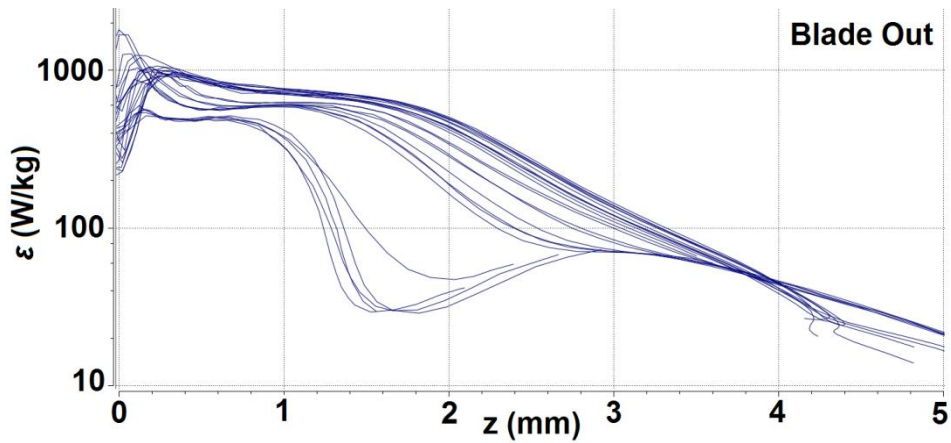
Figure 3.30: Graph of ε vs axial position (z) along streamlines originating at the orifice for blade-out case. 0110 orifice, medium flow rate (0.092 kg·s^{-1})
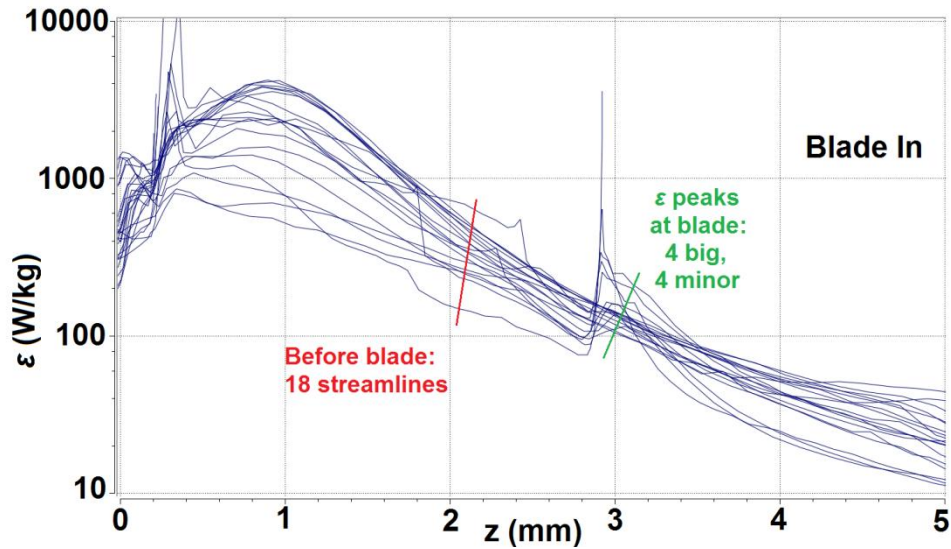
Figure 3.31: Graph of ε vs axial position (z) along streamlines originating at the orifice for blade-in case. 0110 orifice, medium flow rate (0.092 kg·s^{-1})

In Figure 3.30 and Figure 3.31 multiple traces for ε *vs. z* are displayed for blade-out and blade-in cases respectively. Each trace represented a single streamline in the flow domain in 3D space (x and y components were ignored here). The peak ε values were higher for the blade-in case (2 kW·kg^{-1} and 3 kW·kg^{-1}) than for the blade-out case (just below 1 kW·kg^{-1}). The peaks were sharper for blade-in than for blade-out. The exponential decrease was similar for both cases after 2.5 mm, except for

in the blade-in case where a minority of streamlines experienced sharp deflection at the blade (z between 2.9 mm and 3.2 mm was the angle of the blade just behind the front edge), shown by extra peaks in ε graphs.

In the blade-in case, 18 streamlines were seen just before the blade; 4 of those experienced major secondary peaks at the blade; 4 experienced minor peaks, and the remaining 10 experienced no peak at the blade z position, meaning they passed a relatively long way (but still less than 1 mm, c.f. Figure 3.29) from the blade surface with less sharp deviation in path. Hence for around 22% of the flow the blade had a major effect on ε, for 22% a minor effect, and for 56% no effect. (These statistics were accurate to approximately 1 in 18 (5.5%) and a higher accuracy would be obtained from larger sample sizes of streamlines.)

Overall the blade seemed to have a greater effect through the induced changes in recirculation patterns than by the effect seen at the blade edge; ε was raised more at the vena contracta ($z = 1$ mm) than near the blade edges (z = 3 mm); at the vena contracta all streamlines were affected, but only a minority at the blade. It was therefore expected that levels of ε (and Sonolator effects e.g. mixing / emulsification) were marginally higher with the blade in.

3.5.10 Time decay of ε after the orifice

In emulsification, an industrial application of Sonolators, ε is thought to control droplet breakage (Hinze 1955, Davies 1985). Previously, ε had been estimated by dividing power consumption by a suitable volume. Now in CFD, ε from the SST-SAS turbulence model could be interrogated directly.

The information needed about ε was how it affected a typical fluid element travelling through the orifice over time; further work could use this as an input for

population balance modelling of droplet breakage; hence ε was examined on a large number of streamlines transiting the orifice for both blade-out and blade-in cases, plotted against time.
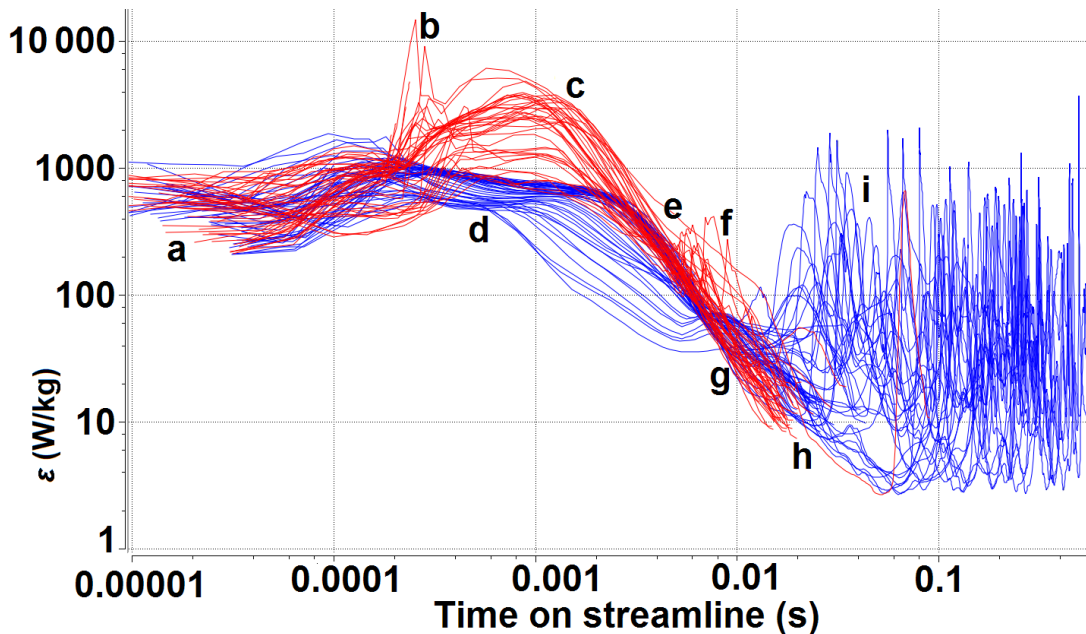
Figure 3.32: Log-log graph of time-averaged ε vs time on streamlines originating at orifice. Up to 200 streamlines illustrated for blade-in (red) and blade-out (blue) cases. 0110 orifice, medium flow rate (0.092 kg·s^{-1})

In Figure 3.32 typical values for ε as the fluid elements transited the orifice can be seen for blade-in (red) and blade-out (blue) cases, with several points of interest labelled with letters:

- a) At the orifice both cases had ε values around 800 W kg^{-1}

- b) and c) showed peak values at vena contracta for blade-in case, whereas d) for blade-out case had similar ε values as at a)

- e) and g) a **power law** decay (straight line on log-log graph) of ε with time was found, with extra peaks at f) for blade-in case. The exponent of t was estimated at between -1.85 and -2.08, in the correlation to give ε. Further work is required to give a more accurate exponent for blade-in and blade-out cases.

- h) for blade-in most streamlines disappeared (exited the Sonolator), whereas for blade-out many streamlines recirculated (evidenced by subsequent peaks) so that at i) only the recirculating streamlines remained.

Previous Sonolator simulations had shown that the two regions of constant ε (on figure: a, d) then decaying ε (on figure: e, g) were typical for Sonolators. Moreover, when the main chamber was longer (as in previous investigations) the power law decay of ε continued for longer than illustrated above. (These simulations used a shorter main chamber to get maximum detail at the orifice; this was therefore a trade-off, given the fixed computational power, with getting results over a longer downstream volume.) Hence in Appendix 2 outlining methodology for Droplet Breakage Simulations, in Appendix Fig 9 a plateau followed by a power law decay region are shown as the main droplet-breaking components of the ε field.

3.5.11 Recirculation – qualitative characterisation

Within the Sonolator main chamber all fluid entered by the orifice, but not all fluid left quickly since some recirculated. It was desired to gather more information on how much fluid recirculated.
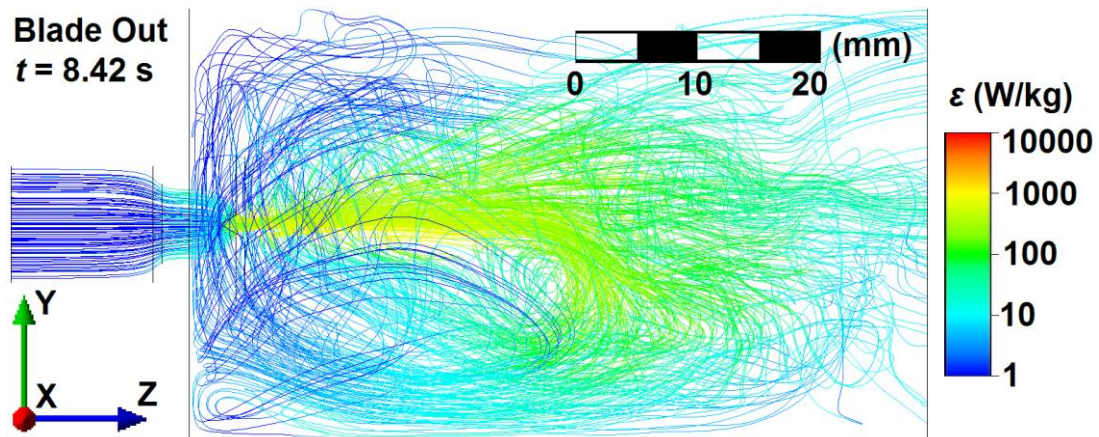
Figure 3.33: Streamline plot (ZY projection) of transient velocity vectors
(using 200 streamlines originating at inlet), coloured by magnitude of
transient ε. 0110 orifice, medium flow rate (0.092 kg·s^{-1})

In Figure 3.33 streamlines are displayed which had been created from an instantaneous snapshot of the transient velocity field. With the approximation that the fluid for a short time afterwards followed the instantaneous streamlines, it was seen that some fluid went straight through the Sonolator, but considerable amount of fluid recirculated, evidenced by recirculating streamlines. It was found very difficult to quantify exactly how much fluid recirculated, however the transient streamlines above seemed to indicate over 50% since only a minority of streamlines exited at the outlet without doubling back.
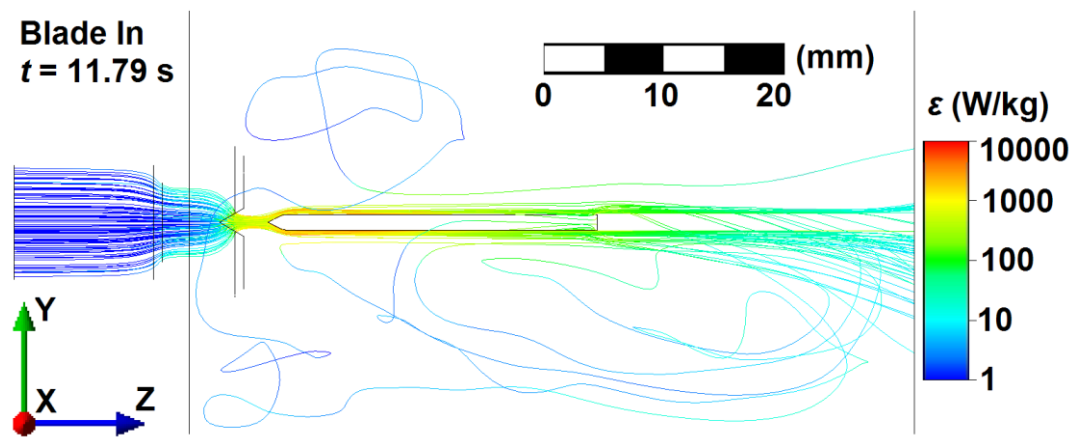
Figure 3.34: Streamline plot (ZY projection) of transient velocity vectors
(using 200 streamlines originating at inlet), coloured by magnitude of
transient ε. 0110 orifice, medium flow rate (0.092 kg·s^{-1})

In Figure 3.34 the same analysis was carried out for transient velocity vectors
from the blade-in case; this had the same number of original streamlines (as in Figure
3.33 for blade-out). This time almost all of the streamlines closely followed the blade
and exited at the outlet; in the region of 3 to 5 streamlines exhibited any recirculation.
(Care ought to be taken since not all 200 streamlines were found to transit the orifice,
moreover the recirculation pattern was longer in this case.) A conservative estimate was
that over 80% of the streamlines went straight through the Sonolator, with the proviso
that further work on a longer main chamber ought to be carried out to check this. Hence
in comparing the two cases, for blade-out case most fluid recirculated, but for blade-in
case most fluid did not recirculate. This is likely to be relevant to further work on
mixing studies.

3.6   Conclusions

The Sonolator CFD simulations gave a wide variety of predictions regarding the 3D transient flow fields within the Sonolator geometry. These predictions are listed below. Suggestions for further CFD experiments are given later in Chapter 7.

- Scaling relations: the mass flow rate was proportional to:

    o Volumetric flow rate

    o Time-averaged velocity field (including orifice measured and superficial velocities)

    o Square root of time-averaged static and total pressure fields (zero reference pressure at outlet)

    o Square root of time-averaged k from SST-SAS turbulence model used. The scaling was good 20 mm after the orifice, and approximate directly after the orifice.

    o Cube root of time-averaged ε from SST-SAS turbulence model used. Again, better scaling at 20 mm after the orifice, approximate scaling directly after orifice.

- The static pressure drop occurred almost entirely at the orifice, with only a relatively small increase where the fluid directly impinged on the blade.

- The discharge coefficient of the Sonolator was consistent with the manufacturer quoted figure of $C_D = 0.79$ (Sonic 2011).

- The transient flow fields inside the Sonolator were fully 3D, turbulent and asymmetric; the time-averaged flow fields were fully 3D, but regular and smooth (away from sharp edges at orifice and blade) with the same rectangular symmetry as the underlying geometry of the Sonolator.

- The basic features of the flow were: a medium velocity inlet region, a high velocity orifice jet, lower velocity dissipation region (downstream of orifice) and recirculation regions (out of plane of the long direction of the orifice).

- Having the blade present directed the flow along the blade and lengthened the recirculation region, making the orifice jet more pinched directly after the orifice.

- As the fluid travelled through the orifice and downstream, the magnitude of velocity, k and ε fields decreased approximately exponentially with distance, and decreased approximately by a power law relationship with time. (These are consistent with each other when considering that time spent at each distance is inversely proportional to velocity.) Using this information it would be possible to construct a model of these variables on a fluid packet, vs distance or time, as the fluid packet travels through the orifice and further downstream. Such a model would have value in further studies such as population balance equations for breakage of emulsion droplets (see Appendix 2).

3.7 Nomenclature & Abbreviations

Symbol   **Description**

A Cross-sectional Area (m^2), of nozzle orifice (unless otherwise stated)

B   Constant (s$^3 \cdot$m^{-1})

dV, dS infinitesimal volume and surface elements in integral calculations

d_{max} Maximum droplet diameter (m)

D$_H$ Nozzle Orifice Hydraulic Diameter (m)

E_{in} Power dissipation introduced by the Sonolator pressure drop (W

E_{vol} Volume integral of ε over the Sonolator (W)

E_{out} (Derived from) surface integral of ε over the Sonolator outlet (W)

$E_{\text{out}+}$ Surface integral of ε over the Sonolator outlet (outgoing only)

k Turbulent kinetic energy ($\text{J}\cdot\text{kg}^{-1}$ or $\text{m}^2\cdot\text{s}^{-2}$) from the SST-SAS model

k_{var} Turbulent kinetic energy ($\text{J}\cdot\text{kg}^{-1}$) calculated from velocity variance

M Mass Flow Rate ($\text{kg}\cdot\text{s}^{-1}$)

p Perimeter (m), of nozzle orifice (unless otherwise stated)

P Local pressure measurement (Pa), total or static as indicated in text

ΔP Pressure drop from inlet to outlet (Pa)

Q Volumetric Flow Rate ($\text{m}^3\cdot\text{s}^{-1}$)

t Time coordinate; time after orifice (s)

T   Ambient Temperature (K)

u_{orif} Orifice superficial velocity ($\text{m}\cdot\text{s}^{-1}$)

u_{meas} Measured orifice velocity (area average over orifice interior surface, $\text{m}\cdot\text{s}^{-1}$)

$\underline{v}$ Velocity field in the flow domain ($\text{m}\cdot\text{s}^{-1}$)

$\underline{x}$ Spatial coordinate vector in the flow domain (m) equal to (x,y,z)

x, y, z Spatial coordinates in the flow domain (m)

z Axial Position (m)

Greek Symbols

ε Local specific turbulent energy dissipation rate ($\text{W}\cdot\text{kg}^{-1}$ or $\text{m}^2\cdot\text{s}^{-3}$)

Θ, θ Conserved variable Θ with a surface flux θ

ρ Water Density under ambient conditions ($\text{kg}\cdot\text{m}^{-3}$)

μ Dynamic viscosity of water under experimental conditions (Pa·s)

σ Interfacial tension ($\text{N}\cdot\text{m}^{-1}$)

v Kinematic viscosity of water ($\text{m}^2\cdot\text{s}^{-1}$)

ω Turbulent frequency (Hz)

Dimensionless Groups

C_D Discharge Coefficient

R   Power balance ratio for Sonolator

R_+ Power balance ratio for Sonolator (outgoing fluid only)

Re   Reynolds Number

y_+ Dimensionless wall distance

Abbreviations

ANSYS   Software developers of the CFX package

CFD   Computational Fluid Dynamics

CFX   Implementation of CFD software by ANSYS

DES   Detached Eddy Simulation

DNS   Direct Numerical Simulation

FDM   Finite Difference Method

FEM   Finite Element Method

FVM   Finite Volume Method

GGI   Generalised Grid Interface joining flow domains at surface meshes.

LES   Large Eddy Simulation

NSE   Navier-Stokes Equations

RANS   Reynolds-Averaged Navier-Stokes turbulence models

RSM   Reynolds Stress turbulence model

S-A   Spalart-Allmaras turbulence model

SAS   Scale Adaptive Simulation (turbulence modelling method)

SST   Shear Stress Transport (a turbulence model)

URANS   Unsteady versions of RANS models

XY	Plane through the Sonolator including the x, y axes
ZX	Plane through the Sonolator including the x, z axes
ZY	Plane through the Sonolator including the y, z axes

3.8   Acknowledgements

3.9   References

- Acheson, D. J., (1990). "*Elementary Fluid Dynamics*", Oxford Applied Mathematics and Computing Science Series, Oxford University Press, ISBN 0-19-859679-0.

- Al-Shemmeri, T., (2012). "*Engineering Fluid Mechnanics*", Ventus Publishing ApS., 17-18.

- Anderson, J. D., (1995). "*Computational Fluid Dynamics: The Basics With Applications*", McGraw-Hill Science, ISBN 0-07-001685-2.

- Batchelor, G. K., (1967). "*An Introduction to Fluid Dynamics*", Cambridge University Press, ISBN 0-521-66396-2.

- Davies, J. T., (1985). "Drop Sizes of Emulsions Related to Turbulent Energy Dissipation Rates", *Chem. Eng. Sci.*, **40(5)**, 839-842.

- Dománski, M., Karcz, J., Bitenc, M. (2014). "Scale-adaptive simulation of liquid mixing in an agitated vessel equipped with eccentric HE 3 impeller", *Chemical Papers*, **68(7)**, 899-912.

- Donea, J., Huerta, A., (2003). "*Finite Element Methods for Flow Problems*", ISBN 0471496669, Wiley, GB.

- Duda, B. M., Menter, F. R., Hansen, T., Esteve, M. J. (2011). "Scale-adaptive simulation of a hot jet in cross flow", *Journal of Physics: Conference Series*, p.042050, **318(4)**, IOP Publishing.

- Egorov, Y., Menter, F. (2008). "Development and application of SST-SAS turbulence model in the DESIDER project", *Advances in Hybrid RANS-LES Modelling*, 261-270, Springer, Berlin, Heidelberg.

- Egorov, Y., Menter, F. R., Lechner, R., Cokljat, D., (2010). "The scale-adaptive simulation method for unsteady turbulent flow predictions. Part 2: application to complex flows". *Flow, Turbulence and Combustion*, **85(1)**, 139-165.

- Eymard, R., Gallouët, T., & Herbin, R. (2000). "Finite volume methods", *Handbook of numerical analysis*, **7**, 713-1018.

- Freeman, J. A., Roy, C. J. (2014). "Verification and validation of Reynolds-averaged Navier–Stokes turbulence models for external flow", *Aerospace Science and Technology*, **32(1)**, 84-93.

- Gabriele, A., Nienow, A. W., Simmons, M. J. H., (2009). "Use of angle-resolved PIV to estimate local specific energy dissipation rates for up- and down-pumping pitched blade agitators in a stirred tank.", article plus later erratum, *Chem. Eng. Sci.*, **64**, 126–143.

- Hinze, J. O., (1955). "Fundamentals of the Hydrodynamic Mechanism of Splitting in Dispersion Processes", *AIChE. Journal*, **1(3)**, 295.

- Hinze, J.O., (1975). "*Turbulence*", McGraw-Hill.

- Holman, J.P., (2002). "*Heat Transfer*, McGraw-Hill.

- Jones, W. P., Launder, B. (1972). "The prediction of laminarization with a two-equation model of turbulence". *International journal of heat and mass transfer*, **15(2)**, 301-314.

- Jošt, D., Škerlavaj, A., Lipej, A. (2012). "Numerical flow simulation and efficiency prediction for axial turbines by advanced turbulence models", *IOP Conference Series: Earth and Environmental Science*, p.062016, **15(6)**, IOP Publishing.

- von Kármán, T., (1963). "*Aerodynamics*", McGraw-Hill, ISBN 978-0-07-067602-2.

- Khan, F.R., (2005). "*Investigation of turbulent flows and instabilities in a stirred vessel using Particle Image Velocimetry*", Ph.D.Thesis, Loughborough University.

- Kolmogorov, A. N., (1941). "The local structure of turbulence in incompressible viscous fluid for very large Reynolds numbers". *Dokl. Akad. Nauk SSSR*, **30(4)**, 299-303).

- Lee, M., Malaya, N., & Moser, R. D. (2013). "Petascale direct numerical simulation of turbulent channel flow on up to 786k cores", *Proceedings of SC13: International Conference for High Performance Computing, Networking, Storage and Analysis* (p. 61). ACM.

- Lide, D.R. (Ed.) (1990). "*CRC Handbook of Chemistry and Physics*", 70th Ed, Boca Raton CRC Press, FL.

- Lomax, H., Pulliam, T.H., Zingg, D.W., (2001). "*Fundamentals of Computational Fluid Dynamics*", Series on Scientific Computation, Springer-Verlag, ISBN 3-540-41607-2.

- Menter, F.R., (1993). "Zonal Two Equation k-ω Turbulence Models for Aerodynamic Flows", *AIAA, 24th Fluid Dynamics Conference, July 6-9, 1993*, Orlando, Florida.

- Menter, F. R. (1994). "Two-equation eddy-viscosity turbulence models for engineering applications", *AIAA Journal*, **32(8)**, 1598-1605.

- Menter, F. R., Egorov, Y. (2010). "The scale-adaptive simulation method for unsteady turbulent flow predictions. Part 1: Theory and model description", *Flow, Turbulence and Combustion*, **85(1)**, 113-138.

- Meslem, A., Bode, F., Croitoru, C., Nastase, I. (2014). "Comparison of turbulence models in simulating jet flow from a cross-shaped orifice", *European Journal of Mechanics - B/Fluids*, **44**, 100-120.

- Navier, C. L. M. H., (1822). "Memoire sur les lois du mouvement des fluides", *Mem. Acad. Sci. Inst. France*, **6**, 389-440.

- Patankar, S., (1980). "*Numerical Heat Transfer and Fluid Flow*", Hemisphere Series on Computational Methods in Mechanics and Thermal Science, Taylor & Francis, ISBN 0-89116-522-3.

- Perry, R. H., Green, D. W., eds., (1998). "*Perry's Chemical Engineers' Handbook*". 7th ed., McGraw-Hill, New York.

- Ryan, D., Simmons, M. and Baker, M. (2011). "Modelling Multiphase Jet Flows for High Velocity Emulsification", *Proceedings of ASME-JSME-KSME Joint Fluids*

Engineering Conference, 24-29 July 2011, Hamamatsu, Japan, Paper number AJK2011-03023.

- Ryan, D., Simmons, M. and Baker, M. (2013). "Investigating Dispersion and Emulsification Processes using a Sonolator Liquid Whistle", *Proceedings of 8th International Conference on Multiphase Flow*, 26-31 May 2013, Jeju, Korea.

- Sonic Corp (2011). "*Sonolator Operating and Instruction Manual*", http://www.sonicmixing.com/Manuals/Sonolator_System_Manual.pdf, downloaded on 27th July 2013.

- Taylor, G. O., (1938). "The spectrum of turbulence", *Proceedings of the Royal Society of London, Series A, Mathematical and Physical Sciences*, **164(919)**, 476-490.

- Tritton, D. J. (1977). "*Physical fluid dynamics*", Oxford, Clarendon Press.

- Wendt, J., (2008). "*Computational Fluid Dynamics: An Introduction*", Springer-Verlag, Berlin, Heidelberg.

- Whalley, P.B., (1996). "*Two-phase flow and heat transfer*", Vol **42** of Oxford chemistry primers, Oxford University Press, UK. ISBN 0198564449.

- Wilcox, D.C. (1988). "Re-assessment of the scale-determining equation for advanced turbulence models", *AIAA Journal*, **26(11)**, 1299-1310.

- Wilcox, D.C. (1998). "*Turbulence modeling for CFD*", **2**, 103-217, La Canada, CA: DCW industries.

Chapter 4   VALIDATION OF CFD SIMULATIONS USING PIV EXPERIMENTAL RESULTS

4.1   Abstract

PIV experiments and CFD simulations were carried out for a Sonolator inline liquid whistle mixer under similar flow scenarios and are compared in this Chapter to validate the CFD simulations. Both global and local validations are performed, the former focussing on the pressure drop across the Sonolator and the latter being carried out by comparison of local values of velocity magnitude, turbulent kinetic energy and local specific turbulent energy dissipation rate. Good agreement was found between velocity magnitude values but agreement was poorer for the turbulent parameters. The reasons for discrepancies are discussed.

4.2   Introduction and Literature Review

In the previous two chapters PIV experiments and CFD simulations carried out on a Sonolator liquid whistle have been described.   CFD simulations for specific applications require validation against experiment to be sure that numerical errors are not significant and that the methodologies applied in the CFD simulations (e.g. choice of turbulence model) are appropriate.   In this chapter, flow field data from PIV and CFD are compared for corresponding flow geometry and conditions.

To date, there is a sparse literature about any aspect of the Sonolator or of liquid whistles in general; only a few accounts of some industrial applications could be found (Clark *et al* 2001, Chand *et al* 2007).   In particular, investigations into the interior workings of the Sonolator using techniques such as CFD and PIV had not been documented, and the comparison between these two techniques not published.   This chapter aims to provide a comparison of PIV and CFD results for the Sonolator (see Ryan, Simmons and Baker 2013 for previous preliminary work on this comparison).

With the steady increase in computational power in recent decades, CFD and PIV have both become viable ways of investigating industrial flows.   Many accounts of PIV experiments, CFD simulations, and combined PIV/CFD investigations now exist. These latter comparisons are especially desirable: PIV provides reliable experimental data but is time-consuming and expensive; CFD requires validation but is cheap relative to PIV (Nakiboğlu *et al* 2009), hence CFD can generate a wider range of results for the same expense. By comparing a representative subset of CFD cases to their corresponding PIV experiments, if good agreement is found then the subset of CFD cases has been validated, moreover since the subset is representative, the whole class of CFD cases can be regarded as validated.   Future investigations of the same type can be carried out via

CFD alone, provided that no significant alterations are made to the CFD modelling assumptions.

Some examples of successful PIV/CFD comparisons for industrial applications include: a rotating disc contactor extractor column (Drumm and Bart 2006), silicone elastomer models of cerebral aneurysms (Ford *et al* 2007), flow through a rough microchannel (Silva, Leal and Semiao 2008), pollution monitoring of an isolated smoke stack in an atmospheric boundary layer (Nakiboğlu *et al* 2009), a fluidised bed (Hernandez-Jiminez *et al* 2011), two phase natural convection (Gandhi, Sathe, Joshi and Vijayan 2011) and a 1.2 MW moving grate combustion boiler (Nussbaumer and Kiener 2013). The wide scope of these applications demonstrates that PIV/CFD comparisons are broadly accepted in the scientific community as a way to validate CFD simulations.

The remainder of this literature review will focus on applications of PIV/CFD comparisons to confined turbulent flows, since the Sonolator and liquid whistles are in this class of flows. Suitable comparisons are found in the literature for: pumps, stirred tanks, and multiphase jet flows.

For pumps: PIV/CFD comparisons were carried out for a radial pump in the impeller and diffuser regions (Feng, Benra and Dohmen 2009) and for a centrifugal pump impeller (Westra, Broersma, van Andel and Kruyt 2010). In both cases the main method of comparing velocities was to plot PIV and CFD results together on a line graph, with velocity on the vertical axis, and distance along a line in the flow domain on the horizontal axis (also used in Nakiboğlu *et al* 2009, Drumm and Bart 2006). The PIV and CFD velocities demonstrated good agreement, in one paper (Westra *et al* 2010) the velocities agreed to within 5%. Turbulence fields were also compared by Feng (2009) using graphs of turbulent intensity *vs* distance; the trends were the same in CFD

and PIV, but with the magnitude underestimated in CFD (also see Nakiboğlu *et al* 2009, where greater variation was found for turbulence than for velocity comparisons). In addition, LDV was found to give better turbulence readings at a point than PIV for geometries where PIV was adversely affected by planar reflections of the laser sheet.

For stirred tanks: PIV/CFD comparisons were carried out for a stirred tank with a pitched blade turbine and baffles (Sheng, Meng and Fox 1998) and for a Rushton turbine with baffles (Ranade, Perrard, Le Sauze, Xuereb and Bertrand 2001). In both cases the CFD was for fully developed flow using steady-state simulations, with boundary conditions at the turbine being modelled with suction and ejection of fluid. The PIV work was not angle resolved for Sheng *et al* (1998), but was angle resolved in the later work (Ranade *et al* 2001). For turbulence models, Sheng *et al* used RNG k-ε and RSM, whereas Ranade *et al* used standard k-ε and RNG k-ε. In both cases, graphs of velocity *vs* distance (along various lines in the flow domain) were used to demonstrate agreement between PIV and CFD, with comparable results across all turbulence models (and no additional accuracy when using the more computationally intensive RSM). Turbulence was also plotted on line graphs; for Sheng *et al* there was qualitative agreement between CFD and PIV of the general pattern of turbulence, but not quantitative agreement in terms of magnitude of turbulence; for Ranade *et al* the standard k-ε model gave good agreement but only after deducting the periodic component of kinetic energy caused by the regular passage of the turbine blades.

Virdung and Rasmuson (2007) compared PIV and CFD measurements for a confined solid-liquid jet. The PIV was carried out using matched refractive indices between solid and liquid phases, and results were obtained up to a solid loading of 1.9 vol%; the accuracy decreased as the solid loading increased. The CFD used a

realisable k-ε turbulence model which was varied between mixture, dispersed and per-phase applications; the latter gave best agreement to PIV, demonstrated by graphs of velocity *vs* distance using both data sources.

To summarise the findings from literature regarding PIV/CFD comparisons: these comparisons have been successfully carried out many times, with CFD validated using PIV data for many industrial applications. Velocity fields between PIV and CFD tend to agree in pattern and magnitude; turbulence fields tend to agree in pattern but not in magnitude. Care ought to be taken when calculating turbulent fields to deduct (where possible) any contribution from periodic motion. Using more complex turbulence models (e.g. RSM over RANS) has not resulted in superior validation to date.

4.3   Comparison Methodology

In order to obtain a good validation it was required that CFD results be in good agreement with 2D PIV results in multiple locations in the XYZ flow domain. CFD simulations were fully 3D and transient; for each simulation the time-averaged velocity vector field $\underline{v} = (u, v, w)$ was available. PIV results were time-averaged over 500 frames, and only measured in two different 2D planes through the flow domain; ZY plane (along Sonolator axis (Z) and orifice short direction (Y)) and ZX plane (along Sonolator axis (Z) and orifice long direction (X)); moreover ZX was not available when the Sonolator blade was installed, due to the blade occupying most of the PIV plane. The components of velocity available in ZY experiments were w (Z direction) and v (Y direction); for ZX, w (Z) and u (X) velocity components were available; this was since 2D PIV measurements of velocity give only the components within the measurement plane.

Hence, given this data it was possible to compare PIV and CFD velocity components w, v on the ZY plane for blade in or out, and components w, u on the ZX plane for blade-out only. Both cases were measurements made on symmetry planes of the Sonolator. Although the third (unmeasured, perpendicular) component of velocity on the symmetry plane was non-zero for each transient frame, the symmetry of the geometry meant the time-averaged velocity field had to be symmetric. Then if the perpendicular component of time-averaged velocity was non-zero (on the symmetry plane) symmetry would be broken; by this reasoning, time-averaged u was zero on ZY plane, and time-averaged v was zero on ZX plane. Hence, with V representing velocity magnitude: on the ZY plane for the time-averaged variables, $V = |\underline{v}| = (u^2 + v^2 + w^2)^{0.5} = (v^2 + w^2)^{0.5}$. By similar reasoning, on the ZX plane for the time-averaged variables, $V = |\underline{v}| = (u^2 + v^2 + w^2)^{0.5} = (u^2 + w^2)^{0.5}$. So time-averaged V could be calculated precisely for both ZX and ZY planes in PIV, and was directly comparable with time-averaged velocity magnitude from CFD.

Comparing V values between CFD and PIV, at any given location in the flow domain, could be done in many ways; two of those were by taking the ratio between the values, or by taking the difference between the values. The advantage of taking the ratio was that this quantity was dimensionless, giving similar comparisons whether local velocity was high or low. The drawback of the ratio was that it could only be used on strictly positive values. Hence velocity magnitude, being always positive, was best compared by using **ratios between CFD and PIV**. Other variables which might sometimes be negative (e.g. u, v, w components of velocity) would have to be compared using differences.

As shown in the literature review, a standard PIV/CFD comparison technique was to plot CFD and PIV velocity magnitudes on graphs of velocity *vs.* distance along multiple lines within the flow domain. However, if the velocity axis was linear then the height between the data series would be proportional to their difference, a dimensional quantity. The choice of log-scale for the velocity magnitude axis ensured nondimensionality; that the height between the data series was proportional to their ratio, the preferred comparison method. Hence **log-scale** was used exclusively for axes plotting velocity magnitude.
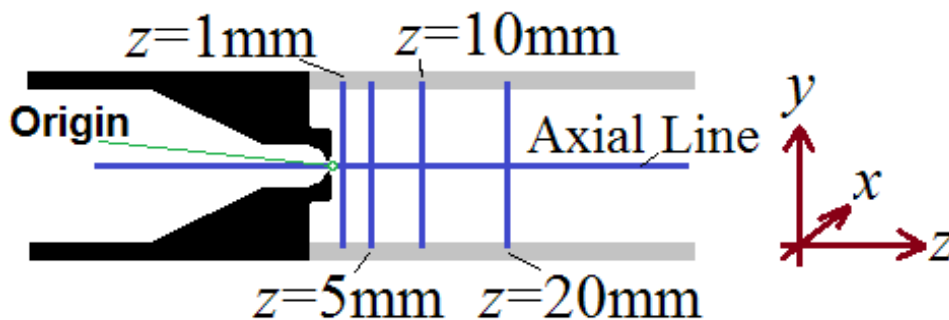
Figure 4.1: Schematic diagram showing lines in the ZY plane along which PIV and CFD results were compared. For PIV, black regions were metal (opaque), grey regions were Perspex (transparent)

Figure 4.1 gives the primary lines in the ZY plane where velocity magnitudes from PIV and CFD were compared by plotting them on a log-scale graph. Precise descriptions of the loci of these lines are: the axial line $(0, 0, z)$; lines in the ZY plane $(0, y, 1)$, $(0, y, 5)$, $(0, y, 10)$, $(0, y, 20)$; corresponding lines (not illustrated) in the ZX plane $(x, 0, 1)$, $(x, 0, 5)$, $(x, 0, 10)$, $(x, 0, 20)$; all these coordinates were measured in millimetres with the origin in the plane of the front of the nozzle, and directly downstream from the orifice. Hence the positions of particular interest were at 1 mm, 5 mm, 10 mm and 20 mm downstream from the orifice, located on the Sonolator axis.

Ratios of velocity magnitudes between PIV and CFD that were close to unity at any given location would represent validation of the CFD at that location. At locations where the ratio was not near unity, reasons would be investigated as to i) possible modelling inaccuracies of the CFD or ii) possible experimental limitations of the PIV.

The same analysis described above for time-averaged velocity magnitude could be used for any time-averaged variable existing in both CFD and PIV which was strictly positive. Two such variables which existed in CFD were k and ε (turbulent kinetic energy and turbulent energy dissipation respectively), originating from the SST-SAS turbulence model used in the simulations. These variables were not directly observable in PIV, however they could be approximated from the velocity data. Hence k and ε will be investigated and compared using the same techniques.

4.4   Results and Discussion

Several PIV experiments were carried out for a Sonolator (described in Chapter 2) and CFD simulations with the same Sonolator geometry and flow conditions were subsequently carried out (described in Chapter 3). Three different sets of data were compared between PIV and CFD: pressure drop, velocity fields, and turbulence fields.

4.4.1   Comparison of pressure drop across the Sonolator

During PIV experiments, mass flow rate was fixed for each individual experiment, and pressure drop across the Sonolator was measured for that experiment. During CFD setup, care had been taken to exactly duplicate the PIV geometry. The CFD experiments were set up to replicate the geometry and flow conditions of each PIV experiment, so mass flow rate at the inlet was fixed at the same value used for PIV. As an output of CFD, pressure drop across the Sonolator was measured for each experiment. These pressure drop variables were therefore available for direct comparison between PIV and CFD. (Note the orifice size codes in the table below are given in Table 1.2, and represent orifice sizes between 0.0037 in^2 and 0.014 in^2 in imperial units or 2.39 mm^2 and 9.03 mm^2 in SI units.)

Table 4.1: Pressure drop results from PIV and CFD for blade-out experiments/simulations, at 7 different mass flow rates and 3 different orifices. Mass flow rates (M), orifice superficial velocities (V_{orif}) also given.

Orifice size code	M (kg·s^{-1})	V_{orif} (m·s^{-1})	ΔP_{PIV} (kPa)	ΔP_{CFD} (kPa)	ΔP_{CFD} / ΔP_{PIV}
0037	0.036	15.2	172.4	152.2	88.3%
0037	0.091	38.4	1094.0	952.6	87.1%
0110	0.046	6.5	34.5	32.1	93.0%
0110	0.092	12.9	137.9	125.7	91.2%
0110	0.182	25.8	540.1	496.3	91.9%
0140	0.047	5.2	20.7	19.9	96.4%
0140	0.182	20.3	326.4	304.0	93.1%

In Table 4.1 the CFD pressure drop as a percentage of the PIV pressure drop is given. The CFD pressure drops gave predictions between 87% and 96.5% of the true pressure drop from PIV experiments, a reasonable agreement. The slight underpredictions were likely due to not simulating the long hose coming out of the Sonolator outlet and going to drain (as present in all PIV experiments), and therefore better agreement would be expected if this outlet hose was simulated too.

Blade-in results were not reported separately since in all cases, in both CFD and PIV, both blade-out and blade-in gave very similar pressure drop results for the same geometry and flow rate. Hence the conclusion was that CFD simulations gave realistic pressure drop predictions which agreed with experiment, starting the case for validating the CFD results.

4.4.2 Comparison of velocity magnitudes in the ZY plane

Velocity data were available from both CFD and PIV in the following flow setups: 0037, 0110 and 0140 orifices for low and high flow rates; in addition, 0110 orifice for medium flow rate. PIV data had been collected for ZY plane (blade-in and

blade-out), and for ZX plane (blade-out only), however the ZX data was omitted here since it had been found to be too sensitive to misalignment of the laser sheet, due to the thinness of the orifice jet being measured. (To obtain accurate PIV results in the ZX plane, the laser sheet would need to be positioned with accuracy of order 0.1 mm with respect to the flattened orifice jet of approximate thin dimension 1 mm. The equipment used only allowed maximum accuracy of order 0.5 mm.)

Using the ZY plane data available, the velocity comparisons were split into three subsections: axial comparison for blade-out, jet cross-section comparison for blade-out, and jet cross-section comparison for blade-in. (There was no axial comparison for blade-in, since the Sonolator axis downstream of the blade was not within the flow domain.)

Before presenting these results, a general comment on the accuracy of PIV results was that: for low flow rates and large orifices the PIV was deemed accurate throughout the whole flow domain; inaccuracies were present for the smallest orifice (0037) and for the highest flow rate for orifices 0037, 0110. For 0037 orifice the jet was too fast to be captured by the smallest laser pulse separation possible on the PIV equipment used. For the highest flow rates used, for the two smaller orifices, cavitation was present after the orifice; this cavitation disrupted the PIV technique (see Figure 2.25 earlier in the PIV results; cavitation regions were observed to move slower than the fast moving jet region surrounding them, so had the tendency to damp PIV readings).

The general comparison technique, supported by the literature review, was to compare PIV and CFD velocities in the flow domain using line graphs of velocity against distance along a line in the flow domain.

For each position compared in the flow domain, and plotted vertically above each point on the horizontal distance axis, either PIV and CFD agreed, or they did not. If they did agree, the CFD could be regarded as validated at that position. If they did not agree, either the PIV or the CFD were inaccurate in some way, requiring further discussion.

The PIV contained some known inaccuracies discussed in Chapter 2. These caused gaps in the PIV data used to validate the CFD data. For this reason, comparisons of CFD between different flow rates were used to help validate the CFD data in the gaps; this was possible given valid CFD data at one flow rate and known scaling rules between the flow rates. Comparisons were also made between different orifice sizes for the same purpose of cross-validating CFD cases where PIV data was missing or inaccurate.

PIV/CFD comparison cases were divided into "edge cases" and "middle cases". The edge cases all had flow rate at an extreme value, either the highest or the lowest investigated for the orifice size. The middle case had a medium flow rate and middle orifice size. To carry out the comparisons between CFD at different flow rates and orifice sizes, montages were made containing the same study for all edge cases (3 orifices, 2 flow rates; 6 in all) which helped to identify potential cross-validations for the CFD data, in the gaps where PIV data was known to be inaccurate.

4.4.2.1   Axial comparison for blade-out

Before producing such a montage for the edge cases as described above, the middle case (0110 orifice, medium flow rate) was examined. Velocity magnitudes from PIV and CFD along the Sonolator axis were plotted for blade-out case. (Note: CFD velocities were available throughout the whole flow domain, however PIV velocities

were only available in the transparent viewing chamber of the Sonolator corresponding to $z \geq 0$ mm.)
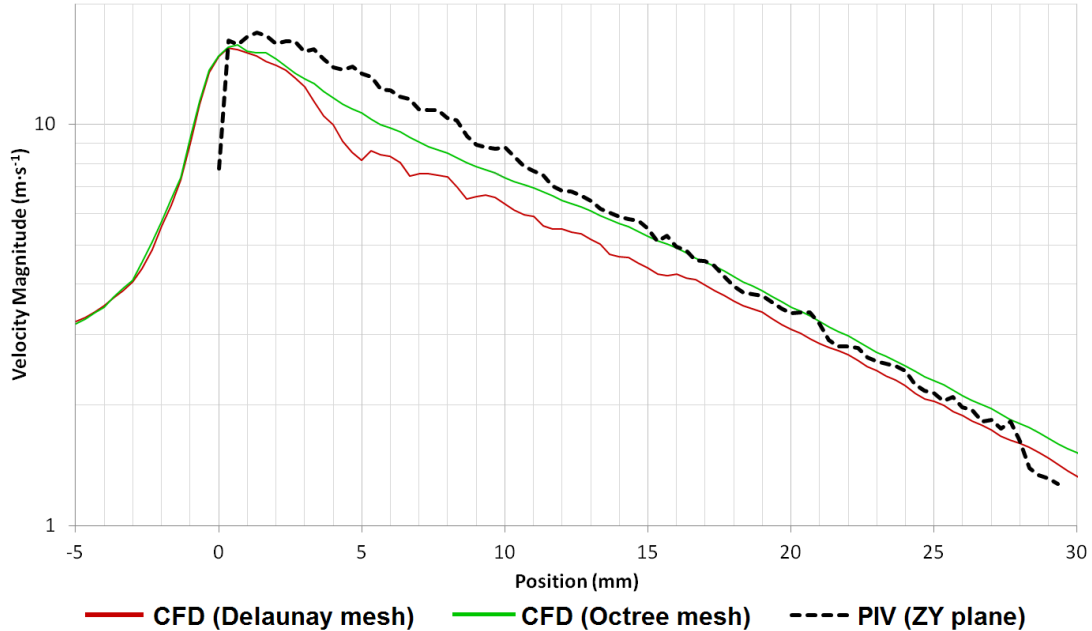
Figure 4.2: Graph of velocity magnitude along the axial line -5 mm $\leq z \leq$ 30 mm; $x = y = 0$ mm. CFD and PIV results compared for 0110 orifice, blade-out, medium flow rate (0.092 kg·s⁻¹). Reference data: Sonolator pressure drop 125.7 kPa for CFD, orifice superficial velocity 12.9 m·s⁻¹, main chamber superficial velocity 0.1 m·s⁻¹.

In Figure 4.2 velocity magnitudes are given for CFD (2 meshes) and PIV along the Sonolator axis (the line $x = y = 0$ mm). Both CFD and PIV showed a peak in velocity of magnitude 17 m·s⁻¹ about 1 mm after the orifice in the jet region, and a subsequent exponential decline in velocity magnitude with distance along the Sonolator (the decreasing linear trend on the graph, coupled with the logarithmic scale of velocity, gives this decreasing exponential trend of velocity with position along the Sonolator). After 15 mm from the orifice (which was at $z = 0$ mm on the horizontal scale), the PIV results were in-between the two CFD series; between 0 mm and 15 mm the PIV results were slightly higher than the CFD results. Overall, for this middle orifice size and flow rate, the agreement between CFD and PIV was good, and the velocity magnitude was

validated in this case. Next the same data will be viewed in a montage for the edge cases:
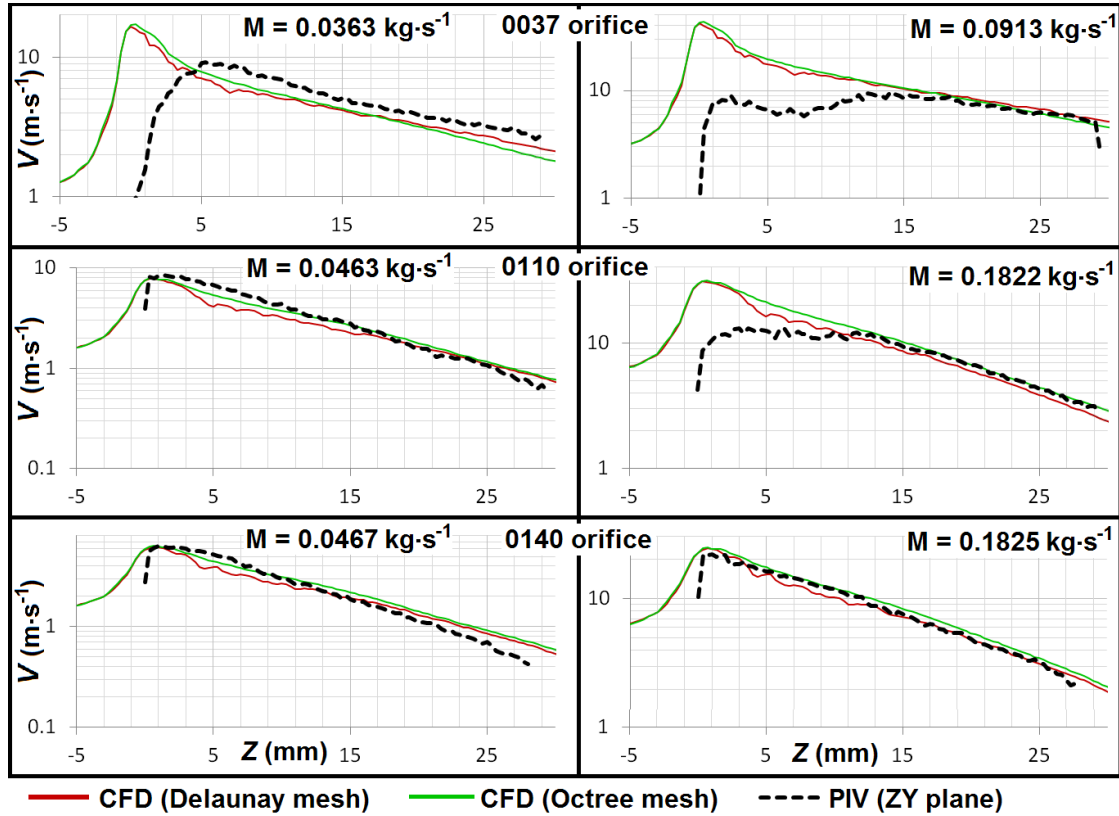
Figure 4.3: Graph of velocity magnitude along the axial line. CFD and PIV results compared for blade-out, ZY plane, low and high flow rates (left, right); orifices of types 0037, 0110, 0140.

The same comparison of CFD and PIV results along the axial line was carried out for the edge cases; all three orifices, lowest and highest mass flow rates, as shown in Figure 4.3. A common feature of all datasets was good agreement between CFD and PIV after $z = 15$ mm with an exponential decline in velocity with position. For three cases (0140 low and high flow rates, 0110 low flow rate) the agreement between CFD and PIV was good enough to provide a complete validation of CFD results along the whole axial line.

In the other three cases before $z = 15$ mm, discrepancies between PIV and CFD were found. For 0037 orifice at low flow rate a source of PIV inaccuracy in high velocity regions was that the laser pulse separation could not be reduced low enough to capture the high velocity flows correctly. For 0037 and 0110 orifices at high flow rate, cavitation was observed visually on the PIV images in the high velocity regions. Both these reasons prevented gathering of accurate PIV data in the same region, and will be observed on subsequent jet cross-sections for both blade-in and blade-out. So can the remaining non-validated CFD cases be validated by other arguments?

For 0110 orifice: the CFD region validated in both cases ($z \geq 15$ mm) indicated that velocity magnitude was proportional to the flow rate. The flow rate ratio was 4 between low and high flow rates, hence the velocity patterns everywhere should also scale with ratio 4. This ratio of velocity magnitudes was indeed observed along the whole Sonolator axis. Hence by a scaling argument, the CFD results for 0110 orifice, high flow rate, were valid along the whole Sonolator axis.

The 0037 orifice results were slightly harder to validate: for high flow rate after $z = 15$ mm there was good agreement; for low flow rate after $z = 15$ mm there was agreement in the velocity pattern, but a slight discrepancy in the height. Moreover in the unvalidated region ($z < 15$ mm) there was no accurate PIV data for 0037 orifice to validate the CFD peak against. Comparing CFD patterns for 0037 orifice with larger orifices, the peak velocity shape for 0037 orifice (both meshes) was similar to that of the larger orifices for Delaunay mesh. This gave some confidence that the 0037 CFD results were physical. Overall then, reasons could be found why the 0037 CFD was valid, but to refine this validation further work would be needed to i) obtain accurate

PIV results for 0037 orifice in high velocity regions, and ii) explain the slight

discrepancy in velocity magnitude for low flow rate between PIV and CFD results.

The arguments above support the conclusion that the velocity magnitude

calculated by the CFD on the Sonolator axis was valid across all orifices and flow rates.

Now the jet cross-sections will be examined to see if the same conclusion can be drawn

there.

4.4.2.2 Jet cross-section comparison for blade-out

Montages of the jet cross-section are given below, for three different distances

from the orifice: 1 mm, 5 mm and 10 mm.
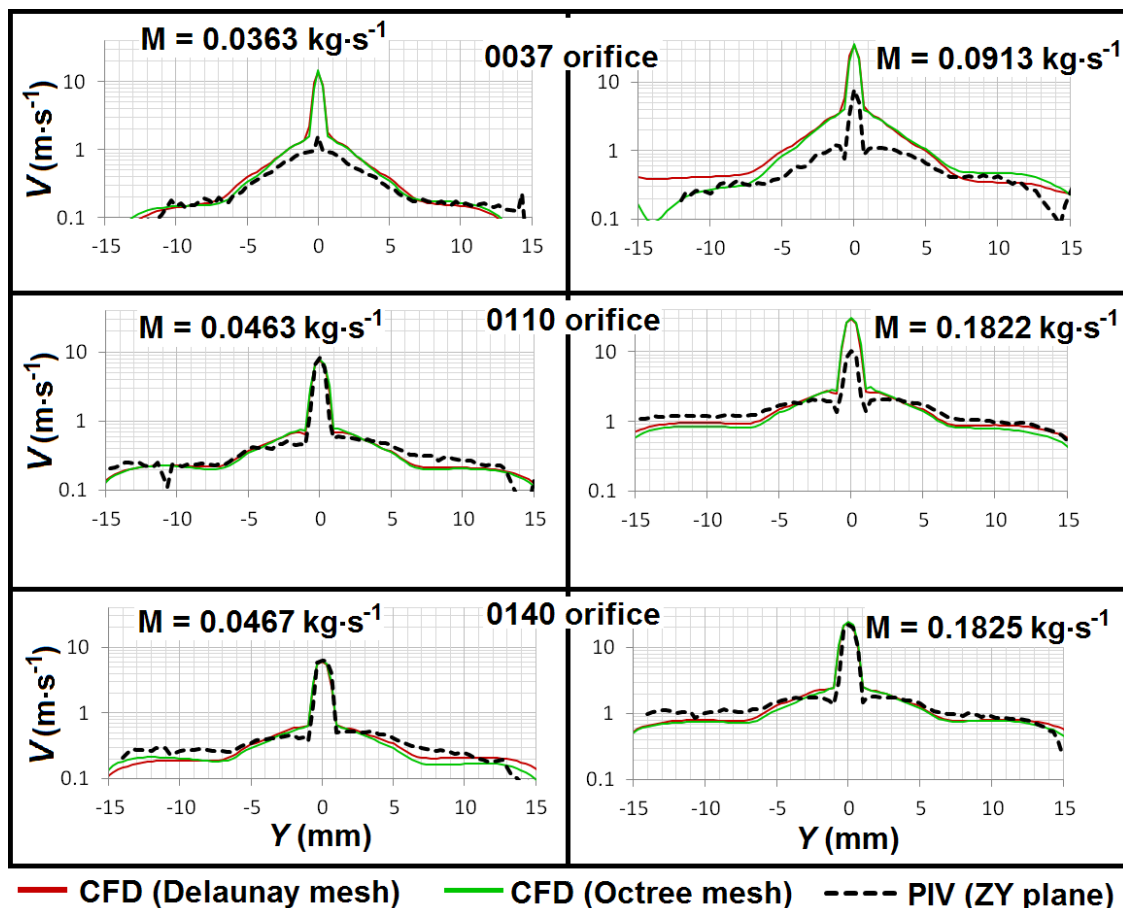
Figure 4.4: Graph of velocity magnitude along line $z = 1$ mm in ZY plane,
blade-out. CFD and PIV results compared for low and high flow rates,
orifices of types 0037, 0110, 0140.

Figure 4.4 shows PIV and CFD comparison of velocity magnitude for the Sonolator's orifice jet in cross-section, for three orifice sizes and two flow rates. The same CFD cases as before (0110 orifice for low flow rate, 0140 orifice for low and high flow rates) can be immediately validated by their excellent agreement to PIV. In these cases the peak velocity magnitude within the jet was seen to be around 10 times as large as mean velocity magnitudes in the recirculation regions surrounding the jet. Before passing judgement on the unvalidated CFD cases, the other two cross-sections are presented below.
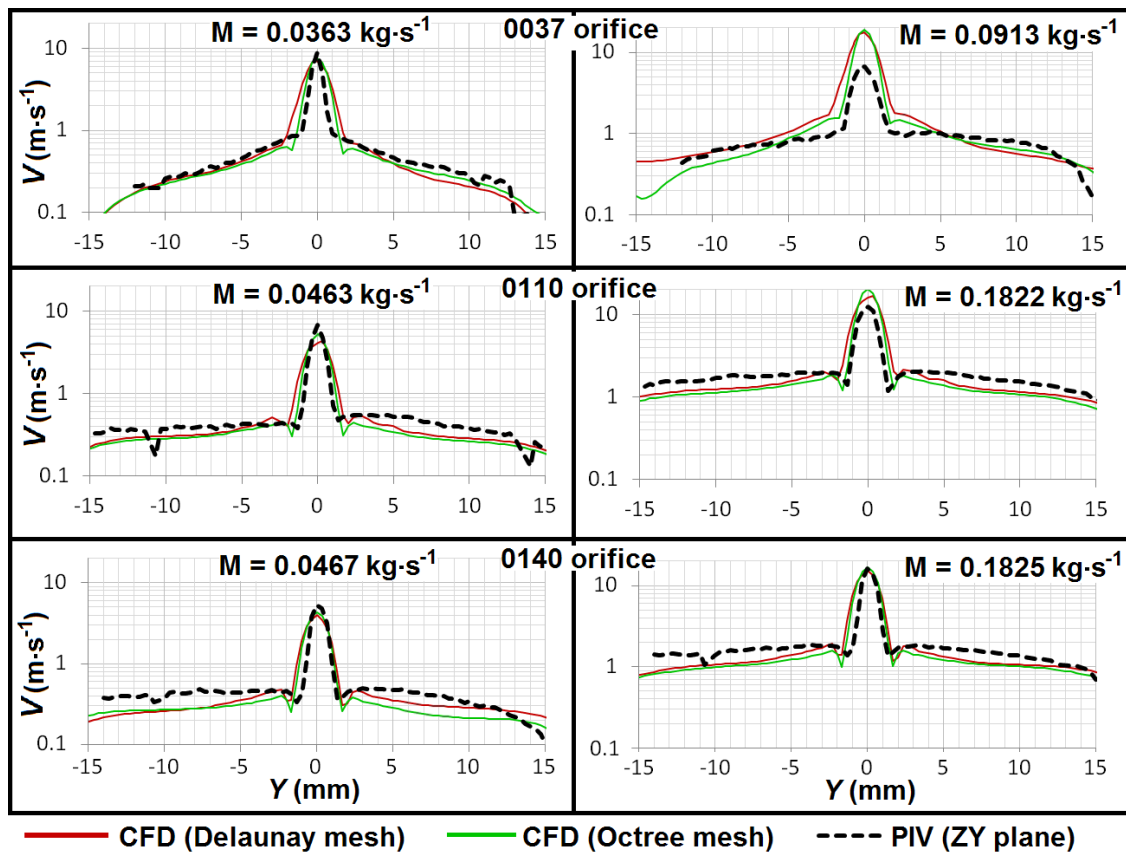
Figure 4.5: Graph of velocity magnitude along line $z = 5$ mm in ZY plane,
blade-out. CFD and PIV results compared for low and high flow rates,
orifices of types 0037, 0110, 0140.

Figure 4.5 shows good agreement between PIV and CFD for all cases except 0037 orifice size at high flow rate, for cross-sections 5 mm after the orifice.
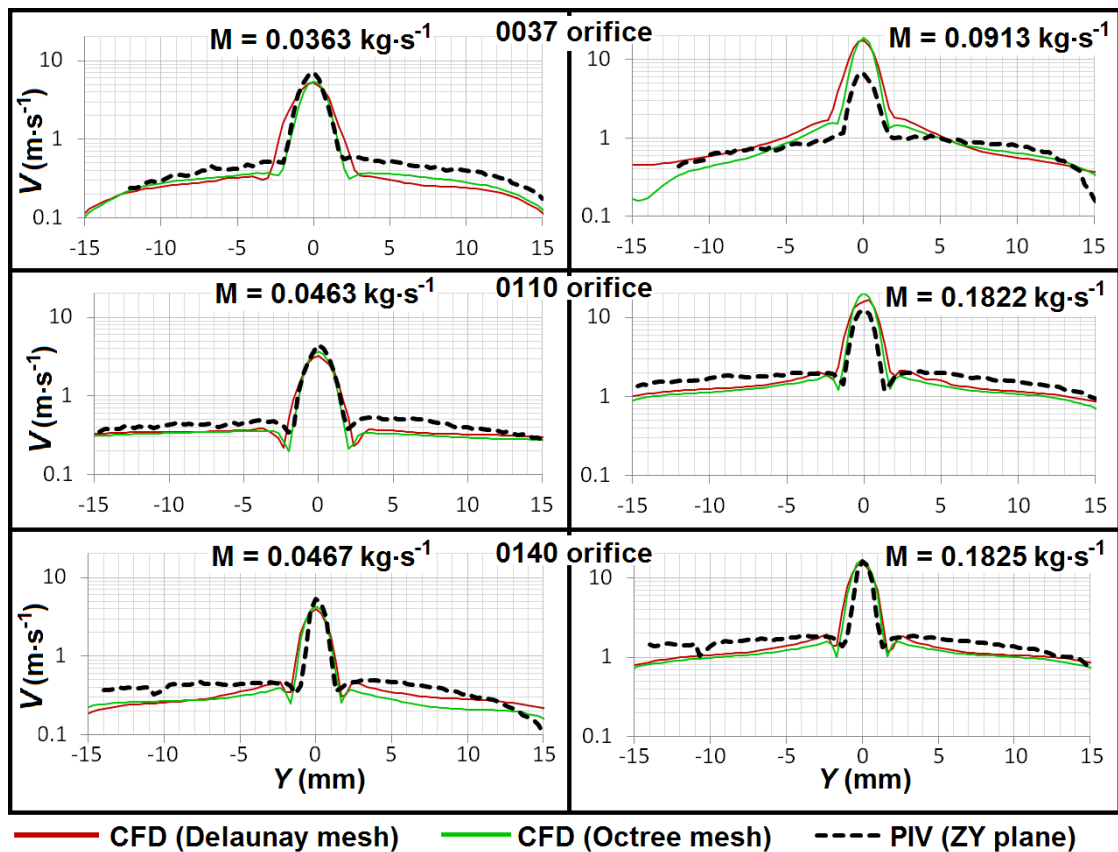
Figure 4.6: Graph of velocity magnitude along line $z = 10$ mm in ZY plane,
blade-out. CFD and PIV results compared for low and high flow rates,
orifices of types 0037, 0110, 0140.

Figure 4.6 shows good agreement at 10 mm after the orifice for the same cases as
at 5 mm after the orifice.

Overall the three jet cross-section montages show a wide range of agreement
between CFD and PIV, validating CFD in many of these cases and at many positions
within the flow. The remaining disagreements were almost all in places where PIV had
been identified as not accurate, and reasons for believing CFD results in those areas
were accurate included i) scaling comparisons between low and high flow rates, and ii)
similarities found in flow patterns between different orifice sizes.

The axis and three cross-sections were subsets of the flow domain with a
representative set of velocities and flow conditions. Hence the validation demonstrated

above for these subsets was good evidence that velocities from CFD were valid across the whole flow domain for the blade-out edge cases considered above, or for interior CFD cases (e.g. medium flow rates, intermediate orifice sizes) carried out in future.

4.4.2.3 Jet cross-section comparison for blade-in

Having discussed the blade-out cases, attention is now turned to the blade-in cases, which represent normal industrial usage of the Sonolator. Since the Sonolator axis lies mostly outside the flow domain (and within the blade), only cross-section CFD/PIV comparisons are carried out here; as before, the comparisons are at $z = 1$ mm, 5 mm and 10 mm after the orifice.
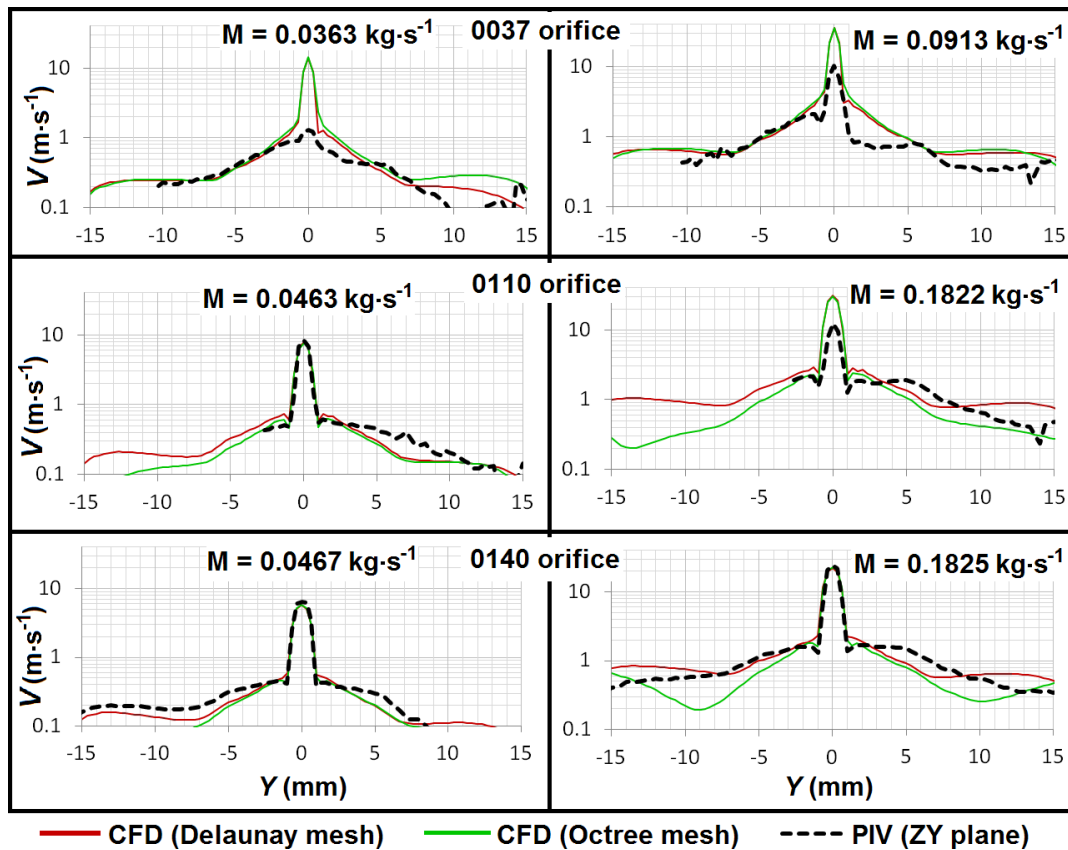
Figure 4.7: Graph of velocity magnitude along line $z = 1$ mm in ZY plane, blade-in. CFD and PIV results compared for low and high flow rates, orifices of types 0037, 0110, 0140.

Figure 4.7 showed excellent agreement between CFD and PIV velocities in the jet region for the normal three cases (0110 low flow, 0140 low and high flow). The same three cases had PIV inaccuracy for reasons discussed above, although attention is drawn to some excellent agreement for 0037 case outside the jet region. Note, this case was just before the blade so PIV could be obtained above and below the blade.
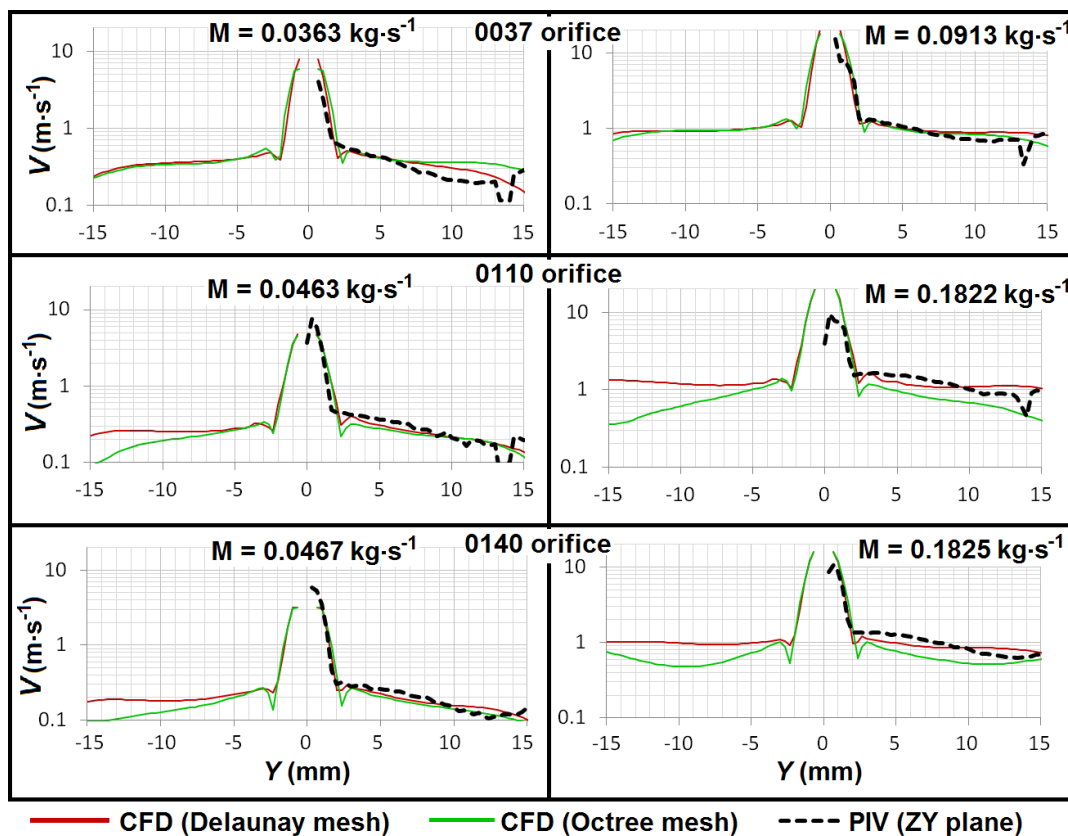
Figure 4.8: Graph of velocity magnitude along line $z = 5$ mm in ZY plane, blade-in. CFD and PIV results compared for low and high flow rates, orifices of types 0037, 0110, 0140.

In Figure 4.8 PIV readings were only obtained for half the flow domain due to the opaque blade blocking light from the other half of the flow domain. Agreement in both split jet and recirculation regions was good, in some cases (0140, low flow rate) excellent.
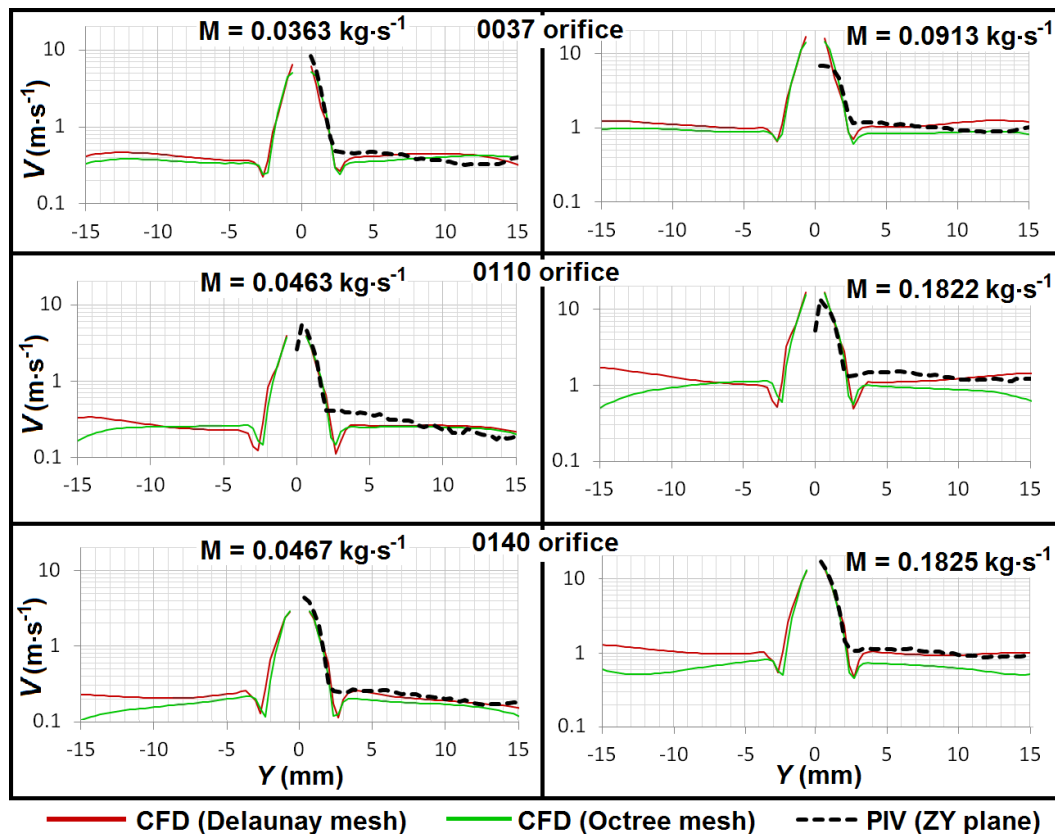
Figure 4.9: Graph of velocity magnitude along line $z = 10$ mm in ZY plane,
blade-in. CFD and PIV results compared for low and high flow rates, orifices
of types 0037, 0110, 0140.

Likewise, in Figure 4.9 agreement between PIV and CFD for both split jet and
recirculation regions was good.

These results for the blade-in cases demonstrated that there was no decrease in
accuracy of CFD simulation going from blade-out to blade-in cases; conversely, in
many cases accuracy seemed to increase. In particular, the new feature of these
simulations (the blade) was shown to be simulated accurately in CFD in terms of the
velocity patterns obtained near it.

The overall conclusion for comparisons of velocity magnitude between CFD and
PIV data was that the PIV data, where accurate, supported validation of the CFD,
moreover that it was reasonable to believe the CFD velocities to be accurate everywhere

in the flow domain, for both blade-out and blade-in simulations, within the scope of orifice sizes and flow rates discussed here. It also showed that the SST-SAS turbulence model used for CFD was suitable for obtaining accurate velocity fields in the Sonolator.

4.4.3   Comparison of turbulence parameters (k, ε)

In the previous section, velocity fields between CFD and PIV were found to be in good agreement and in this section the agreement for the turbulence parameters is explored.

Previous research (cited in the literature review) showed that it was more common for the pattern of turbulence to agree between PIV and CFD, than for the magnitudes to agree. It also found that PIV was not the most accurate technique for experimentally determining turbulence (LDV is more accurate) and that care ought to be taken to deduct periodic components of the kinetic energy.

This section will demonstrate that these problems in precisely validating the turbulence fields have not been overcome by the present research, following as this does in the footsteps of the techniques used previously. Nonetheless, there is as much scientific merit in presenting the limitations of techniques, as of obtaining successful results via those techniques. Hence the turbulence fields are compared below using the same line-graph techniques as for velocity magnitude, doing so in the hope that any limitations in the current techniques can be understood better, and future research aided in identifying improvements in validation techniques.

The turbulent statistics presented in previous chapters were: from PIV (Chapter 2) k_{var} (from velocity variance), $\varepsilon_{\mathrm{de}}$ and $\varepsilon_{\mathrm{sgs}}$ (from DE and SGS models of turbulent dissipation from velocity gradients); from CFD (Chapter 3) k (from SST-SAS), k_{var} (from velocity variance) and ε (from SST-SAS).

4.4.3.1 Comparison of turbulent kinetic energy (k)
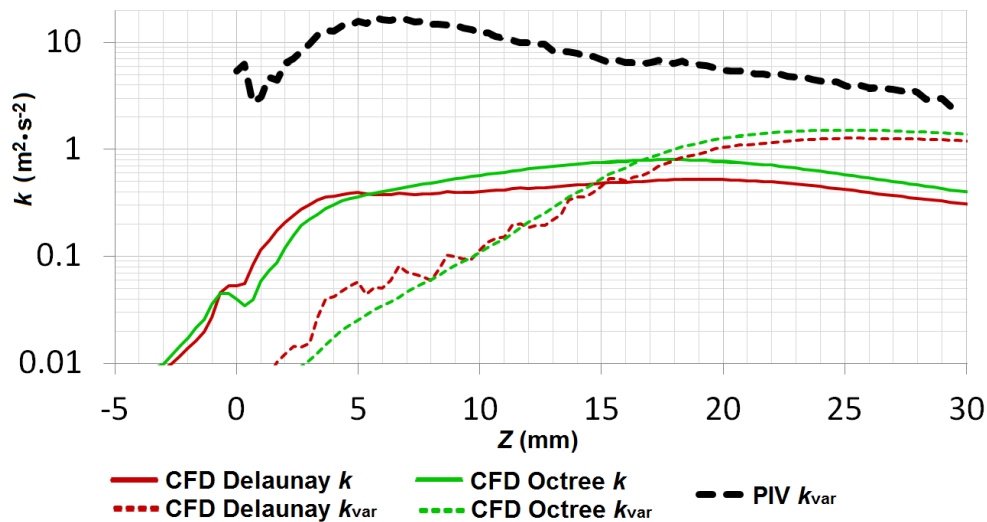
Figure 4.10: Graph of turbulent kinetic energy (k) along the axial line. CFD and PIV results compared for 0110 orifice, blade-out, medium flow rate (0.092 kg·s^{-1}).
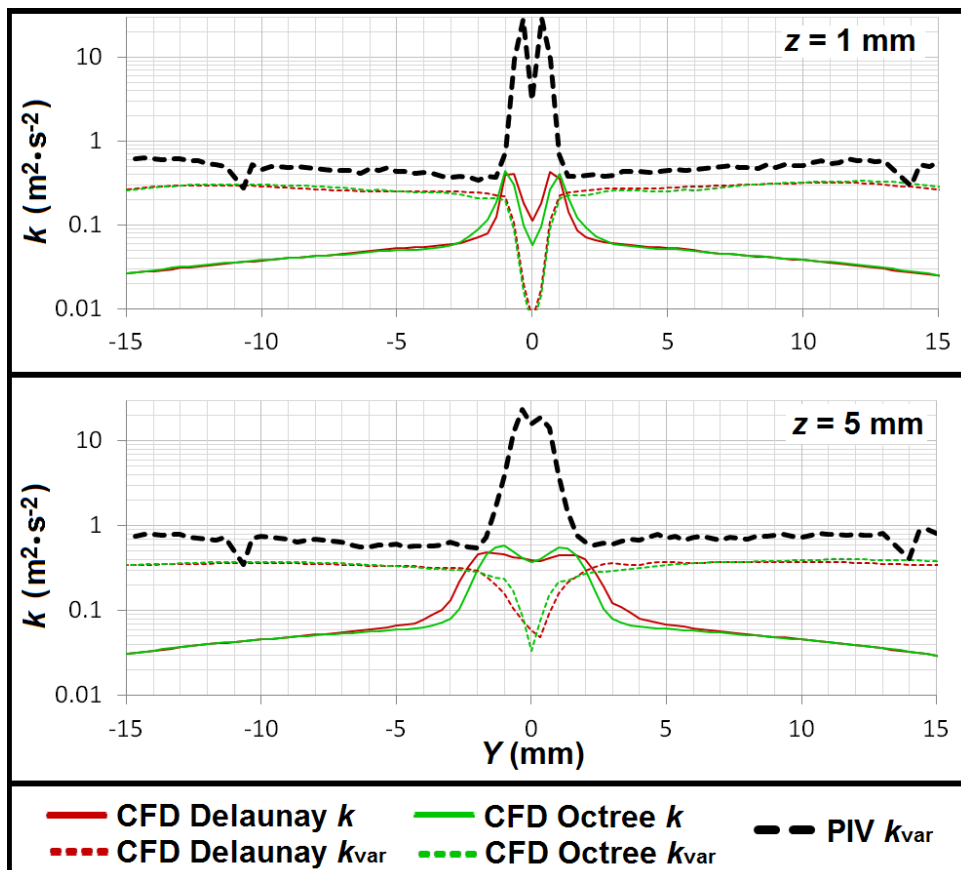
Figure 4.11: Graph of turbulent kinetic energy (k) along cross-sections in ZY plane. CFD and PIV results compared for 0110 orifice, blade-out, medium flow rate (0.092 kg·s^{-1}).
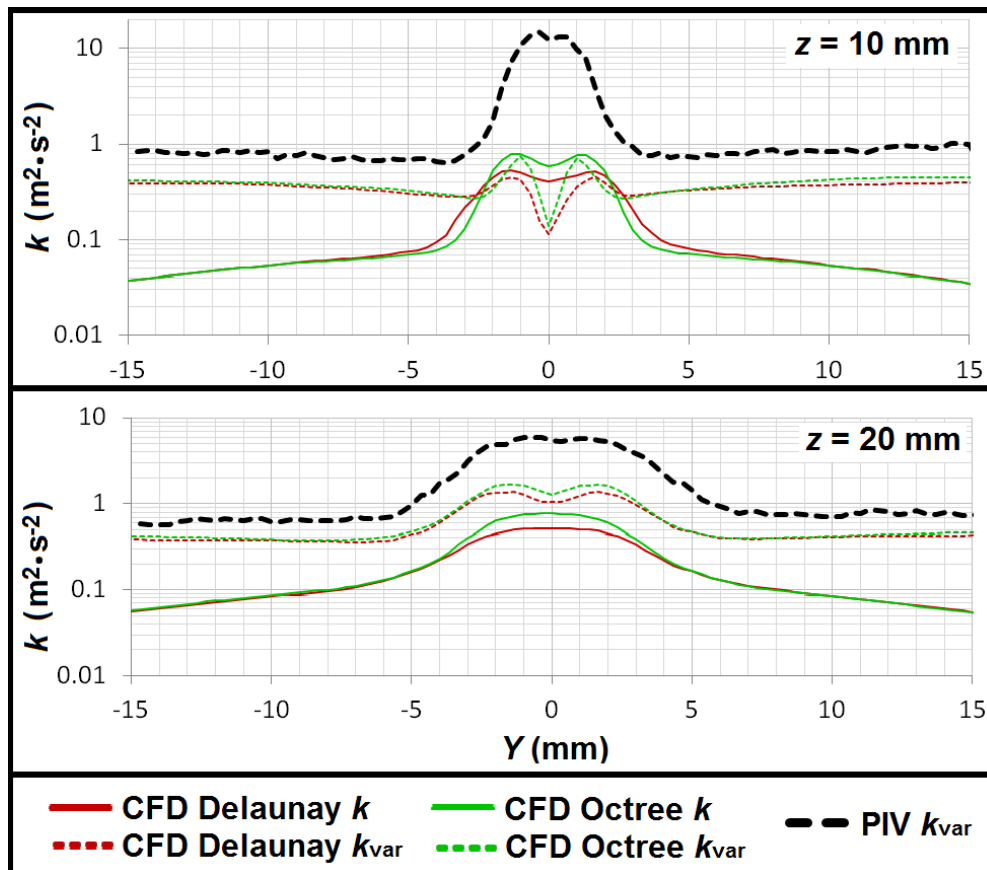
Figure 4.12: Graph of turbulent kinetic energy (k) along cross-sections in ZY plane. CFD and PIV results compared for 0110 orifice, blade-out, medium flow rate (0.092 kg·s⁻¹).

Figure 4.10, Figure 4.11 and Figure 4.12 show line graphs of data from CFD and PIV for various versions of turbulent kinetic energy (k). The lines in the flow domain were: Sonolator axis, cross-sections in ZY plane at 1 mm, 5 mm, 10 mm and 20 mm after the orifice. The case being examined was medium orifice 0110, medium flow rate, blade out. PIV and CFD velocity fields agreed along all of the lines used (this was previously illustrated only for Sonolator axis, but true for the cross-sections too).

However, discrepancies were found for the k data. Firstly, since k_{var} from CFD and PIV models were calculated in a similar manner, it was expected that k_{var} from CFD would give better agreement than k from CFD turbulence model. This was not found to be the case; sometimes k_{var} from CFD went in the opposite direction to k_{var} from PIV

(e.g. in cross-section at $z = 5$ mm at the jet). Hence k_{var} from CFD was abandoned as an unreliable technique, and k from CFD turbulence model used exclusively below. Further work is needed to verify why the two versions of k_{var} gave very different results. One explanation could be pulsing in the PIV pump giving an extra periodic component to PIV velocity variance; the CFD inlet condition was a constant mass flow rate, but the PIV pump output could have oscillated; this oscillation should be checked for in future experiments.

Secondly, k from CFD turbulence model broadly agreed with k_{var} from PIV in so much as the two variables generally moved in the same direction, and had the same pattern. However, inspection of the data indicated that k_{var} from PIV was around 10 to 50 times the magnitude of k from CFD turbulence model. One reason why this might have been the case is that the CFD k data was from transient simulations and included only turbulent components, however the PIV data was time-averaged across 500 PIV frames, and would have included both periodic jet oscillations and true turbulent variation, which increased the k measurements greater than the true value. Since the PIV jet frequency was not found precisely, these periodic jet oscillations could not be removed from the data. Further work is needed to separate out periodic and turbulent components of the PIV data in order to get better agreement with CFD k data and also to compare jet oscillation period and magnitude between CFD and PIV.

Overall then, the k output of the CFD simulations may have been reliable, since the PIV k_{var} was likely to be an overestimate, but it was not possible to confirm the degree of overestimation in these sets of experiments.

4.4.3.2   Comparison of turbulent energy dissipation rates (ε)
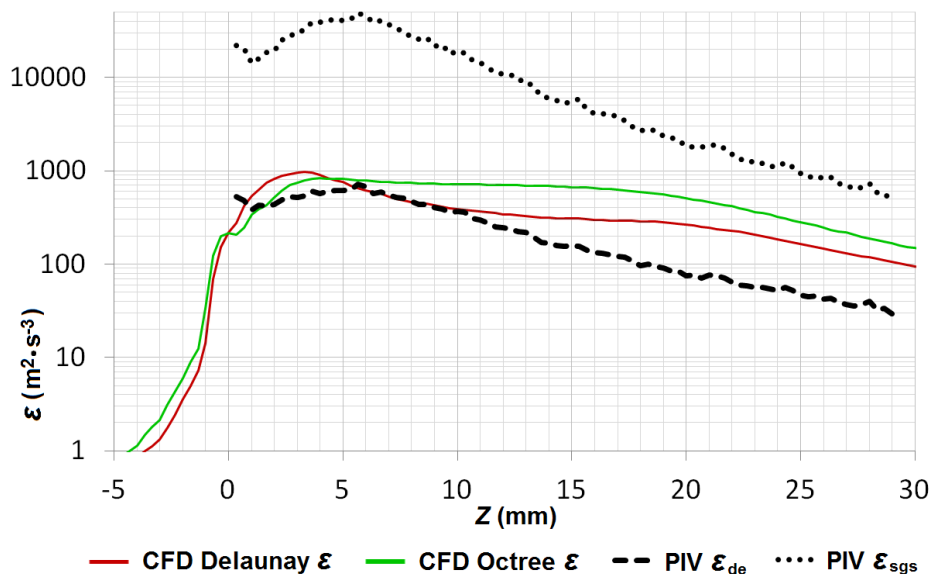
Figure 4.13: Graph of turbulent dissipation rate (ε) along the axial line. CFD and PIV results compared for 0110 orifice, blade-out, medium flow rate (0.092 kg·s^{-1})
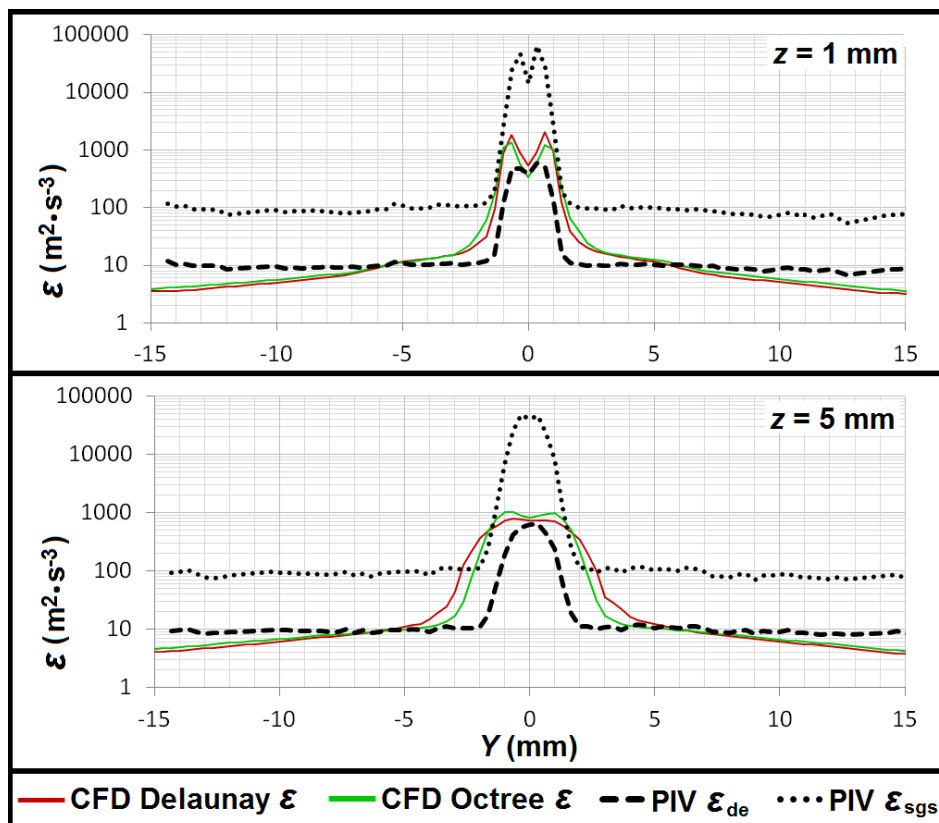
Figure 4.14: Graph of turbulent dissipation rate (ε) along cross-sections in ZY plane. CFD and PIV results compared for 0110 orifice, blade-out, medium flow rate (0.092 kg·s^{-1}).

205
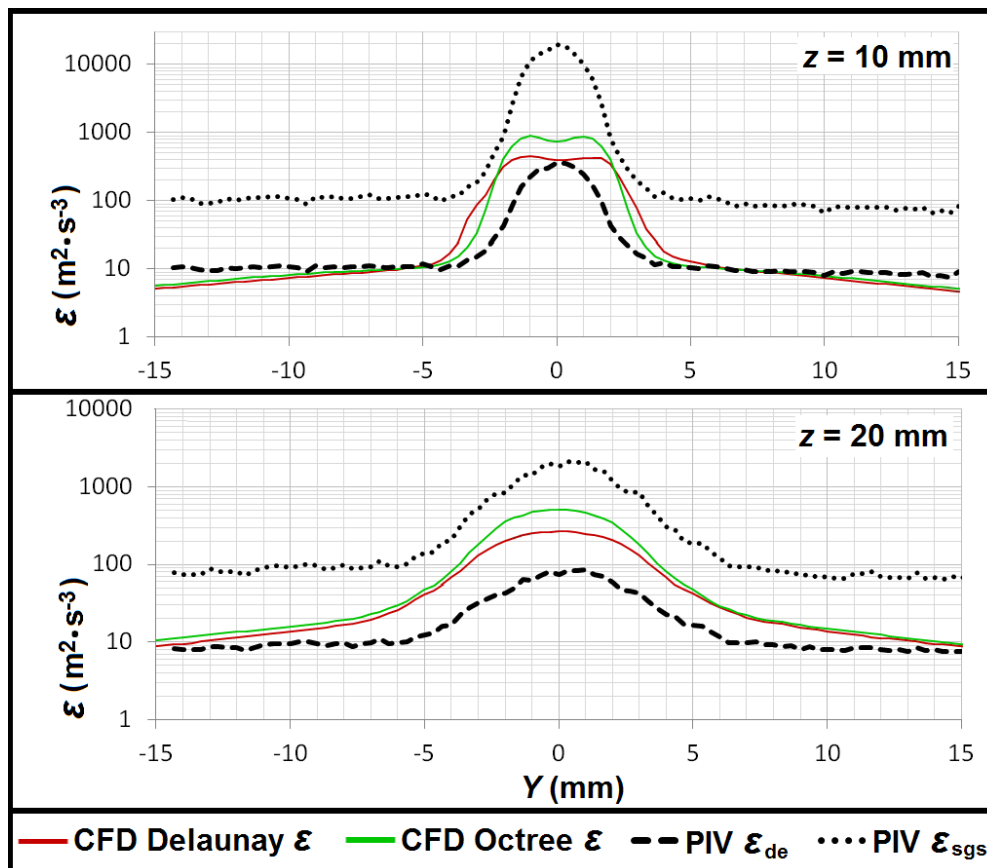
Figure 4.15: Graph of turbulent dissipation rate (ε) along cross-sections in ZY
plane. CFD and PIV results compared for 0110 orifice, blade-out, medium
flow rate (0.092 kg·s^{-1}).

Figure 4.13, Figure 4.14 and Figure 4.15 show the same comparisons (as carried

out for k in the previous section) for various versions of ε. Here the general finding

about ε from CFD (using the SST-SAS turbulence model) was that almost everywhere it

was bounded below by ε_{de} from PIV, and above by ε_{sgs} from PIV. Hence the DE method

provided a lower bound, and the SGS provided an upper bound. This makes sense

because DE (direct evaluation) is an exact evaluation of the turbulent stresses in the

fluid, but for PIV using a grid scale above the Kolmogorov length scale the smallest

eddies are not measured and the turbulent dissipation therefore underestimated.

Conversely, for the SGS (sub-grid scale) method a model is used to estimate the

turbulent stresses below the grid scale and add them back into the ε_{sgs} measurement.

This model, in the absence of detailed eddy size data, cannot give accurate results in every scenario; it assumes (for the basic SGS model used here) a single eddy scale across the whole flow, whereas the Sonolator has wide variations in velocity. The SGS model contains a constant factor (the Smagorinsky constant) of 0.17; other research (Gabriele, Nienow and Simmons 2009) showed that for a stirred tank application a constant of 0.11 gave better results. Hence the SGS model is known to overestimate in some circumstances, and it was thought to do so here since the CFD values for ε were lower.

Two places where a good comparison was obtained between ε_{de} and ε from CFD were: 1) in the recirculation region a long way from the jet, and 2) on the Sonolator axis directly after the orifice, up to around $z = 10$ mm. The reason for the first was likely to be that the lower turbulence levels away from the jet had larger eddy sizes which were better captured by PIV and by the DE method. The reason for the second could be that turbulence was higher on the jet boundary than in the centre of the jet, hence the relatively undisturbed fast region in the jet centre also had eddies captured well by PIV and the DE method.

Overall, the comparison of ε values between CFD and PIV could not provide conclusive validation of ε from CFD, however the magnitude of ε from CFD was within bounds suggested by DE and SGS analysis on PIV data, making CFD ε believable, correlating well with ε_{de} calculated using the DE method on the PIV data.

Comparison graphs for k and ε were also checked for other flow rates, orifice sizes, and for blade-in data. The findings from these other PIV/CFD comparison cases were similar to those presented above for the medium case (medium flow rate, medium orifice size and blade-out) and hence were not illustrated in further detail in this chapter.

One other item of interest for the ε comparison was that ε_{de} and ε_{sgs} were available from PIV data, and it was desired to see if ε_{de} and ε_{sgs} could be derived from CFD data with a better comparison than CFD ε from the SST-SAS turbulence model. For the fully three-dimensional equations for ε_{de} and ε_{sgs} see Khan (2005) or Gabriele, Nienow and Simmons (2009). The result of this exercise was that ε_{de} and ε_{sgs} did not appear to be reliably derived from the CFD data, giving worse agreement than CFD ε presented above, and the hypothesised reason was due to the CFD mesh scale being much bigger than the Kolmogorov length scale.

4.5   Conclusions

CFD simulation results for the Sonolator were compared against experimental results from PIV in order to validate the CFD simulations. Flow variables considered included: pressure drop over the Sonolator, velocity, turbulent kinetic energy (k) and turbulent energy dissipation rate (ε).

- In the literature review, previous research had validated CFD simulations using PIV data for many other fluid flow scenarios. Velocity validation was generally reliable, turbulence variables reliable only in pattern but not in magnitude.

- Predicted pressure drop across the Sonolator from CFD was comparable with pressure drops measured during PIV experiments.

- CFD velocity validation was good where PIV data was known to be accurate. From these validated cases, it was possible to extend validation (by using scaling rules and similarity between geometric cases) to some cases (and locations) where PIV data was found to be less accurate.

- CFD k was similar in pattern to PIV k_{var}, but was lower in magnitude; it could thus not be validated. The extra magnitude of the PIV k_{var} was thought to be due to periodic components which could not be deducted in those experiments. It was therefore possible that CFD k was of the right magnitude.

- CFD ε was bounded in most locations and cases by PIV ε_{de} and PIV ε_{sgs}, and followed their general pattern. In regions with lower turbulence (and fewer sub-grid eddies) CFD ε was of comparable magnitude to PIV ε_{de} and thus validated. In the higher turbulence regions CFD ε could not be explicitly validated, but due to being bounded by PIV ε_{de} and PIV ε_{sgs} it was of a realistic magnitude.

4.6   Nomenclature & Abbreviations

Symbol   Description

k Turbulent kinetic energy (J·kg^{-1} or m^2·s^{-2})

k_{var} k based on statistical variance of velocity field (J·kg^{-1})

M Mass flow rate (kg·s^{-1})

ΔP Pressure drop over Sonolator (subscript of CFD or PIV is the data source)

u, v, w x, y, z components of velocity vector field (m·s^{-1})

$\underline{v}$ Velocity vector field (m·s^{-1})

V Velocity magnitude scalar field (m·s^{-1})

V_{orif} Orifice superficial velocity (m·s^{-1})

x, y, z Coordinates as measured from orifice (m)

X, Y, Z   Coordinates as measured from orifice (m)

Greek Symbols

ε Epsilon, local specific energy dissipation rate (W·kg^{-1} or m^2·s^{-3})

ε_{de} Epsilon derived from DE method (W·kg^{-1})

ε_{sgs} Epsilon derived from SGS method (W·kg^{-1})

Abbreviations / Glossary

0037   Orifice of size 0.0037 in^2 (2.39 mm^2)

0110   Orifice of size 0.0110 in^2 (7.10 mm^2)

0140   Orifice of size 0.0140 in^2 (9.03 mm^2)

2D   Two-dimensional

3D   Three-dimensional

BLOUT   Blade out Sonolator geometry

BLDIN   Blade in Sonolator geometry

CFD   Computational Fluid Dynamics

DE   Direct Evaluation (method of deriving ε from PIV velocity gradients)

Delaunay   A meshing technique used within CFD, based on triangulation

LDV   Laser Doppler Velocimetry

Octree A meshing technique used within CFD, based on subdividing cubes

PIV   Particle Image Velocimetry

SGS   Sub-Grid Scale model (for deriving ε in PIV)

SST-SAS   Turbulence model in CFD

TKE   Turbulent Kinetic Energy ($m^2 \cdot s^{-2}$)

XYZ   The flow domain within x, y and z dimensions.

ZX   A plane defined by Sonolator axis (Z) and orifice long diameter (X)

ZY   A plane defined by Sonolator axis (Z) and orifice short diameter (Y)

4.7   References

- Chand, R., Bremner, D. H., Namkung, K. C., Collier, P. J., Gogate, P. R., (2007). "Water disinfection using the novel approach of ozone and a liquid whistle reactor", *Biochemical Engineering Journal*, **35(3)**, August, 357-364.

- Clark, A., Dewhurst. R. J., Payne, P. A., Ellwood, C., (2001). "Degassing a liquid stream using an ultrasonic whistle", *IEEE Ultrasonics Symposium Proceedings. eds. Yuhas, D. E., Schneider, S. C., Vols 1 and 2 of Ultrasonics Symposium*, 579-582.

- Drumm, C., Bart, H. J., (2006). "Hydrodynamics in a RDC Extractor: Single and Two-Phase PIV Measurements and CFD Simulations", *Chem. Eng. Technol.*, **29(11)**, 1297-1302.

- Ford, M. D., Nikolov, H. N., Milner, J. S., Lownie, S. P., DeMont, E. M., Kalata, W., Loth, F., Holdsworth, D. W., Steinman, D. A., (2007). "PIV-Measured Versus

CFD-Predicted Flow Dynamics in Anatomically-Realistic Cerebral Aneurysm Models", *Journal of Biomechanical Engineering*, **130(2)**, 021015.

- Gabriele, A., Nienow, A. W., Simmons, M. J. H., (2009). "Use of angle-resolved PIV to estimate local specific energy dissipation rates for up- and down-pumping pitched blade agitators in a stirred tank.", article plus later erratum, *Chem. Eng. Sci.*, **64**, 126–143.

- Gandhi, M. S., Sathe, M. J., Joshi, J. B., Vijayan, P. K, (2011). "Two phase natural convection: CFD simulations and PIV measurement", *Chem. Eng. Sci.*, **66**, 3152-2171.

- Hernández-Jiménez, F., Sánchez-Delgado, S., Gómez-García, A., Acosta-Iborra, A., (2011). "Comparison between two-fluid model simulations and particle image analysis & velocimetry (PIV) results for a two-dimensional gas-solid fluidized bed", *Chem. Eng. Sci.*, **66**, 3753-3772.

- Nakiboğlu, G., Gorlé, C., Horváth, I., Beeck, J., Blocken, B., (2009). "Stack gas dispersion measurements with Large Scale-PIV, Aspiration Probes and Light Scattering Techniques and comparison with CFD", *Atmospheric Environment*, **43(21)**, 3396-3406.

- Nussbaumer, T., Kiener, M., (2013). "Moving Grate Combustion Optimisation With CFD And PIV", http://www.ieabcc.nl/workshops/task32_2013_CPH/08_nussbaumer_kiener_paper.pdf, downloaded Aug 2008.

- Ranade, V. V., Perrard, M., Le Sauze, N., Xuereb, C., Bertrand, J., (2001). "Trailing Vortices of Rushton Turbine: PIV Measurements and CFD Simulations with Snapshot Approach", *Trans. IChemE*, **79**.

- Ryan, D., Simmons, M. and Baker, M. (2013). "Investigating Dispersion and Emulsification Processes using a Sonolator Liquid Whistle", *Proceedings of 8th International Conference on Multiphase Flow*, 26-31 May 2013, Jeju, Korea.

- Sheng, J., Meng, H., Fox, R. O., (1998). "Validation of CFD Simulations of a Stirred Tank Using Particle Image Velocimetry Data", *The Canadian Journal of Chemical Engineering*, **76**.

- Silva, G., Leal, N., Semiao, V., (2008). "Micro-PIV and CFD characterization of flows in a microchannel: Velocity profiles, surface roughness and Poiseuille numbers", *Int. J. Heat Fluid Flow*, **29**, 1211-1220.

- Virdung, T., Rasmuson, A., (2007). "Hydrodynamic properties of a turbulent confined solid-liquid jet evaluated using PIV and CFD", *Chem. Eng. Sci.*, **62**, 5963-5978.

- Westra, R. W., Broersma, L., van Andel, K., Kruyt, N. P., (2010). "PIV Measurements and CFD Computations of Secondary Flow in a Centrifugal Pump Impeller", *J. Fluid Eng. (ASME)*, **132**.

Chapter 5   EMULSIFICATION EXPERIMENTS ON A PILOT PLANT SONOLATOR

5.1   Abstract

Experiments have been carried out on a pilot plant liquid whistle in order to characterise emulsification by examining the change in droplet size distributions before and after processing. The equipment was a Model ACIP2 Sonolator. Emulsions of silicone oil in water were created with SLES as surfactant. Variables included mass flow rate, pressure drop across Sonolator, oil viscosity, oil concentration, surfactant concentration, oil inlet condition, orifice size. Droplet size distributions were obtained which characterised the droplet breakage in the Sonolator. Average droplet sizes were examined under a range of experimental conditions in order to determine which variables were significant in affecting emulsification.

5.2   Introduction – the need to characterise droplet breakage in the Sonolator

The Sonolator is an inline fluids processing device of the liquid whistle type which causes mixing of fluids and emulsification of multiphase fluids resulting in finely dispersed droplets. As part of this EngD project it was desired to characterise the Sonolator's emulsification effect by quantifying the reduction in droplet size caused by different combinations of processing conditions such as flow rate and orifice size. This would aid industrial research and development into integrating the Sonolator into existing process lines; costly and lengthy pilot scale experimentation could be streamlined by a better knowledge of what emulsification effect to expect from the Sonolator, existing product lines could be redesigned using the knowledge of the Sonolator's action, new product lines using the Sonolator could also be developed.

This chapter describes emulsification experiments on a pilot plant Sonolator and presentations of the droplet size distribution data, contributing towards aims 2 and 3 listed in Chapter 1, which were to understand the emulsification performance of the Sonolator and provide models predicting droplet size distribution as a function of the processing conditions, and to understand how these distributions change as a function of orifice size.

In particular, given a set of processing conditions, many input variables (mass flow rate, dispersed phase viscosity, etc) are associated with those conditions. This chapter ascertains which of the variables have a significant effect on droplet size when processing on the Sonolator, and which variables do not. Following that, Chapter 6 develops empirical correlations for Sonolator droplet breakage based on the significant variables, in light of droplet breakage theory.

The stages of work required by this characterisation include: a review of existing techniques for characterisation of emulsification; a choice of methods and materials; carrying out droplet breakage experiments on a pilot plant scale Sonolator experimental rig and obtaining fluid samples; obtaining droplet size distributions from processed samples; comparison of droplet size distributions; obtaining of summary information such as average droplet size and width of droplet size distribution; deducing the action of the Sonolator from correlations between relevant variables; comparison of these correlations with theory. This chapter carries out these activities up to the obtaining of summary information on the fluid samples; Chapter 6 continues with correlations and comparison to theory.

5.3   Literature Review

This section contains a review of the existing literature concerning emulsification experiments carried out on fluid mixing devices. No accounts to date have been published in the open literature on the emulsification performance of Sonolators. Preliminary results from the experiments in this chapter were published in Ryan, Simmons and Baker (2013), see Appendix 13 for a copy of the paper. This literature review will focus on previously published emulsification experiments using other high-intensity inline fluid mixing devices.

Emulsification has been characterised for many different fluid mixing devices including the following: injection in pipe flow (Tjaberinga, Boon and Chesters 1993); ultrasonic emulsification (Lin and Chen 2006; Abismaïl, Canselier, Wilhelm, Delmas and Gourdon 1999); Ultra-Turrax device (Abismaïl *et al* 1999); a six vaned rheometer at high shear rate and high dispersed phase volume (Baravian, Mougel and Caton 2007); narrow gap homogenizers (Tcholakova, Denkov and Danner 2004; Vankova,

Tcholakova, Denkov, Ivanov, Vulchev and Danner 2007); valve homogenizers or HPH (Brösel and Schubert 1999; Tesch, Freudig and Schubert 2003); batch rotor stator devices (Maa and Hsu 1996; Padron 2005); inline rotor stator devices (Hall, Cooke, El-Hamouz and Kowalski 2011). All of these generate turbulence which, depending on the exact flow conditions, may break droplets in a similar way to the Sonolator. Some important findings from these papers included choices for: dispersed phase, continuous phase, surfactant, measurement technique, droplet size distribution statistics and relevant methods for presenting these statistics.

The emulsions produced in the above papers were mostly oil in water (O/W). These had higher viscosity for the dispersed phase than for the aqueous continuous phase, except where thickening agents had been introduced into the water (e.g. see Tjaberinga *et al* 1993, Tesch *et a*l 2003, Hall *et al* 2011). One advantage of having water as the continuous phase was that the emulsion samples were of low viscosity at room temperature, and the samples were easy to handle, deflocculate and dilute for measurement.

Dispersed phases investigated included paraffin oil (Tjaberinga *et al* 1993), kerosene (Abismaïl *et al* 1999), diesel fluid (Lin and Chen 2006), mineral and vegetable oil (Brösel and Schubert 1999; Tesch *et al* 2003, Vankova *et al* 2007), soy bean oil (Tcholakova *et al* 2004, Vankova *et al* 2007) and silicone oils of varying viscosity (Padron 2005, Hall *et al* 2011). An advantage of using silicone oil was that the viscosity could be varied over at least three orders of magnitude without affecting other physical properties of the fluid.

Surfactants could be separated into two categories: high molecular weight and low molecular weight. Of the former were PEG 20000 (Brösel and Schubert 1999), AMP

8000 protein (Tcholakova *et al* 2004) and sodium caseinate (Vankova *et al* 2007). Of the latter: Span 80 (Brösel and Schubert 1999; Lin and Chen 2006), Tween 60/80 (Abismaïl *et al* 1999; Tesch *et al* 2003; Lin and Chen 2006), SDS (Tesch et al 2003; Vankova *et al* 2007) and SLES (Hall *et al* 2011). An advantage of low molecular weight surfactants for characterising emulsification is that they migrate to the newly formed droplet interfaces faster than high molecular weight surfactants, minimising re-coalescence of droplets.

Two main measurement techniques in these accounts were: optical/video microscopy followed by counting/sizing of droplet images; and light scattering techniques where the droplet size distributions can be back-calculated from the scattering patterns recorded inside the device. One advantage of the latter technique was that it was extremely fast compared to manual sizing of particles.

Once the droplet size distribution for an emulsion sample was determined it was possible to work out an average droplet size statistic. Most of the literature made use of the Sauter mean diameter d_{32} (generalised moment-weighted average droplet size d_{nm} is defined later in this chapter), with d_{43} used in some papers (Maa and Hsu 1996; Padron 2005; Baravian *et al* 2007) and $d(95)$ which was 95th percentile droplet size used by Vankova *et al* (2007). One reason why d_{32} was used so frequently was that properties of the bulk emulsion often depend on diffusion across the interface, which depends on the amount of interfacial area exposed by the droplets. This is directly related to d_{32} which is an interfacial area weighted average (Padron 2005).

After determining a suitable droplet size statistic, these statistics were typically plotted against a processing condition of interest (e.g. flow rate) for a range of experiments. Tesch *et al* (2003) gave graphs of d_{32} vs energy density; Padron (2005)

gave correlations of droplet size with Weber number, viscosity group and Reynolds number; Hall *et al* (2011) compared droplet size to each different processing variable within a Silverson rotor-stator device. This technique would be suitable for the Sonolator since droplet size could be compared against flow rate, orifice size and dispersed phase viscosity to name three available variables.

Conclusions from the literature review: emulsification in the Sonolator could be investigated with oil in water emulsions using silicone oils of a range of viscosities, a low molecular weight surfactant, laser diffraction droplet size distribution measuring techniques, with analysis of the trend of d_{32} (and perhaps additionally d_{43}) with various processing conditions.

Additional note: this EngD project of investigating emulsification in a Sonolator device is in many ways a sequel to the EngD project of Hall on Silverson rotor-stator devices, which was written up into his thesis (Hall 2012). Since, alongside the Sonolator rig, similar materials and experimental equipment was available for this work, as well as the success of Hall in characterising the Silverson, it was decided to adapt the technique of Hall in using silicone oil in water with SLES pre-emulsions to characterise the Sonolator. Hall's literature review (Hall 2012) contains more detailed information about why laser diffraction in the Malvern Mastersizer 2000 was chosen as the main measurement technique over other relevant techniques such as optical microscopy, electrical sensing and dynamic light scattering. His chapter also contains detailed discussions of the dynamics of droplet dispersion, about how drop size distributions characterise the number or volume distributions of emulsion droplets, and how Sauter mean diameter (d_{32}) characterises the average emulsion droplet size.

5.4   Materials and Methods for emulsification experiments

In this section, the Sonolator and its experimental rigs are first described. The materials used are then specified, together with the matrix of experiments performed out. Particular issues with the general technique of making reliable emulsion samples using the Sonolator are highlighted, together with the choice of appropriate droplet size distribution measurement technique.

5.4.1   Sonolator device

The Sonolator liquid whistles (ex. Sonic Corporation, CT, USA) investigated in these pilot plant studies were Model ACIP2 Sonolators with orifice size codes 0025, 0060, 0080 and 0140 (see Table 1.2 for full explanation of these size codes, which abbreviate orifice sizes between 0.0025 in^2 and 0.014 in^2, or 1.61 mm^2 to 9.03 mm^2 using SI units). The Sonolators were located at Unilever Research & Development, Port Sunlight, UK. Two different Sonolator rigs were used, denoted "Muscle" and "Hair"; the former with smaller orifices and rated to operate under flammable conditions, the latter with larger orifices and pumping capacity.
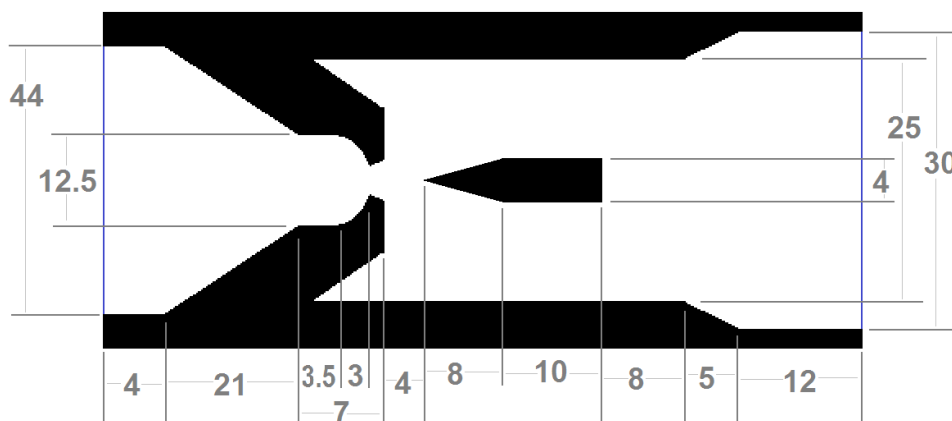
Figure 5.1: Schematic diagram of cross-section through thin axis of orifice, of flow domain inside ACIP2 Sonolator. All dimensions converted to millimetres from original design drawing in inches.

The Model ACIP2 Sonolator (Figure 5.1) consisted of: inlet (on left), orifice, main chamber and blade (middle), outlet (right). Each component shown in Figure 5.1 was cylindrical, except the blade which Figure 5.1 shows in cross-section (extending perpendicular to the plane illustrated). The main chamber had diameter of 25 mm (1 inch on original drawings). The blade was positioned approximately 4 mm after the orifice and could not be adjusted; the fluid flowed above and below the blade. The back-pressure valve was kept open in all but a small number of experiments: it was conical in shape and when closed only allowed fluid to escape from the main chamber in a small circular region, thus increasing pressure in the Sonolator.
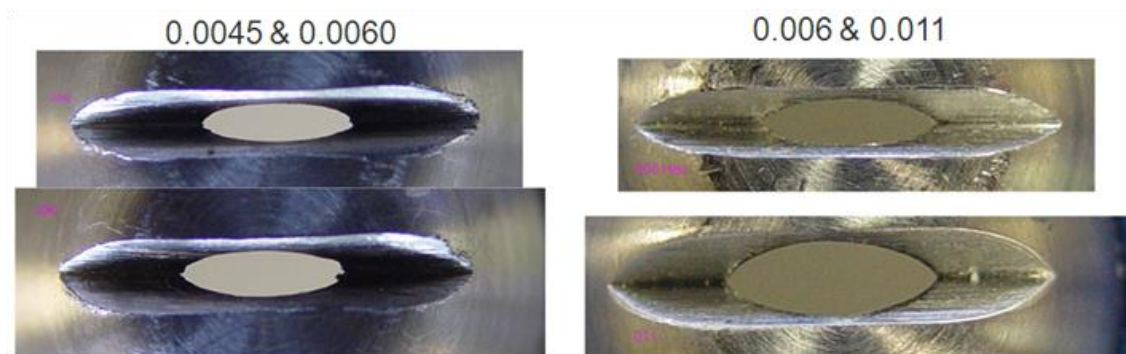
Figure 5.2: Photographs of pilot plant Sonolator orifices 0045, 0060 (two different orifices of same area), 0110.

In Figure 5.2 close-up photographs of various Sonolator orifices are given; on the left from the Muscle rig, and from the right from the Hair rig. It was observed that all orifices were shaped like a "cats-eye". The approximate perimeter was that of two semi-circles. Each orifice was created by milling two cuts at 60° into a hollow steel cone. The intersection of the cavity and the cuts created the orifice. The edges were slightly ragged due to milling imprecision, however this was not considered to adversely affect emulsification.

5.4.2   Sonolator experimental rigs

The main components of the experimental rig (Figure 5.3) were aqueous phase and oil phase vessels, pumps with flow meters, pipe-work of 12.5 mm diameter combining the two streams at a T-junction, the Model ACIP2 Sonolator with backpressure valve and a waste stream with a sampling point.

The pumps for the Hair rig were progressive cavity pumps ex Seepex; those for the Muscle rig were triplex plunger pumps ex Cat (required by Unilever to explore higher pressure drops). All their flowmeters were pre-calibrated at Unilever against timed flows, e.g. by weight of material collected over a set period. This was carried out for a range of pump settings to confirm linearity and accuracy. The calibration of the flowmeters was found to be stable over time; pump re-calibration was rarely needed.
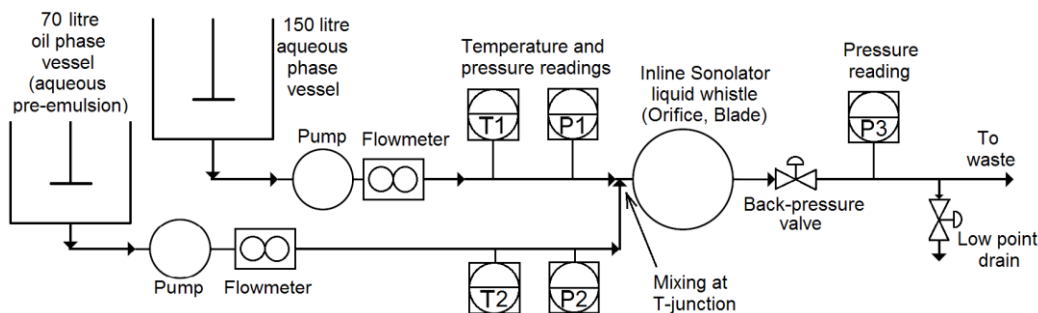
Figure 5.3: Schematic diagram of pilot plant Sonolator process with a oil phase tank pre-emulsion (PE) set-up.

In this setup the oil was introduced into the Sonolator as a coarse pre-emulsion created in the oil phase tank using an impeller. Both oil and aqueous phase tanks had SLES surfactant present at 0.5 wt% which was well above CMC and in excess for this emulsification (Hall *et al* 2011). Moreover since SLES is a small molecule there was fast movement from bulk to surface giving negligible time-dependence of interfacial tension. These factors guaranteed full coverage of emulsion droplets.

The oil phase tank was operated with either 5 wt% or 10 wt% oil. The remainder of both tanks was water. (Exact specifications for materials are discussed Table 5.2 below.) This setup allowed oil concentration to be varied independently of flow rate.
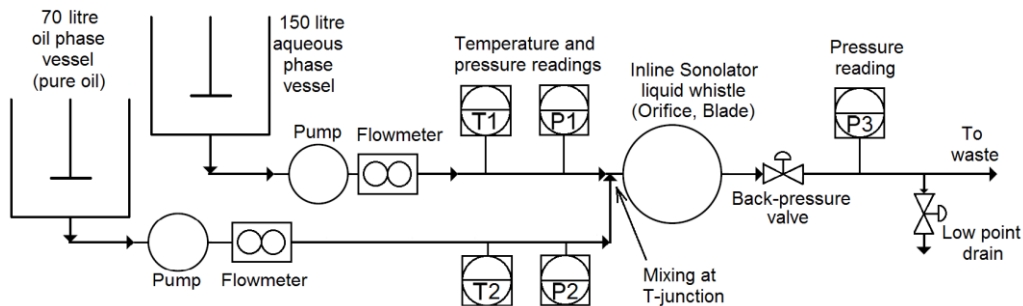
Figure 5.4: Sonolator with oil mixing at T-junction (TMIX). Note that oil phase tank now contained pure oil.
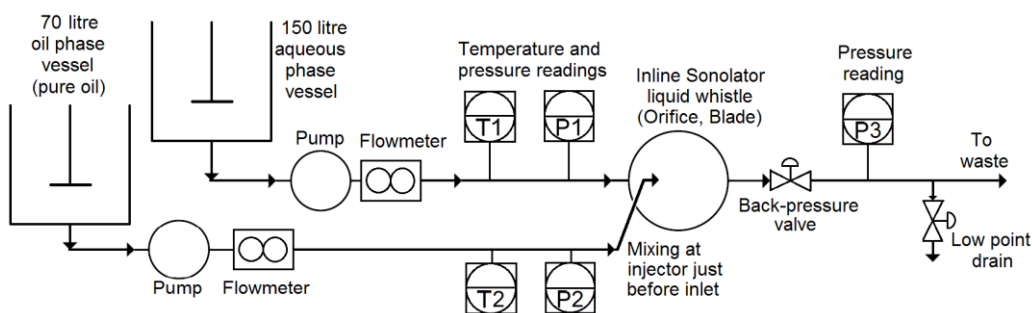
Figure 5.5: Sonolator with oil injection at orifice (INJ).

Two alternative setups to pre-emulsion (PE) were used: mixing at a T-junction (TMIX, Figure 5.4) and injection (INJ, Figure 5.5). These three configurations (PE, TMIX, INJ) are all used in industry, and the effect of these variable setups is discussed below. In the INJ and TMIX setups the oil was present as a pure liquid to be mixed by injection (INJ) or at a T-junction (TMIX) prior to emulsification by the Sonolator. The aqueous phase vessel contained 0.5 wt% SLES solution for all these oil flow rates investigated.

Additional experiments were carried out with the TMIX setup to investigate the effect of varying SLES concentration. This was achieved by making the aqueous phase

vessel contain water only, and adding a third tank and stream with a low percentage of SLES (1.25 wt% in one experiment, 0.03125 wt% in another). By combining streams of pure oil, pure water and SLES solution, emulsification was carried out with flow rates and SLES concentration simultaneously varying over wide ranges. Samples were held stable by sampling into 1 wt% SLES solution at a ratio of approximately 1:1 between the SLES solution and the emulsion sample; this prevented coalescence from altering the droplet size distribution post sampling from the Sonolator outlet.

5.4.3   Materials

The materials used were water, oil and surfactant. The water was demineralised chlorinated mains water, and measured into the tanks using a mass flow meter. The level of chlorination was 1 to 2 parts per million. At this concentration of chlorine, bacterial growth would be prevented, but emulsification would not be significantly affected.

The SLES (sodium laureth sulphate or sodium lauryl ether sulphate) was 1EO grade, Texapon N701, Cognis UK Ltd, Herts, UK; a mixed alkyl (C12-14) ether sulphate anionic surfactant. It had previously been diluted from 70 wt% paste (as supplied) to 28 wt% aqueous solution; this liquid was subsequently added to each tank in the proportion required to achieve the SLES mass fraction specified in the experimental plan.

This SLES had molecular weight of approximately 420 g·mol^{-1}, specific gravity of 1.03 to 1.04, CMC in water of 0.2 mmol dm^{-3} (El-Hamouz 2007). Calculations from this data showed that the CMC (critical micelle concentration) of SLES was around 0.0081 wt% with an air interface. Assuming that with an oil interface the CMC was of approximately equal magnitude, for 0.5 wt% emulsions SLES was present at around 60

times the CMC. Due to this excess of surfactant, droplets would quickly become coated with SLES and become stabilised against coalescence (see Figure 7.14 for evidence that droplets were stabilised).

The silicone oils used were poly-dimethyl siloxane Dow Corning 200 fluids (viscosities in cSt: 10, 350, 10 000) and DC245 fluid (viscosity 3.8 cSt). Note that 1 cSt $= 10^{-6}$ m$^2 \cdot$s$^{-1} = 1$ mm$^2 \cdot$s^{-1}. Also note that the Dow Corning 200 fluids were silicone oils with linear chains of variable length, a longer chain length gave a higher viscosity; whereas the DC245 fluid was pentacyclomethicone with a ring structure which allowed it to have lower viscosity. These materials differed greatly in their viscosities, but other relevant material properties such as interfacial tension with water, density and refractive index were comparable.

The silicone oils were supplied either as pure oils or as concentrated coarse pre-emulsions previously generated using the same methodology for the experiments of Hall *et al* (2011); these concentrated pre-emulsions had as ingredients 50 wt% oil, 49.5 wt% water, 0.5 wt% SLES. In both cases, the final tank pre-emulsion was of 0.5 wt% SLES, 5 wt% or 10 wt% oil and the remainder water, with comparable droplet sizes (see Figure 5.6).

Table 5.1: Material properties under ambient conditions. References: Author's own measurement (a), Hall 2012 (b), Hall, Cooke, El-Hamouz & Kowalski 2011 (c), Manufacturer quoted figures (d), Padron 2005 (e)

Material	Density ($kg·m^{-3}$)	Kinematic Viscosity (cSt)	Surface tension ($mN·m^{-1}$)	Interfacial Tension with 0.5 wt% SLES solution ($mN·m^{-1}$)	Refrac-tive Index
Water	997[a]	0.89	72.0[e]	NA	1.333[a]
DC245	952[a]	3.8[d]	unknown	unknown	1.397[a]
Silicone Oil (10 cSt)	937[c]	10[d]	20.1[b]	10.6[c]	1.399[b]
Silicone Oil (350 cSt)	969[c]	350[d]	21.1[b]	12.3[c]	1.403[b]
Silicone Oil (10 000 cSt)	970[b]	10 000[d]	21.5[b]	unknown	1.404[b]
SLES solution (0.5 wt%)	998[b]	0.90[b]	unknown	NA	1.334[a]

In Table 5.1 the relevant physical properties of materials used are given. The author's own measurements of refractive index were carried out on a RFM340 automatic digital refractometer (Bellingham Stanley Ltd., UK) at Unilever Port Sunlight R&D. This was held at ambient temperature using a Haake DC5 Immersion circulator and Haake K20 Compact Refrigerated Circulator combination. The density measurements were carried out using a density cup at Unilever.

5.4.4 Specification of types of experiments

The Sonolator pilot plant runs could potentially have been configured in many different ways. Variables requiring specification included: mass flow rate (obtained by adjusting set points on the mass flow controllers), orifice size, oil viscosity, oil concentration, surfactant concentration and back-pressure valve position. The experimental rig setup was varied between pre-emulsion (PE), mixing at a T-junction (TMIX) and injection (INJ) shown in Figure 5.3, Figure 5.4 and Figure 5.5 respectively.

Over the course of this project four different sets of pilot plant Sonolator trials were carried out at Unilever R&D, Port Sunlight, the results of each set of trials informing subsequent experimentation. Thirteen different trials were carried out covering many different experimental conditions. Each trial had an experimental plan setting out exact rig specification and materials; in addition a plan for how the mass flow rate set points would be varied throughout the trial. By varying the mass flow rates of the different streams, each trial achieved collection of between 10 and 40 samples representing different experimental conditions of interest regarding emulsification using the Sonolator. The Sonolator data log was checked against the experimental plan to check that timings, actual mass flow rates and percentages from each inlet stream were accurate.

The outline of which experimental conditions were achieved in the four sets of pilot plant trials are given in Table 5.2. Note: orifice size code "0025" meant a manufacturer stated nominal area of 0.0025 in^2 (1.61 mm^2), and similarly for other size codes, see Table 1.2 for full description of orifice sizings.

Table 5.2: Descriptions of Sonolator experimental runs carried out and analysed by David Ryan. Back pressure valve fully open throughout.

Trial-set number	1	2	3	4
Sono Rig	Muscle	Muscle	Hair	Hair
Orifice Type	0025	0025	0080	0080
Oil Inlet Condition	PE	PE	INJ, TMIX	TMIX
Oil Viscosities (cSt)	10, 350	3.8, 350, 10000	10, 350	3.8, 350
Mass Flow Rate Setpoints (kg·min^{-1})	2.0 to 6.0	0.5 to 6.5	7.1 to 17.3	4.4 to 17.3
Setpoints converted to kg·s^{-1}	0.033 to 0.100	0.008 to 0.108	0.118 to 0.288	0.073 to 0.288
Oil weight fractions	0.5 wt% to 10 wt%	0.5 wt% to 5 wt%	2 wt%, 5 wt%	2 wt%, 5 wt%
SLES weight fractions	0.5 wt%	0.5 wt%	0.5 wt%	0.5 wt% to 0.0003 wt%

Before the EngD project was started, some preliminary data were already available courtesy of Prof Adam Kowalski at Unilever R&D, Port Sunlight. Details of the experimental conditions under Prof Kowalski are given in Table 5.3:

Table 5.3: Descriptions of Sonolator experiments carried out by Prof Adam Kowalski. SLES at 0.5 wt%. Oil below 10 wt% in a pre-emulsion from a stirred tank. Hair rig used. Data kindly provided by Prof Kowalski.

Run number	1	2	3	4	5	6
Back Pressure Valve	Closed	Open	Open	Open	Closed	Open
Orifice Type	0060	0060	0060	0080	0140	0140
Oil Viscosities (cSt)	10	10	350	350	350	350
Mass Flow Rate Setpoints (kg·min^{-1})	2.0, 6.0	2.0 to 12.9	2.0 to 13.1	4.0 to 17.0	9.0 to 20.0	9.0 to 20.0
Setpoints converted to kg·s^{-1}	0.033 to 0.100	0.033 to 0.215	0.033 to 0.218	0.067 to 0.283	0.150 to 0.333	0.150 to 0.333

The preliminary runs described in Table 5.3 contained approximately 30 data points in total; the follow up runs described in Table 5.2 added approximately 140 more data points. These results added together gave a substantial set of evidence enabling conclusions about emulsification in the Sonolator to be reached in the results section later on.

Table 5.4: Conversion chart for flow rates in units $kg \cdot min^{-1}$ (inputted on the Sonolator apparatus) and in units $kg \cdot s^{-1}$ (SI units)

Sonolator input flow rate ($kg \cdot min^{-1}$)	SI flow rate ($kg \cdot s^{-1}$)	Sonolator input flow rate ($kg \cdot min^{-1}$)	SI flow rate ($kg \cdot s^{-1}$)
0.5	0.008	6.0	0.100
1.0	0.017	6.5	0.108
1.5	0.025	7.1	0.118
2.0	0.033	9.0	0.150
3.0	0.050	11.0	0.183
4.0	0.067	13.8	0.230
4.4	0.073	16.0	0.267
5.6	0.093	17.3	0.288

Table 5.4 shows the conversions between the mass flow rate set points entered on the Sonolator (in $kg \cdot min^{-1}$) and those used in the results section below (in units $kg \cdot s^{-1}$ which are SI units). For the 0025 orifice, typical low and high flow rates would be below 0.033 $kg \cdot s^{-1}$ and above 0.100 $kg \cdot s^{-1}$ respectively. For the 0080 orifice, typical low and high flow rates would be below 0.118 $kg \cdot s^{-1}$ and above 0.230 $kg \cdot s^{-1}$ respectively. For both orifices, low flow rates produced comparable pressure drops and emulsification conditions, similarly for high flow rates. Low and high also corresponded to the pump speed being near the minimum or maximum attainable on both experimental rigs used.

5.4.5   Details of the experimental procedure

Before each Sonolator experimental run the tanks and pipes were cleaned with hot water and surfactant solution to eliminate any build-up from previous experiments. (This was normally performed at the end of each day, so that the rig was clean for the next day, as well as at ambient temperature when the experiment started). The orifice of correct size was installed.

The tanks were charged with the raw materials as follows: Aqueous phase tanks had water measured into them using a mass flow meter. To obtain the specified mass fraction of SLES, a calculation was performed for the required mass of 28 wt% SLES aqueous solution (a viscous liquid). This mass was weighed on scales, and then dispersed in the tank using an impeller to circulate and mix the fluid; Hall (2012) stated that ten minutes was sufficient to completely dissolve and mix the SLES.

For pre-emulsion (PE) experiments the oil phase tank contained a pre-emulsion of 5 wt% or 10 wt% oil. It was created by diluting oil or existing concentrated pre-emulsion into a SLES solution. The masses of oil or concentrated pre emulsion were obtained and controlled using weighing scales; they were both found to disperse quickly in the SLES solution under low impeller rates (tip speed of around 4 m·s^{-1} as according to Hall 2012) to produce a uniform dilute pre-emulsion. The impeller speed was sufficiently low so that the final pre-emulsion droplet sizes were coarser than the emulsions processed on the Sonolator. To check that this was so, pre-emulsion samples were taken and compared to processed samples. In all cases, the processed samples contained considerably smaller droplets than the pre-emulsions, this is shown in the results section later, e.g. see Figure 5.7. For a similar experiment on an inline Silverson mixer (Hall 2012) it was verified that outlet droplet size and d_{32} were not significantly

dependent upon inlet droplet size. The comparison between PE, INJ and TMIX oil inlet conditions below verified this finding for the Sonolator.

For experiments with pure oil (INJ, TMIX) the oil was weighed on scales and then added directly to an empty tank. Experimental conditions were under ambient conditions, so it was not necessary to wait a long time for the temperature to equilibrate.

At the start of each experiment there was a testing period of at least 2 minutes where every stream was run simultaneously at a medium flow rate to allow pressure drop and flow rates to stabilise. Subsequently, total mass flow rate and percentage flow rates for each stream were varied through time depending on the experimental plan. This happened by fixing each parameter set at the start of a time window. Each time window lasted for between one to three minutes. Emulsions of the same properties were continuously produced on the Sonolator during each window. Since up to thirty seconds was needed mid-experiment for mass flow rates and pressure drops to stabilise, sampling was carried out in the last thirty seconds of each parameter-set window. Sampling occurred from the low-point drain directly after the Sonolator. It was calculated that the emulsion took less than thirty seconds under all flow rates to travel from the Sonolator to the low point drain. This ensured that the sample was representative of the mass flow rates entered in the experimental plan.

5.4.6   Sample Analysis

An accurate measurement technique was needed to measure emulsion droplet size distributions. In Appendix 6 the choice of techniques is discussed, along with evidence that the laser scattering technique selected was both accurate and provided a good characterisation of dispersion in the Sonolator. This appendix contains a detailed discussion of which variables existed in the emulsification experiments. In particular d_{32}

was chosen as the droplet size statistic to consider, and the main flow rate variables were mass flow rate (M), orifice superficial velocity (v), Sonolator pressure drop (ΔP), total power dissipated in the flow (P), and derived epsilon (local specific turbulent energy dissipation rate, ε).

5.4.7   Summary of Materials and Methods

Two Model ACIP2 Sonolators were used to produce silicone oil in water emulsions with SLES as surfactant. Many different experimental parameters were varied, including different flow rates, orifices and oil viscosities. Different droplet size distribution measurement techniques were considered, and laser diffraction was chosen. The specific apparatus used was a Malvern Mastersizer 2000. Experimental technique was chosen to minimise contamination with extraneous particles and cross-contamination between samples, as well as calibrate refractive index appropriately. Measurements were found stable over time and the samples found representative of the original emulsions produced. The measured droplet size distributions form the basis of the following results section.

5.5   Results and Discussion

The direct output of the pilot plant experiments was a large number of emulsion samples. Analysis using a Mastersizer 2000 yielded droplet size distributions for each sample, which are directly compared below for a few chosen cases. In order to compare many droplet size distributions efficiently, statistics derived from these distributions were used to represent the distributions. In most cases the Sauter mean diameter (d_{32}) was the key statistic used. In some cases span (w) and skewness (s) were also considered.

5.5.1   Droplet size distributions (DSDs)

In this first results section, various volume-weighted droplet size distributions (DSD) are presented. These were the output from the Mastersizer 2000 measurements. The data are plotted as continuous curves for easy comparison, however the original data were discretised in 100 size bins from 0.01 μm to 10 000 μm, equally spaced on a logarithmic size scale. The ratio between consecutive length scales was 1.148, e.g. a frequency (vol%) measurement of 8% at 10 μm meant that 8 percent by volume of droplets had diameters between 9.33 μm and 10.71 μm.

5.5.1.1   Pre-emulsion DSDs

Samples were taken from the oil phase tank to determine the DSDs of the coarse pre-emulsions. These were analysed on the Mastersizer, with results presented in Figure 5.6.
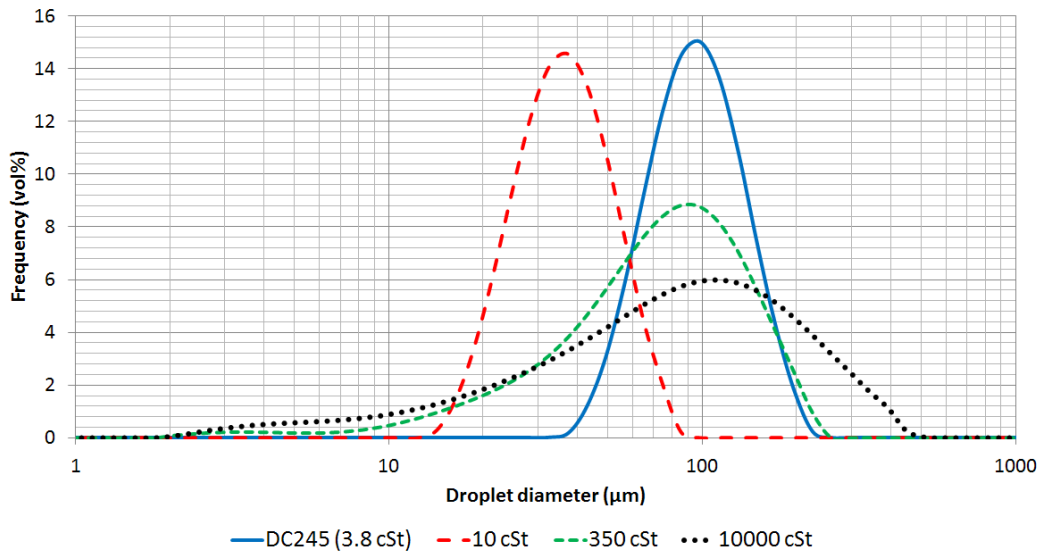
Figure 5.6: Volume weighted droplet size distributions for pre-emulsion samples from the oil phase tank. Silicone oils of viscosity (in cSt) 3.8, 10, 350 and 10 000: d_{32} values (in μm) are 61.32, 42.64, 41.81, 30.64 for each viscosity in turn. Muscle rig, 0025 orifice (from trial-set numbers 1 and 2).

The figure shows that the DSDs for the two low viscosity oils (DC245, 10 cSt silicone oil) were log-normal. The variation in peak droplet size was due to different rates of stirring in the oil phase tank. The higher viscosity 350 cSt and 10 000 cSt oils had a larger spread of droplet sizes in the pre-emulsion and deviated from log-normal behaviour by having a long tail on the left, i.e. their distributions were negatively skewed. For all oils, almost all of the pre-emulsion droplets (by volume) were above 15 μm in size. This implied that when processed samples had DSDs with the majority of droplets below 15 μm, this must be due to the emulsification occurring within the Sonolator.

5.5.1.2 DSDs of pre-emulsions compared to processed samples
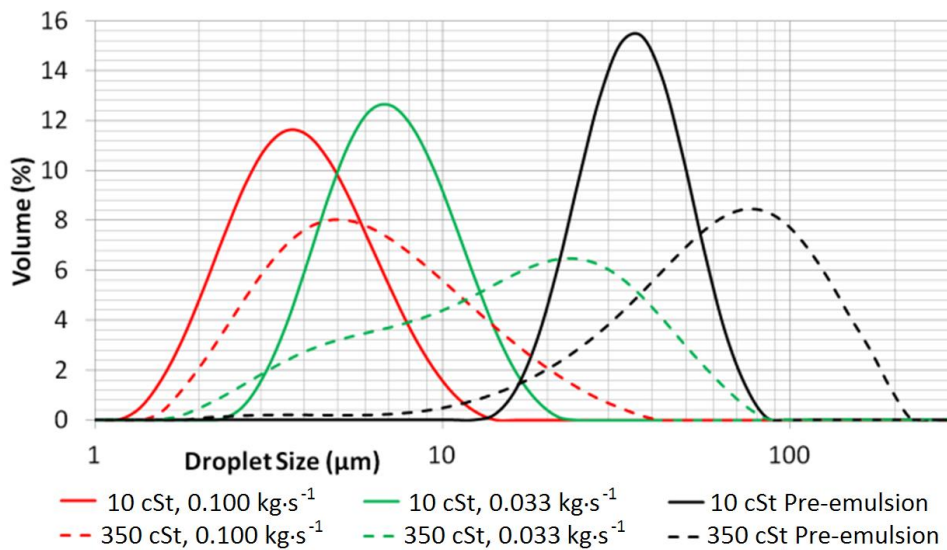
Figure 5.7: Volume weighted DSDs for 10 cSt and 350 cSt oil. Comparison between: pre-emulsion, processing at 0.033 kg·s^{-1}, processing at 0.100 kg·s^{-1} for 0025 orifice.

In Figure 5.7 unprocessed and processed samples are compared for the 10 cSt and 350 cSt oils. In all cases there was a reduction of droplet size after the fluids were processed, this was seen by the distribution shifting towards the left. Moreover, the distributions obtained at 0.100 kg·s^{-1} were shifted further to the left than the corresponding 0.033 kg·s^{-1} distributions, which indicated a further reduction in droplet sizes when processing with higher flow rates.

The 10 cSt distributions stayed log-normal (symmetric about the peak value). The 350 cSt distributions were wider (larger span) than the 10 cSt distributions. The 350 cSt distributions were negatively skewed at low flow rate and positively skewed at high flow rate. These changes in distribution shape may indicate differences in the droplet breakage mechanisms, discussed in Chapter 6.

By comparing the DSDs in Figure 5.7 it was clear that the experiments had succeeded in characterising changes in droplet size distribution due to emulsification in

the Sonolator. The next section illustrates the behaviour of the measured DSDS under wider ranges of experimental conditions.

5.5.1.3   Effect of mass flow rate and oil viscosity upon the DSDs

Pre-emulsions of silicone oils with four different viscosities (in cSt: 3.8, 10, 350, 10 000) were processed on the Sonolator. Five different flow rates were used in sequence (in kg·s^{-1}: 0.033, 0.050, 0.067, 0.083, 0.100) with a 0025 orifice.
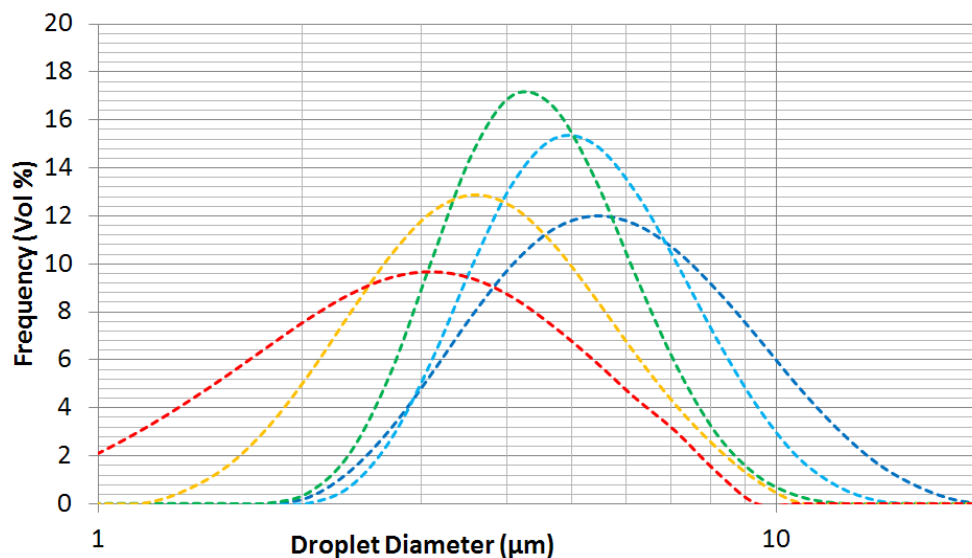
Figure 5.8: Droplet size distributions for DC245 (3.8 cSt) at mass flow rates evenly spaced from 0.100 kg·s^{-1} (red, on left) down to 0.033 kg·s^{-1} (blue, on right). Orifice size code 0025.

Figure 5.8 shows that for the 3.8 cSt oil the distributions were log-normal, with slightly narrower distributions for the middle flow rates (e.g. 0.067 kg·s^{-1} in green), with a single peak droplet size which decreased as mass flow rate increased. This dependency was expected: higher mass flow rates were expected to produce higher energy dissipation rates (when other factors are fixed) due to dimensional considerations showing that energy dissipation rate would scale according to the cube of mass flow rate; existing theories of droplet breakage in turbulent flow (to be explored in

depth in Chapter 6) give that droplet size decreases as energy dissipation rate increases, e.g. see Hinze (1955).
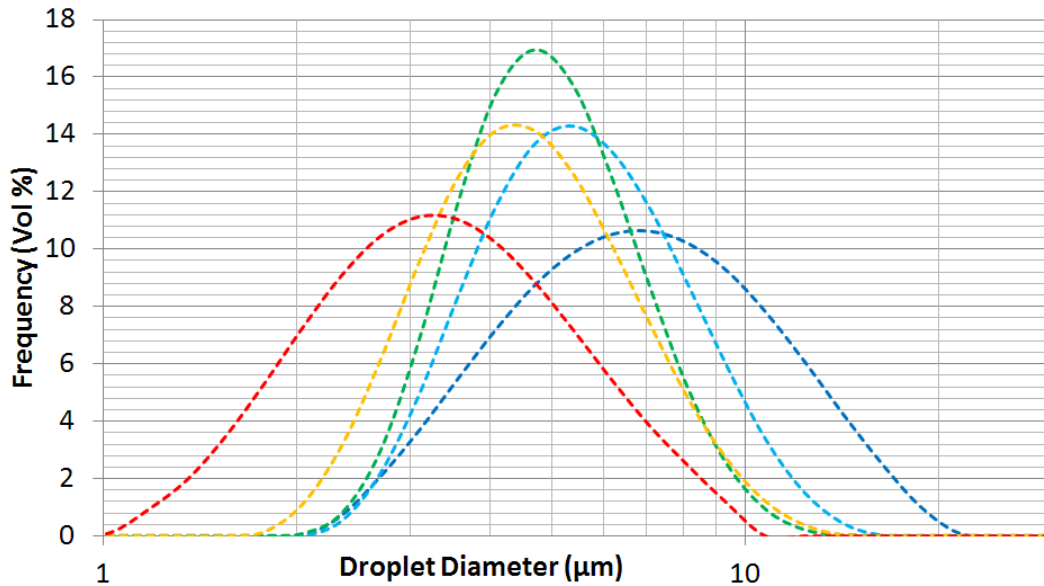
Figure 5.9: DSDs for 10 cSt silicone oil. Mass flow rates from 0.100 kg·s^{-1} down to 0.033 kg·s^{-1}. Orifice size code 0025.

Figure 5.9 shows that for 10 cSt silicone oil the results were very similar; larger flow rates produced smaller droplets, with approximately log-normal behaviour throughout. A comparison of droplet sizes (d_{32}) is given in Table 5.5 below.
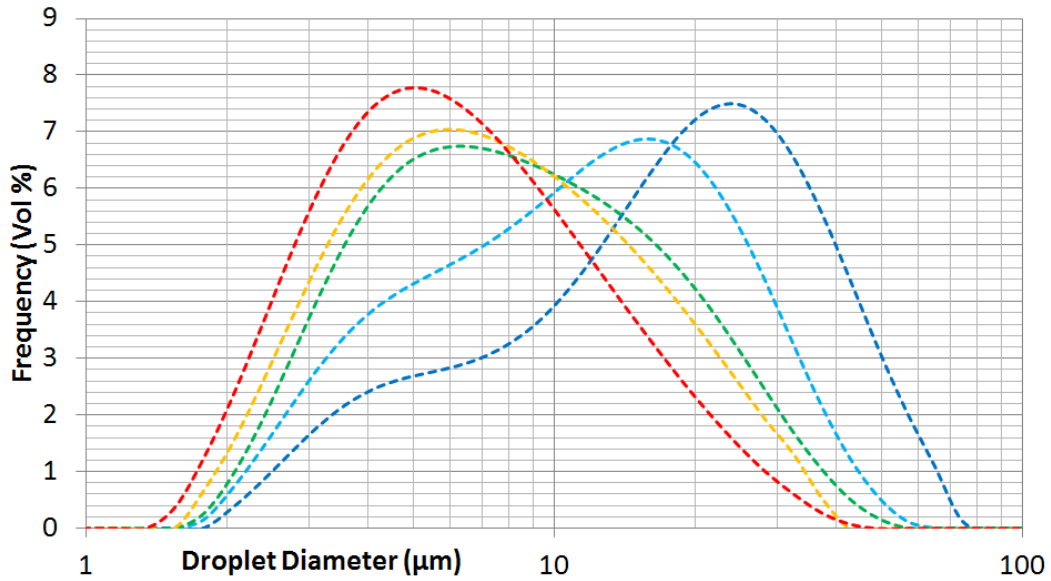
Figure 5.10: DSDs for 350 cSt silicone oil. Mass flow rates from 0.100 kg·s^{-1} down to 0.033 kg·s^{-1}. Orifice size code 0025.

Figure 5.10 shows that for 350 cSt oil as flow rate increased the droplet sizes decreased. This time however the distributions were not log-normal. Instead of the peak droplet size shifting smoothly towards the left (i.e. modal droplet size reducing) as flow rate increased, now the distributions appeared to skew towards the left by the right hand peak reducing in size and the left hand peak increasing in size, with no pronounced intermediate size peak for intermediate flow rates. This caused the distributions to be negatively skewed for low flow rates (large droplets) and positively skewed for high flow rates (small droplets). As stated before, this is an indication that different droplet breakage mechanisms may be in operation as the viscosity of the oil is increased from 10 cSt to 350 cSt.
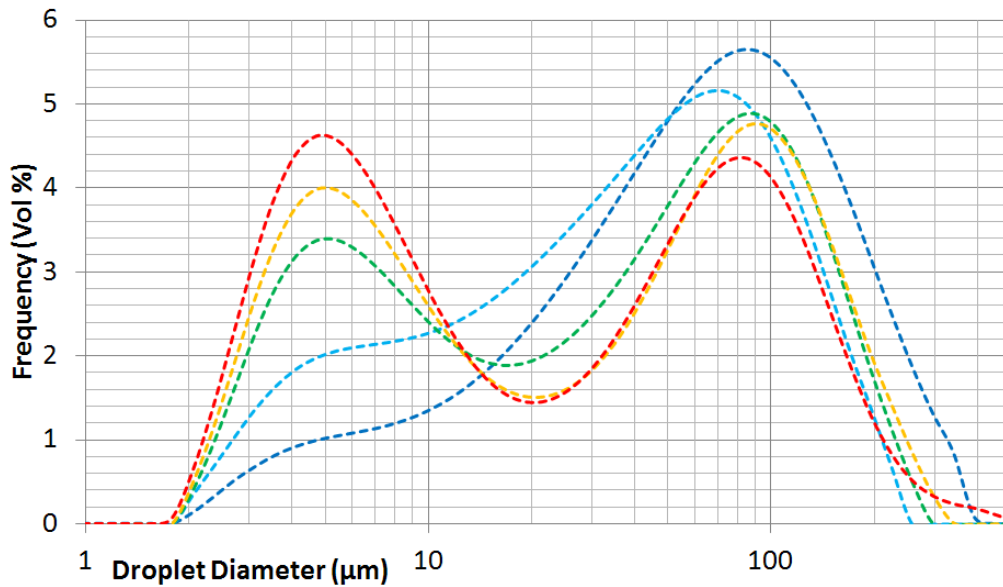
Figure 5.11: DSDs for 10 000 cSt silicone oil. Mass flow rates from
0.100 kg·s^{-1} down to 0.033 kg·s^{-1}. Orifice size code 0025.

Figure 5.11 shows that for 10 000 cSt oil although there is a droplet size reduction seen as mass flow rate increased, the distributions had become bimodal as viscosity increased further, and the main effect as flow rate increased was to reduce a peak on the right hand side for large droplets and to increase a peak on the left hand side for small droplets. This indicated a very different droplet break-up mechanism from oils of viscosity 10 cSt and below, and that possibly 350 cSt oil had a break-up mechanism intermediate between 10 cSt and 10 000 cSt cases.

Table 5.5: Values for d_{32} for different mass flow rates and oil viscosities. Oil at 10 wt% or less, SLES at 0.5 wt%, 0025 orifice.

Mass flow rate (kg/min)	Mass flow rate (kg/s)	Pressure Drop (kPa)	d_{32} (µm) for DC245 (3.8 cSt)	d_{32} (µm) for 10 cSt silicone oil	d_{32} (µm) for 350 cSt silicone oil	d_{32} (µm) for 10000 cSt silicone oil
2	0.033	503	5.24	6.08	11.17	24.75
3	0.050	1,140	4.88	5.18	8.14	15.63
4	0.067	2,022	4.21	4.66	6.59	12.20
5	0.083	3,187	3.36	4.27	5.99	10.97
6	0.100	4,598	2.42	3.01	5.15	9.63

In conclusion to this section: droplet sizes were seen to reduce when either increasing mass flow rate or reducing dispersed phase viscosity (see d_{32} values in Table 5.5). Lower viscosity oils had log-normal distribution, higher viscosity oils became skewed and then bimodal, indicating a different droplet breakage mechanism as viscosity increased. This is considered in Chapter 6.

Note: Table 5.5 above implies an orifice discharge coefficient of 0.64, which varies from the value 0.79 calculated from CFD results elsewhere in this thesis. The variation is likely to be due to the manufacturer stated orifice size (0.0025 in^2) being nominal, since the orifice size was determined by the positioning of two cuts made into a metal nozzle, whereas the CFD orifice size was measured directly in software.

5.5.2   Variables affecting average droplet size

The droplet size distributions were discrete, containing up to 100 size bins between 0.01 µm and 10 000 µm: summarizing this information into a small number of statistics was desirable. Three main types of statistic were considered: average droplet size, width of distribution, skewness of distribution. The average droplet size is considered in this section; the latter two in the next section.

With regards to average droplet size in emulsions from the pilot plant Sonolator experiments, three aspects are considered here: discussion of which Sonolator variables might affect average droplet size, choice of which statistic best describes the average droplet size, and illustration of the effect of different variables on the chosen droplet size statistic.

In Appendix 7 the choice of variable to represent flow rate was discussed. The choices available were: mass flow rate, jet velocity, pressure drop, power dissipation, epsilon (four variants given). This appendix concluded that pressure drop was the best variable to use for flow rate, since with the existing data set pressure drop factored out the effect of changes of geometry (e.g. orifice size) best.

In Appendix 8 the variables "oil weight fraction", "oil inlet condition" and "back pressure valve position" were found to not have a significant effect on d_{32}, which measured droplet size. The variable "orifice size" did not have any further effect on d_{32} except for its effect on influencing pressure drop over the Sonolator. In addition, the emulsification effects were found to be reproducible across multiple experimental rigs.

5.5.2.1   Variables with significant effect on d_{32}

Some remaining variables were found to have a significant effect on the final droplet size distribution, in particular on the average droplet size (d_{32}). These are illustrated below.

5.5.2.1.1   Effect of Pressure drop (representing flow rate)
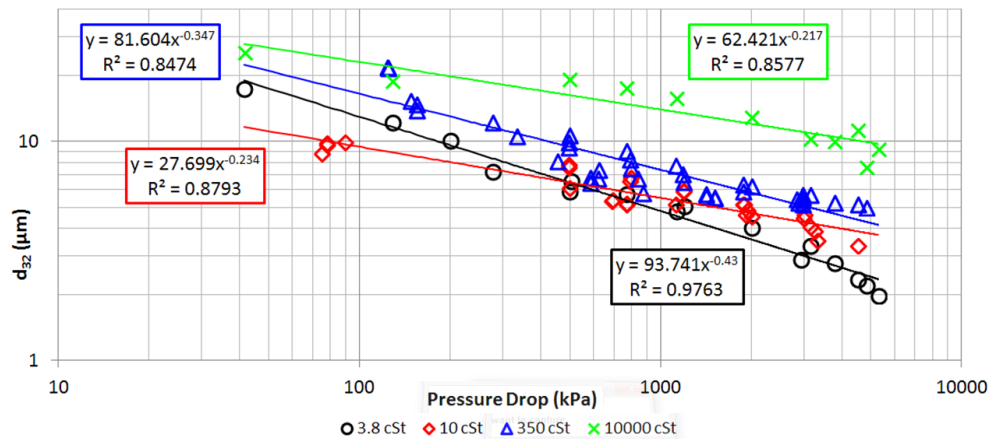
Figure 5.12: Graph of d_{32} vs pressure drop for four different oil viscosities. SLES constant at 0.5 wt%, multiple orifices and experimental conditions included.

The data displayed in Figure 5.12 showed that as the pressure drop increased the measured d_{32} generally decreased, with some scatter. Considering that these individual data points came from many different experimental conditions and orifices (as explained in the previous subsection on insignificant variables) the level of scatter was low enough to conclude that a real effect on d_{32} had taken place when pressure drop had increased; R^2 values were all above 0.84 for all four oil viscosity series. The scatter of the data about the trendline was random, indicating that power law models were appropriate between d_{32} and pressure drop. The slopes of the correlation curves varied from -0.21 to -0.43 between different oil viscosities, with no clear trend seen as oil viscosity increased. Explaining this effect will be left for the later discussion of theoretical explanations for the experimental data.

5.5.2.1.2   Effect of Oil viscosity
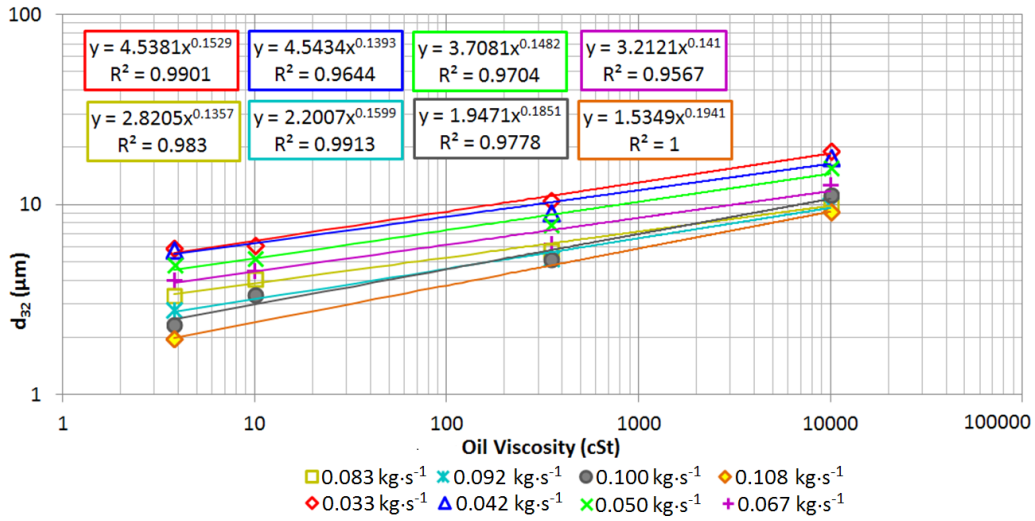
Figure 5.13: Graph of d_{32} vs oil viscosity for eight different mass flow rates.
SLES constant at 0.5 wt%, orifice size 0025 only.
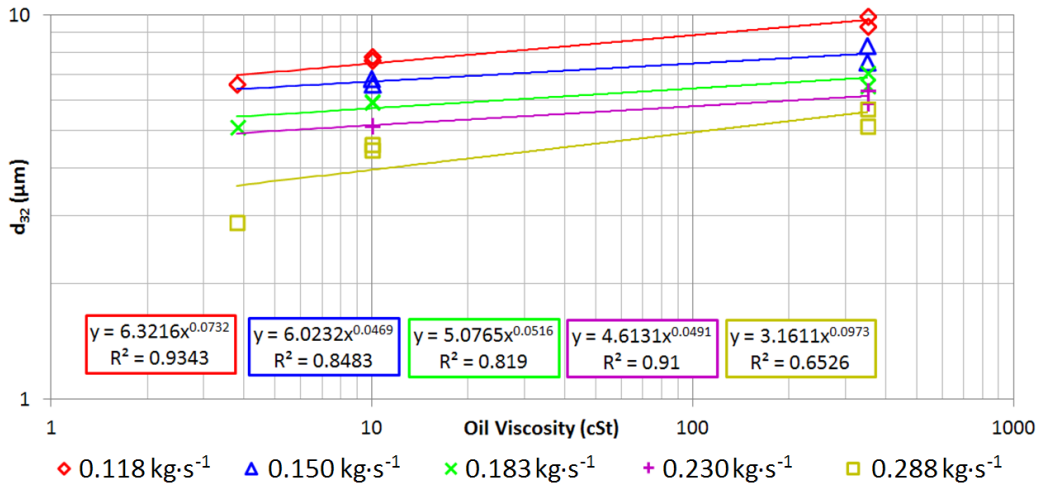
Figure 5.14: Graph of d_{32} vs oil viscosity for five different mass flow rates.
SLES constant at 0.5 wt%, orifice size 0080 only.

In Figure 5.13 and Figure 5.14 data series are seen for d_{32} vs oil viscosity, each for a range of different mass flow rates (within a similar experiment type), and for orifice sizes 0025 and 0080 respectively. In each it is seen that as oil viscosity increased, droplet size also increased. For the smaller orifice: coefficients of determination (R^2) were above 0.95, and slopes around 0.15 (see Ryan *et al* 2013). For the larger orifice: R^2 was above 0.81 for four out of five series, and slopes were between 0.046 and 0.098.

Discussion regarding the variation about these two data sets is reserved for later. It was clear at this stage, however, that oil viscosity affected the final droplet size significantly, but the effect was not as large as for pressure drop as evidenced by the lower slope magnitudes.

5.5.2.1.3 Effect of SLES weight fraction

For DC245 (3.8 cSt) and 350 cSt silicone oil, trials were run on the Sonolator with orifice size 0080, TMIX oil inlet condition. For DC245, SLES weight fraction was varied from 0.005 (0.5 wt%) down to 0.000003 (0.0003 wt%). For 350 cSt oil, SLES weight fraction was 0.005 (0.5 wt%) and 0.00013 (0.013 wt%) down to 0.000003 (0.0003 wt%).
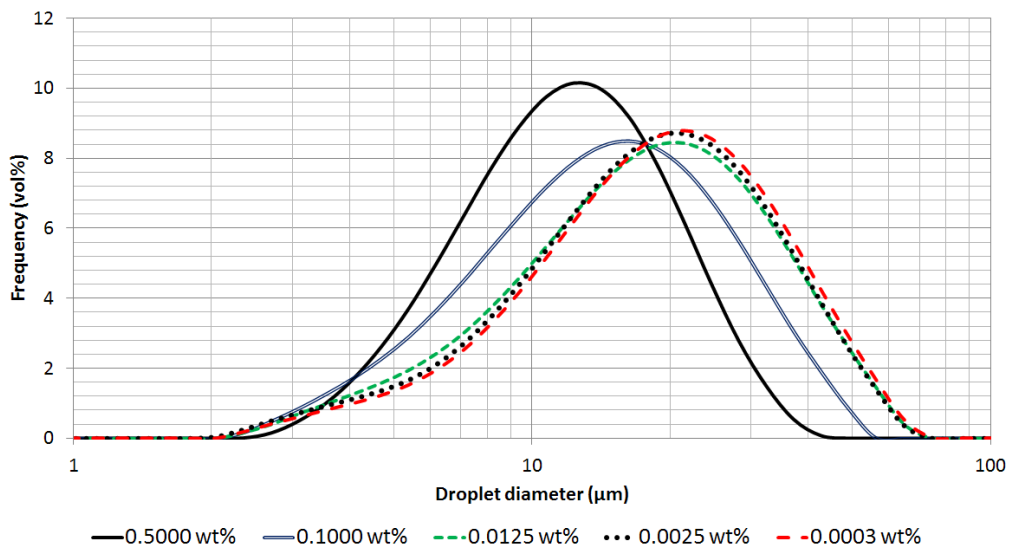
Figure 5.15: Droplet size distributions for variable SLES concentration, DC245 (3.8 cSt), 0.073 kg·s^{-1}, orifice size 0080, TMIX.
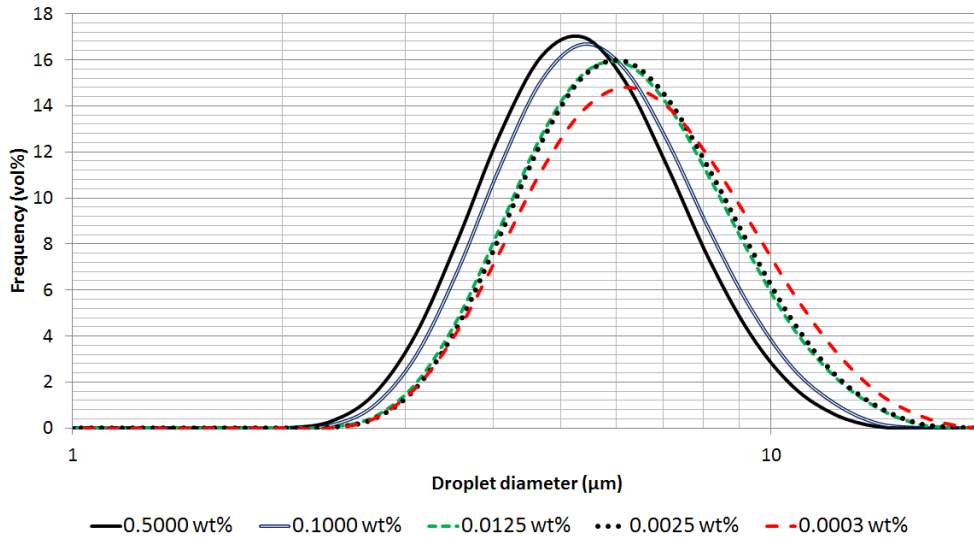
Figure 5.16: Droplet size distributions for variable SLES concentration, DC245 (3.8 cSt), 0.183 kg·s^{-1}, orifice size 0080, TMIX.

In Figure 5.15 for a low flow rate (0.073 kg·s^{-1}), droplet size distributions were seen to shift slightly to the right (larger droplets) as SLES concentration was lowered. The distributions stabilised when SLES was reduced to 0.0125 wt%. A similar shift was also found in Figure 5.16 for a higher flow rate (0.183 kg·s^{-1}). Here the change was less abrupt and did not seem to have stabilised even at 0.0003 wt%.
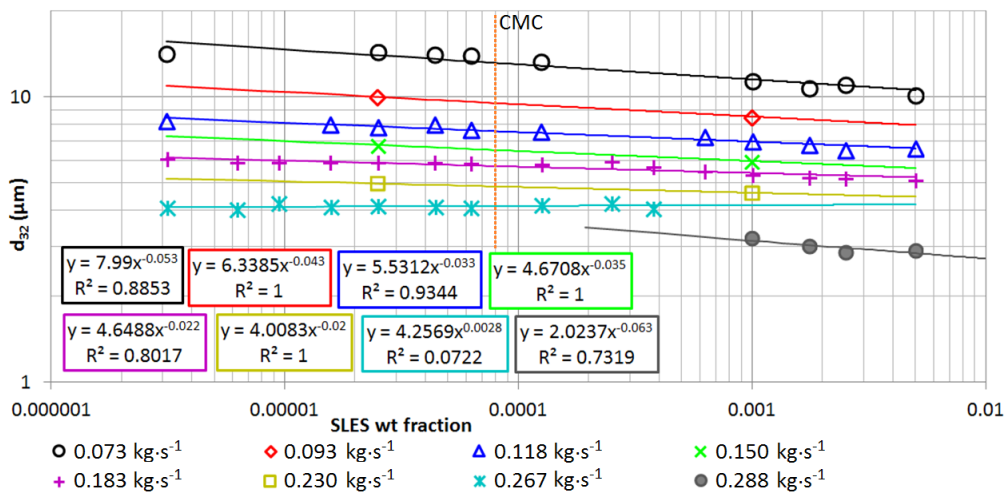
Figure 5.17: Graph of d_{32} vs SLES weight fraction for eight different mass flow rates. 3.8 cSt oil, orifice size 0080 only.

In Figure 5.17 eight different data series for different flow rates are shown, on a graph of d_{32} vs SLES concentration. Trendlines have been added. The slope of trendlines was low and slightly negative: from 0.003 down to -0.063. Scatter about these trendlines was low, as evidenced by generally high R^2 values. Different flow rates had different amounts of data; the biggest data set was 0.183 kg·s^{-1} with 15 different SLES concentrations, a slope of -0.022 and R^2 of over 0.8. Overall, for DC245 (3.8 cSt) there was a small but significant effect of SLES concentration on drop size.
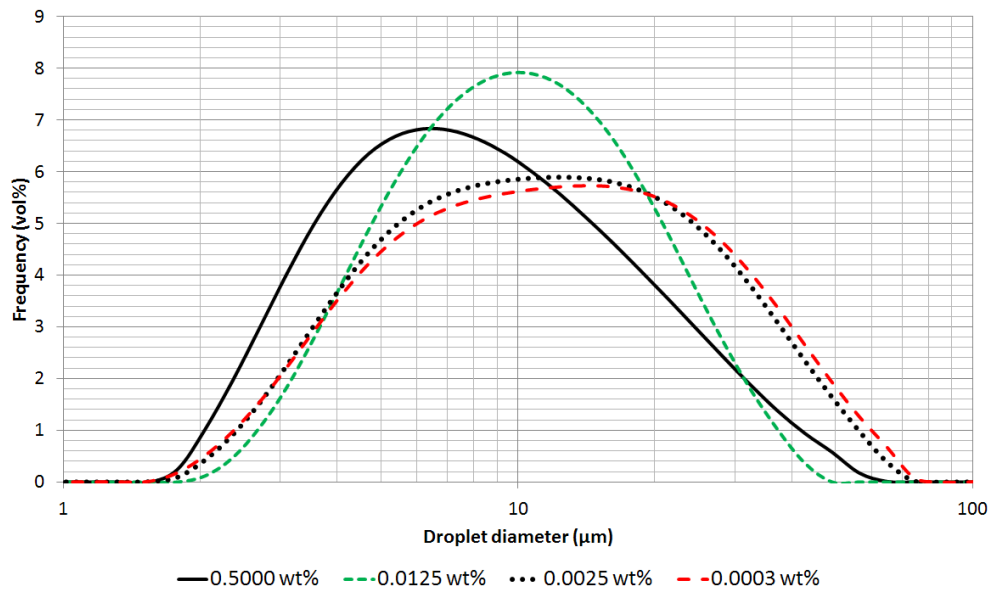
Figure 5.18: Droplet size distributions for variable SLES concentration, 350 cSt oil, 0.183 kg·s^{-1}, orifice size 0080 only, TMIX.

In Figure 5.18 droplet size distributions are shown for four SLES concentrations at 0.183 kg·s^{-1} with 350 cSt oil. The smallest droplets come from the highest SLES concentration (0.5 wt%). The distributions seemed to have stabilised when SLES was reduced down to 0.0025 wt%, indicating that below this concentration the SLES present did not significantly affect droplet breakage.
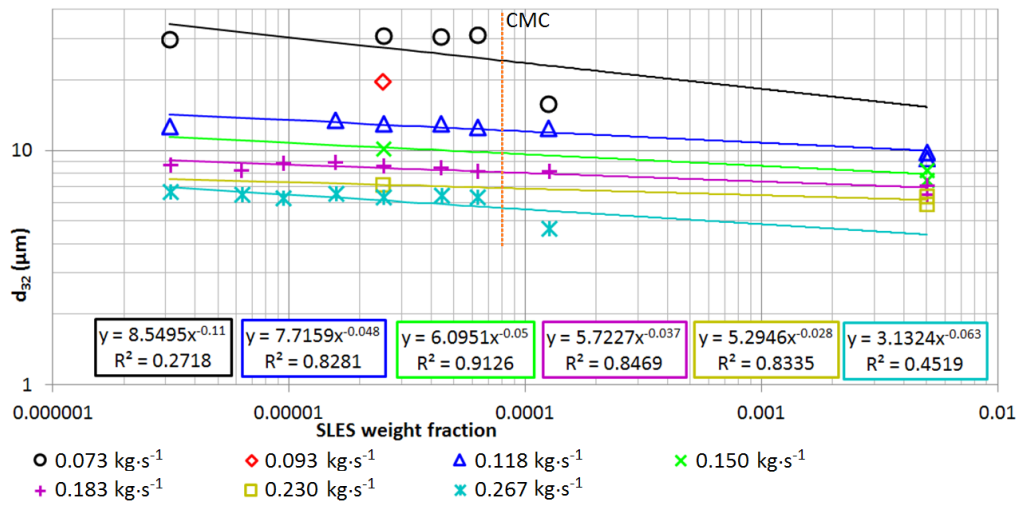
Figure 5.19: Graph of d_{32} vs SLES weight fraction for seven different mass flow rates. 350 cSt oil, orifice size 0080 only.

In Figure 5.19 the trends of d_{32} for varying SLES concentration for 350 cSt oil are shown. Only part of the SLES concentration range could be fully explored in the experimental time available. Power-law trendlines were fitted, with reasonably strong correlations except for two outliers (see below). Overall, there was a small but significant increase in droplet size as SLES concentration was lowered.
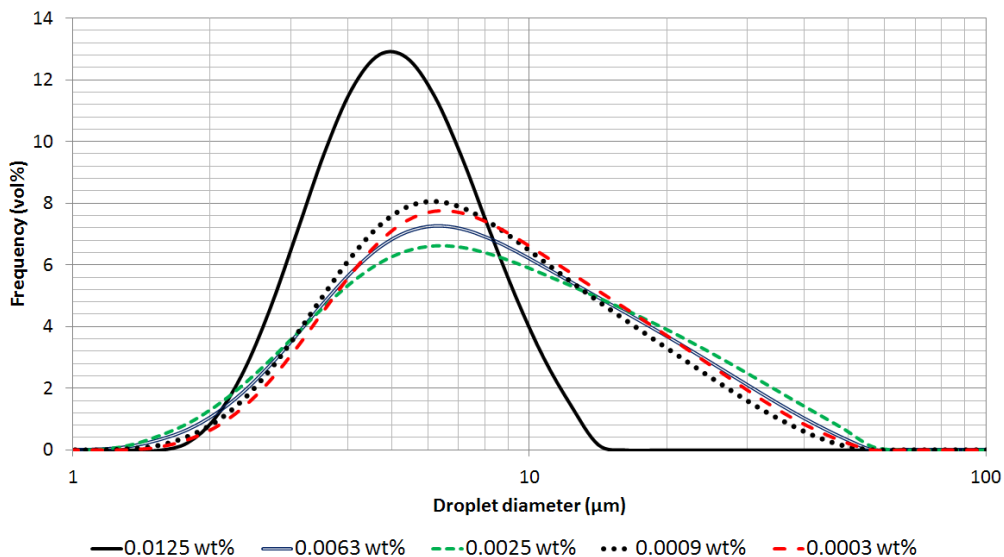
Figure 5.20: Droplet size distributions (illustrating outlier) for variable SLES concentration, 350 cSt oil, 0.267 kg·s^{-1}, orifice size 0080, TMIX.
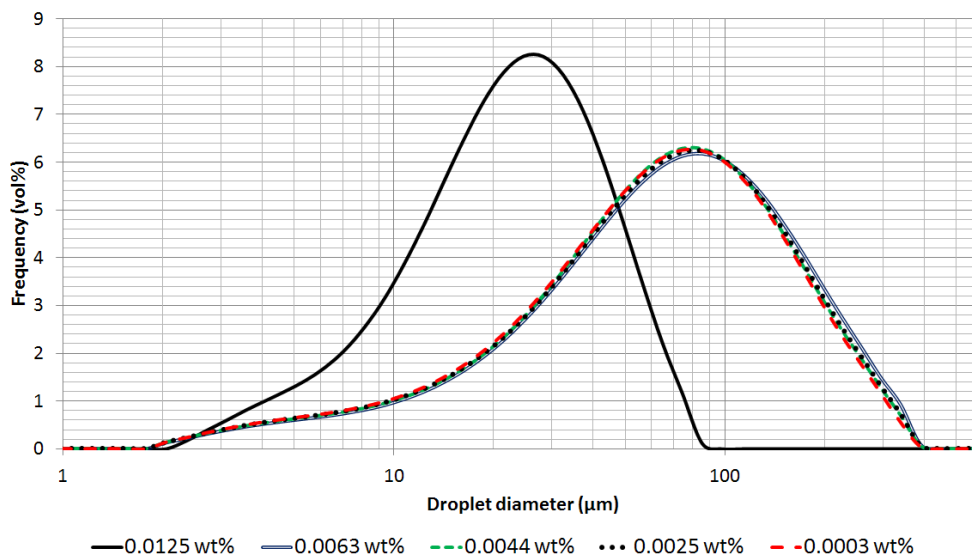
Figure 5.21: Droplet size distributions (illustrating outlier) for variable SLES concentration, 350 cSt oil, 0.073 kg·s^{-1}, orifice size 0080, TMIX.

In Figure 5.19 there were outliers for d_{32} values in the 0.267 kg·s^{-1} and 0.073 kg·s^{-1} flow rates. Figure 5.20 and Figure 5.21 examine the corresponding DSDs for the outliers (compared to some non-outlier DSDs). For both outliers, smaller droplets were produced with the SLES concentration above CMC (0.008 wt%), whereas for the rest of the data (in both flow rates) larger droplets were produced with SLES concentration below CMC. Interfacial tension during emulsification may therefore account for these outliers. Above the CMC interfacial tension is constant, but as SLES concentration is reduced below the CMC, interfacial tension rises steeply. Therefore, the non-outlier data were all produced at a higher interfacial tension, resulting in larger droplet sizes. Further experimentation is therefore required not to resolve the "outliers" but to explain why intermediate flow rates (e.g. 0.118 kg·s^{-1} and 0.183 kg·s^{-1} in Figure 5.19) did not show the same rapid change in droplet size, nor was it apparent for 3.8 cSt series in Figure 5.17.

5.5.2.1.4   Conclusion on significant variables affecting d_{32}

Pressure drop (as flow rate variable) was found to affect d_{32} the most, with power law indices between -0.21 and -0.43. Oil viscosity also had a significant effect, with power law indices between 0.13 and 0.20 for a small orifice (type 0025) and 0.046 to 0.098 for a larger orifice (type 0080). SLES concentration had a small but significant effect where decreased levels of surfactant appeared to increase droplet size. Questions remain about the large ranges of power law indices found for different data sets, and lack of rapid change in droplet size above/below SLES CMC for some experiments.

5.5.2.2   Conclusions on all variables with respect to d_{32}

A large number of variables which existed during Sonolator emulsification were discussed. Drop sizes in the "model emulsion" system were best represented by the d_{32} statistic. Flow rates were best represented by pressure drop, and significantly affected d_{32}, as did oil viscosity and SLES concentration to lesser extents. Other factors such as oil concentration (up to 10 wt%), oil inlet condition, back pressure valve position and orifice size did not significantly affect d_{32}, after any effect they had on pressure drop was factored out. Results were independent of the experimental rig used.

5.5.3   Span and Skewness

Other statistics are important to describe the droplet size distributions of emulsion droplets, other than just the d_{32} to represent an average drop size. How the distribution is shaped around that average is a question of industrial relevance.
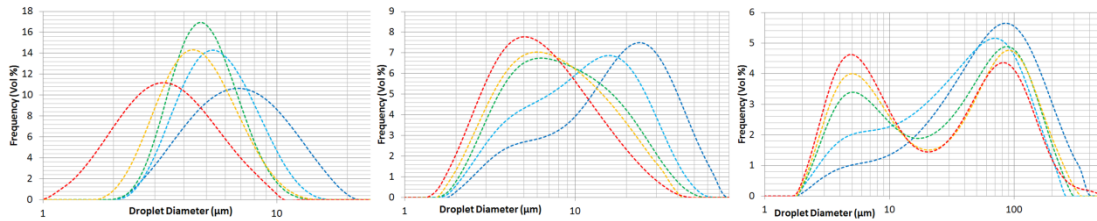
Figure 5.22: Droplet size distributions for five mass flow rates from
0.100 kg·s^{-1} (red) evenly spaced down to 0.033 kg·s^{-1} (blue) on orifice size
0025, for viscosities 10 cSt (left), 350 cSt, 10 000 cSt (right).

In Figure 5.22 the shape of droplet size distribution is compared for three viscosities, each illustrating five different flow rates. For lower viscosity oil (10 cSt) the distributions were approximately log-normal and unskewed, with some variation in distribution width. For 350 cSt oil there was a widening of the distribution and some skewness which varied according to flow rate. For 10 000 cSt the distributions were very wide and the distributions had become in some cases bimodal.

Statistics exist to quantify span (width, w) and skewness (s) in distributions in which a logarithmic size scale is appropriate:

$$w = \sqrt{\frac{d(90)}{d(10)}} \qquad \text{Eq. (5.1)}$$

(Reference: Hall 2012, Seville 1997)

$$s = \frac{\log_n \left(\frac{d(90)}{d(50)} \middle/ \frac{d(50)}{d(10)} \right)}{\log_n \left(\frac{d(90)}{d(10)} \right)} \qquad \text{Eq. (5.2)}$$

(Reference: Hall 2012, Vanoni 2006)

In Eq. (5.1) and Eq. (5.2) statistics for logarithmic span (w) and logarithmic skewness (s) are given. The $d(k)$ function is the diameter of the kth percentile droplet in

the volume-weighted droplet size distribution. (The logarithmic base (n) in Eq. (5.2) can be chosen freely (e.g. n = 10) since the skewness statistic can be proven independent of this choice.)
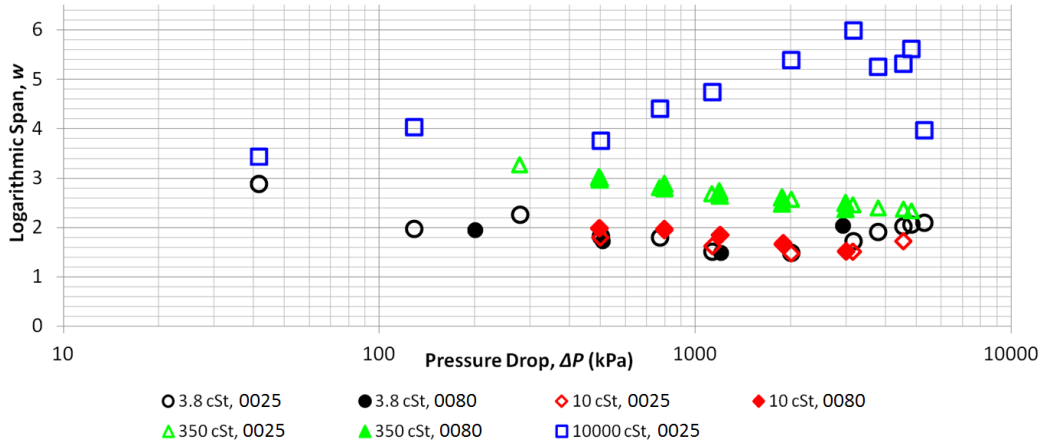
Figure 5.23: Graph of logarithmic span (*w*) vs pressure drop for four different viscosities of oil and two different orifice sizes

In Figure 5.23 the logarithmic span (*w*) is plotted against pressure drop for a range of oil viscosities and two orifice sizes. There was a clear effect of oil viscosity on *w*: for the low viscosity oils (DC245, 10 cSt silicone oil) the span was almost constant around 1.8, but for 350 cSt the span was larger, in the range 2.2 to 3.3, with a negative slope (against pressure drop). For more viscous oil, 10 000 cSt, span values were all above 3, and became even larger (up to 6) for high pressure drops. Orifice size, however, appeared not to influence the span of the droplet size distribution. The filled (orifice size 0080) series almost coincided with the hollow (orifice size 0025) series. This indicated that for 10 cSt oil, scaling up on pressure drop did not significantly change the width of the droplet size distribution.
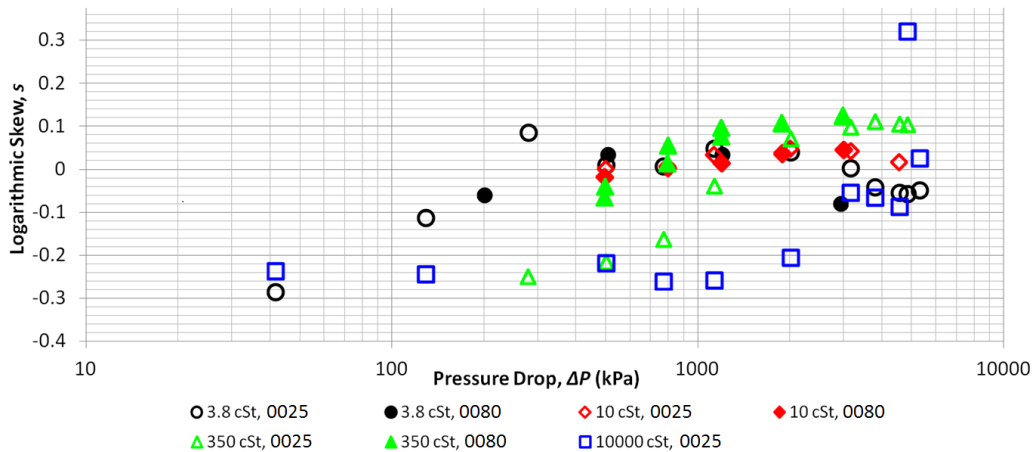
Figure 5.24: Graph of skew (logarithmic) vs pressure drop for four different
viscosities of oil and two different orifice sizes

In Figure 5.24 the corresponding values of skewness are plotted, for the same data as the previous graph. Again, the low viscosity oils, being approximately log-normal in shape, had skewness of about zero. However, 350 cSt data went from being negatively skewed at low pressure drop to positively skewed at high pressure drop. The 10 000 cSt data was also skewed in this manner, although it stayed negatively skewed for a much higher range of pressure drops, becoming positively skewed very quickly at a high pressure drop. Interestingly, although every other data series on this and the previous graph showed that orifice size did not affect span/skew, the 350 cSt data indicated that the orifice size did affect the skewness. However, the inlet method was also varied: for orifice size 0025 the data was PE (pre-emulsion) only, and for orifice size 0080 the data was TMIX or INJ. Further experiments ought to be done to find if skewness really does depend on either orifice size or oil inlet condition, or whether some other factor caused the data sets to deviate.

Overall; the data indicated that span increased only with higher oil viscosity (not with orifice size) and that skewness was zero for low viscosity oils and variable for higher viscosity oils, with patterns in skewness which did not follow a simple power

252

law according to increased viscosity or other variables. Moreover, these changes in span and skewness with increased oil viscosity indicated changes in droplet disruption mechanism as oil viscosity increased.

5.6   Conclusions

Emulsification in a pilot plant scale Sonolator has been characterised using emulsions of silicone oils (with four different viscosities between 3.8 cSt and 10 000 cSt) in water with SLES as surfactant. Droplet size distributions have been obtained for this system using a laser scattering measuring technique and using a variety of operating parameters.

The average droplet size was best characterised by d_{32} (out of d_{32}, d_{43}, volume weighted median and volume weighted modal droplet sizes) since d_{32} was the most repeatable measure of droplet size, and the industrial applications often had emulsion properties related to the effective surface area of the emulsion droplets.

After considering correlations of d_{32} with eight different flow rate variables (including mass flow rate and estimated turbulent intensity at the orifice), it was found that d_{32} correlated best with pressure drop. Oil viscosity was found to have a significant effect on d_{32}, and SLES concentration was also found to have a minor effect.

Insignificant variables for predicting droplet size included: back-pressure valve position, oil weight fraction (to 10 wt%), oil inlet condition (pre-emulsion, mixing at T-junction, injection), orifice size (when predicting d_{32} from pressure drop).

For fixed oil viscosity, given a specific pressure drop to create a specific droplet size, the distribution shape (span, skewness) was found to be constant, so it was not found possible to use other parameters to fine tune the droplet size distribution shape; this shape should be considered a characteristic of the Sonolator.

5.7   Nomenclature & Abbreviations

Symbol   Description

A_o Area of Sonolator orifice (m^2)

a_s Specific surface area (m^{-1}, or $m^2 \cdot m^{-3}$)

C   Constant in equation for epsilon

$d(k)$ Diameter of the kth percentile droplet in the volume-weighted DSD (m)

$f(x)$ number-weighted droplet size distribution (x being the diameter)

d_{32} Volume-surface (Sauter) mean diameter (m)

d_{43} Volume-weighted mean diameter (m)

d_{nm} Generalized moment-moment mean diameter (m)

L Characteristic length scale chosen in Sonolator (m) for ε calculations

M Mass flow rate ($kg \cdot s^{-1}$)

P Power dissipated in Sonolator (W)

ΔP Pressure drop over Sonolator (kPa)

Q Volumetric flow rate ($m^3 \cdot s^{-1}$)

s Logarithmic skewness of a droplet size distribution

v Jet velocity after Sonolator orifice ($m \cdot s^{-1}$)

w Logarithmic span of a droplet size distribution

x variable on horizontal axis of graph

y variable on vertical axis of graph

Greek Symbols

ε Epsilon, local specific turbulent energy dissipation rate ($W \cdot kg^{-1}$ or $m^2 \cdot s^{-3}$)

ρ Fluid density ($kg \cdot m^{-3}$)

Dimensionless groups

φ Dispersed phase volume fraction

C_D Discharge coefficient of Sonolator orifice

R^2 Coefficient of determination – near to 1 for a good correlation

Abbreviations

NNNN   Sonolator orifice size code; orifice of area 0.NNNN inches squared.

CMC   Critical micelle concentration (of a surfactant).

DSD   Droplet size distribution.

EngD   Engineering Doctorate (UK)

INJ   Oil inlet condition of being injected at the orifice.

PE   Oil inlet condition of aqueous pre-emulsion with 0.5 wt% SLES.

RI   Refractive Index.

SLES   Sodium laureth sulphate, or sodium lauryl ether sulphate.

TMIX   Oil inlet condition of mixing at a T-junction.

5.8   Acknowledgements

5.9   References

- Abismaïl, B., Canselier, J.P., Wilhelm, A.M., Delmas, H., Gourdon, C., (1999). "Emulsification by ultrasound: drop size distibution and stability", *Ultrasonics Sonochemistry*, **6**, 75-83.

- Baravian, C., Mougel, J., Caton, F., (2007). "Characterization of Dynamical Emulsification Process in Concentrated Conditions", *AIChE. Journal*, **53(8)**, 1994-2000.

- Brösel, S., Schubert, H., (1999). "Investigations on the role of surfactants in mechanical emulsification using a high-pressure homogenizer with an orifice valve", *Chem. Eng. Processing*, **38**, 533-540.

- El-Hamouz, A., (2007). "Effect of surfactant concentration and operating temperature on the drop size distribution of silicon oil water dispersion", *Journal of Dispersion Science and Technology*, **28(5)**, 797-804.

- Goloub, T., and Pugh, R. J., (2003). "The role of the surfactant head group in the emulsification process: Single surfactant systems", *Journal of Colloid and Interface Science*, **257**, 337-343.

- Hall, S., Cooke, M., El-Hamouz, A., Kowalski, A.J., (2011). "Droplet break-up by in-line Silverson rotor–stator mixer", *Chem. Eng. Sci.*, **66**, 2068-2079.

- Hall, S. (2012). "*Scale-up of Emulsification in Inline Rotor-Stator Mixers*", EngD Thesis, University of Birmingham, UK.

- Hinze, J. O., (1955). "Fundamentals of the Hydrodynamic Mechanism of Splitting in Dispersion Processes", *AIChE. Journal*, **1(3)**, 295.

- Leng, D. E., and Calabrese, R. V., (2004). "Immiscible liquid-liquid systems", *Handbook of Industrial Mixing: Science and Practice*, Paul, E. L., Atiemo-Obeng, V. A. and Kresta, S. M., (Eds.), John Wiley & Sons, Inc., Hoboken, New Jersey, USA.

- Lin, C.Y., Chen, L.W., (2006). "Emulsification characteristics of three- and two-phase emulsions prepared by the ultrasonic emulsification method", *Fuel Processing Tech.*, **87**, 309-317.

- Maa, Y.F., Hsu, C., (1996). "Liquid-liquid emulsification by rotor/stator homogenization", *J. Controlled Release*, **38**, 219-218.

- Padron, G. A., (2005). "*Effect of surfactants on drop size distribution in a batch rotor-stator mixer*", PhD Thesis, University of Maryland, College Park, MD, USA.

- Perry, R. H., Green, D. W., eds., (1998). "*Perry's Chemical Engineers' Handbook*". 7th ed., McGraw-Hill, New York.

- Ryan, D., Simmons, M. and Baker, M. (2013). "Investigating Dispersion and Emulsification Processes using a Sonolator Liquid Whistle", *Proceedings of 8th International Conference on Multiphase Flow*, 26-31 May 2013, Jeju, Korea.

- Seville, J. P. K., Tuzun, U., and Clift, R., (1997). "*Processing of particle solids*", Chapman and Hall, London, UK.

- Sonic Corp (2011). "*Sonolator Operating and Instruction Manual*", http://www.sonicmixing.com/Manuals/Sonolator_System_Manual.pdf, downloaded on 27th July 2013.

- Tcholakova, S., Denkov, N.D., Danner, T., (2004). "Role of surfactant type and Concentration for the Mean Drop Size during Emulsification in Turbulent Flow", *Langmuir*, **20(18)**, 7444-7458

- Tesch, S., Freudig, B., Schubert, H, (2003). "Production of Emulsions in High-Pressure Homogenizers − Part I: Disruption and Stabilization of Droplets", *Chem. Eng. Technol.*, **26(5)**, 569-573.

- Tjaberinga, W.J., Boon, A., Chesters, A.K., (1993). "Model Experiments and Numerical Simulations on Emulsification under Turbulent Conditions", *Chem. Eng. Sci.*, **48(2)**, 285-293.

- Vankova, N., Tcholakova, S., Denkov, N.D., Ivanov, I.B., Vulchev, V.D., Danner, T., (2007). "Emulsification in turbulent flow 1. Mean and maximum drop diameters in inertial and viscous regimes", *J. Colloid Interface Sci.*, **312**, 363-380.

- Vanoni, V. A., (2006). "*Sedimentation engineering*", American Society of Civil Engineers, Reston, Virginia, USA.

- Walstra, P., (1983). "Formation of emulsions", *Encyclopedia of Emulsion Technology*, Volume **1**, Becher, P., (Ed.), Marcel Dekker, New York, USA.

- Walstra, P., and Smulders, P. E. A., (1998). "Emulsion formation", *Modern Aspects of Emulsion Science*, Binks, B. P., (Ed.), The Royal Society of Chemistry, Cambridge, UK.

Chapter 6   EMULSIFICATION EXPERIMENTS – THEORY AND CORRELATIONS

6.1   Abstract

Droplet sizes were predicted using an empirical correlation in the form of a power law, using previous work to characterise emulsification in a Sonolator liquid whistle using silicone oils of varying viscosity emulsified with water and SLES surfactant. Indices in this power law were compared to experimental results in the literature for other emulsification devices, and to those predicted from the theories of droplet breakage in turbulent inertial flow. Scale up from pilot plant to factory scale was considered and a method developed to determine whether drop size scales on pressure drop or on epsilon with a large increase in orifice area.

6.2 Introduction and Literature Review for Droplet Breakage theories and experiments

In Chapter 5 results were presented for emulsification on a pilot plant Sonolator. These experiments characterised droplet breakage in the Sonolator for a range of flow conditions. The key outputs were droplet size distributions from each experiment, in particular average droplet size data for each set of flow conditions.

In this chapter the literature is first reviewed to find theories of droplet breakage and emulsification in different flow regimes; secondly the Sonolator is assessed to find which breakage regime ought to apply; thirdly a correlation is developed for the experimental data from Chapter 5; fourthly this correlation is compared to theoretical predictions for relevant breakage regimes, and fifthly scaling relations from pilot scale to factory scale are considered, in particular a method for determining whether droplet size scales up on pressure drop or epsilon for a large increase in orifice area; this was necessary since the emulsification data in Chapter 5 was not able to settle this question using the range of orifice sizes available.

Droplet breakage theory applied to the Sonolator had not previously been published by other authors, however preliminary results from this work were presented at ICMF 2013 conference, see Appendix 13 for a copy of the paper (Ryan, Simmons and Baker 2013).

6.2.1 Forces on a droplet and capillary / Weber number

A droplet in a flow can remain stable with the same diameter, or can be broken by the external forces from the flow. If stable, the internal cohesive forces are greater than the external disruptive forces; if broken, the external forces are greater than the internal

forces. Internal forces in emulsion droplets come from two main sources: interfacial tension, and viscosity which causes resistance to deformation.

External forces depend on the type of flow. In laminar flow, the external forces can be simple shear or hyperbolic. In turbulent flow the external forces depend on droplet size compared to the strong eddies at the Kolmogorov length scale; larger droplets are in the turbulent inertial breakage regime, and smaller droplets in the turbulent viscous regime, these are all defined below in the section on turbulent breakup.

The ratio of external disruptive forces to internal cohesive forces is a dimensionless quantity known as the capillary number (Ca) in laminar flow, or the Weber number (We) in turbulent flow and is a main factor determining the droplet breakage regime.

Experimental apparatus used to investigate these regimes includes: for laminar flow, pipes at low Reynolds number and roll mills; in turbulent flow stirred tanks have been investigated in depth, and more recently in-line mixers were investigated. The Sonolator is one such in-line mixer.

6.2.2 Laminar droplet breakage

Two-dimensional laminar regimes include: rotation, simple shear, hyperbolic flow (see Figure 6.1 below); three-dimensional laminar regimes also exist which incorporate varying degrees of shear and elongation. In these 2D or 3D laminar regimes the amount of droplet disruption is related to the velocity gradient (Walstra & Smulders 1998).

Figure 6.1:Comparison of 2D flow regimes, droplet shapes, velocity gradients and rotation rates (reproduced from Walstra 1983)

Actual droplet breakage mechanisms in laminar flow include: elongation followed by formation of two bulges at the ends with a narrowing waist which splits once to give binary breakage; binary breakage with satellite droplets occurs when the narrow waist separates in more than one place; elongation into a long thread (capillary) which breaks into many small and roughly equally sized droplets, deformation to a rugby-ball shape and tip streaming of many much smaller droplets from the pointed ends (Figure 6.2).
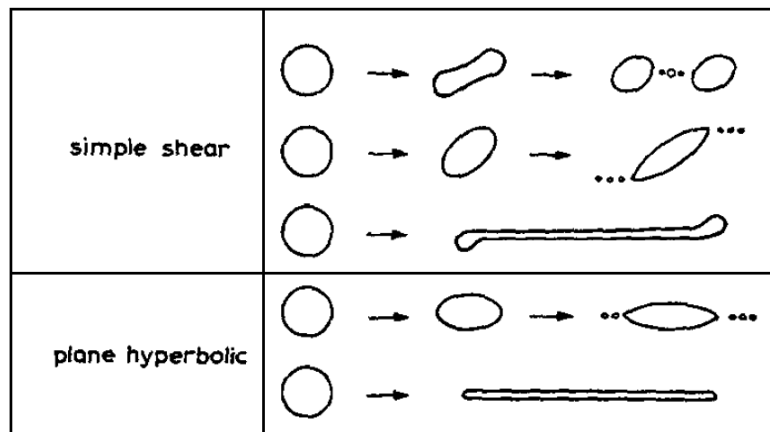
Figure 6.2: Illustration of droplet breakage mechanisms in laminar flow (reproduced from Walstra 1983)

The exact pattern of droplet breakage is affected by: viscosity ratio between dispersed and continuous phases; surfactant concentration compared to either the CMC or the amount needed to coat droplet interfaces; the rate of increase of deformation rate towards or over the critical deformation rate in laminar flow. In laminar flow, no droplet breakage occurs without a critical deformation rate being exceeded. Taylor (1934) produced photographs of many of these break-up modes in laminar flow using a four-roller apparatus.

6.2.3   Turbulent droplet breakage

Small-scale spatial structures in turbulence are difficult to measure directly. Taylor (1938) made an assumption known as the "frozen turbulence hypothesis": when the mean flow rate past a point is suitably high then velocities measured with high temporal resolution correspond to the small-scale spatial structure of the turbulence as it sweeps past the point. This is valid when the magnitudes of the turbulent fluctuations are much smaller than the mean flow rate, and helped to ascertain the energy spectrum in turbulent flow.

Kolmogorov (1941) studied the statistics of the turbulent energy cascade which transfers kinetic energy from large length scales to small length scales. This allows energy input at large length scales (e.g. forcing flow through a Sonolator orifice) to break oil droplets at small length scales, and gives rise to theories of droplet breakage in turbulence. He assigned microscales for length (l_e) and time (t_e) defined in Eq. (6.1) and Eq. (6.2) which characterise the size and duration of the smallest turbulent eddies. These microscales depend only on kinematic viscosity of the continuous phase (v_c) and local specific turbulent energy dissipation rate, epsilon (ε).

$$l_e = \left(\frac{\nu_c^3}{\varepsilon}\right)^{1/4}$$

Eq. (6.1)

$$t_e = \left(\frac{\nu_c}{\varepsilon}\right)^{1/2}$$

Eq. (6.2)

The largest turbulent eddies are at length scales (L) comparable with the flow geometry. Turbulence always has high Reynolds number, and $l_e << L$. For some intermediate length scales l such that $l_e << l << L$, Kolmogorov argued for "local isotropy", which is that the statistical properties of velocity caused by turbulent eddies of size l are the same at every point in a small (local) neighbourhood, and in every direction, and depend only on the energy input. Although the theory of local isotropy is very widely applied, due to simplifications which can be made in the mathematics, care ought to be taken since for at least some larger length scales in much real world apparatus, the turbulence is not completely isotropic. (Previous PIV studies of the Sonolator had indicated anisotropic turbulence directly after the orifice, see Chapter 2.)

Shinnar & Church (1960) state that l_e has been experimentally verified to be the eddy scale of maximum energy dissipation, hence smaller eddies do not exist due to the energy already having been dissipated; the energy cascade from large scales to small scales ends at (or around) l_e. This experimentally verifies that the constant in Eq. (6.1) is approximately unity.

Droplet breakage occurs when the external disruptive forces upon a droplet are larger than the internal cohesive forces. There are two main cases for modelling the external disruptive force, and two for the internal cohesive force. Regarding external forces, if the droplet is larger than l_e (e.g. $l_e << d << L$ for a breaking droplet of diameter d) then the droplet tends to be broken apart by pressure fluctuations from multiple turbulent eddies surrounding the droplet. This case is the turbulent inertial (TI) regime.

Alternatively, if the droplet is smaller than l_e (e.g. $d \ll l_e$) then the viscous shear inside a single eddy tends to be the dominating factor, hence this case is called the turbulent viscous (TV) regime. Regarding internal forces: for low-viscosity dispersed phases, the cohesive force comes from interfacial tension. For high-viscosity dispersed phases, the cohesive forces (or resistance to deformation) comes from the viscous force opposing deformation. These two regimes (low / high viscosity) can also be separated out by considering the deformation time compared to the characteristic time of the surrounding turbulent eddy (TV) or eddies (TI). For further discussion about these cases see Walstra & Smulders (1998), Padron (2005), Hall (2012).

Hence there are four turbulent break-up regimes: low (dispersed phase) viscosity TI, high viscosity TI, low viscosity TV and high viscosity TV. Each of these has a different correlation for final maximum (or d_{32}) droplet size as a function of flow variables such as: local specific turbulent energy dissipation rate (epsilon), continuous phase density, continuous phase viscosity, dispersed phase viscosity, interfacial tension. Such correlations assume that droplet breakage occurs to equilibrium, and the inputs are constant over time, e.g. constant density, interfacial tension, etc.

In the Sonolator after the orifice (where droplet breakage is believed to occur) the Reynolds number is in the turbulent range. Moreover, the droplet sizes are initially much larger than the associated Kolmogorov microscale, and stay larger throughout emulsification. Hence breakage occurs fully within the turbulent inertial (TI) regimes, and equations which deal with the TI regime are considered below.

$$d_{\max} = C \cdot \varepsilon^{-2/5} \rho_c^{-3/5} \sigma^{3/5} \qquad \text{Eq. (6.3)}$$

Eq. (6.3) was given by Hinze (1955) for inviscid TI droplet breakage. He assumed local isotropy in inviscid flow for dilute dispersed phase. This predicted $d_{\max}$ (maximum

stable droplet size) at equilibrium from dissipation rate (ε), interfacial tension (σ) and continuous phase density (ρ_c).

The dependence of d_{max} upon ε was a power law of index -0.4; for apparatus where ε is proportional to flow rate cubed (e.g. the Sonolator) the dependence of d_{max} upon flow rate (mass or volumetric) would therefore be a power law of index -1.2.

$$d_{max} = C \cdot \varepsilon^{-2/5} \rho_c^{-3/5} (\sigma + \beta \mu_D V')^{3/5} \qquad \text{Eq. (6.4)}$$

Davies (1985, 1987) modified Hinze's equation in Eq. (6.3) to model non-zero viscosity. This was done by modifying the critical Weber number during breakage to have two terms, one for interfacial tension (σ) and an extra term for dispersed phase viscosity (μ_D) scaled by a constant determined from experiment (β) and the size of local velocity fluctuations (V'), giving Eq. (6.4) above.

For low μ_D, Eq. (6.4) reduces to Eq. (6.3), which is therefore a general correlation for predicting equilibrium droplet size in low-viscosity TI breakage.

$$d_{max} = C \cdot \varepsilon^{-1/4} \rho_c^{-3/4} \mu_D^{3/4} \qquad \text{Eq. (6.5)}$$

For high μ_D, Eq. (6.4) simplifies by removal of the σ term. In addition, the fluctuating velocity V' can be modelled by $(\varepsilon d)^{1/3}$ in homogeneous turbulent flow. Using the diameter of interest ($d = d_{max}$) and substituting all these into Eq. (6.4) and solving for d_{max}, Eq. (6.5) above is obtained. Walstra & Smulders (1998) gave an equivalent equation for high-viscosity TI breakage (note their units of ε were W m^{-3} instead of W kg^{-1}, but the two equations become identical when converting all three input quantities into those of the same units). In this high-viscosity TI case, droplet size is expected to scale with $\varepsilon^{-0.25}$, which in the Sonolator is flow rate to the power -0.75.

Hence, Eq. (6.3) from Hinze (1955) is suitable for predicting droplet size in low-viscosity TI breakage, Eq. (6.5) from Walstra & Smulders (1998) is suitable for

predicting droplet size in high-viscosity TI breakage, and Eq. (6.4) from Davies (1985, 1987) gives a prediction of what should occur to droplet sizes between these two regimes.

In addition, when taking slopes of graphs of droplet size (d_{max}) *vs* dispersed phase viscosity (μ_D), for fixed ε, Davies equation predicts a slope of 0 at low viscosity, 0.75 at high viscosity, and a smooth interpolation from 0 to 0.75 between these two extreme cases. This prediction will be compared to experimental data below.

6.2.4   Existing droplet breakage experiments

Many of these droplet size correlations were developed to explain existing emulsification experimental data on droplet breakage. Note that turbulent inertial (TI) experiments are generally easier to carry out since the final droplet size is larger and requires less energy to access. In addition, TI emulsification is of more interest when considering the Sonolator, as demonstrated later in section 6.3.2. In Eq. (6.6) the general form of an individual correlation (or part of a correlation) is given. In the experiments discussed below the index is synonymous with the power A_i the variable must be raised to in order to be proportional to droplet size (d_{32}).

$$d_{32} \propto N^{A_1} \text{ or } Re^{A_2} \text{ or } \varepsilon^{A_3} \text{ or } We^{A_4} \text{ or } \mu_d^{A_4} \qquad \text{Eq. (6.6)}$$

Chen & Middleman (1967) investigated emulsification of dilute low-viscosity oils (< 25 cSt) in water using a stirred tank. The droplet size distribution (volume weighted) was normal. Mean and standard deviation of droplet sizes were used to find a distribution function. The mean used was d_{32}; the standard deviation was found to be constant across different (low-viscosity) oils and different agitation rates. The slope of d_{32} *vs* N (rpm) was found to be -1.14, close to the theoretical index of -1.2 for low viscosity TI break-up.

Arai, Konno, Matunaga & Saito (1977) investigated dispersion of polystyrene-o-xylene solutions (oil phase) in water using a stirred vessel. The viscosity range was 0.7 cSt to 1500 cSt. Their graphs of d_{32} vs N (rpm) had slopes of approximately -1.2 for low viscosity dispersed phase and -0.75 for high viscosity dispersed phase which agreed with the theory of turbulent inertial break-up for low and high viscosity oils. Also, their graph of d_{32} vs *oil viscosity* had slope zero for low viscosity, a gradual change (as per Davies 1985, 1987) to slope 0.75 for viscosities 100 cSt to 1000 cSt. Above 1000 cSt the slope reduced, which they explained by saying that very viscous droplets no longer had time to return to spherical in between perturbations from subsequent turbulent eddies; the cumulative stretching from these caused smaller droplet sizes than predicted by theory.

Calabrese, Chang & Dang (1986) investigated O/W dispersions in stirred tanks for varying oil viscosity (100 cSt to 10 000 cSt) and constant interfacial tension of 37.8 mN·m^{-1}; d_{32} was found to correlate to Reynolds number to index -0.76 to -0.77 for high viscosity, and index -1.18 to -1.38 for lower viscosity, as predicted for the TI regime. They stated that: trends in the droplet size distribution coincide with those of the mean droplet size, which was taken to be d_{32}; that droplet size distributions broaden as dispersed phase viscosity increases; $d_{max} \cdot d_{32}^{-1}$ is constant over varying energy dissipation rates, but increases as oil viscosity increases (presumably due to the broadening of the DSD). Low viscosity (<500 cSt) oil dispersions had DSDs that were normally distributed in number or in volume. High viscosity (>5000 cSt) oil dispersions had log-normal number distributions. The intermediate viscosity oil (1000 cSt) had a more erratic DSD which was harder to classify, being an intermediate case.

In their discussion, Calabrese *et al* (1986) quote Stephenson (1974), Collins & Knudsen (1970), Konno *et al* (1983), Ali *et al* (1981) and Chang *et al* (1981) in describing a spectrum of breakage modes which tended to be bursting at low oil viscosities (large number of daughter drops, narrow size distribution) towards stretching at high oil viscosities (a ligament is stretched which splits into a number of daughter drops with wider size distribution). In this way, observations of individual droplet break-ups in turbulence helped to explain the increase in DSD width as viscosity increases.

Wang & Calabrese (1986) extended the work of Calabrese *et al* (1986) to oil viscosities in the range 1 cSt to 1000 cSt and interfacial tensions in the range 1 mN·m^{-1} to 45 mN·m^{-1} using aqueous phases with differing methanol concentrations. For the highest viscosity oil (1000 cSt) interfacial tension was found to determine whether break-up was in a "moderate viscosity" or "high viscosity" regime; for all lower viscosity oils the "moderate viscosity" regime obtained.

Davies (1987) plotted data from a wide variety of emulsification devices onto a d_{32} vs epsilon graph. The devices included static mixers, agitated vessels, colloid mills, liquid whistles and valve homogenizers. The data points fell between two parallel lines of slope -0.4; this validated Eq. (6.3) for low viscosity TI; the constant in this equation thus had quite a narrow range across a large number of devices.

Ludwig, Flechtner, Pruss & Warnecke (1997) considered formation of emulsions in a screw loop reactor. The slope of d_{max} vs epsilon was -0.4 on a log-log plot, and similar patterns to Arai *et al* (1977) were found for the d_{max} vs oil viscosity plot: flat for low viscosity, sharp gradient around 100 cSt, levelling off at higher viscosities. This

shows that the droplet breakage mechanisms in turbulent inertial flow are independent of the exact device used.

Various authors have investigated dependence of droplet size on disperse phase viscosity in high pressure homogenizers (HPH). Quoted indices of dependence include: 0.7 (Pandolfe 1981), 0.4 (Karbstein 1994), 0.33 (Walstra & Smulders 1998), so there is a considerable discrepancy here. HPH are similar to the Sonolator in that emulsification in both devices is carried out by forcing a multiphase liquid through a small opening.

Hall (2012) considered existing results concerning batch and in-line rotor-stator devices: for batch devices Francis (1999) and Calabrese (2000) droplet size correlated with Weber number to the power -0.58, very close to the (low-viscosity TI) theoretical value of -0.6; Puel *et al* (2006) also obtained a Weber number index of -0.6; for in-line devices Koglin, Pawlowski & Schnoring (1981) obtained droplet size correlation with epsilon to power -0.4; other breakage regimes are also covered.

In general, there is good experimental evidence to support Eq. (6.3) for low viscosity droplet breakage in the turbulent inertial (TI) regime, and also Eq. (6.5) for higher viscosity breakage; Eq. (6.4) is supported in a limited range but with some evidence of a variation in slope for very high dispersed phase viscosities, and some variation in reported viscosity index for high pressure homogenizers.

6.2.5   Overall findings from literature

Literature was consulted concerning the theory of emulsification and existing experimental results. Although laminar flow can be used to break droplets, most industrial devices used to make emulsions (stirred tanks, colloid mills, valve homogenizers, etc.) use turbulent flow to break droplets efficiently to very small sizes. These sizes are predicted, up to a proportionality constant, by the theories of turbulent

break-up in TI and TV regimes, and depend on whether droplet viscosity is low or high. Experimental evidence generally shows good agreement with these theories in terms of the slopes of d_{32} vs *variable* graphs.

6.3   Determination of regime of droplet breakage in the Sonolator

The Sonolator creates emulsions in-line by passing a multiphase fluid through a pipe with a restriction consisting of a narrow orifice, along with a blade and back-pressure valve. Emulsification was thought to occur in the jet region directly after the orifice, with or without the blade present. The flow conditions, droplet sizes and droplet viscosities were examined in this region to determine whether the flow was laminar or turbulent; if turbulent, which of the four regimes described in the literature obtained.

6.3.1   Determination of Laminar or Turbulent regime

The Reynolds number (Re) in Eq. (6.7) was used to determine whether the Sonolator was in laminar or turbulent flow during the emulsification experiments. For flow regimes where $Re < 2300$, pipe flow is laminar; for $Re > 4000$ pipe flow is turbulent (Holman 2002). The Sonolator was similar to pipe flow, so it was expected that these same numerical ranges held for the onset of turbulence in the Sonolator.

$$Re = \frac{U \cdot L}{v_C}$$ Eq. (6.7)

Re was calculated from a characteristic velocity (U), a characteristic length scale (L) and the kinematic viscosity of the fluid (continuous phase, v_c). The Reynolds number was calculated both at the restriction caused by the narrow orifice and in the whole main chamber which was shaped like a pipe.

Table 6.1: Reynolds Number statistics summarizing 175 different pilot plant experiments. Average and standard deviation (SD) calculated using logarithms of original data.

	Min	Avg-SD	Average	Avg+SD	Max
Reynolds Number at Orifice	7,403	37,815	68,325	123,451	143,206
Reynolds Number in Main Chamber	471	3,336	6,856	14,091	18,853

Reynolds numbers were calculated across all pilot plant experiments, 175 in total, at both the orifice and the main chamber. These were summarized in Table 6.1 by their range, mean average and standard deviation (SD) about the mean. Values for *mean±SD* were provided to give a range for approximately 68% of the data, assuming *Re* values were normally distributed. Reynolds numbers were all above 7000 at the orifice. This implied that the flow at the orifice was fully turbulent. The jet after the orifice therefore contained turbulence. Since droplet breakage was thought to occur in and around this jet, breakage occurred in a turbulent region.

Moreover, in most experiments the Reynolds number remained above 2500 in the whole of the main chamber (average *Re* was 6856, average minus one standard deviation (log-scale) was 3336); the lowest main chamber *Re* recorded was 471. Reynolds numbers in the main chamber were calculated using a superficial velocity, which was an underestimate of the true local velocities; previous PIV results showed that local velocities in the Sonolator main chamber were an order of magnitude higher than the superficial velocity, due to the large amounts of recirculation and also turbulence convected downstream from the turbulent jet. Hence the Reynolds numbers in the main chamber were all larger than approximately 4000, and droplet breakage in the Sonolator was not in a laminar region, but in a fully turbulent region.

6.3.2   Determination of Turbulence Regime (TI or TV)

The Kolmogorov eddy length scale (l_e) given earlier in Eq. (6.1) was calculated from the continuous phase kinematic viscosity (ν_c, measured variable) and a derived variable to describe the turbulence, epsilon (ε), which was the local specific turbulent energy dissipation rate. For pilot plant experiments epsilon was not measurable, however it could be estimated from the orifice jet velocity and from a characteristic length scale. This length scale was chosen to be the square root of the nominal orifice area. The equation for epsilon (given on page 373 in Appendix 6) had the advantage of being based on measurable quantities, since jet velocity was volumetric flow rate divided by orifice area.

The literature describes turbulent inertial (TI) and turbulent viscous (TV) droplet breakage regimes: in the former the final droplet size is larger than the smallest turbulent eddy length scales as characterised by the Kolmogorov length scale (l_e); in the latter, final droplet size is smaller than l_e. (In Table 6.2 below, l_e is defined in Eq. (6.2), and d_{32} on p371 in Appendix 6.)

Table 6.2: Kolmogorov length scale (l_e) statistics summarizing 175 different pilot plant experiments. Average and standard deviation (SD) calculated using logarithms of original data.

	Min	Avg-SD	Average	Avg+SD	Max
Kolmogorov Length Scale (l_e, μm)	0.76	1.02	1.55	2.36	5.22
d_{32}/Kolmogorov Length Scale	2.2	3.3	4.7	6.6	13.9

In Table 6.2 statistics are given for the Kolmogorov length scales for all 175 pilot plant experiments. For each experiment the ratio $d_{32} \cdot l_e^{-1}$ was calculated: statistics for this are also given in the table. Generally, in TI breakage this ratio should be greater

275

than unity, and for TV breakage this ratio should be less than unity. Since this ratio was mostly in the range 3.3 to 6.6, and never went below 2.2, it was concluded that droplet breakage in these 175 pilot plant experiments in the Sonolator occurred in the turbulent inertial (TI) regime.

6.3.3   Determination of Viscosity Regime (Low or High)
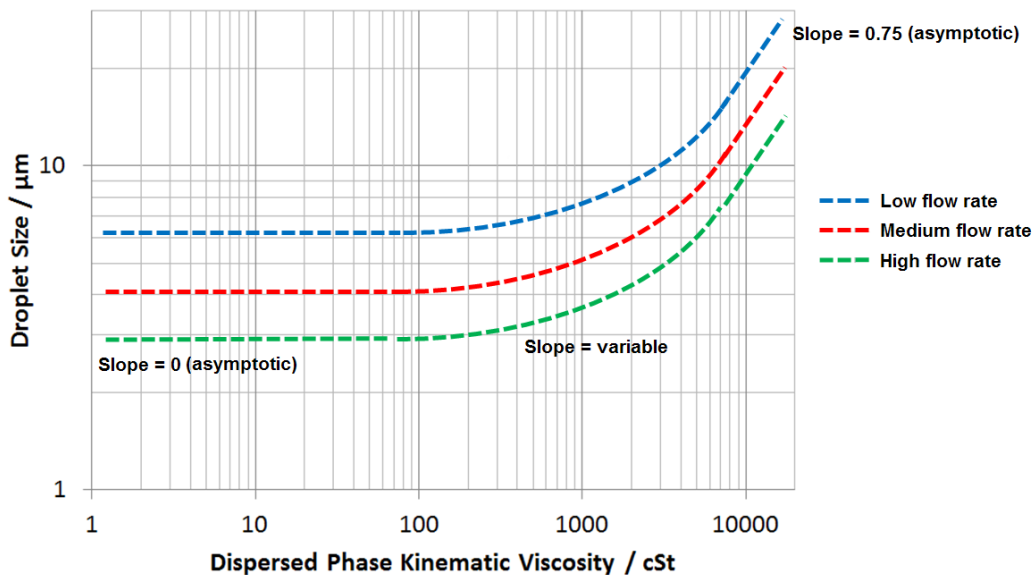
Figure 6.3: Schematic diagram of Davies' equation predictions for droplet size vs dispersed phase viscosity curves for low medium and high flow rates.

Davies' Eq. (6.4) reduces to two different asymptotic correlations for dependence of droplet size on ε; one correlation for low viscosity (dispersed phase) breakage, and a different correlation for high viscosity breakage, with smooth interpolation between them. These are illustrated in a schematic diagram in Figure 6.3 where a low-viscosity TI breakage regime has slope 0, and a high-viscosity TI breakage regime has slope 0.75. Later Davies' prediction of two distinct asymptotic regimes will be compared to experimental data.

Davies obtained his equation by considering how the internal cohesive forces in a droplet include both interfacial tension and viscosity related terms. During turbulent

droplet breakage, as the dispersed phase changes from low to high viscosity, the dominant internal cohesive force inside droplets changes from interfacial tension to droplet viscosity (i.e. viscous resistance to deformation). There were two dimensionless groups which were candidates to describe this change: a group derived from force ratios (Capillary number, Ca), and one derived from time ratios (T), both defined below:

$$Ca = \frac{\mu_{\mathrm{D}}V'}{\sigma} = \frac{\mu_{\mathrm{D}}\varepsilon^{1/3}d^{1/3}}{\sigma} \qquad \text{Eq. (6.8)}$$

In Eq. (6.4) from Davies (1987), the comparative effects of interfacial tension (σ) and dispersed phase dynamic viscosity (μ_{D}) as cohesive forces were included in the term $\sigma + \beta\mu_{\mathrm{D}}V'$. Ignoring the constant β, which Davies quoted as being of order unity, Eq. (6.8) compared the relative size of the interfacial tension and dynamic viscosity contributions to droplet cohesion, this is the Capillary number (Ca).

$$t_{\mathrm{def}} = \frac{\nu_{\mathrm{D}}}{\varepsilon^{2/3}d^{2/3}} \qquad \text{(TI regime)} \qquad \text{Eq. (6.9)}$$

(Reference: Walstra & Smulders 1998)

$$\mathrm{T} = \frac{t_{\mathrm{def}}}{t_{\mathrm{e}}} = \frac{\nu_{\mathrm{D}}}{\varepsilon^{1/6}d^{2/3}\nu_{\mathrm{C}}^{1/2}} \qquad \text{(TI regime)} \qquad \text{Eq. (6.10)}$$

An alternative dimensionless group, T in Eq. (6.10), was obtained by dividing the characteristic deformation time of a viscous droplet, t_{def} in Eq. (6.9), by the characteristic time scale of the smallest turbulent eddy, t_{e}, the Kolmogorov time microscale defined earlier in Eq. (6.2). The deformation time t_{def} could be calculated from ε, dispersed phase kinematic viscosity ν_{d} and droplet diameter (d). This diameter d was of the final droplet size, so d_{32} was substituted in here.
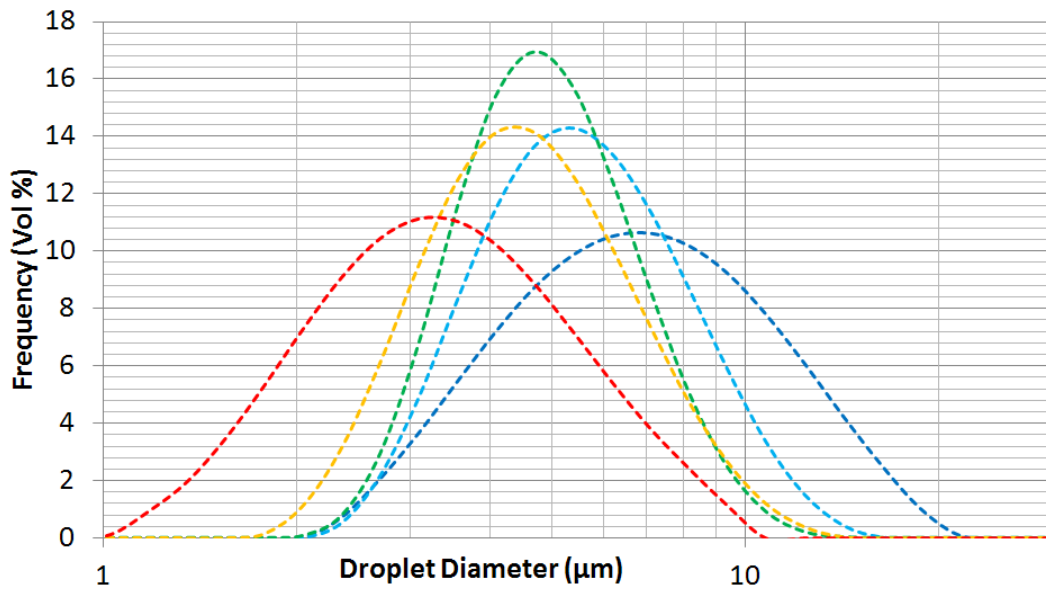
Figure 6.4: DSDs for 10 cSt silicone oil. Mass flow rates evenly spaced from 0.100 kg·s^{-1} (red, on left) down to 0.033 kg·s^{-1} (blue, on right). Orifice size code 0025.
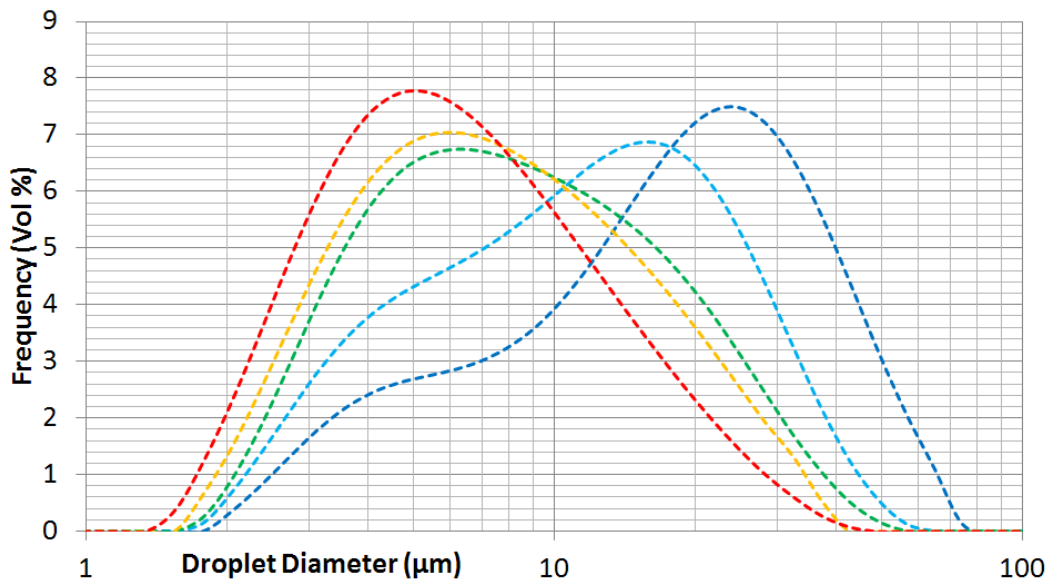
Figure 6.5: DSDs for 350 cSt silicone oil. Mass flow rates from 0.100 kg·s^{-1} down to 0.033 kg·s^{-1}. Orifice size code 0025.
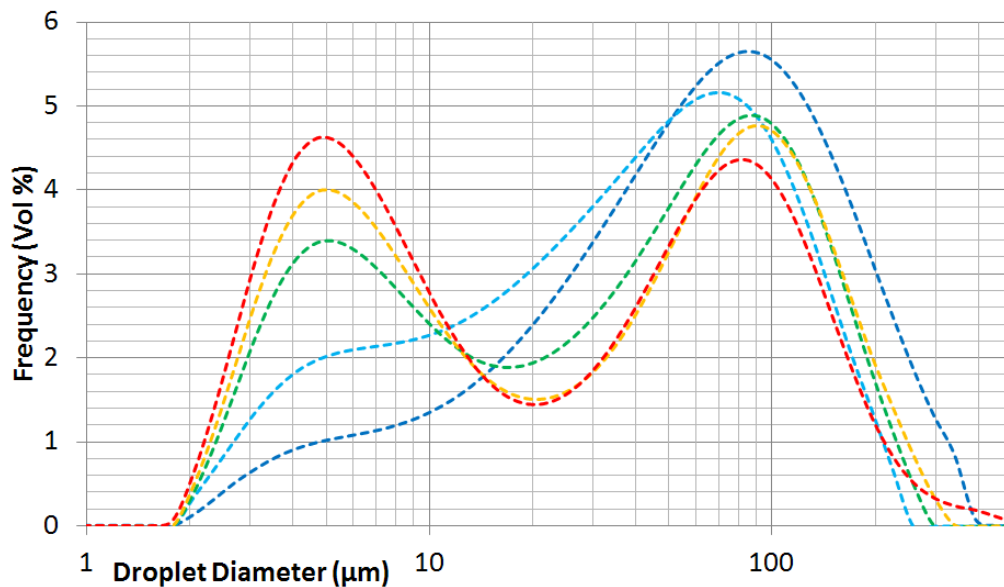
Figure 6.6: DSDs for 10 000 cSt silicone oil. Mass flow rates from 0.100 kg·s^{-1} down to 0.033 kg·s^{-1}. Orifice size code 0025.

Figure 6.4, Figure 6.5 and Figure 6.6 (repeated from Figure 5.9, Figure 5.10 and Figure 5.11) were typical droplet size distributions obtained for emulsification experiments on 10 cSt, 350 cSt and 10 000 cSt dispersed phases respectively. (Note: the orifice size codes are listed in Table 1.2.) A shift from narrow symmetric distributions towards wider skewed (or bimodal) distributions occurred as viscosity increased from 10 cSt to 350 cSt. The literature review described the transition from low-viscosity TI to high-viscosity TI in terms of DSDs becoming wider and less symmetric. Hence Figure 6.4 and Figure 6.5 provide qualitative experimental evidence that the TI regime change had occurred somewhere between 10 cSt and 350 cSt.

The quantities Ca and T were calculated for all 175 pilot plant experiments, separately for all four oil viscosities, and summarized in Table 6.3 and Table 6.4 respectively. (The interfacial tension used in Ca was taken from Hall *et al* (2011), see Table 5.1; DC245 and 10 000 cSt oil values were estimated at 11 mN·m^{-1}.) By comparing what happened to these two dimensionless groups as viscosity increased

from 10 cSt to 350 cSt, the regime change was described in terms of how dimensionless

numbers crossed a critical point.

Table 6.3: Statistics of Ca values (four different viscosities of oil)

Ca	Min	Avg-SD	Avg	Avg+SD	Max	Ratio Max/Min
DC245 (3.8 cSt)	0.08	0.20	0.29	0.43	0.53	6.32
10 cSt silicone oil	0.26	0.45	0.77	1.30	1.56	6.03
350 cSt silicone oil	10.9	19.0	27.7	40.6	57.5	5.28
10 000 cSt SO	255	609	1251	2567	2359	9.25

In Table 6.3 Ca was seen to be in the range 0.08 to 1.56 for the low viscosity oil

experiments, and 10.89 to 2400 for high viscosity. The transition from low-viscosity to

high-viscosity TI break-up occurred between 10 cSt and 350 cSt, which indicated a

transition point of Ca between 1.56 and 10.89. The geometric mean of 1.56 and 10.89

was 4.12, hence the critical point for Ca thus defined was approximately 4.

The ratio between the maximum and minimum values of Ca was calculated for

each oil viscosity. This ratio was in the range 5.2 to 9.3. It was also observed that ranges

of Ca for 3.8 cSt and 10 cSt overlapped. From this it was concluded that for fixed oil

viscosity Ca varied considerably, and a group which depended only on oil viscosity and

not on other variables (as far as possible) would be more useful for characterising the

effect of viscosity.

Table 6.4: Statistics of T values for four different viscosities of oil

Dispersed Phase	Min	Avg-SD	Avg	Avg+SD	Max	Ratio Max/Min
DC245 (3.8 cSt)	1.44	1.61	1.76	1.93	2.25	1.56
10 cSt silicone oil	4.08	4.16	4.79	5.51	6.60	1.62
350 cSt silicone oil	79.6	106.4	125.2	147.3	182.7	2.30
10 000 cSt SO	1948	1968	2428	2995	3905	2.00

In Table 6.4 T was seen to be in the range 1.44 to 6.60 for the low viscosity oil experiments, and 79.6 to 4000 for high viscosity. The transition from low-viscosity to high-viscosity TI break-up occurred between 10 cSt and 350 cSt, which indicated a transition point of T between 6.60 and 79.6. The geometric mean of 6.60 and 79.6 was 22.92, hence the critical point for T thus defined was approximately 23.

Moreover, since the ratios between maximum and minimum T for each viscosity were less than 2.5, the range of values of T for each viscosity varied by less than a factor of 2.5. Hence, T characterised the effect of increasing viscosity more specifically than Ca.

A question remained about why the critical points of both T and Ca were not equal to unity. (Shinnar & Church (1960) confirmed via experiment that l_e in Eq. (6.1) had constant approximately equal to unity, however critical Reynolds number for turbulence is very high, around 4000.) Davies (1987) introduced a constant β in front of the terms which contribute to Ca and showed it was device dependent and also dependent on non-Newtonian behaviour. Such dependencies mean critical Ca value could not always be equal to unity. For T, some researchers (Walsta & Smulders 1998) hypothesised that droplets break after multiple eddy encounters, each eddy further elongating the droplet. Hence the relevant eddy time in Eq. (6.10) should not be that of

an individual eddy, but that of multiple eddies. With a substitution $t_e \rightarrow N \cdot t_e$, for N separate eddies, the critical T would be restored towards unity from the value given earlier of 23.

6.3.4 Conclusions regarding droplet breakage regime

Conditions were examined in the Sonolator during droplet breakage in the pilot plant experiments described previously. The flow was always fully turbulent, so laminar droplet breakage regimes were discounted. Final droplet sizes were always above the Kolmogorov length scale l_e, so turbulent viscous (TV) regimes were discounted; this showed that during the pilot plant trials the turbulent inertial (TI) regimes always obtained. Both the low-viscosity and high-viscosity TI regimes were thought to be relevant to the Sonolator, based on the wide variation in droplet viscosity and the changes in droplet size distribution shape as viscosity increased. Two dimensionless numbers based on relevant forces and timescales respectively were examined in order to determine critical values for the transition between TI regimes in the Sonolator.

6.4   Development of correlation for Sonolator pilot plant data

This section moves temporarily away from considering theoretical droplet break-up mechanisms and regimes towards developing a correlation for the actual droplet sizes presented previously, after which this correlation will be compared to the known mechanisms.

In Chapter 5 the three variables which were found to significantly affect average droplet size (d_{32}) were: pressure drop over the Sonolator, dispersed phase viscosity and SLES concentration. Graphs of d_{32} vs these variables were plotted on log-log axes (Figure 5.12, Figure 5.13, Figure 5.14, Figure 5.17 and Figure 5.19). Each graph contained many series, one for each distinct set of experimental conditions. Each data series was approximately linear on the log-log graph. This indicated that a power law correlation to predict d_{32} from these three variables was appropriate.

Indices were calculated by averaging the individual slopes for each data series on the log-log graph, and weighting these by the number of points in each data series. Only data series with at least 2 distinct data points (for 2 different values of the variable) were used.

$$\frac{d_{32}}{1\ \mu\text{m}} = 57.12\ \left(\frac{\Delta P}{1\ \text{kPa}}\right)^{-0.4061} \left(\frac{\nu_{\text{D}}}{1\ \text{cSt}}\right)^{0.1119} w_{\text{SLES}}{}^{-0.03846} \qquad\qquad \text{Eq. (6.11)}$$

The correlation for droplet size is given in Eq. (6.11), where droplet size is d_{32}, pressure drop is ΔP, dispersed phase (oil) viscosity is ν_{d} and SLES weight fraction is w_{SLES}. Each constant or index is given to 4 significant figures. Note that the first three of these terms were dimensional; the correlation was non-dimensionalised by dividing the dimensional terms by the unit used in the calculations.
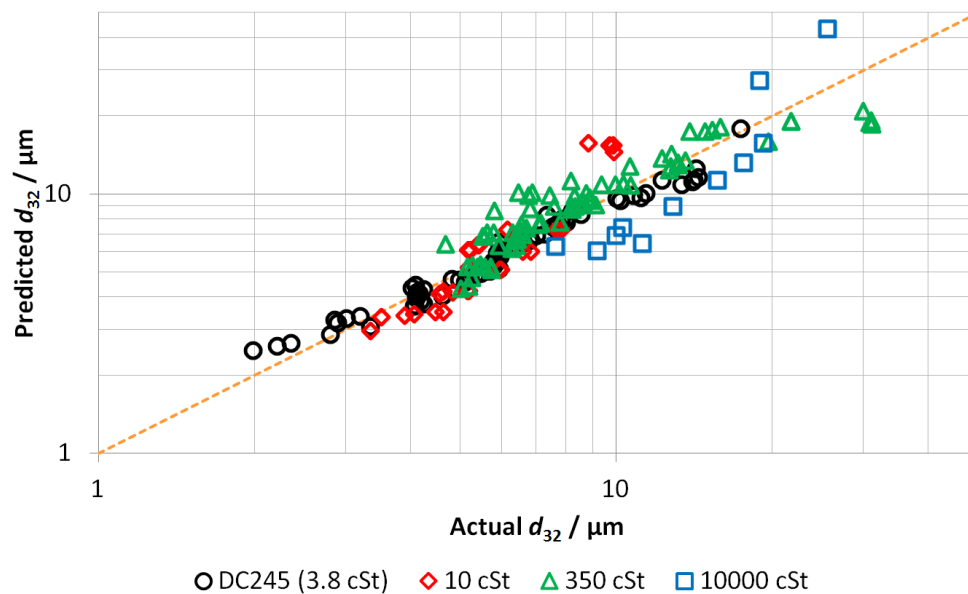
Figure 6.7: Graph of predicted vs actual droplet sizes for different oil viscosities. Line in red is equality between predicted and actual. $R^2 = 0.870$

Predicted droplet size is compared to actual droplet size in Figure 6.7. The data are found to cluster around the line of equality shown in orange. The spread of the data was elliptical around the line of best fit, indicating good agreement between predicted and actual values. This indicated that a single power law was appropriate to model droplet size for all viscosities. In particular, there was no significant difference in goodness of fit between the lower viscosity oils and the higher viscosity oils.

The coefficient of determination (R^2) was 0.870 indicating reasonable predictive capability. Sources of scatter remaining were expected to include: smaller effects of "insignificant" variables, errors in experimental or sample analysis techniques, impurities in water or other materials used, inherent randomness in droplet breakage processes.

On a previous graph of d_{32} vs $\varDelta P$ (Figure 5.12) indices of dependence were -0.430, -0.234, -0.347 and -0.217 for viscosities 3.8 cSt, 10 cSt, 350 cSt and 10 000 cSt respectively; these gave some discrepancies from -0.4061, the index for $\varDelta P$ in Eq.

(6.11). In addition, the indices were slightly different to the correlation previously found (Ryan *et al* 2013) which had pressure drop index -0.3 (instead of -0.4061), viscosity index 0.15 (instead of 0.1119), no index for SLES weight fraction since the data did not exist at that time. In order to understand these differences, the data sets of individual slopes (from which the average slopes were constructed) were examined.

6.4.1   Index of pressure drop
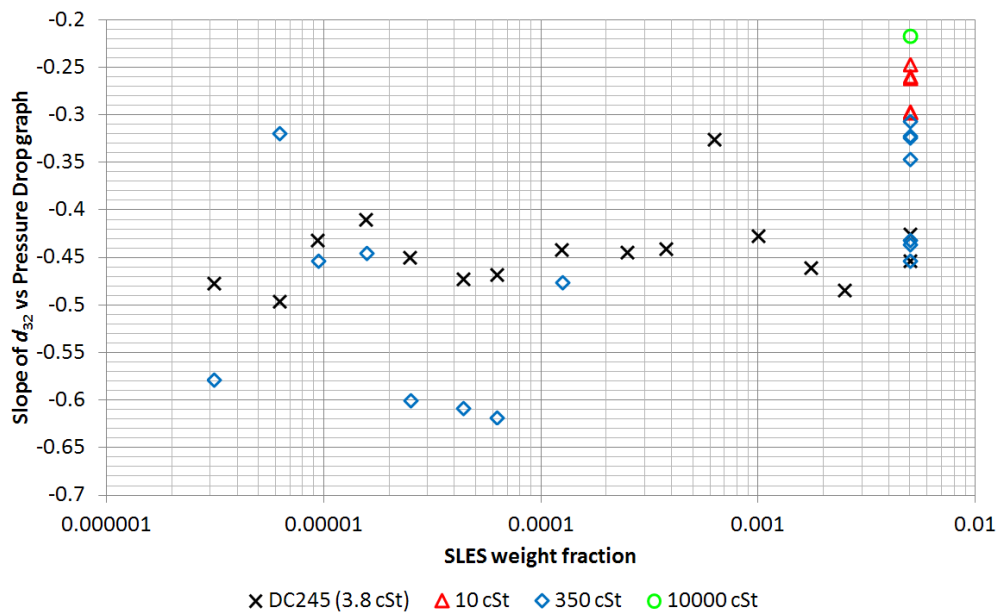
Figure 6.8: Graph of Slope (of d_{32} vs *pressure drop graph*) vs SLES weight fraction. Four different viscosity series illustrated.

In Figure 6.8 the slopes for d_{32} vs *pressure drop* were seen to be in the range -0.22 to -0.62. No consistent trend was seen either with viscosity or with SLES weight fraction. The reason why earlier work produced a pressure drop index of -0.3 was because the earlier data (SLES weight fraction of 0.005 only) showed slopes clustering around a higher value. The reason why the indices for four viscosities separately had three out of four greater than -0.4061 (see Figure 5.12) due to higher weightings of 0.5 wt% SLES data, with more data collected there and smaller slopes. Overall though, the slope of -0.4061 characterised the individual slopes in Figure 6.8 well.

6.4.2   Index of viscosity
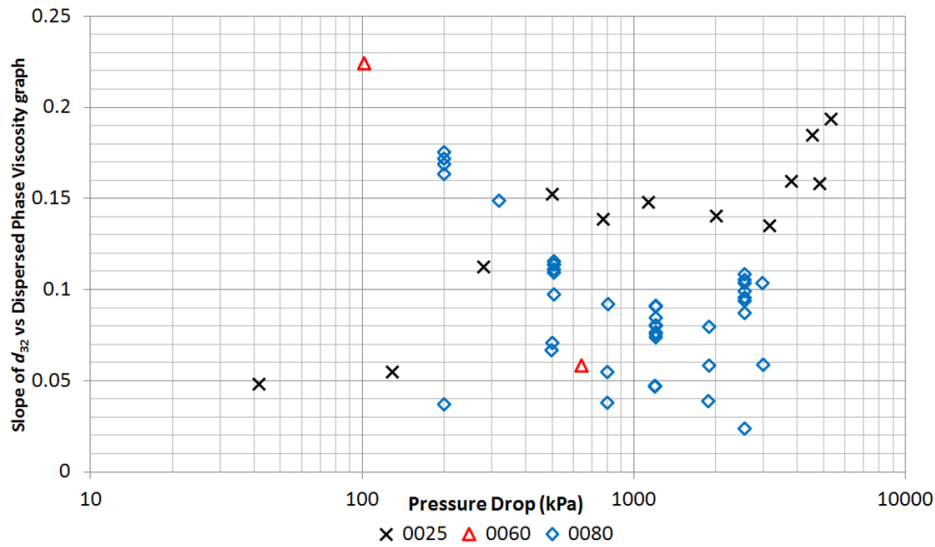
Figure 6.9: Graph of Slope (of d_{32} vs *dispersed phase viscosity*) vs Pressure Drop. Three orifice series illustrated.

Considering the slopes in Figure 6.9 which were averaged to give slope of 0.1119 for *viscosity* in the correlation for d_{32}, there was quite a lot of scatter vertically, with a range of 0.02 to 0.23. Previously in Figure 5.13 and Figure 5.14 a difference in slope was noted between a small orifice (type 0025) and a large orifice (0080). Now with all the slopes displayed, the picture was slightly more complex: the 0025 slopes started off small at low pressure drop and increased as pressure drop became larger, whereas the 0080 slopes started off large at low pressure drop and decreased thereafter. However, there was a large degree of scatter; this was seen clearly in the 0080 data series, which contained multiple data points for multiple SLES concentrations. (No consistent dependence of this slope on SLES concentration was found either.) So the best interpretation of Figure 6.9 was that slope (of d_{32} vs *viscosity*) was not dependent on either pressure drop or orifice size, but was noisy instead, and possessed a constant average of 0.1119 which represented it reasonably well.

6.4.3   Index of SLES concentration
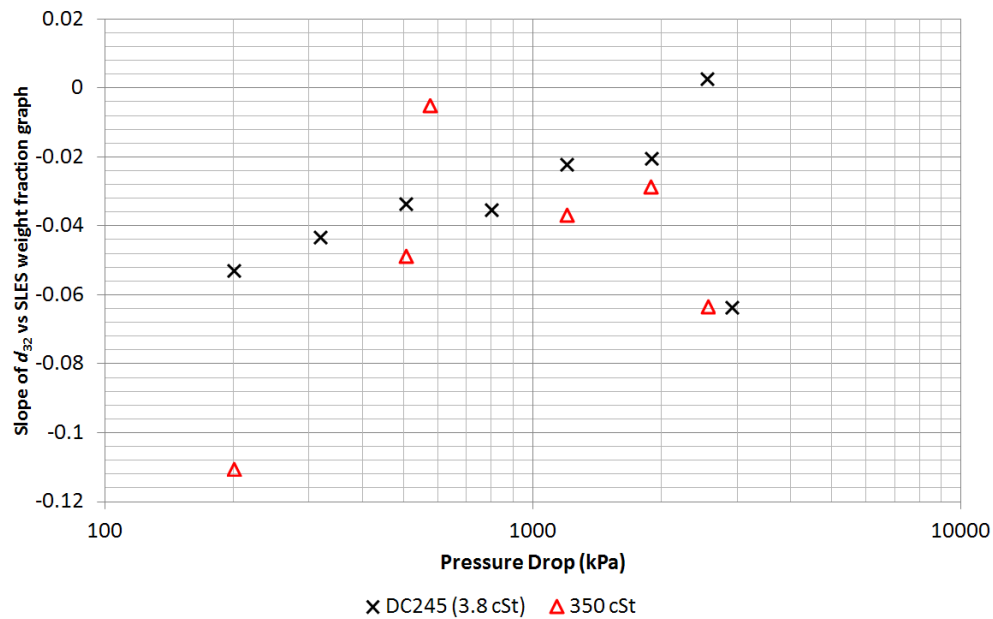
Figure 6.10: Graph of Slope (of d_{32} vs *SLES weight fraction*) vs Pressure drop. Two different viscosity series illustrated.

In Figure 6.10 the slopes which were averaged to give SLES concentration dependence of index -0.03846. No consistent trend was seen in this slope as pressure drop was varied, for either low viscosity (3.8 cSt) or high viscosity (350 cSt) oils. Although there were a couple of outliers and a medium amount of scatter, overall a constant slope of -0.03846 summarized the SLES dependence well.

6.4.4   Conclusion regarding slopes in correlation

After examining the data behind each of the three averaged slopes in the d_{32} correlation, no consistent trends were found to indicate that these slopes themselves vary according to another variable, hence the (constant) averaged slopes were taken as the best representative of sets of slopes data with a medium degree of scatter, and the correlation in Eq. (6.11) with constant powers and R^2 value of 0.870 was taken as the final prediction of droplet size from this work. The same correlation was suitable for

287

modelling droplet sizes with reasonably good accuracy for both low and high viscosity

dispersed phases.

6.5 Comparison of theoretical and empirical drop size correlations

In previous sections the theoretical dependencies of droplet size upon epsilon and viscosity was examined, and an empirical correlation was developed for actual Sonolator pilot plant data. These are now compared and contrasted below with literature-based correlations

Table 6.5: Theoretical and empirical drop size correlations

Author	Droplet size proportional to	Regime	Type	Pow(ε)	Pow(μ_d)
Hinze (1955)	$\varepsilon^{-0.4} \rho_c^{-0.6} \sigma^{0.6}$	TI (inviscid)	Theoretical	-0.4	0
Davies (1987)	$\varepsilon^{-0.4} \rho_c^{-0.6} \sigma^{0.6} (1+ \beta\mu_d V'\sigma^{-1})^{0.6}$	TI (all)	Theoretical	varies	varies
Walstra & Smulders (1998)	$\varepsilon^{-0.25} \rho_c^{-0.75} \mu_d^{0.75}$	TI (high dispersed phase viscosity)	Theoretical	-0.25	0.75
Pilot plant data correlation	$\varepsilon^{-0.2707} \mu_d^{0.1119} w_{SLES}^{-0.03846}$	Sonolator	Empirical	-0.2707	0.1119

In Table 6.5 the theoretical correlations for both TI regimes are presented next to the droplet size correlation obtained above. Note: empirical indices of kinematic viscosity (ν_d) and dynamic viscosity (μ_d) were the same since the fluid in these experiments was always water, with constant density; these were used respectively in Eq. (6.11) and Table 6.5 above. Also, in Eq. (7.26) pressure drop (ΔP) was shown to be generally proportional in the Sonolator to epsilon $\varepsilon^{2/3}$ hence the empirical result in Table 6.5 gave a droplet size proportionality of $\Delta P^{-0.4061}$.

In previous work based on a smaller data set Ryan *et al* (2013) reported epsilon index of -0.2 and viscosity index of 0.15 – the results presented here supersede those and are expected to be more general, adding a term for surfactant concentration.

The theoretical and experimental results (except Davies 1987) were in the form of power laws. These were convenient because the effect of each term was independent, i.e. in the power law model epsilon had an independent effect on droplet size from the effect of viscosity. Power laws were also convenient since, when comparing them, it was only necessary to compare how the indices for the same variable changed.

The epsilon (ε) indices in Table 6.5 were compared: the empirical index of -0.2707 was in the range of -0.4 to -0.25 for theoretical low and high viscosity TI break-up. This empirical index indicated that the regime was closer to high viscosity TI.

The dispersed phase viscosity (μ_d) indices in Table 6.5 were compared: the empirical index of 0.1119 was in the range of 0 to 0.75 for low and high viscosity TI break-up. (Note that Hinze (1955) used an assumption of inviscid flow, however his assumptions would also be true for low viscosity dispersed phase, where viscous forces << interfacial forces. In that case, the index of dependence on the dispersed phase viscosity would be zero.) This empirical index for viscosity indicated that the break-up regime was closer to low viscosity TI.

Two other pieces of evidence were considered: firstly that between Figure 6.4 and Figure 6.5 there was clear evidence for a change in droplet breakage mechanism between 10 cSt and 350 cSt; secondly, that in Eq. (6.11) and Figure 6.7 a single correlation was found suitable to predict droplet sizes in both regimes, with no obvious "kink" indicating two different underlying regimes.

Hence the Sonolator's behaviour was within the bounds provided by low and high viscosity TI theories, however it did not consistently fit either model, nor seem to fit either model at different times under different working conditions. Instead, it appeared to occupy an intermediate regime.

Walstra & Smulders (1998) stated that the droplet breakage regimes described in literature were idealised situations, and that intermediate regimes may occur in practice. Between low and high viscosity TI regimes, it is clear that in reality both interfacial tension and viscous resistance to deformation both act simultaneously as cohesive forces in a droplet. Also, between TI and TV regimes a droplet not too much bigger than l_e might undergo both turbulent inertial break-up from small eddies, and some degree of turbulent viscous break-up from larger eddies which are all simultaneously present.

Other assumptions which were present in the idealised theories did not necessarily hold in Sonolator experiments. The theories assume that droplets break to equilibrium, since the theories had in mind systems like stirred tanks where the conditions are held for hours at a time; however in the Sonolator the multiphase fluid traverses the Sonolator in a few tenths of a second, so breakage may well not continue to completion. Experimental time to investigate this possibility was lacking, and remains as further work.

Also assumed is that turbulence is isotropic: the Sonolator has a highly turbulent flattened jet in which all three components of turbulence, in terms of standard deviations of velocity in the three Cartesian directions, are different to each other. However, the theories in the literature only address the situation of isotropic turbulence

due to the large mathematical simplifications in such an assumption. Further work is indicated in understanding non-isotropic systems from a theoretical standpoint.

Given that the Sonolator data best fits the power law correlation given in Eq. (6.11), and that the pressure drop (or epsilon) index is intermediate between low and high viscosity TI theoretical values; examination of the indices for SLES concentration and viscosity remains.

Droplet size had a small dependence on surfactant (SLES) concentration, of empirical index -0.03846, for values of SLES weight fraction in the range 0.0003 wt% to 0.5 wt%. The CMC for SLES was estimated at 0.008 wt%, so the range of surfactant concentrations investigated was both above and below the CMC. From smallest to largest SLES concentrations was an increase in SLES concentration of 1600 times. The empirically estimated effect on droplet size of this increase in SLES concentration was therefore to change droplet size by a factor of $1600^{-0.03846} = 0.753$ times. Theoretically, interfacial tension should decrease from the oil-water value of 38 mN·m^{-1} (quoted from Calabrese *et al* 1986) to the oil-SLES-water value of around 11 mN·m^{-1}, which is a factor of 0.2895 times. The interfacial tension index was 0.6 (for low-visc TI) or 0 (or hi-visc TI), hence droplet size should change by $0.2895^{0.6} = 0.475$ times to $0.2895^{0} = 1$ times (unchanged). Since $0.475 < 0.753 < 1$, the effect of surfactant concentration was in the range predicted by theory via the interfacial tension term.

However – measured interfacial tension of liquids at rest varies according to surfactant concentration not by a power law, but an "S" shaped curve (level, then change in height, then level again), with the largest effect of changing surfactant concentration around the order of magnitude of the CMC. In Figure 5.17, no such sudden effect on d_{32} was seen as SLES concentration increased through 0.008 wt%

(0.00008 SLES weight fraction); instead of S-shaped series, the series looked straight, and power laws were indicated.

The theoretical models in the literature assume that interfacial tension is a constant. Behaviour such as dynamic interfacial tension varying as interfaces stretch during droplet breakage, becoming depleted in surfactant, and then surfactant later adsorbing from solution onto the depleted interfacial areas to restore interfacial tension to its initial level; droplet breakage models which incorporate such details are lacking in the literature. It is hoped that these results of power law dependency on surfactant concentration stimulate the development of new theoretical explanations.

Droplet size dependency upon dispersed phase viscosity (see Figure 5.13 and Figure 5.14) was also a power law with fixed viscosity index of 0.1119 across a wide range of viscosities. This conflicted with the most accepted theoretical explanation, Davies (1987) in Eq. (6.4), which covers the whole of the TI regime, including intermediate viscosities, and predicts an effective viscosity index varying between 0 and 0.75. The experimental literature sometimes verified Davies' equation across all viscosities (Wang & Calabrese 1986), sometimes verified it only for below 1000 cSt (Arai *et al* 1977, Ludwig *et al* 1997) and sometimes provided constant but different indices (0.7 (Pandolfe 1981), 0.4 (Karbstein 1994), 0.33 (Walstra & Smulders 1998)).
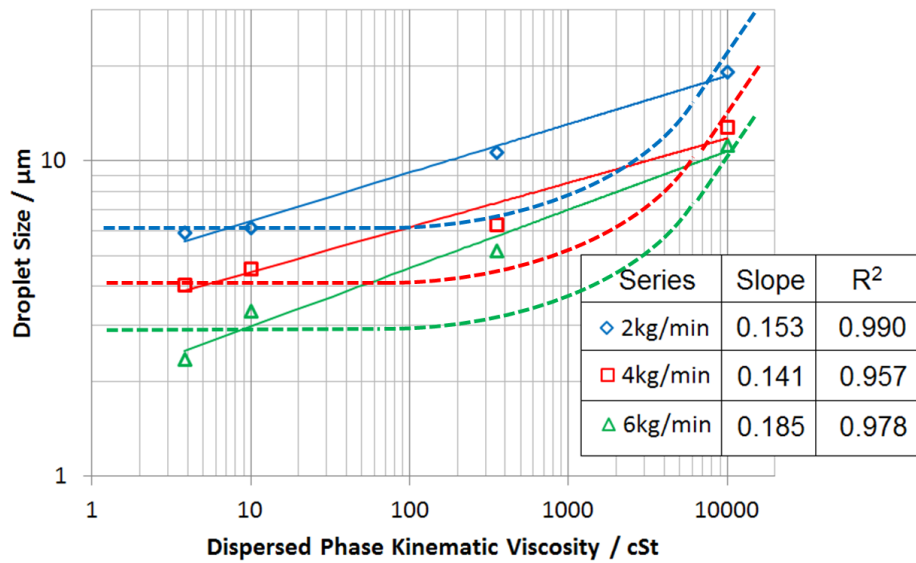
Figure 6.11: Comparison of power law trends (solid lines) with Davies-type trends (dashed line).

Figure 6.11 shows some of the Sonolator data from Figure 5.13 along with power-law trend lines (solid) and trend lines as predicted by Davies (1987). There was no evidence in the data of a region of gradient zero, an intermediate slope and then a region of slope 0.75 as predicted by Davies. Hence although Davies' Eq. (6.4) has been verified in the literature for some systems, it could not be verified for the Sonolator, which is why a fixed power-law index of 0.1119 was used instead; although this index was lower than other researchers' indices, it was clear from the data that higher fixed indices would not fit the data.

One possible explanation would be as follows: in the literature some of the *drop size* vs *viscosity* data series were flat at low viscosities, sharply upwards at around 100 cSt to 1000 cSt, and then flat thereafter (Arai *et al* 1977, Ludwig *et al* 1997). Such a curve would be possible to fit to the existing data, due to there only being measurements at 4 viscosity points. Further work is therefore suggested to investigate the Sonolator with a more detailed set of dispersed phase viscosities, say with 10 different viscosities

roughly equally spaced from 1 cSt to 10 000 cSt, and verify what the shape of the whole curve is; whether the fixed index model or the Davies' model is supported.

Hence the three indices in the empirical model were compared to theory and literature, and although within the bounds provided by the literature, each index provoked further questions about how to fit theoretical models to the experimental data, which ought to be resolved with further work.

6.6 Factory scale-up

The main question addressed in this section is: supposing experimental data was available similar to that developed in the pilot plant experiments (Chapter 5) but for much larger orifices (say 10 or 100 times bigger); what analysis would distinguish between whether the data supported scaling up on pressure drop, versus scaling upon a variant of epsilon? The current data set contains a limited ranges of orifice sizes (denoted by orifice sizes 0025 to 0140) and does not provide a final answer for which out of pressure drop or epsilon is the "true" scaling up variable.

In Table 7.5 (p379 in Appendix 7) the power of different flow rate variables to predict d_{32} was compared. Sonolator total pressure drop was found to give the best predictions, but epsilon based on any of three specific length scales was found to be almost as good, given the limited range of orifice sizes. Here epsilon based on square root of orifice area will be considered since it has the simplest mathematical description.

The geometry which was most important for affecting droplet size was the orifice size; other geometric parameters such as main chamber diameter, distance to the blade, etc, were not thought to be of primary relevance. Hence the scaling up considerations here concern orifice size only; for a very large increase in orifice area it would be

possible to increase other geometric length scales, e.g. to increase the main chamber diameter also; this would not affect the analysis below.

In Eq. (6.11) d_{32} was proportional to $\Delta P^{-0.4061}$, the main empirical correlation produced in this thesis for droplet size prediction in emulsification using the Sonolator. In Table 6.5 this was stated as equivalent to d_{32} proportional to $\varepsilon^{-0.2707}$. Strictly speaking, these cannot both simultaneously be true; however the current data set does not rule either option out. With a large scale up and further experiments, the data should clarify which of these was the "true" correlation.

In Eq. (7.23) ΔP was proportional to U^2, for U the jet superficial velocity. U was equal to $Q \cdot A^{-1}$, volumetric flow rate divided by orifice area, see Eq. (7.22). Hence ΔP was proportional to $Q^2 \cdot A^{-2}$.

Similarly, in Eq. (7.25) ε was proportional to $U^3 \cdot L^{-1}$, for L a suitable characteristic length scale. Here, L was taken to be $A^{0.5}$, the square root of orifice area. Hence ε was proportional to $Q^3 \cdot A^{-3.5}$.

Using these proportionalities, the empirical correlation in terms of either pressure drop or epsilon became: d_{32} proportional to $\Delta P^{-0.4061} = Q^{-0.8122} \cdot A^{0.8122}$, or d_{32} proportional to $\varepsilon^{-0.2707} = Q^{-0.8122} \cdot A^{0.9476}$. Hence the dependency on volumetric flow rate (Q) was seen to be the same in both cases, and only the dependency on orifice area (A) distinguished the two cases.

Let there be experiment 1 with low orifice area A_1, volumetric flow rate Q_1 and average drop size ($d_{32} = $) d_1, and experiment 2 with high orifice area A_2, volumetric flow rate Q_2 and average drop size d_2.

The change in drop size, given "pressure drop" was the "true" scale up parameter, would be:

$$R_{\Delta P} = \frac{d_2}{d_1} = \frac{C_{\Delta P} Q_2{}^{-0.8122} A_2{}^{0.8122}}{C_{\Delta P} Q_1{}^{-0.8122} A_1{}^{0.8122}} = \left(\frac{Q_2}{Q_1}\right)^{-0.8122} \left(\frac{A_2}{A_1}\right)^{0.8122} \qquad \text{Eq. (6.12)}$$

Notice the constant in the proportionality, $C_{\Delta P}$, cancelled out. Similarly, if "epsilon" was the "true" scale up parameter:

$$R_{\varepsilon} = \frac{d_2}{d_1} = \frac{C_{\varepsilon} Q_2{}^{-0.8122} A_2{}^{0.9476}}{C_{\varepsilon} Q_1{}^{-0.8122} A_1{}^{0.9476}} = \left(\frac{Q_2}{Q_1}\right)^{-0.8122} \left(\frac{A_2}{A_1}\right)^{0.9476} \qquad \text{Eq. (6.13)}$$

So $R_{\Delta P}$ and R_{ε} would be the ratios seen in each case. These are different from each other by the following factor:

$$\frac{R_{\varepsilon}}{R_{\Delta P}} = \left(\frac{A_2}{A_1}\right)^{0.9476} \Bigg/ \left(\frac{A_2}{A_1}\right)^{0.8122} = \left(\frac{A_2}{A_1}\right)^{0.1354} \qquad \text{Eq. (6.14)}$$

Suppose d_{32} was known for a small orifice size. Suppose orifice size increased by 10 times. Based on scaling up by epsilon or by pressure drop, new d_{32} could be predicted for both scale ups, and the ratio between these two new predictions would be $10^{0.1354} = 1.366$. This factor is quite small, and explains why the two cases have not been clearly distinguished to date. The hope is that given d_{32} for much larger orifices, the methodology above could provide a final answer for which scaling up method emulsification in turbulent inertial flow actually obeys.

6.7   Conclusions

Experimental work upon a pilot plant Sonolator generated a large data set of droplet size distributions which had average droplet sizes characterised by an empirical model and compared to both existing experiments and theories of droplet breakage.

- Although sparse literature was available regarding emulsification in the Sonolator, much literature was available to describe both theoretical mechanisms of emulsification and droplet sizes from emulsification experiments on other devices.

- Breakage in the Sonolator was fully in turbulent regimes; in the O/W experiments here the regime was turbulent inertial (TI) regime, and carried out in both the low viscosity and the high viscosity sub-regimes.

- An empirical correlation was developed to predict d_{32} of Sonolator emulsions from Sonolator pressure drop, dispersed phase oil viscosity and SLES concentration. These three variables were the significant variables found in Chapter 5.

- A power law was found appropriate, with indices of dependence: -0.4061, 0.1119, -0.03846 for the three variables respectively.

- These indices were within the ranges provided by the low and high viscosity TI break-up regimes described in literature, however did not fit exactly into either category. Intermediate regimes were postulated, as supported by some experiments in the literature.

- A method was developed for determining whether droplet size scales on pressure drop or on epsilon, for a large increase in orifice area.

6.8   Nomenclature & Abbreviations

Symbol   Description

C   Numerical constant in a correlation

d	General droplet size (m)
d_{32}	Sauter mean diameter (m)
d_{max}	Maximum stable droplet size in turbulent flow (m)
l	Length scale intermediate between Kolmogorov microscale and flow geometry (m)
l_e	Kolmogorov eddy length microscale (m)
L	Characteristic length scale (for Re) (m)
L	Length scale of overall flow geometry (m)
N	Angular velocity in stirred tank experiments in literature (rpm)
ΔP	Pressure drop across Sonolator orifice (Pa)
t_{def}	Deformation time of a droplet due to viscosity (s)
t_e	Kolmogorov eddy time microscale (s)
U	Characteristic velocity (for Re)
V'	"V prime" – size of average velocity fluctuation (m s)
w_{SLES}	Concentration of SLES (w/w)

Units

cSt	centistokes, unit of kinematic viscosity; equivalent to $10^{-6}\,\mathrm{m^2\,s^{-1}}$

Subscripts

c	continuous phase (water)
d	discrete phase (oil)
e	eddy
max	maximum (droplet size)
def	deformation

Greek Symbols

β beta, constant relating effect of viscosity to interfacial tension

ε epsilon, local specific turbulent energy dissipation rate ($m^2 \cdot s^{-3}$ or $W \cdot kg^{-1}$)

ν_c kinematic viscosity of continuous phase ($m^2 \cdot s^{-1}$)

ν_d nu, kinematic viscosity of dispersed phase ($m^2\, s^{-1}$)

μ_d mu, dynamic viscosity of dispersed phase (Pa s)

ρ_c rho, density of continuous phase($kg\, m^{-3}$)

σ sigma, interfacial tension ($N\, m^{-1}$)

Dimensionless Groups

Ca   Capillary Number

R^2 Coefficient of determination, close to unity when scatter is close to zero.

Re   Reynolds Number

T   Time ratio between deformation time of a droplet and characteristic time scale of smallest turbulent eddy

We   Weber Number

Abbreviations

CMC   Critical micelle concentration (of a surfactant in aqueous solution)

DSD   Droplet size distribution

O/W   Oil-in-water (emulsion)

SD   Standard Deviation

SLES   Sodium lauryl ether sulphate

TI   Turbulent inertial droplet breakage regime

TV   Turbulent viscous droplet breakage regime

6.9   Acknowledgements

6.10 References

- Ali A. M., et al, Yuan H. H. S., Dickey D. S., Tatterson G. B., (1981). "Liquid Dispersion Mechanisms in Agitated Tanks. I: Pitched-Blade Turbine", *Chem. Eng. Commun.*, **10(4-5)**.

- Arai, K., Konno, M., Matunaga, Y., and Saito, S., (1977). "Effect of dispersed-phase viscosity on the maximum stable drop size for breakup in turbulent flow", *Journal of Chemical Engineering of Japan*, **10**, 325-330.

- Calabrese, R. V., Chang, T. P. K., Dang, P. T., (1986). "Drop breakup in turbulent stirred-tank contactors Part I: Effect of dispersed-phase viscosity", *AIChE Journal*, **32(4)**, 657-666.

- Calabrese, R. V., Francis, M. K., Mishra, V. P., Phongikaroon, S., (2000). "Measurement and analysis of drop size in a batch rotor-stator mixer", *Proceedings of the 10th European Conference on Mixing*, van den Akker, H. E. A., and Derksen, J. J., (Eds.), The Netherlands, July 2-5, 2000, Elsevier Science, Amsterdam, pp. 149-156.

- Chang, T. P. K., Sheu Y. H. E., Tatterson G. B., Dickey D. S., (1981). "Liquid Dispersion Mechanisms in Agitated Tanks. II: Straight-Blade and Disc Style Turbines", *Chem. Eng. Commun.*, **10(4-5)**, 215-222.

- Chen H. T., Middleman S., (1967). "Drop size distribution in agitated liquid-liquid systems", *AIChE Journal*, **13(5)**, 989-995.

- Collins S. B., Knudsen J. G., (1970). "Drop Size Distributions Produced by Turbulent Pipe Flow of Immiscible Liquids", *AIChE. J.*, **16(6)**, 1072-1080.

- Davies J. T., (1985). "Drop Sizes of Emulsions Related to Turbulent Energy Dissipation Rates", *Chem. Eng. Sci.*, **40(5)**, 839-842.

- Davies J. T., (1987). "A Physical Interpretation of Drop Sizes in Homogenizers and Agitated Tanks, Including the Dispersion of Viscous Oils", *Chem. Eng. Sci.*, **42(7)**, 1671-1676.

- Francis M. K., (1999). *"The development of a novel probe for the in situ measurement of particle size distributions, and application to the measurement of drop size in rotor-stator mixers"*, PhD Thesis, University of Maryland, College Park, MD, USA.

- Hall S., Cooke M., El-Hamouz A., Kowalski A.J., (2011). "Droplet break-up by in-line Silverson rotor–stator mixer", *Chem. Eng. Sci.*, **66**, 2068-2079.

- Hall, S. (2012). *"Scale-up of Emulsification in Inline Rotor-Stator Mixers"*, EngD Thesis, University of Birmingham, UK.

- Hinze, J. O., (1955). "Fundamentals of the Hydrodynamic Mechanism of Splitting in Dispersion Processes", *AIChE. Journal*, **1(3)**, 295.

- Holman, J.P., (2002). "*Heat Transfer*, McGraw-Hill.

- Karbstein H, (1994). Ph.D. Thesis, University of Karlsruhe.

- Koglin B., Pawlowski J., Schnoring H., (1981). "Kontinuierliches emulgieren mit rotor/statormaschinen: Einfluss der volumenbezogenen dispergierleistung und der verweilzeit auf die emulsionsfeinheit", *Chemie Ingenieur Technik*, **53(8)**, 641-647.

- Kolmogorov A. N. (1941). "The Local Structure of Turbulence in Incompressible Viscous Fluid for Very Large Reynolds Numbers", *Proceedings of the Royal Society of London, Series A - Mathematical Physical and Engineering Sciences*, **434(1890)**, 9-13.

- Konno M., Aoki M., Saito S., (1983). "Scale Effect on Breakup Process in Liquid-Liquid Agitated Tanks", *J. Chem. Eng. Japan*, **16**, 312.

- Ludwig A., Flechtner U., Pruss J., and Warnecke H-J., (1997). "Formation of emulsions in a screw loop reactor", *Chemical Engineering Technology*, **20**, 149-161.

- Padron G. A., (2005). "*Effect of surfactants on drop size distribution in a batch rotor-stator mixer*", PhD Thesis, University of Maryland, College Park, MD, USA.

- Pandolfe W.D. (1981). "Effect of Dispersed and Continuous Phase Viscosity on Droplet Size of Emulsions Generated by Homogenization", *J. Disp. Sci. Technol.*, **2**, 459.

- Puel F., Briancon S., Fessi H., (2006). "Chapter 6: Industrial technologies and scale-up", *Microencapsulation: Methods and Industrial Applications*, 2nd Ed., Benita, S., (Ed.), Drugs and the Pharmaceutical Sciences, Vol. **158**, CRC Press Taylor & Francis Group, 149-182.

- Ryan, D., Simmons, M. and Baker, M. (2013). "Investigating Dispersion and Emulsification Processes using a Sonolator Liquid Whistle", *Proceedings of 8th International Conference on Multiphase Flow*, 26-31 May 2013, Jeju, Korea.

- Shinnar R., Church J. M., (1960). "Statistical theories of turbulence in: predicting particle size in agitated dispersions", *Industrial and Engineering Chemistry*, **52**, 253-256.

- Stephenson R., (1974). "The Effect of Agitation on Stirred Suspension Drop Size: A Model Study", *Inst. Chem. Eng. Symp. Ser. No. 38*, C4.1-22.

- Wang C. Y., Calabrese R. V., (1986). "Drop Breakup in Turbulent Stirred-Tank Contactors Part II: Relative Influence of Viscosity and Interfacial Tension", *AIChE Journal*, **32(4)**, 667-676.

- Walstra, P., (1983). "Formation of emulsions", *Encyclopedia of Emulsion Technology*, Volume **1**, Becher, P., (Ed.), Marcel Dekker, New York, USA.

- Walstra, P., and Smulders, P. E. A., (1998). "Emulsion formation", *Modern Aspects of Emulsion Science*, Binks, B. P., (Ed.), The Royal Society of Chemistry, Cambridge, UK.

Chapter 7   OVERALL CONCLUSIONS AND FURTHER WORK

7.1   Overall Conclusions

This thesis had a natural division into CFD/PIV work (Chapter 2, Chapter 3 and Chapter 4) and emulsification theory/experiments (Chapter 5 and Chapter 6).

The main output of the CFD/PIV work was a detailed knowledge of the velocity fields inside the Sonolator from CFD, which validated well against the PIV experimental data through two planes of interest. The velocity field was identified from CFD as being fully 3D, and PIV data showed it was fully turbulent in the region after the orifice. Common flow features were identified such as the orifice jet, the region where the jet dissipated, recirculation regions, and how the jet split and followed the blade (when present).

The Sonolator caused a sizable pressure drop. It was verified that this was almost entirely due to the orifice and that the blade had almost no contribution to pressure drop. The discharge coefficient from CFD agreed well with the manufacturer stated value of 0.79. The power balance showed that the pressure drop was accounted for by turbulent dissipation (ε). The turbulent variables ε and k had similar patterns between CFD and PIV. The magnitudes, however, varied; a problem also found in other investigations reported in the literature; further work remains to find a better way of validating these turbulent parameters. For a small packet of fluid transiting the orifice, there was a power law decay of velocity, ε and k after the orifice with respect to time, which could form an input for droplet breakage simulations (Appendix 2). Finally, cavitation was observed visually from PIV work, and also aurally which provided a technique for identifying the onset of cavitation (see Appendix 1).

The main output of the pilot plant experiments was confirmation that d_{32} was a good measure of average droplet size and that it was affected primarily by Sonolator pressure drop, then by dispersed phase viscosity, and with a small effect from surfactant concentration. These factors could be put together to give a power law empirical correlation for predicting d_{32}, which was found to be sufficient across all experimental parameters investigated, including for both low and high viscosity, and before/after the onset of cavitation (approximately 150 kPa) which verified that cavitation was not the primary means of breaking droplets.

 Given that the emulsification conditions investigated were in the turbulent inertial (TI) regime from emulsification theory, the correlation was intermediate between the low and high viscosity dispersed phase cases of TI droplet breakup, indicating the existence of intermediate cases, as already supported by some previous experiments in the literature.

The shape of the droplet size distribution created by the Sonolator was of a fixed width for given dispersed phase viscosity, in particular it would not be made any narrower by any choice of operating conditions, although it would be possible to widen it by varying flow rate. Some operating conditions which did not appear to affect emulsification were back-pressure valve position, oil weight fraction (up to 10 wt%), whether the dispersed phase entered the inlet at a T-junction, injector or as a pre-emulsion. When scaling on pressure drop, the orifice size did not significantly affect the droplet size, although this was only tested at pilot plant scale and not at factory scale.

The consequences of the above conclusions are that during industrial research and development much more data on the performance of the Sonolator is now available to

help guide design choices about how to integrate the Sonolator into process lines. In particular, for the sponsoring company these data will help move from batch processes towards continuous processing, making judgements about where the Sonolator is the best processing device for a particular application, and incorporating the Sonolator accordingly.

7.2   Further work suggestions

The following suggestions follow each of the major 5 results chapters (PIV, CFD, PIV/CFD comparison, pilot plant experiments, droplet breakage theory and correlations) as well as further headings for droplet breakage simulations and a suggested timeline for Unilever to use the outputs of this thesis to maximise the impact of the knowledge gained:

7.2.1   From PIV experiments

- Higher temporal resolution measurements using laser doppler anenometry in a few locations, in order to determine the main frequencies of the period components of the jets.

- If PIV acquisition rate improves, repeat PIV to separate out the periodic component of the whole velocity field. (This might help provide a better validation of k_{var} between CFD and PIV.)

- Repeat experiments with orifice type 0037 using lower laser pulse separations to provide accurate velocity measurements at the orifice.

- Design a means for positioning the laser accurately enough to carry out blade-out measurements reliably in the ZX plane (through the Sonolator axis and long axis of orifice).

- Design a means for firmly positioning the blade centrally and reducing oscillation level to below 0.1 mm. This would allow blade-in measurements in the ZY plane to be obtained more reliably near the blade edge.

- Higher spatial resolution PIV measurements to measure the velocity profile near the blade, and to get higher accuracy k and ε measurements

- Measure any oscillation in pump output (CFD was for constant flow rate).

7.2.2 From CFD simulations

- Repeat CFD with more time-steps in order to get better convergence, needed due to some asymmetries in graphs in low velocity regions.

- CFD fluid simulations incorporating models of multiphase (oil + water) flow.

- CFD models including cavitation (see Appendix 1 for evidence of cavitation).

- CFD models of fluid flow including rapid up and down blade oscillations.

- Recalculate turbulent kinetic energy calculated from velocity variance (k_{var}) after subtracting all periodic components of the flow, and ascertain which applications k or k_{var} are better suited to.

- Find a general decay equation for the dependence of ε on time after orifice.

- Use the ε decay model as an input for population balance models of droplet breakage. Model development has been illustrated in Appendix 2.

7.2.3 From PIV/CFD comparison

- Validate CFD near orifice, for orifice type 0037, after PIV with lower laser pulse separation has been carried out.

- Verify why similar calculations of k_{var} from PIV and CFD gave different results

- Compare jet oscillation frequency and magnitude between CFD and PIV.

7.2.4 From pilot plant emulsification experiments

- Investigation into whether temperature, fluid density or outlet pressure significantly affect emulsification.

- Further emulsification experiments with 350 cSt silicone oil and changing the amount of silicone oil between 0.01 wt% and 0.5 wt% - see if the 2 outliers for 0.073 kg·s^{-1} and 0.267 kg·s^{-1} were a real effect or not.

- Emulsification with oil present at 10 wt% to 50 wt% to see if oil concentration becomes significant.

- Emulsification for more oil viscosities, e.g. more than four viscosities between 1 cSt and 10 000 cSt, and also viscous oils above 10 000 cSt.

- Different Sonolator orifice setups, e.g. rectangular, square, circular orifices, multiple orifices, etc., to see if orifice shape is a significant factor in emulsification.

- Further investigation as to whether skewness in droplet size distributions of 350 cSt oil depend on orifice size or oil inlet condition.

- Investigation into multiple pass emulsification with the Sonolator (see Hall (2012) for a Silverson investigation into multiple passes) to determine if droplet breakage is complete after a single pass through the Sonolator.

- The same experiments at factory scale to help determine whether drop size correlates better to epsilon or to pressure drop over the Sonolator.

7.2.5 From droplet breakage correlations and theory

- A more detailed investigation of the full viscosity range from 1 cSt to 10 000 cSt to find out whether the dependence of d_{32} on oil viscosity is linear (as per empirical correlation presented here) or whether several regimes are found (e.g. slope 0 for low viscosity, slope 0.75 for moderate viscosity as per Davies (1987) model, with

possible inclusion of a low positive dependence for higher viscosities, as per Arai et al (1977)).

- Understanding non-isotropic turbulence theoretically (perhaps in terms of whether turbulent energy dissipation rate could be directional?) and applying that knowledge to the non-isotropic turbulent jet present in the Sonolator.

- Theoretical models for predicting how intermediate surfactant concentrations affects dynamic interfacial tension during droplet breakage, and thus droplet size.

7.2.6   Droplet Breakage Simulations

To link the emulsification experiments to the theoretical knowledge derived from CFD and PIV, it was desired to model the individual droplet breakage history through the Sonolator. Data was available from CFD for ε vs time after the orifice for a small region of fluid transiting the orifice. Preliminary **droplet breakage simulations** have been carried out which take this data and use it to model the forces on individual droplets, causing their breakage due to binary breakage models or other models, and giving rise to a predicted droplet size distribution which can be compared with experiment. For more information please see **Appendix 2**; it is suggested that these type of investigations are a natural follow-up research project to this thesis. The major obstacle is determining the correct breakage mode, since all knowledge of these inside the Sonolator rely on unsubstantiated and approximate models.

7.2.7   Timeline for Unilever to use project outputs

This EngD research project on the Sonolator has produced many outputs which could be of benefit to Unilever if implemented, however there is a danger of losing the

knowledge unless no further action is taken. Table 7.1 below provides a suggested list

of actions for the sponsoring company, Unilever, with approximate timings:

Table 7.1: Timeline of Unilever actions based on Sonolator research project outputs

Action	Approximate timing for Unilever
Enter this EngD document into Unilever corporate reporting system	1 month
Make a calculation tool to predict onset of cavitation to help predict Sonolator equipment performance	3 months
Also make a tool to predict energy dissipation rates in Sonolators	3 months
Incorporated new knowledge from this thesis into company technical training documents for process engineers in R&D, supply chain, factories	6 months
All other key knowledge integrated into engineering design tools	9 months
Update Sonolator factory design documentation according to new insights from this research	9 months
Invest in commissioning a Sonolator plant to use the knowledge from this thesis	1 year
Initial production started at Sonolator factory for some of the better understood products, e.g. shampoos, shower gels, conditioners	3 years
Sonolator factory implementation completed, a wide variety of products now made using Sonolators	5 years

Hence this EngD thesis, sponsored by Unilever R&D and EPSRC UK, has

resulted in a large body of knowledge being gained by Unilever and helping their R&D

and factory production. In addition, through this EngD document being publicly

available, and the planned publication of further papers from it, UK industry in general

has gained insights into potential new processes incorporating Sonic Corp's Sonolator

devices.

APPENDICES

Appendix 1   Cavitation observations

Abstract

Cavitation was visually observed during PIV experimentation on a Sonolator liquid whistle with a Perspex main chamber. Experiments were undertaken to investigate cavitation onset and intensity. Visual and aural measurement methods were developed. Cavitation number was used to predict at which total pressure drop the flow in the Sonolator would cavitate. Discrepancies were found between experimental onset values and theoretical values from cavitation number.

Introduction

During PIV work cavitation was visually observed in the Sonolator for blade in (Figure 7.1, Figure 2.34) and blade out (Figure 2.13, Figure 2.25). It was desired to identify the flow rate which caused the onset of cavitation; in Figure 2.25 it was seen to be between the "medium" and "high" flow rates. The manufacturer claims that cavitation in the Sonolator is essential to the operation of the Sonolator, e.g. for droplet breakage (Sonic 2011). Although existing work (Chapter 6) indicates that droplet breakage would occur in the absence of cavitation, it was still thought worthwhile to investigate cavitation in more detail.

This appendix presents preliminary work to identify the onset and intensity of cavitation in a quantitative way. Potential measurement methods included visual or aural methods since cavitation produced both a visual disturbance (an irregular reflective cavitation region) and high pitched crackling or hissing noise, becoming louder and more high pitched at even higher flow rates.

Literature Review

Walstra (1983) stated that cavitation could occur in a valve homogenizer which was similar to the Sonolator liquid whistle in that both devices force fluid at high pressure through a small gap; this literature source agreed with the experimental fact that cavitation was visually observed after the orifice in the Sonolator. Walstra also stated that the effect of cavitation upon droplet breakage was similar to that of the turbulent inertial (TI) regime, since both depend on pressure fluctuations to break droplets. This effect was considered in Chapter 6.

For measuring cavitation: microphones, accelerometers or pressure transducers have previously been used to record audio from cavitating processes. Sound intensity could be found as a function of frequency via Fourier analysis. Specific high frequency bands could be identified within which cavitation noise dominated (Pearsall 1966; Kurzhals 1977; Hakansson et al 2010; Quan et al 2011). This indicated that an audio recording technique with frequency spectrum analysis was appropriate to investigate when and if the Sonolator was cavitating.

Visual method for measuring cavitation

Appendix Fig 1: Photograph of Perspex Sonolator at high flow rate with twin cavitation jets originating from orifice

The Sonolator had an 0110 orifice inserted and the blade removed, see Chapter 2 for the experimental procedure for running the Sonolator with water. The mass flow rate was increased until at a medium-high flow rate a clear cavitation region appeared. This is illustrated in Appendix Fig 1. The cavitation looked like twin white jets emanating from the orifice. The shape of these jets indicated that it was the sharp upper and lower edges of the orifice from which cavitation came. This was corroborated by the fact that behind the blade cavitation also appeared preferentially (Figure 2.34), so cavitation was observed normally behind sharp edges in the flow.

Flow rate was varied over a wide range for orifices 0037, 0110 and 0140. The cavitation jet, if visible, had its length measured visually using a ruler held against the outside of the Perspex section. This technique was approximate, with accuracy no better than within 0.5 mm, and with some errors in 3D perspective inherent. However it was a good preliminary method since it was very simple to carry out.
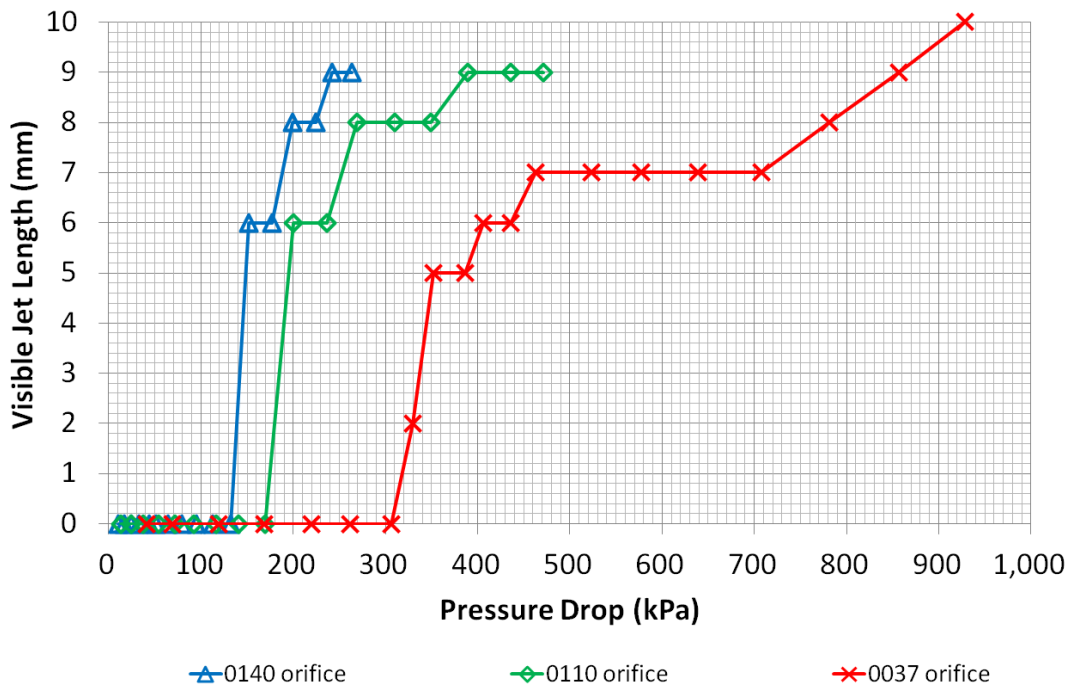
Appendix Fig 2: Graph of Cavitation Jet Length vs Pressure for three orifices.

In Appendix Fig 2 cavitation onset was seen at 142 kPa, 185 kPa and 318 kPa for 0140, 0110 and 0037 orifices respectively; these values were calculated by averaging the last zero measurement (no jet seen) and the first non-zero measurement when cavitation jet became visible.

Cavitation number and theory of cavitation onset

$$\text{Ca} = \frac{p - p_v}{\frac{1}{2}\rho U^2} = \frac{98\,125\text{ Pa}}{\frac{1}{2}\rho U^2} \qquad \text{Eq. (7.1)}$$

(Reference: Batchelor 1967)

The cavitation number in Eq. (7.1) gave a condition under which theory indicated cavitation should occur, which was where $\text{Ca} < 1$ within the flow. Ca after the orifice depended on local static pressure (p) which was approximately the same as the pressure at the outlet, atmospheric pressure (101 325 Pa). Ca also depended on vapour pressure of water (p_v) which was 3200 Pa at 25°C, density of the continuous phase (ρ) which was that of water, 997 kg·m^{-3}; and local flow velocity magnitude (U) which was dependent on position in the flow.

Within the orifice jet, U increased very rapidly and Ca became smaller, sometimes below 1 if U became large enough. After the velocity peak, U decreased and Ca increased, explaining why cavitation was only in a limited region near the orifice jet.

$$U = \frac{Q}{A} = C_D \sqrt{\frac{2\Delta P}{\rho}} \qquad \text{Eq. (7.2)}$$

(Reference: Perry 1998)

To calculate Ca at the orifice, the local flow velocity U was assumed to be the orifice superficial velocity $Q \cdot A^{-1}$, where Q was the volumetric flow rate and A was the

orifice area. Perry (1998) gave an equation for orifice flow, Eq. (7.2), which related the pressure drop over the whole Sonolator (ΔP) to the flow velocity U via a discharge coefficient (C_D). This discharge coefficient had previously been investigated and found to be almost constant over a wide range of flow rates and almost equal to the manufacturer recommended value of 0.79 (Sonic 2011) so the approximation $C_D = 0.79$ was made.

$$\frac{1}{2}\rho U^2 = C_D{}^2 \Delta P$$

<div align="right">Eq. (7.3)</div>

$$Ca = \frac{p - p_v}{C_D{}^2 \Delta P} = \frac{98\,125 \text{ Pa}}{C_D{}^2 \Delta P} = \frac{157\,226 \text{ Pa}}{\Delta P}$$

<div align="right">Eq. (7.4)</div>

Eq. (7.2) for U was rearranged to give Eq. (7.3), which was then substituted into Eq. (7.1) for Ca to give Eq. (7.4) which related Ca to the reciprocal of the pressure drop. Eq. (7.4) implied that cavitation should occur whenever total Sonolator pressure drop increased above 157 226 Pa. This theoretical result was independent of orifice size A.

This gave a discrepancy between theoretical arguments that cavitation should appear at a fixed pressure drop independent of orifice size (Eq. (7.4)), and the experimental data in which cavitation appeared at higher pressure drops for smaller orifice sizes (Appendix Fig 2).

Aural method for measuring cavitation

To shed light on this mystery, cavitation was investigated more accurately using a similar audio technique to that described in the literature quoted above. A RadioShack "Sound Level Meter" was held in place against the Perspex Sonolator section just above the orifice, using a seal of soft putty. This ensured that the only high frequency sounds recorded were those from inside the Sonolator, since high frequencies from elsewhere in the room (such as from the pumps) would be attenuated by the solid obstacle of the seal.

The audio output was sent to software "Audacity" which recorded a 44.1 kHz ".wav" audio file. A Fast Fourier Transform was used to find the frequency spectrum of a suitable 20 second portion of this audio to give sound intensities (in dB) at each frequency. These data were exported to Excel.

To obtain cavitation measurements for each Sonolator run, the following analysis was followed. A background curve of dB vs frequency was present with this microphone. Each measurement therefore consisted of subtracting the background from a spectrum of a Sonolator recording. A suitable background was prepared using a recording of the Sonolator, but with the pumps switched off. This technique gave sensitivity for high frequencies (>3 kHz) as accurate as ±0.1 dB.

Cavitation was found to give characteristic peaks in the 3 kHz to 11 kHz frequency bands. If no cavitation was visually observed, these frequencies were not present, but if cavitation was visually observed, sharp peaks appeared in various locations between 3 kHz and 11 kHz. Hence the cavitation measurement was chosen to be the mean-average dB value for all frequency bands between 3 kHz and 11 kHz.
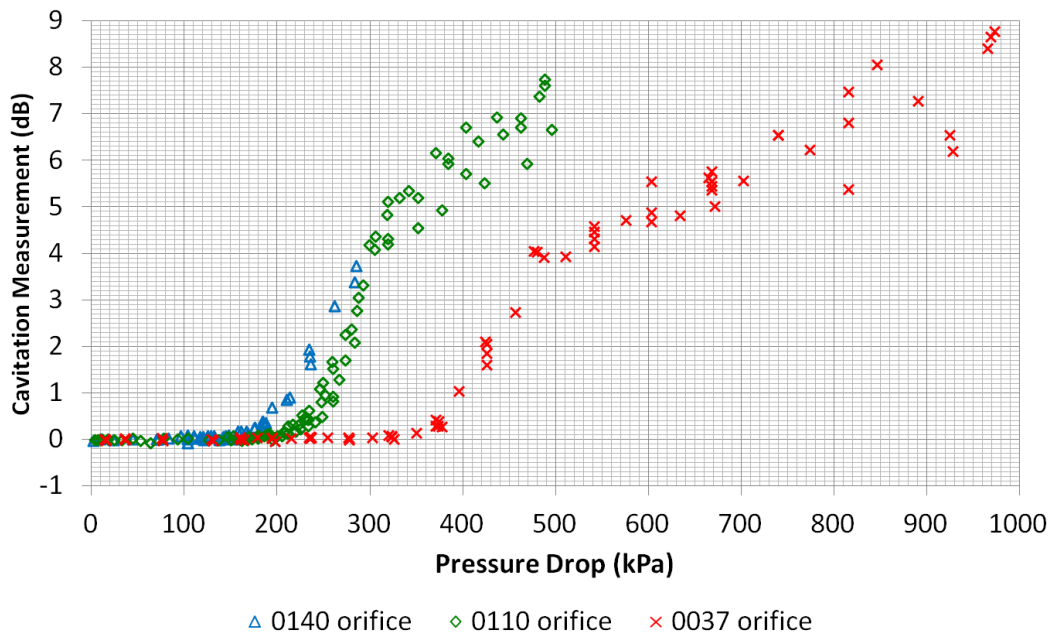
Appendix Fig 3: Audio cavitation measurement vs Pressure Drop.

In Appendix Fig 3 results are presented for cavitation measurements for three orifices and a wide range of pressure drops set by the user. The characteristic curve for each orifice had four parts: firstly a zero cavitation region, then an onset region (where the reading curves up from 0 dB to around 0.5 dB), then a region with linear increase and low scatter, then a region with lower linear increase and higher scatter.

Due to the level of scatter it was found useful to take the averages of cavitation measurements made over small ranges of pressure drops. These ranges were chosen to be evenly spaced on a logarithmic scale, with 50 ranges per order of magnitude. The averaged cavitation measurements are presented on another scatter diagram below, with interpolation lines between scatter points to give estimated cavitation measurements in-between data points and for those pressure drop ranges with no measurements in.
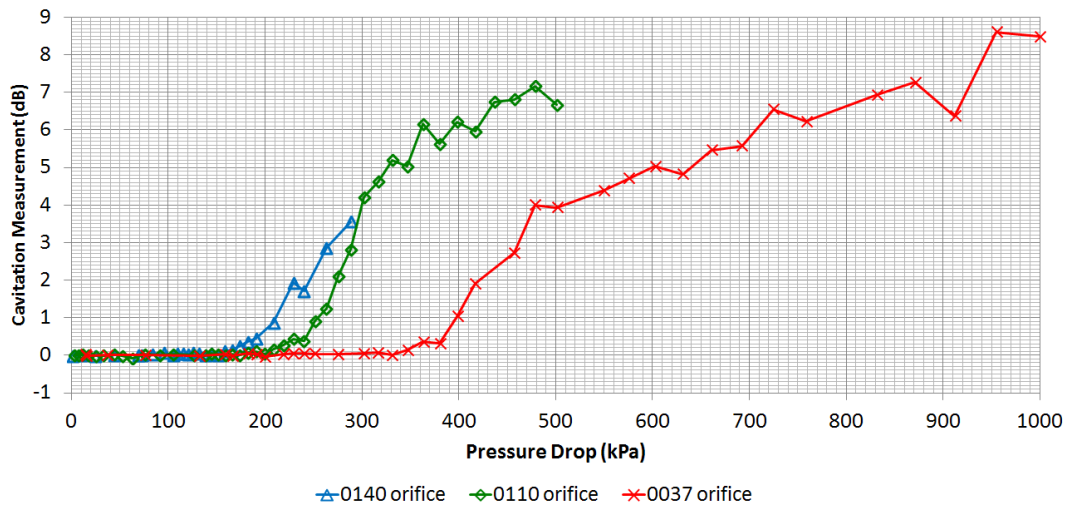
Appendix Fig 4: Average cavitation measurement vs Pressure drop range.

The cavitation measurement curves shown in Appendix Fig 4 had become much cleaner with the removal of scatter. It was still not clear what the pressure drops were at onset of cavitation for the three orifices. To locate these, the graph was rescaled to have pressure drops between 100 kPa and 400 kPa only, and cavitation measurements in the range -0.1 dB to 0.5 dB. (Negative measurements were possible since the background represented an average non-cavitating flow, and other non-cavitating flows might randomly have a lower intensity of high frequency sound in the 3 kHz to 11 kHz range.)
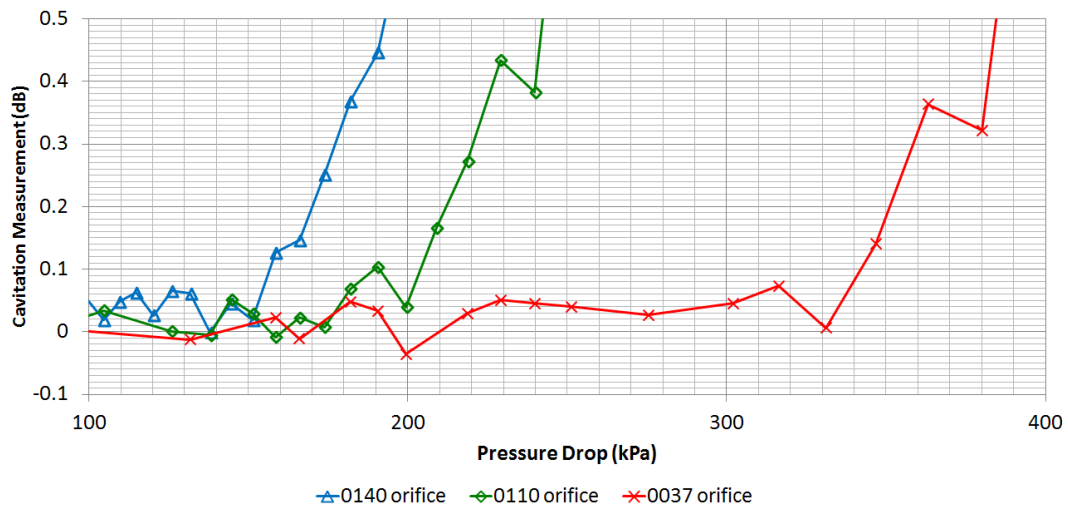
Appendix Fig 5: Cavitation vs Pressure Drop (zoomed).

For each orifice there was a period of no cavitation, and a sudden increase in cavitation measurement during onset of cavitation. No background reading reached 0.08 dB, so onset of cavitation was taken to be 0.08 dB. This gave cavitation onset at 155 kPa for 0140 orifice, 185 kPa for 0110 orifice and 340 kPa for 0037 orifice. These aural onset measurements agreed well with the visual onset measurements of 142 kPa, 185 kPa and 318 kPa found for each orifice respectively.

Effect of cavitation upon droplet breakage

In Chapter 5 droplet breakage experiments were described for a silicone oil in water coarse pre-emulsion with 0.5 wt% SLES as surfactant, being processed on a Sonolator with pressure drops between 50 kPa and 5200 kPa, silicone oil viscosities between 3.8 cSt and 10 000 cSt. (The orifice size was found to be factored out by using pressure drop as the flow rate variable.) Droplet size distributions were typically described using d_{32} which was plotted against pressure drop for each dispersed phase oil viscosity.
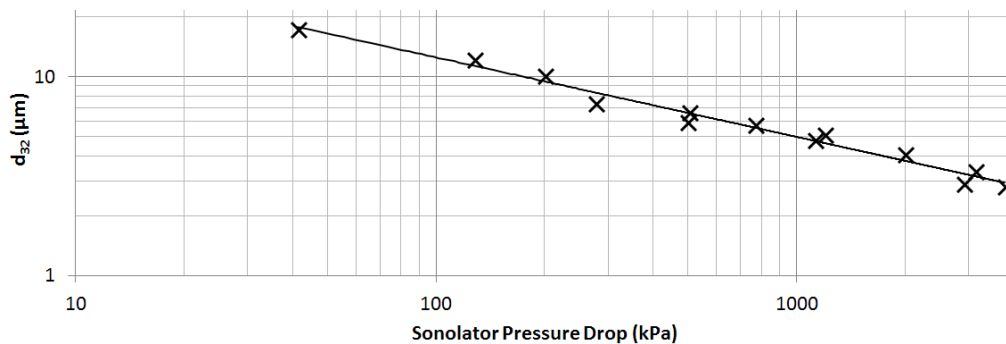
Appendix Fig 6: Graph of d_{32} vs Sonolator Pressure Drop for 3.8 cSt silicone oil.

In Appendix Fig 6 with d_{32} plotted against pressure drop on log-log axes, the trend of the data did not deviate markedly from a straight line. This data included points above and below the onset of cavitation, and within the range of cavitation onsets found

earlier (140 kPa to 340 kPa). Hence for emulsification of 3.8 cSt oils, the onset of cavitation was not shown to either increase nor decrease droplet size.
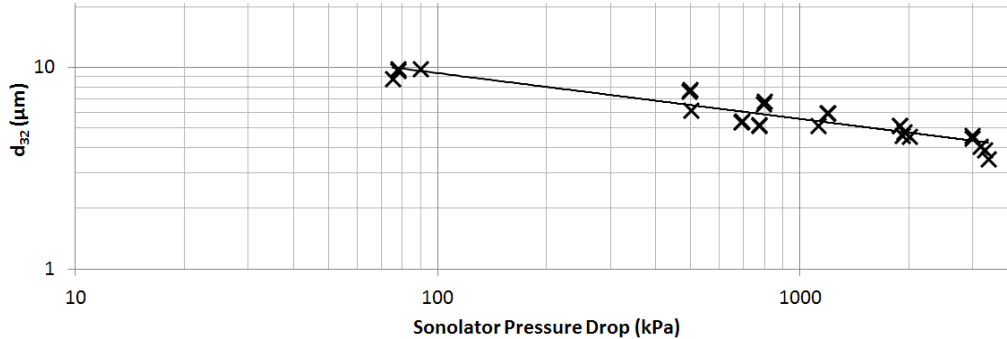
Appendix Fig 7: Graph of d_{32} vs Sonolator Pressure Drop for 10 cSt silicone oil.

The same analysis was carried out (Appendix Fig 7) for a 10 cSt silicone oil. Although data was not available in the range of cavitation onsets (140 kPa to 340 kPa), the data on either side of this range showed a trend which was a straight line, so again cavitation was not shown to either increase nor decrease droplet size.

Overall it was concluded from the data available for multiple pressure drops, oil viscosities and orifice sizes that the onset of cavitation did not significantly affect the efficiency of emulsification and that droplet breakup would happen regardless of whether the system was cavitating or not.

Other preliminary findings

- Darbandi and Sadeghi (2009) give 225 kPa as the pressure drop at which vapour cavitation occurs for a CFD simulation of a circular orifice. This is in-between the experimental values (both visual and aural) above for 0110 and 0037 orifices, so corroborates the order of magnitude of cavitation onset.

- Rig noise from the pumps was lower frequency than 3 kHz, and so could be separated out from the cavitation noise. This was a pre-requisite for reliable aural cavitation measurements

- The onset of cavitation and measured cavitation intensity was independent of the position of the microphone on the Perspex section; above the orifice, to the side of the orifice, or just above the outlet.
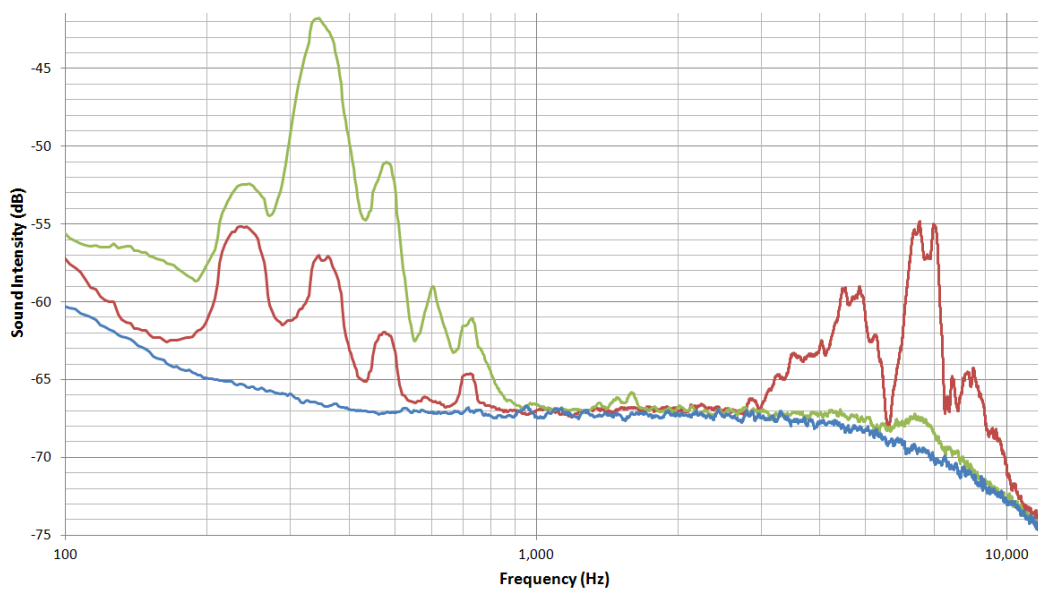
Appendix Fig 8: Graph of sound intensity vs frequency for: background (blue), water flow above onset of cavitation (red), water with air bubbles flow (green).

- Adding air bubbles into the water suppressed cavitation sounds in 3 kHz to 11 kHz band, but increased the sound intensity from 200 Hz to 800 Hz, see Appendix Fig 8. Freudig, Tesch & Schubert (2002) distinguish between three types of cavity formation when pressure is lowered: vapour cavitation (true cavitation) when liquid vaporises, degassing where dissolved air comes out of solution, and pseudocavitation where undissolved air bubbles expand. They also state that vapour cavitation has a higher frequency sound than pseudocavitation (air in transit). Hence

by adding air at the inlet Appendix Fig 8 showed a transition from true water vapour cavitation to air bubble pseudocavitation;

- Freudig et al (2002) state that out of these three mechanisms only vapour cavitation contributes to droplet disruption. Behrend & Schubert (2001) state that a few small air bubbles may be necessary to seed cavitation, but that too much air would cushion the effect of cavity collapse, presumably the mechanism by which pseudocavitation prevents droplet disruption. Since it is expected that coarse emulsion droplets could seed cavitation as effectively as a small quantity of air bubbles, adding air is undesirable when trying to increase droplet breakage.

Conclusions

- A Perspex Sonolator section was used to visualise the flow in the Sonolator.

- Cavitation was observed visually and aurally.

- Precise measures of cavitation are possible using analysis of the audio spectrum.

- The measurements do not depend on microphone position and were sensitive due to subtraction of background readings.

- Smaller orifices were found to cavitate at higher pressure drops, which requires explanation given that theory predicts that cavitation onset should be independent of orifice size.

Further work

- Investigate why cavitation onset appeared to depend on orifice size.

- Investigate effect of water temperature upon cavitation onset and intensity.

- Redo audio studies with a blade in, and investigate whether blade presence or position affects cavitation onset.

- Do a detailed cavitation onset vs back-pressure study.

- Investigate whether the presence of a second phase (e.g. emulsion droplets) increases or decreases cavitation

- Investigate whether high viscosity continuous phases affect cavitation onset by viscous resistance to bubble expansion.

- Investigate how cavitation (or lack of cavitation) affects droplet breakage when other conditions are held constant: this could be investigated with more precise control over back-pressure.

Nomenclature & Abbreviations

Symbol	Description
A	Area of Sonolator orifice (m^2)
C_D	Coefficient of discharge (e.g. see Perry 1998)
p	Local pressure in the flow field
p_v	Vapour pressure of the fluid
ΔP	Pressure drop over Sonolator (Pa)
Q	Volumetric flow rate (m$^3 \cdot$s^{-1})
U	Local velocity at flow (m$\cdot$s^{-1}); superficial velocity at Sonolator orifice

Greek Symbols

ρ	Density of fluid (997 kg$\cdot$m^{-3} for water)

Dimensionless Groups

Ca	Cavitation number (see Bachelor 1967)

Acknowledgements

- Duncan Court, Unilever R&D Port Sunlight, UK for training on recording audio samples from process equipment, and software processing of these samples in Audacity.

- Robert Sharpe (Bob) and Phil Harris (Bill), Chemical Engineering workshop, University of Birmingham for making and improving the Perspex rig.

References

- Batchelor, G. K. (1967). "*An Introduction to Fluid Dynamics*", Cambridge University Press, UK.

- Behrend, O., Schubert, H., (2001). "Influence of hydrostatic pressure and gas content on continuous ultrasound emulsification", *Ultrasonics Sonochemistry*, **8**, 271-276.

- Darbandi, M., Sadeghi, H., (2009). "A Study on Flow Through an Orifice with Prediction of Cavitation and Hydraulic Flip", *Proceedings of the ASME 2009 Fluids Engineering Division Summer Meeting*, FEDSM2009.

- Freudig, B., Tesch, S., Schubert, H. (2002). "Production of emulsions in high pressure homogenizers - Part 2: Significance of cavitation for size reduction droplets", *Chemie Ingenieur Technik*, **74(6)**, 880-884.

- Håkansson, A., Fuchs, L., Innings, F., Revstedt, J., Bergenståhl, B., Trägårdh, C., (2010). "Visual observations and acoustic measurement of cavitation in an experimental model of a high-pressure homogenizer", *Journal of Food Engineering*, **100(3**), 504–513.

- Kurzhals, H. A., (1977). "*Untersuchungen über die physikalisch-technischen Vorgänge beim Homogenisieren von Milch in Hochdruck-*

Homogenisiermaschinen", Doctoral Thesis, Technischen Universität Hannover, Hannover.

- Pearsall, I. S. (1966). "Acoustic Detection of Cavitation", *Proc. Instn. Mech. Engrs.*, 1966-67 181 (3A). Paper 14.

- Perry, R. H., Green, D. W., eds., (1998). "*Perry's Chemical Engineers' Handbook*". 7th ed., McGraw-Hill, New York.

- Quan, K. M., Avvaru, B., Pandit, A. B. (2011). "Measurement and Interpretation of Cavitation Noise in a Hybrid Hydrodynamic Cavitating Device", *AIChE. Journal*, **57(4)**, 861-871.

- Sonic Corp (2011). "*Sonolator Operating and Instruction Manual*", http://www.sonicmixing.com/Manuals/Sonolator_System_Manual.pdf, downloaded on 27th July 2013.

- Walstra, P., (1983). "Formation of emulsions", *Encyclopedia of Emulsion Technology*, Volume **1**, Becher, P., (Ed.), Marcel Dekker, New York, USA.

Appendix 2   Droplet Breakage Simulations

Abstract

Droplet breakage simulations were carried out for a Sonolator inline liquid whistle mixing device. Monodispersed oil droplets of varying dispersed phase viscosity were introduced at the inlet. A model for local specific turbulent energy dissipation rate from CFD was used to give a maximum stable droplet size at each point in time. Individual droplet breakage was modelled using a volume conservation method and binary droplet breakage into uneven portions. Using large numbers of droplet breakage events the volume weighted droplet size distributions were constructed and compared for different dispersed phase viscosities and breakage mechanisms.

Introduction

Previously for a Sonolator liquid whistle two separate pieces of work had been developed: firstly a profile of epsilon (local specific turbulent energy dissipation rate, ε) for a typical portion of fluid along a typical streamline as water passes through the Sonolator orifice, and secondly an experimental characterisation of droplet breakage in the Sonolator using a silicone oil in water pre-emulsion with SLES surfactant.

It was thought that the epsilon profile was responsible for droplet breakage in the Sonolator, e.g. the theories of Hinze (1955) and Walstra & Smulders (1998) regarding droplet breakage in turbulent inertial flow. Therefore, it was desired to model in depth the processes along a typical streamline which used the epsilon profile and gave rise to the observed droplet size distribution. This was done by modelling each stage of droplet breakage as one or more large droplets transit the orifice and iteratively break into smaller droplets until the final size is attained.

328

Summary of literature regarding population balance methods

The underlying equations thought to govern a two-phase flow of a coarse pre-emulsion of oil in water are based on the Navier-Stokes equations for a single phase system, which contains continuity and momentum equations. Solving these requires a suitable discretisation of the problem, such as a Direct Numerical Simulation (DNS), see Marden, Marshall and Bakker (2004). Since a DNS requires spatial resolution down to the Kolmogorov length scale, and is currently computationally intractable for complex flows, including the Sonolator orifice, turbulence models are often used which reduce accuracy but greatly increase tractability.

To extend flow simulations to two phases means ideally performing DNS on each phase separately, and linking the two phases through suitable interface physics at the boundary. This also requires a Kolmogorov length scale knowledge of the interface location and momentum, which is again intractable. If surfactant is present, or one phase is partially soluble in the other, the complexity increases again. The current status of multiphase flow simulation is that of computational intractability as bad as or worse than performing a single phase DNS, hence models to simplify multiphase breakage are sought.

Droplet breakage simulations have been carried out in the literature using population balance modelling (PBM) techniques (Ramkrishna 2000). Rather than a computationally expensive tracking of the interface, the droplet breakage problem is simplified by only considering the evolving droplet size distribution (DSD) according to suitable population balance equations (PBE) which conserve the total mass of dispersed phase. This requires a discretisation in space and time; considerable computational

saving can be made by having a single spatial point, or tracking a single region of fluid along a streamline (as in the current work).

The DSD itself also requires discretisation; two main methods include: splitting the DSD into discrete bins, and specifying the moments of the continuous distribution up to a highest moment with algebraic closure using the quadrature method of moments (QMOM) method.

For the evolution of the DSD two main processes are considered; droplet breakage and coalescence. An example of using flow data to guide PBM comes from Jaworski *et al* (2007) who modelled droplet breakage in a Kenics static mixer, integrating PBM with CFD so that local flow conditions guided droplet breakage. Here also the local flow conditions obtained from CFD work will guide the droplet breakage in a fluid region transported along a streamline travelling through the Sonolator orifice.

Materials and Methods for Droplet Breakage Simulations

For the Sonolator, coalescence was expected to be minimal due to the presence of surfactant (see Chapter 5) hence only droplet breakage needed to be modelled. This meant that there were no drop-drop interactions to be modelled; an individual drop would either split into two non-interacting droplets, or stay unchanged to become part of the final droplet size distribution.

Without any drop-drop interactions, a third option for modelling the DSD was possible. In the literature the DSD was modelled as a series of bins, or a series of moments. With no interactions, the DSD could be modelled directly as individual droplets transiting the orifice and undergoing droplet breakage depending on the conditions at each point during their transit.

Relevant conditions during transit of an individual droplet include: density and viscosity of continuous and dispersed phases, interfacial tension, time elapsed since the orifice (t), current droplet diameter (d), values for turbulent dissipation (ε) with respect to that time, values for the maximum stable droplet size for that turbulent intensity (d_{max}), probability $P(D)$ that a droplet will break based on the dimensionless diameter $D = d / d_{max}$, a method for determining how big the daughter droplets are, and length of time taken to break a droplet (Δt) as a function of d and ε.
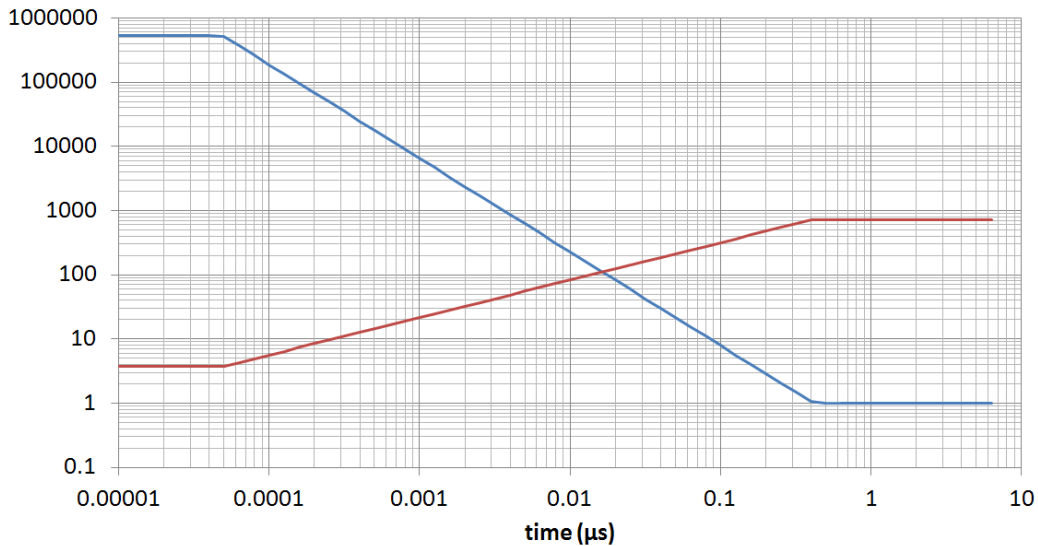
Appendix Fig 9: Values used for $\varepsilon(t)$ (decreasing, blue) and $d_{max}(t)$ (increasing, red) in simulations.

From earlier CFD work (e.g. see earlier Figure 3.32), along a typical streamline the value of $\varepsilon(t)$ peaks sharply after the orifice, and then decays with an approximate power law dependency on time after the orifice as the flow goes downstream. This was modelled by a fixed epsilon value for a fixed length of time, then an power law decay function thereafter, terminated by a long constant value of ε at a low level, giving a piecewise linear function on a log-log graph of ε against time after the orifice, presented above in Appendix Fig 9. Also, d_{max} (given density and interfacial tension) could be

directly derived from ε according to the method of Hinze (1955) and likewise was a piecewise linear function on log-log axes, also plotted above.

In Appendix Fig 10 below $P(D)$ is given, which were the values used in simulations for the probability $P(D)$ that a droplet of dimensionless diameter D will break. If a droplet was bigger than d_{max} then it always broke ($P(D) = 1$); if it was less than half of d_{max} then it did not break ($P(D) = 0$); in between these two extremes the probability function was linearly interpolated. This introduced a random factor into the droplet breakage simulations.
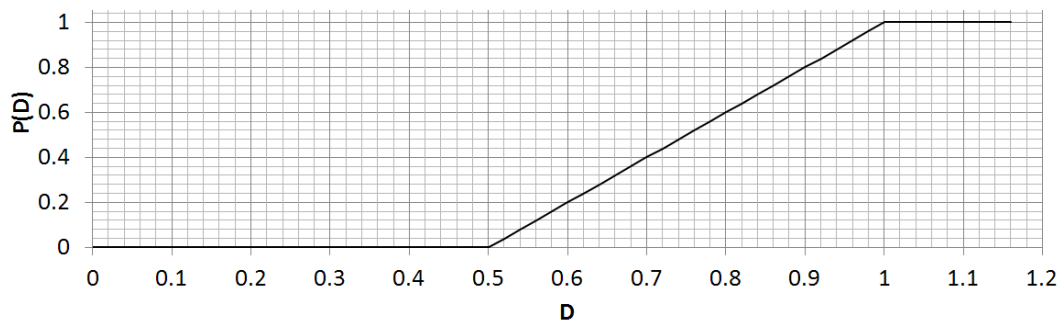
Appendix Fig 10: Values used for $P(D)$, the probability that a droplet breaks based on D, the ratio of its diameter compared to $d_{\text{max}}(t)$ the Hinze model of maximum droplet size.
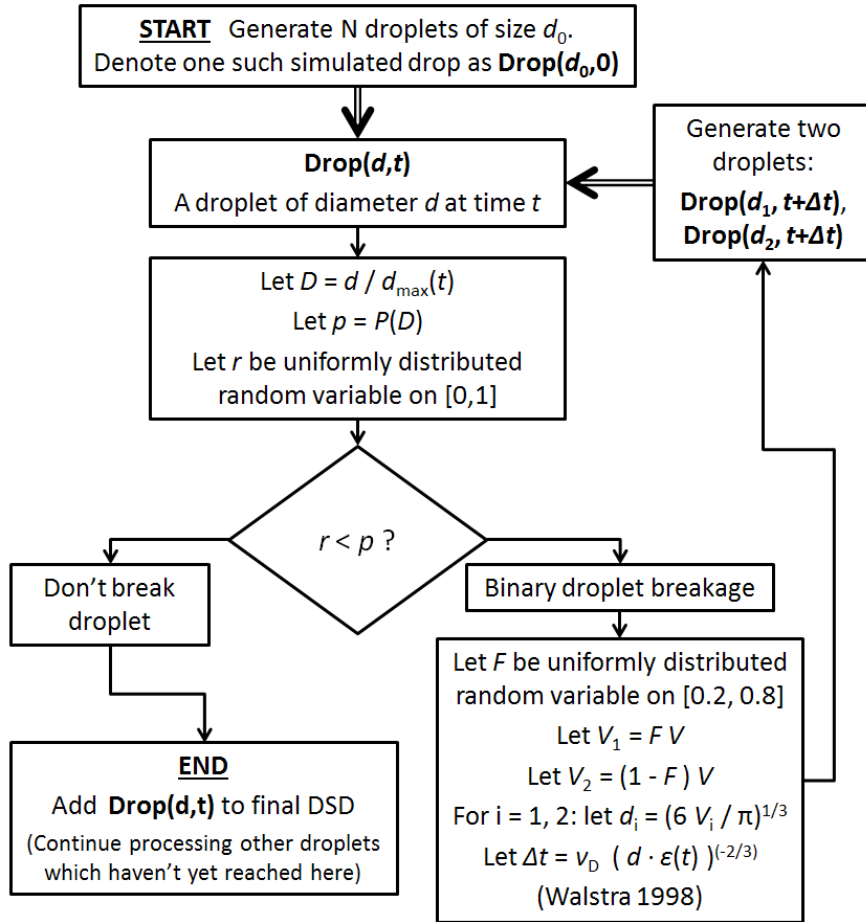
Appendix Fig 11: Flow chart of droplet breakage model. A single arrow represents processing of a single droplet, a multiple arrow that of multiple droplets.

In Appendix Fig 11 the procedure for carrying out the simulations is given as a flowchart, which is described as follows. Start with a set of N droplets of initial diameter d_0, which are then simulated to enter the Sonolator orifice at time $t = 0$. Each droplet is simulated separately. Comparing its diameter to d_{max}, it either breaks or it doesn't (using the breakage function $P(D)$). If not, the droplet is added to the final set of simulated droplets; since ε was decreasing the droplet is now stabilised. If however the droplet does break, then its daughter fragments will be created (and original droplet removed) and the simulation will continue with the daughter fragments.

In these simulations the breakage was always binary, with volume fractions taken at random within a subset of [0, 1]; the narrower the subset, the more even the breakage.

An example would be: take the range [0.2, 0.8] (as illustrated in the flowchart), an uneven breakage scheme. Generate a random number uniformly on this range. Say it was 0.43. Then split the parent droplet to have daughter droplets with volume fractions 0.43 and 0.57.

Each daughter droplet was created at a later time than the original droplet. If the original droplet was broken at time t, both daughter droplets were iteratively simulated starting at time $t+\varDelta t$. To calculate $\varDelta t$, the length of time the original droplet took to break, this was assumed to be equal to the droplet deformation time in turbulent inertial (TI) flow. Walstra and Smulders (1998) gave a proportionality for this quantity in terms of d, ε and dispersed phase kinematic viscosity ν_D. This proportionality was used in these simulations with constant equal to unity.

The simulation continued until all daughter droplets had been broken down to a size such that they could no longer be broken any further by the prevailing conditions described by ε and d_{max}. At that point the simulation was ended and the droplet size distributions were plotted. Examples are given in the results below.

Results

Droplet breakage simulations in the Sonolator were carried out for binary breakage of 35 μm droplets. Dispersed phase viscosity was varied between 10 cSt and 350 cSt. The six volume fraction ranges used were: 0.5 (breakage into even portions), [0.49, 0.51], [0.46, 0.54], [0.4, 0.6], [0.2, 0.8] and [0.01, 0.99].
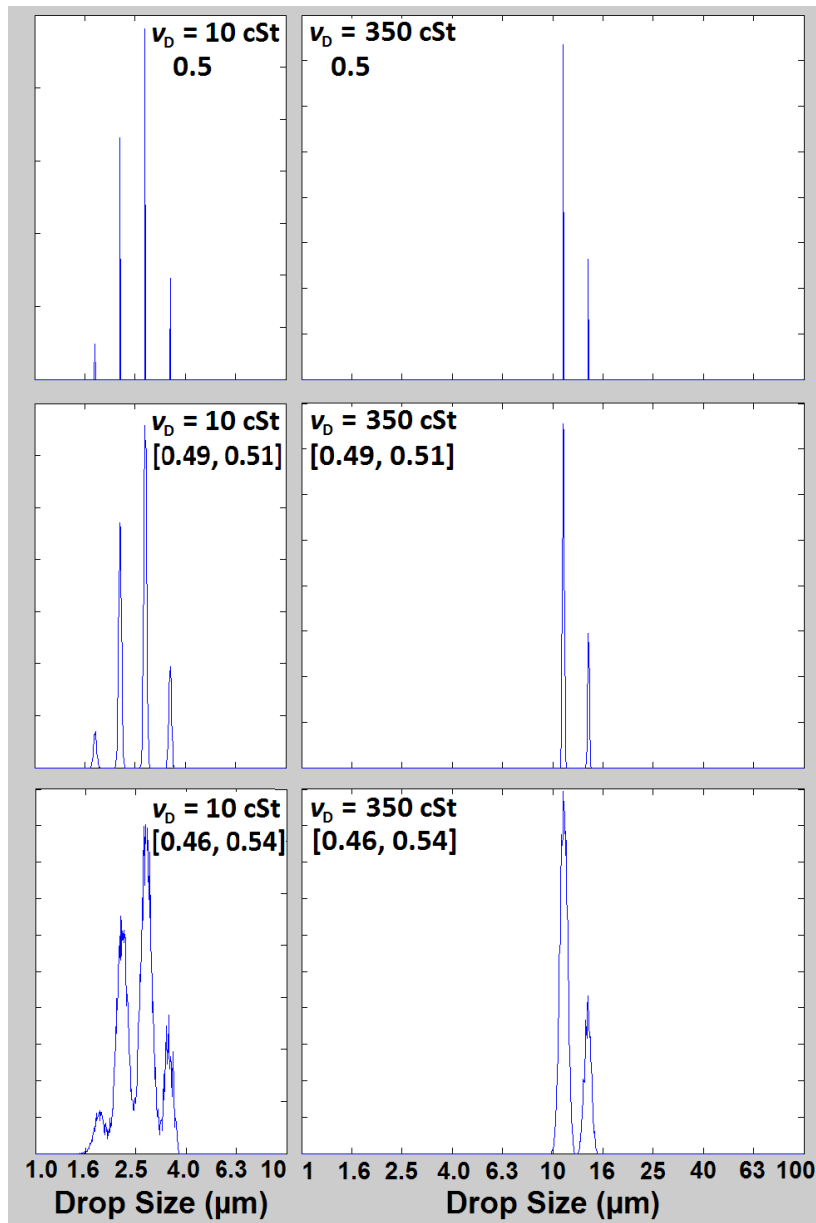
Appendix Fig 12: Even binary breakage of monodispersed initial droplets of diameter 35 μm, volume-weighted DSDs illustrated. Viscosity of dispersed phase either 10 cSt or 350 cSt. The breakage scheme is denoted [r, 1-r]. For even schemes, r is near 0.5.
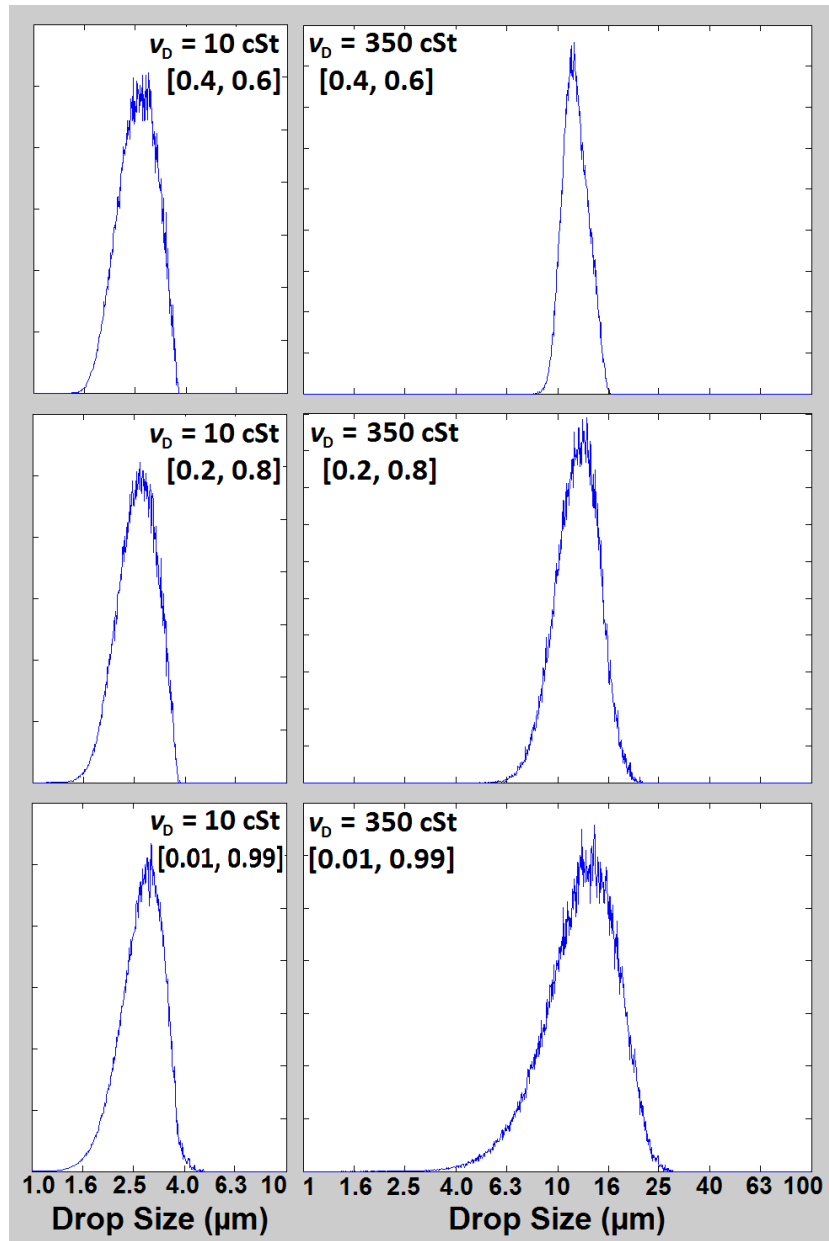
Appendix Fig 13: Uneven binary breakage (Volume-weighted DSDs).

Results of droplet breakage simulations for the Sonolator (with 35 μm monodispersed droplets at the inlet) are given above in Appendix Fig 12 for even breakage (all breakage using ranges 0.46 to 0.54) and Appendix Fig 13 for uneven breakage (breakage schemes at least as wide as 0.4 to 0.6). The even breakage schemes are seen to give multiple peaks, but the uneven breakage schemes did not; the multiple peaks were due to the monodispersed input droplets being broken an integer number of

times into even fractions. The emulsification experiments on the Sonolator (see Chapter 5) used polydispersed pre-emulsions; however even if they used monodispersed pre-emulsions it seems unlikely that multiple peaks would survive due to the stochastic nature of turbulent break-up. Therefore, from this evidence the Sonolator would be more likely to use an uneven scheme of binary droplet breakage than an even scheme.

Comparing 10 cSt graphs to 350 cSt graphs for uneven breakage schemes, the higher viscosity simulations had larger output droplets. The reason in the simulation for this was that breakage time for higher viscosities was longer, and subsequent iterations were using lower values of ε and higher values of d_{max}. Again, larger final droplet size for higher viscosity dispersed phase agreed with emulsification experiments.

Comparing 10 cSt graphs for different (uneven) breakage schemes; [0.4, 0.6] gave similar results to [0.01, 0.99]. This was due to droplets breaking quickly and reaching d_{max} while ε was still relatively high; even the larger fragments produced had time to break many times eventually reaching a similar eventual size to the smaller fragments.

Comparing 350 cSt graphs for the same schemes, there was a large difference between [0.4, 0.6] and [0.01, 0.99] breakage schemes, in particular the latter DSD was much wider. This was because the length of time taken to break droplets was long enough for ε to rise significantly and freeze the droplets into their final size, in particular freezing the uneven large and small fragments in place, and widening the DSD for more uneven breakup schemes. Since in emulsification experiments the higher viscosity oils produced wider DSDs, this was evidence that a very uneven breakage mechanism resulted from turbulent dispersion of high viscosity oils in the Sonolator. Alternative mechanisms would include high viscosity oils stretching into long filaments which would produce large numbers of daughter droplets (more than binary breakage),

some very small and others expected to be larger; this would still be an uneven breakup mechanism due to the random eddies causing uneven stretching of the filament.

Conclusions

Preliminary droplet breakage simulations were carried out for a Sonolator. The key inputs were a binary breakage scheme and a set of values for turbulent dissipation rate *vs* time from CFD. Even breakage schemes were found to cause unphysical multiple peaks, but more uneven breakage schemes had features noted beforehand from pilot plant emulsification studies. Some features of the results such as wider distributions for higher viscosity oils (given a very uneven breakup mechanism) suggested that the very uneven breakup mechanisms were more likely to be the types of mechanism operating in the Sonolator.

Further work

- Try breakage models other than binary breakage. The number of daughter droplets could be a function of how much bigger the current droplet is than the maximum stable size, i.e. for large droplets they could shatter into 10 or even 100 daughter droplets in one stage.

- Use multiple models for epsilon based on multiple flow rates and multiple orifice sizes.

Nomenclature & Abbreviations

Symbol	Description
d	Droplet diameter (m)
d_{max}	Max droplet diameter in turbulent inertial flow (m, see Hinze 1955)
$P(D)$	Probability that a droplet will break based on d / d_{max}

Δt Time taken for droplet to break (s)

t Time after Sonolator orifice (s)

Greek Symbols

v_D Dispersed phase kinematic viscosity ($m^2 \cdot s^{-1}$)

ε Local specific turbulent energy dissipation rate ($W \cdot kg^{-1}$)

Abbreviations

CFD   Computational Fluid Dynamics

DNS   Direct Numerical Simulation

DSD   Droplet Size Distribution

PBM   Population Balance Modelling

PBE   Population Balance Equations

QMOM   Quadrature Method of Moments

SLES   Sodium laureth sulphate, or sodium lauryl ether sulphate.

References

- Hinze, J. O., (1955). "Fundamentals of the Hydrodynamic Mechanism of Splitting in Dispersion Processes", *AIChE. Journal*, **1(3)**, 295.

- Jaworski, Z., Pianko-Oprych, P., Marchisio, D.L., Nienow, A.W., (2007). "CFD Modelling of Turbulent Drop Breakage in a Kenics Static Mixer and Comparison with Experimental Data", *Chem. Eng. Research and Design*, Trans IChemE, Part A, **85(A5)**, 753-759.

- Marden Marshall, E., and Bakker, A., (2004). "Computational fluid mixing", *Handbook of Industrial Mixing: Science and Practice*, Paul, E. L., Atiemo-Obeng, V. A. and Kresta, S. M., (Eds.), John Wiley & Sons, Inc., Hoboken, New Jersey, USA, 257-343.

APPENDICES

- Ramkrishna, D., (2000). "*Population balances: Theory and applications to particulate systems in engineering*", Academic Press, San Diego, USA.

- Walstra, P., and Smulders, P. E. A., (1998). "Emulsion formation", *Modern Aspects of Emulsion Science*, Binks, B. P., (Ed.), The Royal Society of Chemistry, Cambridge, UK.

Appendix 3 PIV derivation of k and ε values

The work below fits after the third paragraph in section 2.4.10 to derive the equations quoted later in that section.

$$\overline{f(w,v)} = \text{mean } f(w,v) \text{ over valid data set D} = \frac{\sum_D f(w,v)}{|D|} \qquad \text{Eq. (7.5)}$$

Given a fixed location (z, y); a set D of $0 \leq |D| \leq 500$ repetitions of velocity measurements (w, v) were available. For any function f of the velocity components w, v, Eq. (7.5) gives the definition used for the time-average of f which was the average of all valid velocity vectors across the data set D. Since different locations contained different values of $|D|$, different sizes of set of valid velocity vectors, this method ensured all time-averaged calculations used the correct denominator in the division in Eq. (7.5).

The time-averaged values of velocity components w and v were then calculated by substituting $f(w, v) = w$ and $f(w, v) = v$ respectively into Eq. (7.5). The time-averaged values of w^2 and v^2 was also calculated for use in the variance calculation afterwards.

$$k = \frac{1}{2}\text{var}(\underline{v}) = \frac{1}{2}(\text{var}(u) + \text{var}(v) + \text{var}(w)) \qquad \text{Eq. (7.6)}$$

Calculation of turbulent kinetic energy (k) is defined in Eq. (7.6), see Gabriele, Nienow and Simmons (2009) where var(v) given above is equivalent to RMS of v defined in their paper. This calculation of k required knowledge of all three components of the velocity field $\underline{v} = (u, v, w)$, however from 2D PIV the component u (in ZY plane analysis) was not available.

$$\text{var}(u) \cong \frac{1}{2}(\text{var}(v) + \text{var}(w)) \qquad \text{Eq. (7.7)}$$

Using the isotropic assumption in Eq. (7.7), the variance of u was estimated to be the average of the variance of the other two components.

$$k = \frac{3}{4}(\text{var}(v) + \text{var}(w)) = \frac{3}{4}(\tilde{v} + \tilde{w}) \qquad \text{Eq. (7.8)}$$

Hence by substituting Eq. (7.7) into Eq. (7.6), an estimate for k in Eq. (7.8) was constructed. (Note that the variance of a quantity is the same as the RMS of the fluctuating component of that quantity, which is the third part of Eq. (7.8) above.)

$$\text{var}_{\text{pop}}(w) = \frac{\sum(w - \overline{w})^2}{|D|} = \frac{\sum w^2}{|D|} - \left(\frac{\sum w}{|D|}\right)^2 \qquad \text{Eq. (7.9)}$$

Individual variances such as var(w) in Eq. (7.8) were calculated using Eq. (7.9) which decomposed variance into contributions from time-averages of both w and w^2. The advantage of this decomposition was that it was not necessary to know the time-averaged value of w in advance. Since the number of data points was large (over 100) the population variance was very close to the sample variance, so the population variance was used exclusively.

Two different estimates for local specific turbulent energy dissipation rate (epsilon or ε) were also made; these were denoted ε_{de} and ε_{sgs}; they were based on the direct evaluation (DE) and sub-grid scale (SGS) approaches described in Khan's thesis (2005) and Gabriele, Nienow and Simmons (2009). Both required calculating spatial gradients in velocity components, and required multiple isotropic assumptions given by Khan.

$$\varepsilon_{\text{de}} = \upsilon_{\text{C}} \left[2\overline{\left(\frac{\partial w'}{\partial z}\right)^2} + 2\overline{\left(\frac{\partial v'}{\partial y}\right)^2} + 3\overline{\left(\frac{\partial w'}{\partial y}\right)^2} + 3\overline{\left(\frac{\partial v'}{\partial z}\right)^2} + 2\overline{\frac{\partial w'}{\partial y} \cdot \frac{\partial v'}{\partial z}} \right]$$

Eq. (7.10)

(υ_{c} is the continuous phase kinematic viscosity.)

$$\varepsilon_{\text{sgs}} = (C_S \Delta)^2 \left[4\overline{\left(\frac{\partial w'}{\partial z}\right)^2} + 4\overline{\left(\frac{\partial v'}{\partial y}\right)^2} + 2\overline{\left(\frac{\partial w'}{\partial y}\right)^2} + 2\overline{\left(\frac{\partial v'}{\partial z}\right)^2} \right]^{3/2}$$

Eq. (7.11)

(C_s is the Smagorinsky constant, estimated at 0.17, and Δ is the grid scale which was approximately 0.27 mm.)

Equations for ε_{de} and ε_{sgs} are given in Eq. (7.10) and Eq. (7.11) respectively, quoted with small adaptations of terminology from Khan (2005). The method for working out individual derivatives was as follows:

$$w' = w - \overline{w} = w - \frac{\sum w}{|D|} \quad \text{(similarly for } u, v\text{)}$$

Eq. (7.12)

$$\frac{\partial w'}{\partial z} = \frac{\partial}{\partial z}(w - \overline{w}) = \frac{\partial w}{\partial z} - \frac{\partial \overline{w}}{\partial z}$$

Eq. (7.13)

$$\left(\frac{\partial w'}{\partial z}\right)^2 = \left(\frac{\partial w}{\partial z}\right)^2 - 2\frac{\partial w}{\partial z} \cdot \frac{\partial \overline{w}}{\partial z} + \left(\frac{\partial \overline{w}}{\partial z}\right)^2$$

Eq. (7.14)

$$\overline{\left(\frac{\partial w'}{\partial z}\right)^2} = \overline{\left(\frac{\partial w}{\partial z}\right)^2} - 2\overline{\frac{\partial w}{\partial z} \cdot \frac{\partial \overline{w}}{\partial z}} + \overline{\left(\frac{\partial \overline{w}}{\partial z}\right)^2}$$

Eq. (7.15)

$$\overline{\left(\frac{\partial w'}{\partial z}\right)^2} = \overline{\left(\frac{\partial w}{\partial z}\right)^2} - 2\frac{\partial \overline{w}}{\partial z} \cdot \frac{\partial \overline{w}}{\partial z} + \left(\frac{\partial \overline{w}}{\partial z}\right)^2$$

Eq. (7.16)

$$\overline{\left(\frac{\partial w'}{\partial z}\right)^2} = \overline{\left(\frac{\partial w}{\partial z}\right)^2} - \left(\frac{\partial \overline{w}}{\partial z}\right)^2$$

Eq. (7.17)

$$\overline{\left(\frac{\partial w'}{\partial z}\right)^2} = \overline{\left(\frac{\partial w}{\partial z}\right)^2} - \left(\frac{\partial \overline{w}}{\partial z}\right)^2$$

Eq. (7.18)

Eq. (7.18) shows how to calculate an individual component for ε_{de} or ε_{sgs} in Eq. (7.10) and Eq. (7.11). These components are broken down into a time average of a squared gradient component, and a square of a time-averaged gradient component. All of these time-averages were calculated using Eq. (7.5) across all adjacent pairs of valid

velocity vectors where gradients could be calculated. Note that calculation of the cross term in Eq. (7.10) required four adjacent velocity vectors in order to calculate it. The sets D across which these time-averaged functions of velocity gradients were calculated were sparser than the underlying valid set, since valid pairs (or valid groups of four) were required for gradients (or gradient cross-terms).

(References and nomenclature in this appendix are given in Chapter 2.)

Appendix 4   PIV seeding bubbles and particles

Calculation of Stokes number for silver seeding particles

Neutrally buoyant silver-coated glass seeding particles of average diameter 10 μm were used. To check that they followed the flow faithfully the Stokes number (Stk) was calculated from a characteristic velocity gradient U, a characteristic length scale L and a characteristic time scale τ; this time scale depended in turn upon the particle density (ρ_d), the particle diameter (d) and the continuous phase dynamic viscosity (μ_c). Equations are given above in Eq. (2.2) and Eq. (2.3) for Stk and τ respectively.

It was only necessary to calculate Stk at the location of highest velocity gradient where the particles were most likely to fail to follow the flow. This location was found just after the orifice, where the turbulent jet intersected the recirculating fluid. The velocity gradient was of the same magnitude as the orifice superficial velocity.

Table 7.2: Stokes number calculations: particle density (ρ_d) 997 kg·m^{-3}; particle diameter (d) 10 μm; continuous phase viscosity (μ_c) 10^{-3} Pa·s give characteristic time (τ) of 5.54×10^{-6} s.

Orifice Type	Characteristic Length Scale (L, mm)	Area (mm^2)	Maximum Mass Flow Rate (kg·s^{-1})	Maximum Orifice Superficial Velocity (U, m·s^{-1})	Maximum Stokes Number (Stk)
0037	1.0	2.39	0.09128	38.4	0.212
0110	2.0	7.10	0.18223	25.8	0.071
0140	2.2	9.03	0.18249	20.3	0.051

Stokes numbers (Stk) were calculated at the orifice for three different orifices, at the maximum flow rate used for each; the values are given in Table 7.2 with in all cases Stk < 1. Tropea, Yarin and Foss (2007) showed that in this range particles followed the flow closely, with less than 1% inaccuracy for Stk < 0.1. Hence for the Sonolator it was

concluded that the silver seeding particles used followed the flow very closely and were capable of giving accurate PIV results.

Accuracy of using gas bubbles

During commissioning of the Perspex experimental rig for PIV it was found that gas bubbles appeared in the flow directly after the orifice. For a fuller discussion of the nature of these bubbles, see Appendix 1 in which cavitation and degassing in the Sonolator are discussed; the origin of the bubbles was water vapour cavitation and degassing of dissolved air. Dieter *et al* (1994) gives an example of conducting PIV with 50 μm hydrogen bubbles, c.f. Melling's (1997) list of PIV seeding particle attributes.

At low mass flow rate no gas bubbles were produced, so silver particles were required to seed the flow for imaging. Above the onset of cavitation gas bubbles were produced; as mass flow rate increased there were enough gas bubbles to completely seed the flow for PIV, making silver particles unnecessary. On the PIV photographs these gas bubbles were up to 3 pixels in diameter, which was around 50 μm, with Stk calculated at less than 0.1 due to their much lower density than silver particles. Therefore these gas bubbles were also suitable as PIV seeding particles.

Due to the different properties of 10 μm silver particles and gas bubbles of diameter up to 50 μm, experiments were carried out to check PIV gave the same results with both types of reflective particle. An intermediate flow rate was used which had just enough gas bubbles to seed the flow, but for which it was possible to put enough silver seeding particles in to swamp the effect of the gas bubbles and give a silver-particle-dominated PIV reading.

(a) Cavitation and gas bubbles only   (b) 10 µm silver particles added
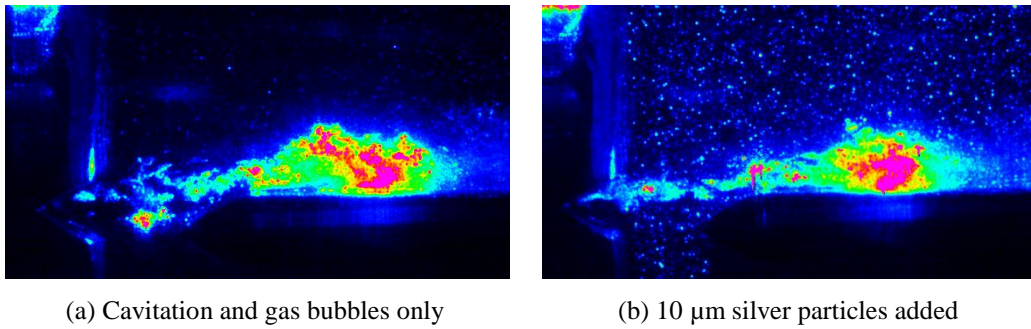
Figure 7.1: PIV images generated using different types of seeding particle.
Contrast enhanced using a pseudocolour scale.

Figure 7.1 shows individual PIV images for an intermediate flow rate after onset of cavitation, with gas bubbles only (a) and with silver particle excess (b). The PIV vectors produced from the image pairs therefore tracked flow trajectories of (a) gas bubbles and (b) silver particles. This allowed a direct comparison between the two reflective particle types. Using 500 image pairs from each type of experiment, two velocity data sets were produced to compare the experiments.
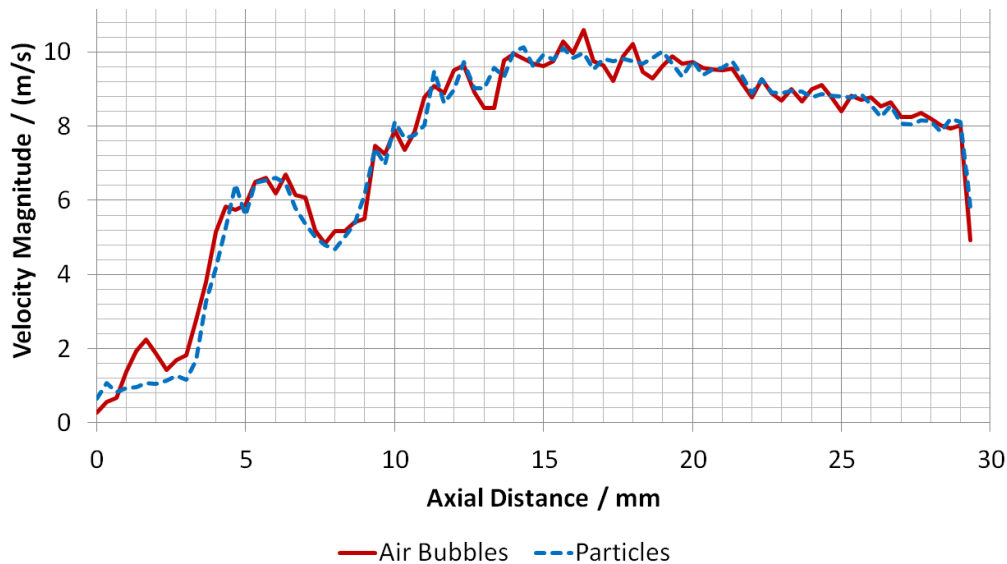
Figure 7.2: Comparison of PIV velocity measurements along a line in the
axial direction, 1 mm above orifice

The two velocity data sets were compared along several lines through the flow field; a typical comparison is given in Figure 7.2. The two sets of velocity magnitudes had a small degree of scatter, and within that degree of variation the two data sets coincided almost everywhere.

It was therefore concluded that the gas bubbles were as accurate as the 10 µm silver particles for usage as PIV seeding particles, under similar experimental conditions to those used here. Either type of seeding particle could be chosen without loss of accuracy.

Due to this finding, the general experimental procedure was to start with a high flow rate and carry out PIV seeded only with gas bubbles. As the flow rate was reduced in subsequent experiments, 10 µm silver particles were added as necessary for extra seeding particles in order to maintain the required seeding particle density given above.

Appendix 5   CFD preliminary simulations to ensure simulation accuracy

Varying simulation duration to ensure statistical convergence of time-varying measurements

Flow field quantities available in CFD included velocity components, pressure and turbulence variables. By averaging these over many time frames it was possible to obtain the corresponding average flow fields. Time frames were taken at regular intervals; 10 ms was found to be short enough to give well converged average results. The time steps used were much shorter than 10 ms (determined dynamically from the Courant number), hence many time steps were present in each time frame, and many time frames in each simulation.

Simulations of total duration 0.1 s, 0.25 s, 0.5 s, 1 s, 2 s and 4 s were carried out, and the time-average velocity magnitudes compared, in order to observe how many seconds of simulation time were necessary to get statistical convergence for the flow fields.
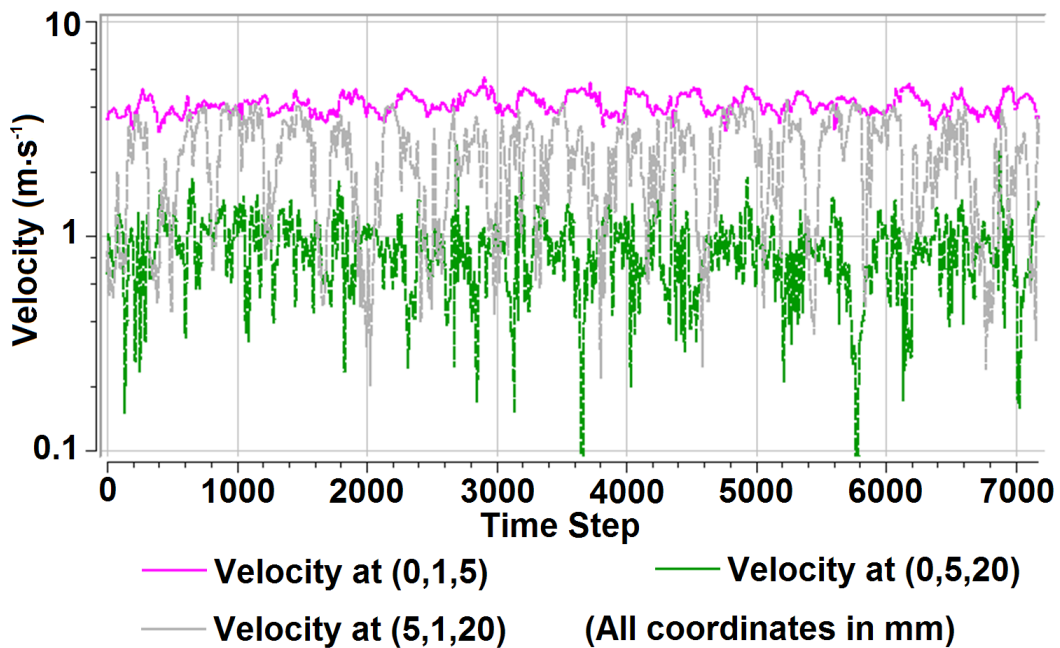
Figure 7.3: Graph of Velocity Magnitude (in m·s^{-1}) at a point vs Time Step, for simulation of duration 4 s. Coordinates (in mm) of the three points are: (5,1,20), (0,1,5), (0,5,20); origin is orifice, Z-axis is Sonolator axis, X, Y directions are long, short axes of orifice.

Figure 7.3 shows how the velocities measured at 3 points during the simulation changed with respect to time step. (One time step was approximately 0.56 ms in this simulation, which gave 1780 time steps per second of simulation time. Transient results were recorded around every 18 time steps, which was about every 10 ms.) The pink line illustrates transient velocity magnitudes 1 mm above the jet and 5 mm downstream from the orifice. In this location transient velocities fluctuated irregularly around a value of approximately 4 m·s^{-1}. These fluctuations has frequency of around 4 Hz and were irregular or noisy. All frequencies (whether regular or irregular) were much lower than the 1780 Hz rate of occurrence of time steps. Hence the time step was small enough in this simulation to resolve the transient details of the flow. The grey line (velocities at a point 1 mm above the jet, 5 mm out of the centreline, and 20 mm downstream from the orifice) and green line (5 mm above the jet and 20 mm downstream) showed smaller

velocity magnitudes but oscillations of the same period of around 4 Hz. It was concluded that the Sonolator jet with this orifice and flow rate, with the blade out, had regular fluctuations across the whole flow field, a feature seen clearly in 3D graphical analysis carried out. Further evidence for this is shown in a video provided in Appendix 14 as a CD insert.
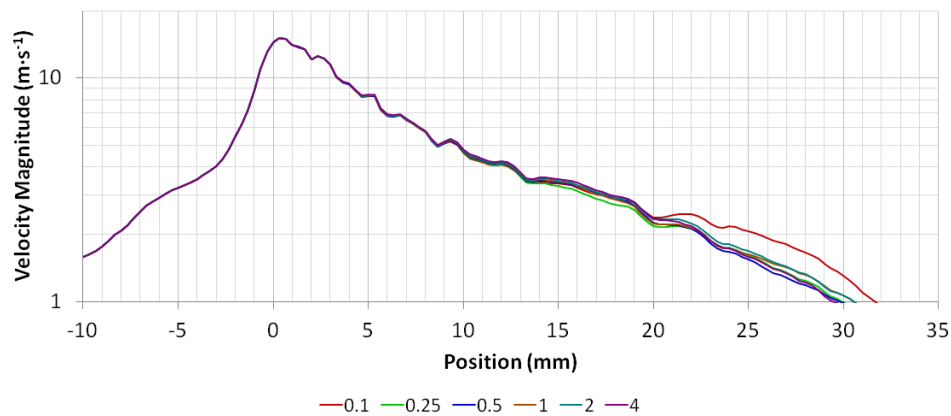
Figure 7.4: Graph of Velocity Magnitude vs Position along the Sonolator axis for 0110 orifice, med flow rate (0.092 kg·s^{-1}) for six different simulation durations (in seconds).
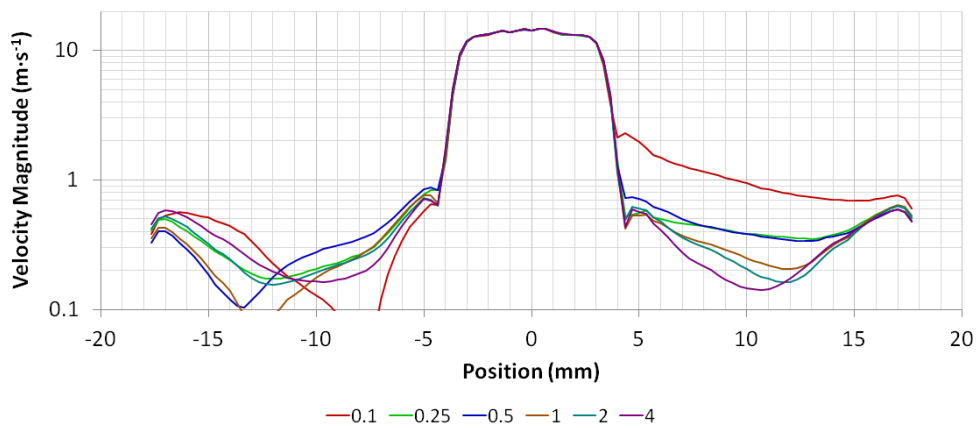
Figure 7.5: Graph of Velocity Magnitude vs Position along a line in the X direction passing through (0,0,1) coord (in mm) for six different simulation durations (in seconds).
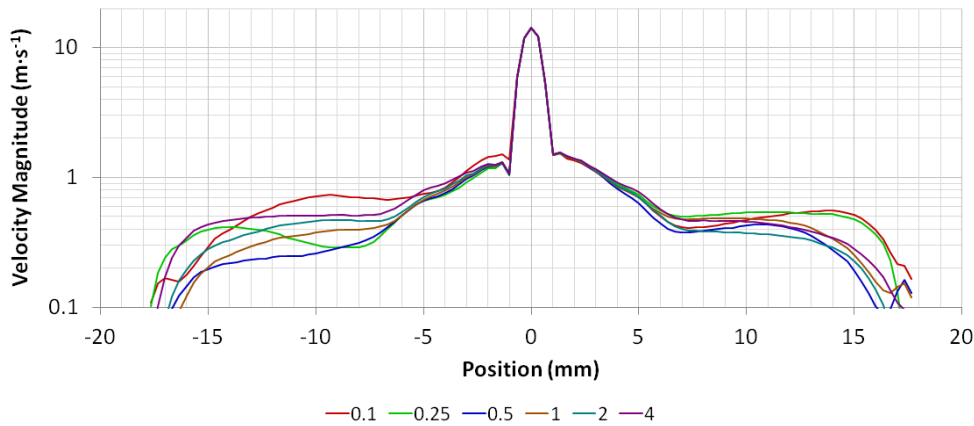
Figure 7.6: Graph of Velocity Magnitude vs Position along a line in the Y direction passing through (0,0,1) coord (in mm) for six different simulation durations (in seconds).

Graphs in Figure 7.4, Figure 7.5 and Figure 7.6 show the time-averaged velocity magnitude along various axes of interest, for six different simulation durations between 0.1 s and 4 s. Since the vertical axes are logarithmic, the vertical differences between data series give the ratios between the velocity magnitudes. Figure 7.4 shows that along the axis the peak velocities before the orifice, at the orifice and in the turbulent jet had converged even after only 0.1 s, up to 10 mm downstream of the orifice. Between 10 mm and 20 mm small differences started to emerge, which were largest in the 0.25 s data series. After 20 mm downstream of the orifice, the 0.1 s data series was noticeably different from the other five data series, showing that here the velocity magnitudes had not converged accurately enough after 0.1 s. Cross-sections in different directions (Figure 7.5, Figure 7.6) showed that the jet region (in the centre) had converged even after only 0.1 s, however the recirculation region surrounding the jet showed much variance in the ratios between measurements. The 0.1 s data series was the outlier in enough places to judge that it had not statistically converged. The 0.5 s data series was also an outlier in parts of the flow, and sometimes in the other direction to the 0.1 s series. This could be due to the average velocity magnitudes oscillating up and down as

the underlying flow undergoes periodic changes; the length of time-averaging affecting this direction of oscillation of the average.
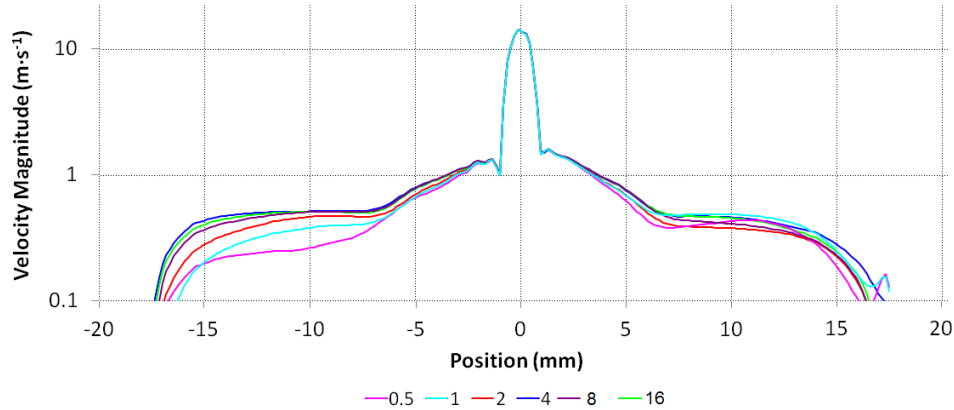
Figure 7.7: Graph of Velocity Magnitude vs Position along a line in the Y direction passing through (0,0,1) coord (in mm) for six different simulation durations (in seconds).

It was desired to check whether longer time scales were necessary for even better convergence, so simulations were extended to 8 and 16 seconds. Comparisons were made between six durations from 0.5 s to 16 s. Figure 7.7 gives one comparison for velocity magnitudes on a line in the Y direction, 1 mm after the orifice. It was found the three longest durations, 4 s, 8 s and 16 s simulations, clustered on all such graphs. The 0.5 s and 1 s results were significantly different from this cluster and judged "not converged"; the 2 s results were marginal in terms of convergence. By 4 s the simulation was judged fully converged, since its results were very close to those at 8 s and also those at 16 s.

Identifying this earlier time (4 s) as the time of convergence allowed later experiments to be stopped at a comparable time. Four seconds represented around 17 to 18 of the large-scale oscillations of the flow field, and two seconds represented around 8 to 9 of these oscillations. In order for a general simulation to converge, transient

samples ought to be taken repeatedly from all points on this oscillation cycle, for between 8 and 20 cycles (since each cycle was slightly chaotic and different, so many different cycles ought to be sampled). The sample time of 10 ms was sufficient to resolve the detail of individual cycles. General simulation length therefore was chosen to be between 8 and 20 complete cycles in order to ensure full convergence. When computational resources permitted, simulations were extended to 15 to 20 cycles to increase accuracy. Note that the exact simulation time therefore depended on the flow rate, since the flow oscillated faster when the flow rate was higher.

The purpose of this section of work was to determine a suitable simulation duration. It was judged from the data above that the simulation had converged, especially in the high-velocity region of interest near the orifice and in the jet, after 2 to 4 seconds of simulation time for this flow rate, and in general 8 to 20 oscillations of the flow field if those oscillations were in evidence. For blade-out simulations where oscillations were not so pronounced (due to the blade blocking the main up/down mode of fluid oscillation) the simulation length would remain 2 to 4 seconds.

Varying Arithmetic Precision and Courant Number

The two variables Courant Number (Maximum over the flow domain) and Arithmetic Precision (single or double precision arithmetic) were tested to see if they affected the outcome of CFD simulations Three cases were tested: a base case (A) and two variants: B with Courant Number reduced from 200 to 20, and C with Arithmetic Precision increased from single to double. These three simulations are listed in Table 7.3, with some sample results following:

Table 7.3: Simulations carried out to test effect of arithmetic precision and Courant number upon flow field.

Simulation	Courant Number	Arithmetic Precision
A	200	Single
B	20	Single
C	200	Double
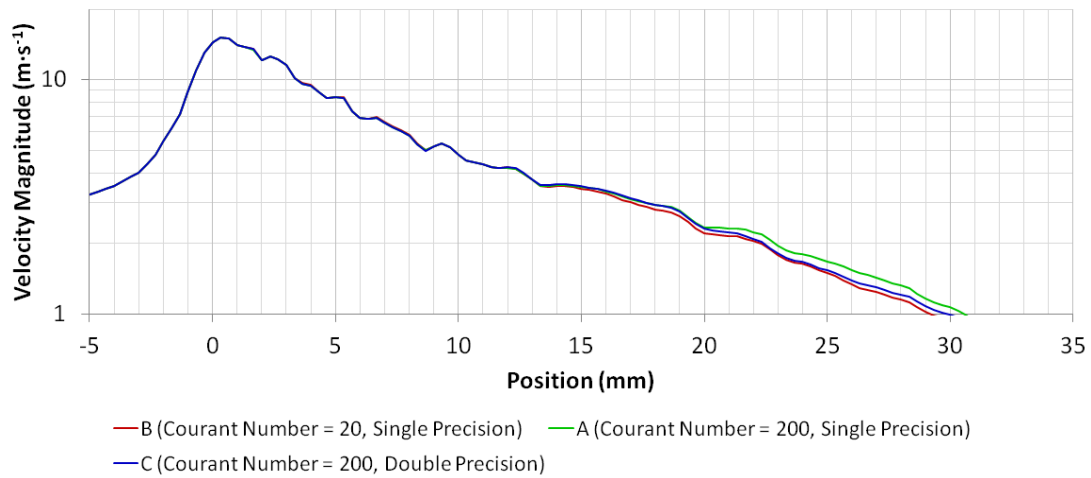
Figure 7.8: Graph of Velocity Magnitude vs Position along the Sonolator axis for 0110 orifice, med flow rate (0.09161 kg·s^{-1}).
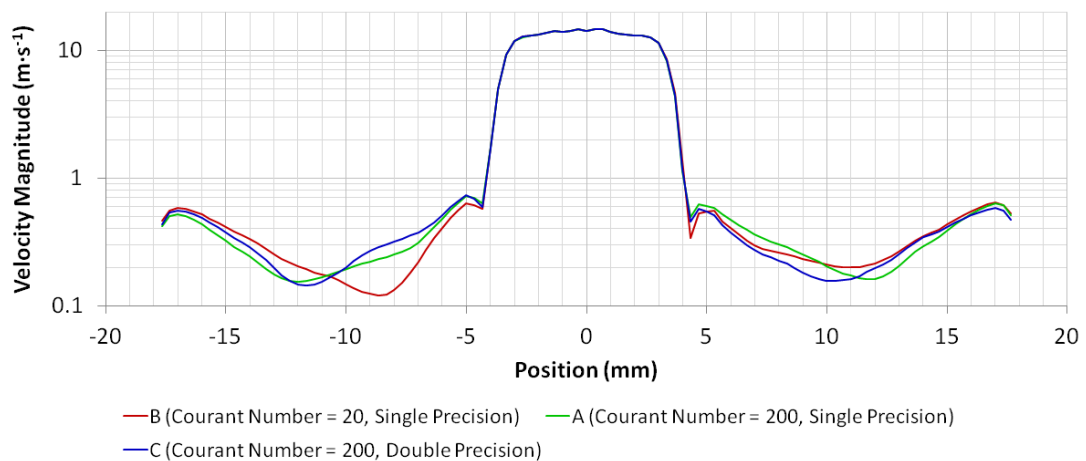
Figure 7.9: Graph of Velocity Magnitude vs Position along a line in the X direction passing through (0,0,1) coord (in mm).
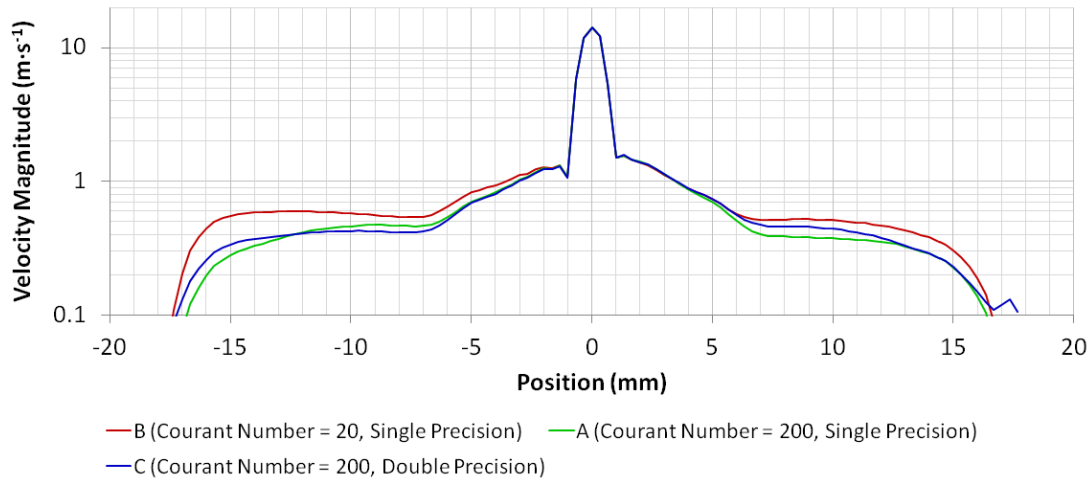
Figure 7.10: Graph of Velocity Magnitude vs Position along a line in the Y
direction passing through (0,0,1) coord (in mm).

Graphs in Figure 7.8, Figure 7.9 and Figure 7.10 show the velocity magnitude
along various axes of interest, with the three data series plotted together for comparison.
All vertical axes are logarithmic. In Figure 7.8 the peak velocity was found to be
indistinguishable between the three cases, and only when velocity reduced below
2 m·s^{-1} could the three cases be separated on the graph. Likewise, Figure 7.9 shows a
cross-section of the jet in its widest (X) direction. Within the jet the velocities match
well, and outside of the jet the differences amounted to less than approximately
0.1 m·s^{-1}. In Figure 7.10 where the cross-section is in the thin (Y) direction, this
agreement was also found within the jet, with some minor variation (up to 0.2 m·s^{-1})
outside the jet.
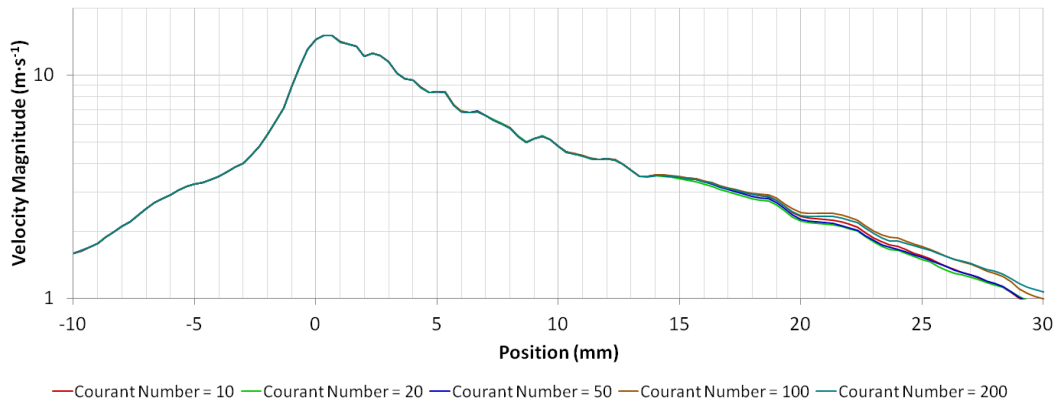
Figure 7.11: Graph of Velocity Magnitude vs Position along the Sonolator axis for 0110 orifice, med flow rate (0.09161 kg·s^{-1}).

In case any behaviour of interest had been missed, a wider variety of Courant numbers were also investigated, from 10 to 200. In Figure 7.11 the velocity magnitudes along the axis were plotted for these five series. No significant variation was seen along the axial line, or during further investigations within the high velocity region. It was concluded that CFD could be carried out at any desired Courant number where the simulation was stable: from 10 to 200 is illustrated above. Further work extended this range to 300, the approximate limiting Courant Number for simulations to successfully complete; above this number the simulations did not reliably complete.

Overall, it was clear that the two variables Courant Number and Arithmetic Precision had no major effect on the velocity field, and were very well matched within the jet region. Since this was the case, subsequent simulations would:

- Use single precision arithmetic

- Use a high enough Courant number to make the simulation run in a tractable amount of time, up to 300.

Varying mesh density and type

For the CFD results to be trustworthy it was necessary to demonstrate their mesh independence. Previously in Figure 7.11 a low density Delaunay mesh had been used. Now in Figure 7.12 the previous results were compared with medium and high density Delaunay mesh results, as well as results from three Octree meshes of varying mesh density. In order to further demonstrate trustworthiness, sample experimental results were also plotted. (These results were taken from PIV experiments described in Chapter 2; for a full comparison see Chapter 4.)
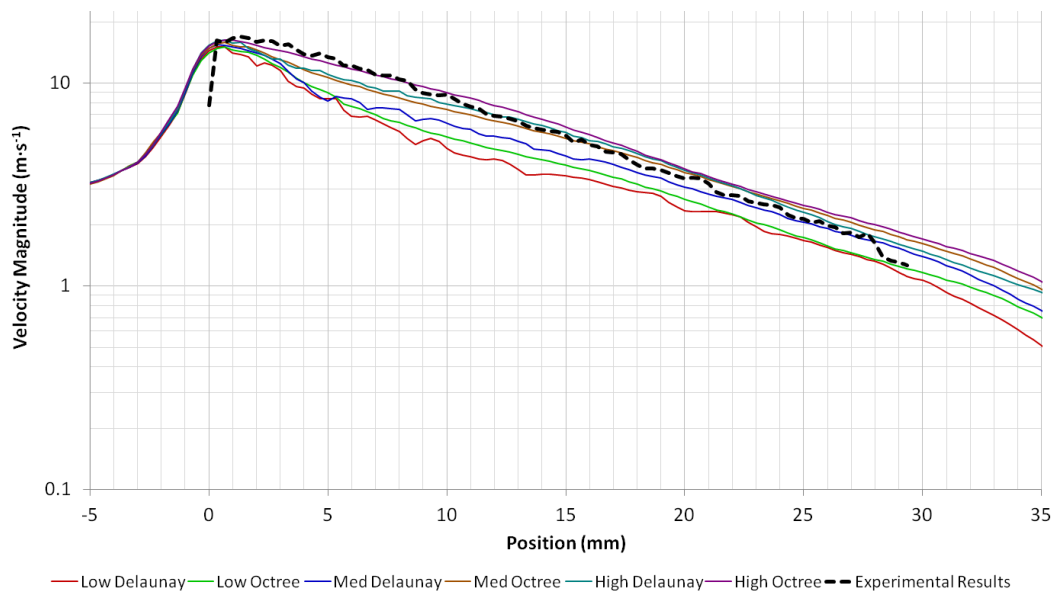
Figure 7.12: Graph of Velocity Magnitude vs Position along the Sonolator axis for 0110 orifice, med flow rate (0.0916 kg·s^{-1}); three mesh densities (low, med, high) and two mesh types (Delaunay, Octree) were used.

In Figure 7.12 all the six CFD data sets agreed before the orifice and at the peak velocity region in and just after the orifice. Some mesh dependence was found from 2 mm to 30 mm after the orifice; however the rate of decrease of velocity magnitude, approximately exponential, was seen to be the same in all six cases. Octree meshes gave more physical smooth decreases in velocity magnitude, whereas low and medium

density Delaunay meshes were affected by coarseness of the mesh which gave bumps as artefacts in the graphs. The meshes which gave velocity results closest to the sample experimental results were medium and high density Octree meshes, and high density Delaunay mesh. From this it was concluded that when increasing mesh density and seeking the point at which the results had converged, this point was after the low density meshes and before the high density meshes. Hence the low density meshes were no longer used.

Each of the high density mesh simulations was computationally expensive to use. Due to the large number of simulations required, it was not found practical to use these meshes in the bulk of the CFD results. Since the medium density Octree mesh was found to give simulations as accurate as the high density meshes, it was used for the bulk of the results. The medium density Delaunay mesh was used to generate comparison data sets for mesh independence demonstrations.

Checking boundary layers

Boundary layers were present in four locations: the inlet wall, orifice wall, main chamber wall and blade. Velocity gradients were expected to be high here, and were resolved using a "prism layer" of thin mesh cells close to the wall, up to 4 cells from wall to main flow region. It was verified in CFD-Post that velocities in this prism layer varied continuously and quickly from zero at the wall to non-zero in the main flow region. Average y_+ (dimensionless wall distance) was obtained from ANSYS CFD-Post output. The average found to be 10 for a typical simulation, with a range of 0 to 75. The turbulence model used (SST-SAS) was able to resolve the flow for both low or high values of y_+. Overall, the boundary layer was found to be simulated appropriately.

Checking global conservation of mass

Mass is always conserved in processes such as fluid flows. Hence the mass flow rate at the outlet of the Sonolator, measured during the simulations, must match the mass flow rate at the inlet that was specified in the boundary conditions. Due to the fluid being an incompressible liquid of constant density there was a corresponding conservation of volume, i.e. volumetric flow rate at outlet must match that at inlet.

Local conservation of mass in individual mesh cells was monitored by the simulations. Simulations in each time step were required to converge to at least one part in ten thousand, for most simulations the convergence was much higher than this. This convergence was a root-mean-square average of the degree to which each mesh cell failed to conserve mass (and other conserved quantities such as momentum were also monitored). The question was whether this high degree of local conservation of mass gave rise to a similarly high global conservation of mass between the Sonolator's inlet and outlet.

The global conservation was measured using the following technique: Both inlet and outlet surfaces were perpendicular to the z axis in the simulations. Therefore, the w component of velocity (the velocity component in z direction) was perpendicular to both the inlet and the outlet. ANSYS CFD-Post allowed area integrals of velocity in the z direction to be calculated over both inlet and outlet surfaces; these gave the respective volumetric flow rates.

Typical results (for 0110 orifice with medium flow rate and blade out, final time step) were 9.168×10^{-5} m^3 s^{-1} at the inlet and 9.370×10^{-5} m^3 s^{-1} at the outlet. Taking the ratio between these showed a total conservation error of 2.2%. Other orifices and flow rates were investigated, as well as blade in simulations, and conservation errors were

comparable. This level of accuracy in global mass flow rate conservation was judged suitably high for the purposes here.

Appendix 6   Sample Analysis detail

Choice of sample analysis technique

Many different techniques exist for measuring droplet size distributions: for example dynamic light scattering (DLS) for 1 nm to 1 µm particles, Coulter counting for 0.4 µm to 400 µm particles, laser diffraction for 0.05 µm to 300 µm particles, Phase-Doppler anemometry, video microscopy; these are all described in Padron (2005) with the merits of each method discussed in depth.

For the purposes of this study, a technique was required which could be used for off-line analyses of samples of emulsions in size ranges including 1 µm to 100 µm. DLS was not possible since the emulsion droplets were larger than 1 µm. Coulter counting had the disadvantage that large droplets could potentially block the measurement orifice; the pre-emulsions used in this study would contain droplets large enough to do this. Phase Doppler anemometry, an online measurement of both velocity and size, could not cope with the smallest particles expected in the emulsions produced on the Sonolator. Video microscopy was possible, but required a very large number of individual particles to be analysed to obtain accurate results: potentially very time consuming and with issues of sampling error.

Laser diffraction was attractive since it operated off-line, was fast and convenient to carry out taking around 5 minutes per emulsion sample, was flexible to measure any combination of emulsion droplet sizes, was most accurate for spherical particles such as those in an emulsion, and required no calibration against a standard since it operated from fundamental light scattering principles. Disadvantages of the light diffraction technique included sensitivity to dirt and air bubbles, and erroneous selection of material properties (refractive indices), both of which could cause erroneous peaks in

the final distribution due to the model inappropriately fitting the scattering pattern measured. In addition, dilution was necessary in order to get the laser obscuration in the correct range, which risked changing the sizes in the sample. By adding SLES to the water diluents this risk was minimised.

Particle or droplet size analysis by laser diffraction was made practical by computers to solve the inverse algorithms to calculate the drop size distributions from the measured diffraction patterns and stable low-cost lasers and detectors. It operated by time-averaging the amount of detected light at various angles, given a laser flux at zero angle, and employed an inverse algorithm to determine which particle size distribution must be present to scatter the light as detected (Hall 2012).

Description of laser scattering technique used

A Malvern Mastersizer 2000 (Malvern Instruments, Malvern, UK) with a Hydro SM small volume dispersion unit was used to characterise the samples (Figure 7.13). It operated by measuring light scattered from a laser beam travelling through a dilute emulsion sample, and solving for the droplet size distribution from the scattered light using Mie scattering theory. This same device had previously been used by Hall to characterise similar emulsions, and its mode of operation with advantages and disadvantages was discussed in depth there (Hall 2012).

Figure 7.13: Malvern Mastersizer 2000 being used to measure aqueous
samples.

Each emulsion sample was measured in the dispersion unit in the following way:
The cuvette of the Mastersizer was cleaned at the start of the experiment with SLES
solution to eliminate any oil droplets on the glass; it was found not necessary to repeat
this later on as long as the dispersant contained SLES. The dispersant in the Hydro SM
was dilute SLES solution (0.1 wt% to 0.5 wt%) made from diluting 10 wt% SLES
solution with distilled water, which prevented oil droplets from depositing on the
cuvette and the tubing of the Mastersizer. This SLES solution had effectively the same
refractive index as water (Table 5.1) to 2 decimal places. It was filled in such a way as
to eliminate as many air bubbles as possible, in particular the impeller in the Hydro SM
dispersant unit was set not too high to discourage foaming, around 1300 rpm.

After the laser diffraction background was stable, the background measurement
was taken for at least ten seconds on the Mastersizer, and had to be low enough to

demonstrate the initial cleanliness of the system without any dispersed droplets or contaminants. During this time, the emulsion sample was gently agitated in order to break any flocculation of droplets and ensure each emulsion droplet was separated.

Between five droplets and five millilitres of emulsion sample were added to the Hydro SM; enough to produce a laser obscuration of between 5% and 20% in the Malvern which was the manufacturer recommended range for measurement; enough droplets for a high enough reading compared to the background, but not high enough to give significant error from multiple droplet diffraction. At least two separate measurements of at least ten seconds each were carried out on each sample, so that results could be corroborated, and that erroneous peaks due to contaminants could be spotted and the measurement repeated using clean dispersant. Both red light and blue light measurements were used which increased accuracy, especially for small droplets.

Accuracy of Droplet Size Distribution measurements

Repeat experiments were included in each experiment setup, where all experiment parameters were identical but samples were taken at two widely separated times in the experiment. Mastersizer measurements for these pairs were compared. In general there was very good agreement between such droplet size distributions (DSDs), showing that both the experiment and the measurement were repeatable.

Occasionally contaminants were present in the sample or dispersant which caused erroneous peaks to appear in the droplet size distribution. These normally showed a few volume percent of the distribution to be either much smaller or much larger than the rest of the distribution. One characteristic of this was that the peak appeared on a measurement, but not on the subsequent measurement (since every measurement was carried out at least twice). The DSDs produced by the Mastersizer were individually

examined, and were rejected for re-measurement if the two or three measurements did not agree, especially if multiple peaks appeared on only one of the measurements.

Other causes of multiple peaks were: choosing wrong refractive indices for continuous and dispersed phases, and not putting enough emulsion sample in the Mastersizer to give a light scattering significantly above background. The latter fault was corrected generally by increasing the laser obscuration in the Mastersizer to 10% to 15%; eliminating the former is discussed below.

Selection of continuous and dispersed phase refractive indices

The Mastersizer 2000 operates on the principle of solving an inverse problem. Given a droplet size distribution and laser light transmitted through a droplet-containing region, a level of scattering is produced which can be calculated from Mie theory. The inverse problem which the Mastersizer software carried out was to deduce the DSD from the light scattering pattern. In order to do this, the continuous and dispersed phase refractive indices were required. Suitable accuracy was 2 decimal places. Water has an RI of 1.333 (Table 5.1). The dispersed phase was DC245 (3.8 cSt) or silicone oils of viscosity 10 cSt, 350 cSt or 10 000 cSt. Measurements were made of their refractive indices (Table 5.1) showing bulk oil RI values in the range 1.397 to 1.404.

The refractive indices of the individual droplets coated with SLES may have varied from the 1.40 value (to 2 dps) of the bulk property. The refractive index of 28 wt% SLES solution was measured at 1.370 by the author using the refractometer described earlier; this was greater than the RI of 1.333 for pure water. It is expected that the RI of pure solid SLES is therefore much greater than 1.370. It was therefore feasible that small oil droplets coated with a continuous layer SLES, in water, had true refractive indices greater than the RI of the bulk material.

Hall *et al* (2011) used a calibrated RI value of 1.42 for Mastersizer analysis of the same silicone oil / SLES / water system described earlier. Since the true RI of the droplets was not known, calibration of refractive index was carried out by varying RI across a range and choosing the RI value which minimised the residuals, as well as giving believable droplet size distributions (e.g. omitting any erroneous peaks like those described earlier). These residuals were the error between the true scattering pattern and the scattering pattern produced by the modelled DSDs. For further detail, please see Hall (2012), especially his Appendix B regarding drop size measurement.

In this work, a similar calibration was carried out. It was found that when RI was in the range 1.42 to 1.44 the modelled droplet size distributions (solutions of the inverse scattering problem) were almost identical and d_{32} values in particular were almost constant. The usual value for RI was 1.42, increasing this value up to 1.44 as necessary to eliminate spurious peaks in the Mastersizer analysis.

Evidence of sample stability over time

Pure oil in water emulsions would be expected to coalesce quickly. As previously shown, SLES was usually present at many times the CMC value, and its addition would be expected to prevent coalescence of newly formed droplets. Padron (2005) stated that adding surfactant would stabilise a sample removed from a system, making it representative of that system. Calculations showed that assuming each SLES molecule occupied 0.6 nm^2 on the emulsion droplet surface (Goloub & Pugh 2003), **average** drop size of 0.2 µm (very small!), oil phase fraction of 10 wt%, SLES concentration of 0.5 wt%, average molar mass of 420 g·mol^{-1} for SLES; then the surfactant supply was 143% of that necessary to cover all the droplet surfaces entirely. Since measured drop sizes were almost always above 1 µm and oil phase fraction was usually 2 wt% or

5 wt%, surfactant was judged to be in excess supply throughout and capable of fully stabilising the droplets.

For the experiments to characterise emulsification in the Sonolator, the emulsion samples taken had to be stable from the time of emulsification until the time of measurement on the Mastersizer, in order for the results to be meaningful.
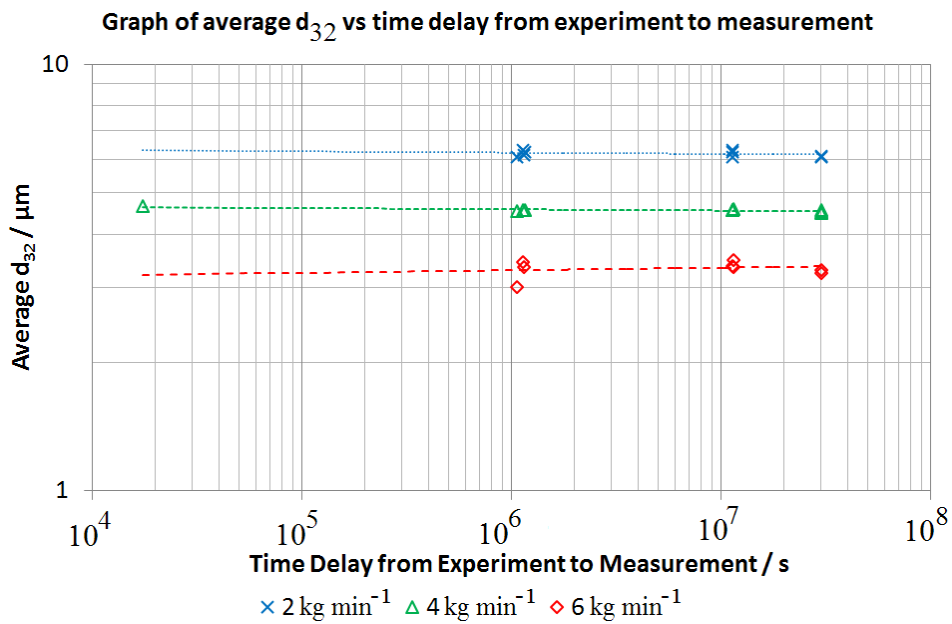
Figure 7.14: Graph of d_{32} vs time delay from experiment to measurement. Three flow rates illustrated for 10 cSt silicone oil. Time delays shown are equivalent to between 4 hours and 350 days.

Emulsion samples from weeks 1 and 2 were kept under ambient conditions (temperature between 22°C and 27°C) and repeatedly sampled using the Mastersizer at various intervals from less than one day to several months, giving a variable delay between experiment and measurement. Figure 7.14 shows how d_{32} measured on a Mastersizer varied with respect to time; no significant change in d_{32} was found with respect to time as evidenced by the flat trend-lines.

The question nevertheless remained whether there was significant change in DSD from the moment of emulsification to when the sample was measured at several hours

old. For these reasons this is unlikely or irrelevant: firstly, the data in Figure 7.14 extrapolated backwards gives no reason to believe droplets were of significantly different size at the time of emulsification. Secondly, as previously explained the surfactant was always present in a large excess for the amount needed to coat emulsion droplets (except in Week 4 experiments where SLES concentration was purposefully reduced well below 0.5 wt%) so the droplet size distribution would be expected to stabilise in less than a second as the emulsion surfaces became saturated with surfactant and the emulsion exited from the droplet breakage region.

For these reasons, the silicone oil / water / SLES emulsion stability was suitable for the characterisation of the Sonolator.

Discussion of which variables to measure and analyse

The pilot plant Sonolator experiments had many different variables associated with them. These could be broadly classified as: input, measured and derived variables. Input variables were fixed by the experimenter at the start of the experiment. Measured variables were outputted by physical measurements during the experiments or during later sample analysis. Derived variables were not directly observable but derived from other variables. All of the variables in these three categories which were considered are listed below in Table 7.4:

Table 7.4: List of input, measured and derived variables.

Input	Measured	Derived
Oil stream inlet condition (PE: oil pre-emulsion; TMIX: oil stream mixed at T-junction upstream of Sonolator inlet; INJ: oil stream injected at orifice)	*From Mastersizer 2000*:	Peak epsilon after orifice (epsilon or ε is local specific turbulent energy dissipation rate; it scales with velocity cubed, but can only be estimated here by defining a characteristic length scale)
Fluid density (held at approximately 997 kg·m^{-3} during these experiments since all samples were dilute aqueous emulsions)	1) Sauter mean diameter (Volume-surface mean diameter, d_{32})	Jet length (the jet starts at the orifice, but needs a cut-off point defined)
Temperature and pressure (held at ambient conditions throughout experiments; approximately 25°C, 1.01 kPa)	2) Volume mean diameter (d_{43})	Volumetric flow rate (Q, mass flow rate divided by constant density)
Mass flow rate (M) set point	3) Median and Mode diameters (from volume weighted distribution)	Orifice superficial velocity (v, Volumetric flow rate divided by orifice area)
Oil weight fraction (related to φ, dispersed phase volume)	4) Span (w) and Skewness (s) parameters	
SLES weight fraction	*From Sonolator rig data*:	
Oil viscosity	5) Measured mass flow rate (M)	
Orifice area (A_o)	6) Pressure drop (ΔP)	
Blade present (or not) and its position		
Back pressure valve position		

Variables which were not investigated

Not all of these variables were investigated during emulsification experiments: varying working fluid density (ρ) or temperature, or varying ambient (outlet) pressure remains as further work. Volumetric flow rate (Q) was disregarded; constant density rendered it proportional to mass flow rate (M). Measured mass flow rate was disregarded since the rig data showed it was always within 1% of mass flow rate set point at the sample times. Jet length was not observable in the opaque Sonolator set-up, so could not be derived through any convincing method.

Choice of variable to represent "average" droplet size

For this simple silicone oil in water with SLES emulsion system, the main physical descriptor for each sample was the emulsion droplet size distribution, and the most important feature of that was an average droplet size. However, there was no unique way to define that average size for two reasons: firstly the distribution could be weighted by number, length, surface area or volume; secondly because given a particular distribution different averages exist such as mean, median and mode.

In the analysis which followed, volume weighting was chosen since the frequencies in the distribution corresponded to a volume of oil present as particular droplet diameters, an industrially useful measure. Later on in Eq. (5.1) and Eq. (5.2) the span (w) and skewness (s) were defined as depending on 10th, 50th (median) and 90th percentiles of the volume weighted distribution.

Different averages available as direct outputs from the Mastersizer analysis were: d_{32}, d_{43}, volume-weighted median and volume-weighted mode. A general definition of d_{nm} is given in Eq. (7.19), where $f(x)$ is the number weighted droplet size distribution:

$$d_{nm} = \sqrt[n-m]{\frac{\sum x^n f(x)}{\sum x^m f(x)}} \qquad (n > m) \qquad \text{Eq. (7.19)}$$

(Reference: Walstra 1983)

Out of these four distinct measures of average droplet size, d_{32} was chosen to be "the" average in subsequent analysis for two reasons. Firstly, many industrially useful properties of emulsions depend on the effective surface area of the emulsion per unit volume (a_s); d_{32} is directly related to this effective surface area in Eq. (7.20), where φ is the dispersed phase volume. Secondly, d_{32} was found to be the most repeatable measure of the four. Some emulsion samples had their droplet size distributions measured

multiple times, and the mean and standard deviations of each type of average were found. The lowest error (standard deviation divided by mean) was found overall for the d_{32}, especially for 10 000 cSt oil where bimodality made other averages such as the mode change rapidly due to only small changes in the relative sizes of the two peaks.

$$a_s = \frac{6 \cdot \varphi}{d_{32}}$$
<div align="right">Eq. (7.20)</div>

(Reference: Leng and Calabrese 2004)

Hence the words "average drop size" will hereafter be synonymous with "d_{32}", or "averages of multiple d_{32} values" where appropriate.

Definition of flow rate variables

In the earlier list of variables, many of them were related to flow rate, e.g. mass flow rate (M), Sonolator pressure drop (ΔP), various epsilon (ε) measures, etc. Some others were not, e.g. orifice size (A_o), back pressure valve position, oil inlet condition, etc. In this second list, each variable could be investigated by varying it between 2 or more positions, and seeing what effect was had upon a graph of drop size (d_{32}) vs flow rate. In order to do this, the best flow rate variable had to be selected. This section investigates which flow rate variable was most appropriate to plot on the x-axis of a d_{32} vs flow rate graph.

The flow rate variables were: mass flow rate (M), orifice superficial velocity (jet velocity, v), Sonolator pressure drop (ΔP), total power dissipated in the flow (P), derived epsilon (local specific turbulent energy dissipation rate, ε). Volumetric flow rate (Q) was not investigated since in these experiments it was directly proportional to mass flow rate (M). Equations for each variable are as follows:

$$Q = \frac{M}{\rho} \qquad \text{Eq. (7.21)}$$

$$v = \frac{Q}{A_\mathrm{o}} \qquad \text{Eq. (7.22)}$$

$$\Delta P = \frac{1}{2}\,\rho\left(\frac{v}{C_D}\right)^2 \qquad \text{Eq. (7.23)}$$

(Reference: Perry 1998)

$$P = Q \cdot \Delta P \qquad \text{Eq. (7.24)}$$

Fluid Density (ρ) was that of water and constant across all experiments, due to the low oil volume fractions used. Sonolator orifice discharge coefficient (C_D) was investigated and found to be approximately a constant of value 0.79 across different flow rates and orifice areas; this agreed with the value stated by the manufacturer (Sonic 2011). Orifice area (A_o) was constant in each individual experiment, but not constant across all runs.

Epsilon (ε) was specific turbulent energy dissipation rate in the region of droplet breakage, a region likely to be close to the orifice, and in/around the turbulent jet. The variable ε could not be measured directly. A model for ε was desired in terms of jet velocity (v) and a characteristic length scale (L). Dimensional analysis was carried out on these three variables in terms of their units of length [L] and time [T]: ε had units [$L^2 T^{-3}$], v had units [L T^{-1}] and L had units [L]. This gave Eq. (7.25) where ε was proportional to v^3 and inversely proportional to L:

$$\varepsilon = C\,\frac{v^3}{L} \qquad \text{Eq. (7.25)}$$

To determine the constant C in Eq. (7.25) it was not possible to use data from Sonolator emulsification experiments since local values for ε after the orifice were

unknown. Earlier (see Chapter 3) CFD simulations had been carried out for the Sonolator, in which 3D data for all of ε, v and L were available. These data were gathered for multiple flow rates and orifice sizes: ε was chosen to be the maximum value of turbulent ε after the orifice, and L the square root of orifice area; with these assumptions C was found to have value of 0.008669. (However in the results section below when different choices of L are compared only Eq. (7.25) will be used, factoring out the effect of the constant using correlations instead of magnitudes.)

Some different choices of characteristic length scale (L) for the Sonolator included: orifice short diameter, orifice long diameter, difference between these two, square root of orifice area, jet length scale, distance from orifice to vena contracta, distance over which epsilon (in CFD work) drops by a fixed factor, say by a factor of 10. There was no *a priori* reason for choosing one of these length scales above another. In the results below, four different epsilons have been calculated for comparison, based on the first four characteristic length scales listed above, since these were measurable and the latter length scales were not.

Based on the above equations, the following proportionalities were found:

$$M \propto Q \propto v \propto \sqrt{\Delta P} \propto \sqrt[3]{P} \propto \sqrt[3]{\varepsilon} \qquad \text{Eq. (7.26)}$$

The only directly measurable quantities above were mass flow rate (M) and Sonolator pressure drop (ΔP). During rig commissioning it was found that mass flow rate squared was almost exactly proportional to pressure drop. This was tested across flow rates between 0.025 kg·s^{-1} to 0.108 kg·s^{-1}; coefficient of determination (R^2) was 0.9999, which verified the above proportionality.

Appendix 7   Choice of variable to represent "flow rate"

The overall aim of these experiments was to understand how different variables affect the emulsion properties, in order to build predictive capability. In particular, it was desired to predict d_{32} from as few variables as possible with as much accuracy as possible. Hence the flow rate variables were compared by ranking how strong the correlations were with d_{32}. This was carried out separately for different oil viscosities and for SLES at 0.5 wt% only, but all other experimental conditions were grouped into one data set.

Eight different variables were plotted against d_{32}, each graph with four series for the four different oil viscosities. The eight variables were: mass flow rate (Figure 7.15), jet velocity (Figure 7.16), pressure drop (Figure 7.17), power dissipation (Figure 7.18), epsilon based on: square root of nominal orifice area (Figure 7.19), orifice short diameter (Figure 7.20), orifice long diameter (Figure 7.21) and orifice diameter difference (Figure 7.22). Data obtained for different size orifices were combined into the same series so that if one (or more) of the eight variables caused orifice size to be factored out automatically, it would give a better correlation, showing that the variable could predict droplet size for multiple orifices.
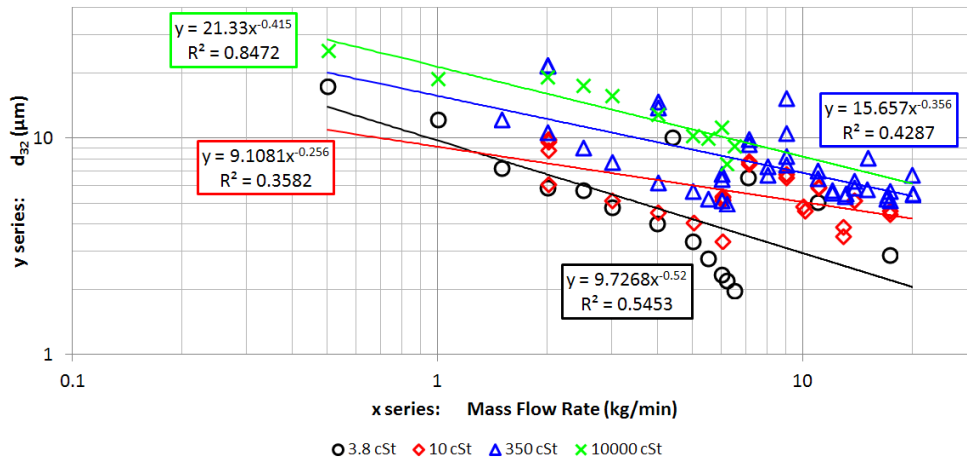
Figure 7.15: Graph of d_{32} vs Mass Flow Rate. Four data series for: 3.8 cSt, 10 cSt, 350 cSt and 10 000 cSt oil. All experiments had SLES present at 0.5 wt%. Data from all trials listed above, excluding 0080 trials by D Ryan.
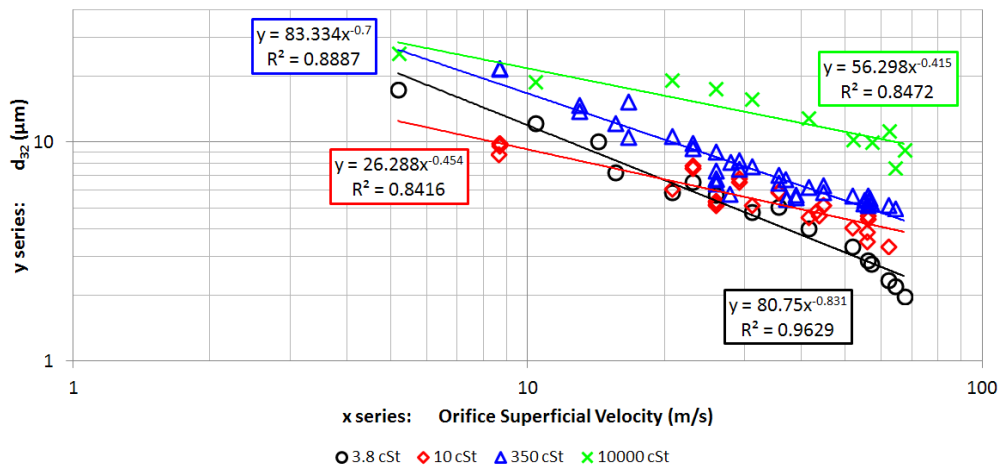
Figure 7.16: Graph of d_{32} vs orifice superficial velocity (which is the same as jet velocity). Same data as previous figure.
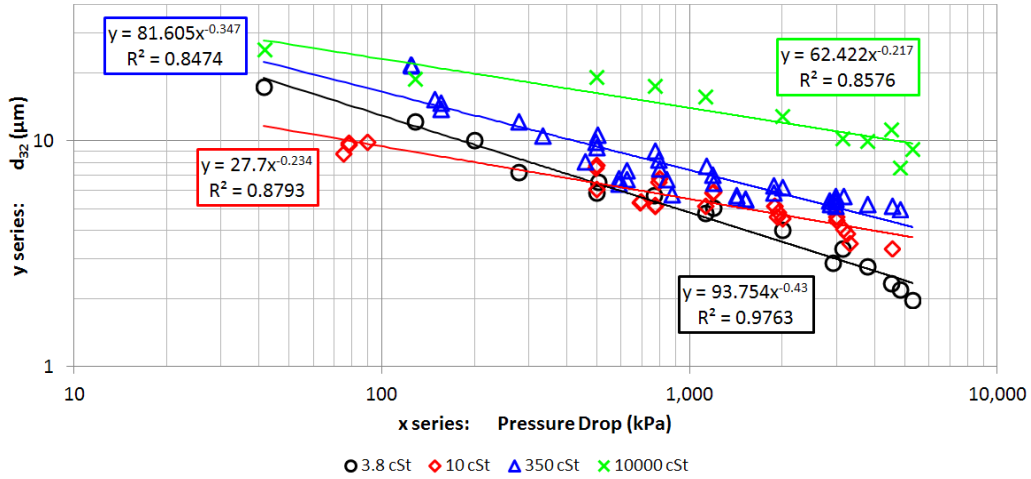
Figure 7.17: Graph of d_{32} vs Sonolator pressure drop.
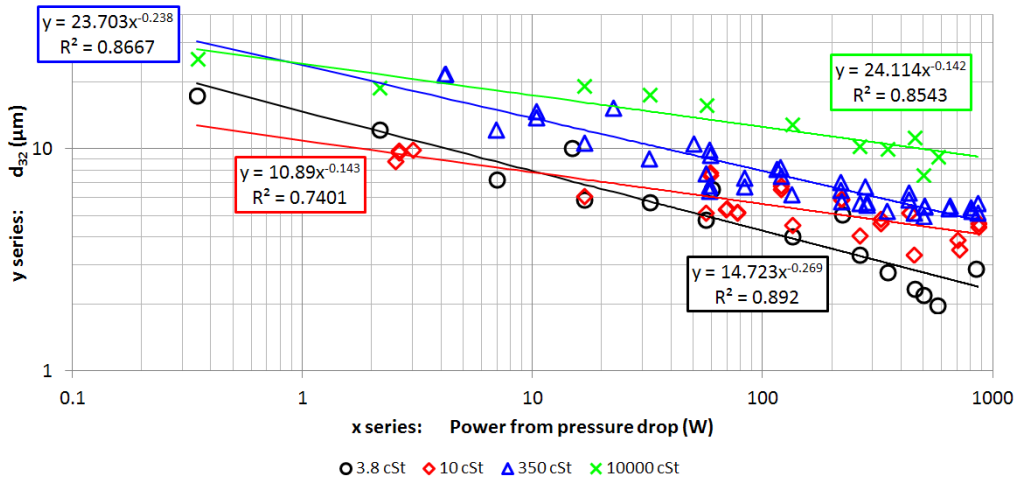
Figure 7.18: Graph of d_{32} vs power dissipated.
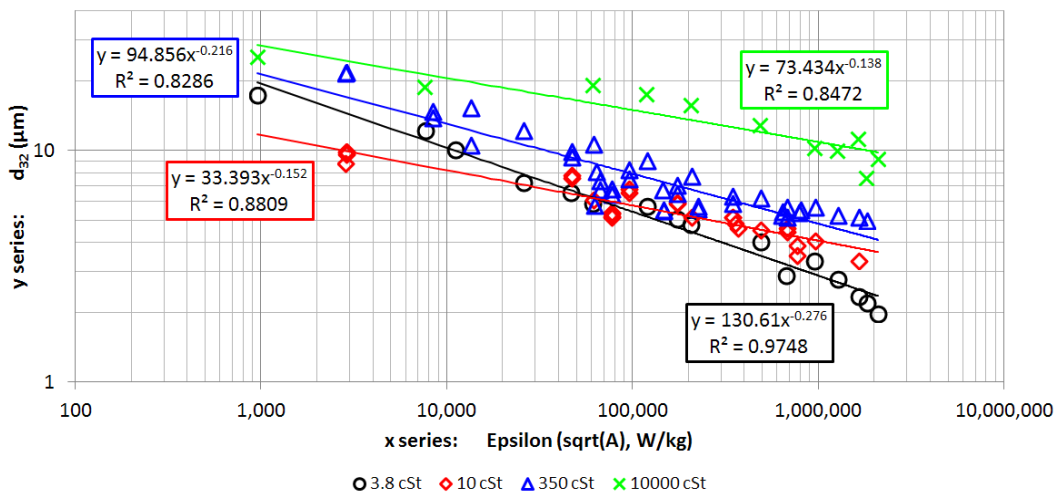
Figure 7.19: Graph of d_{32} vs epsilon (characteristic length is the square root of nominal orifice area).

377
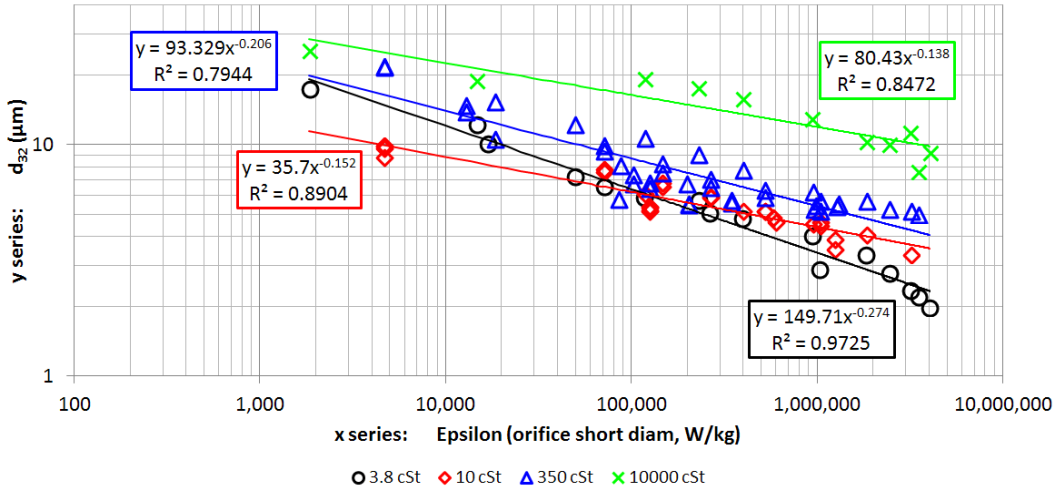
Figure 7.20: Graph of d_{32} vs epsilon (char. length is orifice short diameter).
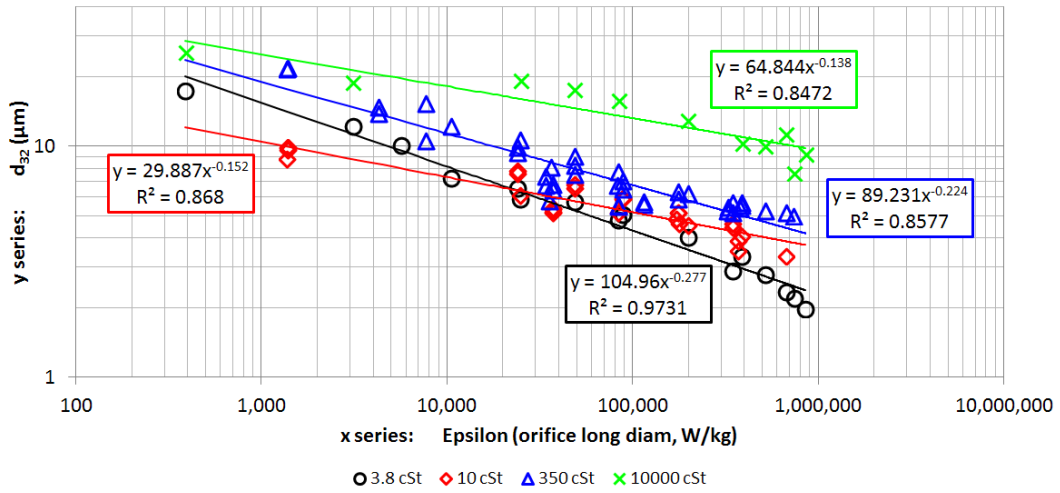
Figure 7.21: Graph of d_{32} vs epsilon (char. length is orifice long diameter).
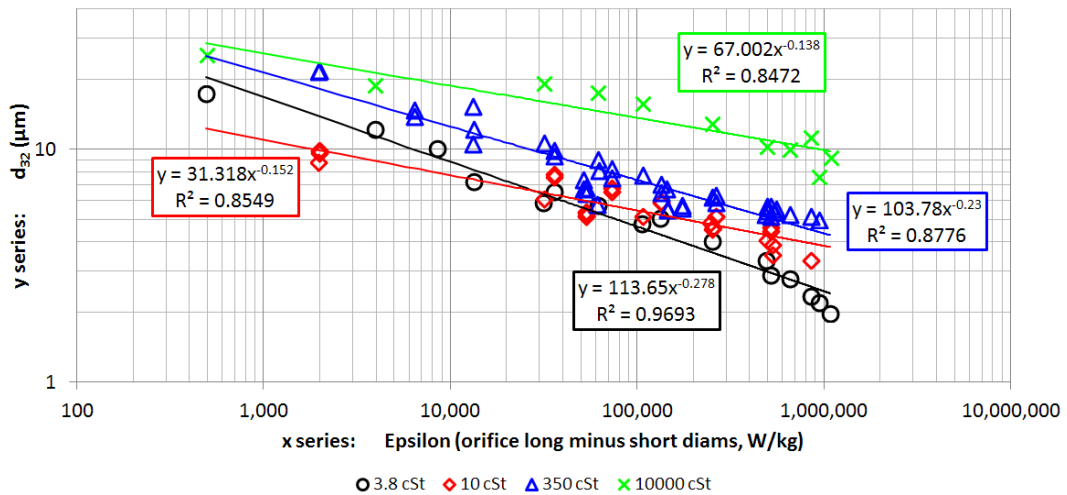
Figure 7.22: Graph of d_{32} vs epsilon (char. length is different between orifice long and short diameters).

The eight "d_{32} vs flow rate variable" comparisons, with four correlations each for four different oil viscosities, are presented in Figure 7.15 to Figure 7.22; the lines of best fit and correlations (of the form $y = A\,x^B$) were added using Microsoft Excel: y was d_{32} and x was the flow rate variable.

A visual inspection showed that mass flow rate (Figure 7.15) did not form good correlations. The data for oils of viscosities 3.8 cSt (DC245), 10 cSt and 350 cSt each formed two different data series. As expected, each data series was for a different size of orifice. Larger orifices for a fixed mass flow rate gave lower pressure drop, hence lower energy dissipation rates, lower droplet disruption and thus larger droplets. It was found that "d_{32} vs mass flow rate" graphs were valuable only for fixed orifice size. When the orifice size varied in a particular data set, a different variable was appropriate. The other seven variables (Figure 7.16 to Figure 7.22) all formed better correlations with d_{32} than mass flow rate; these correlations were compared in Table 7.5:

Table 7.5: Coefficients of determination (R^2) for correlations between d_{32} and each flow rate variable on the x-axis. Total score was the sum of the four R^2 values.

X-axis variable	R^2 3.8cSt	R^2 10cSt	R^2 350cSt	R^2 10000cSt	Total score	Total - Max
Mass Flow Rate	0.545	0.358	0.429	0.847	2.179	-1.381
Orifice Superficial Velocity	0.963	0.842	0.889	0.847	3.540	-0.020
Sonolator Pressure Drop	0.976	0.879	0.847	0.858	3.561	0.000
Power due to Pressure Drop	0.892	0.740	0.867	0.854	3.353	-0.208
Epsilon based on sqrt(A)	0.975	0.881	0.829	0.847	3.532	-0.029
Epsilon based on short orifice diameter	0.973	0.890	0.794	0.847	3.505	-0.056
Epsilon based on long orifice diameter	0.973	0.868	0.858	0.847	3.546	-0.015
Epsilon based on difference between orifice diameters	0.969	0.855	0.878	0.847	3.549	-0.012
					3.561	Max

In Table 7.5 the coefficients of determination (R^2) are presented; all correlations were quite good (near to 1), except for those for the mass flow rate variable. This meant that the other variables could predict d_{32} quite well in the relevant ranges of experimental conditions.

To determine the best variable of these seven, the sum of the R^2 (four for each variable) was formed, and the variables compared based upon this sum. The maximum of 3.561 was achieved by the variable "Sonolator Pressure Drop". By subtracting this value (Total – Max column) it was seen that "Orifice Superficial Velocity" as well as three of the epsilon variables were also good predictors of d_{32}. Less good was "Power Dissipation" and the epsilon based on short orifice diameter. The worst was "Mass Flow Rate" due to the multiple orifices in the data.

In conclusion to the investigation of which variable to plot d_{32} against, **pressure drop** was the variable of choice which appeared to be best at factoring in changes of geometry, e.g. by varying the orifice size; however some of the epsilon variables were not significantly worse. Pressure drop was still preferred since it was directly measurable; the epsilons were not directly measurable and also required a choice of characteristic length scale to be made without (yet) having a sound basis for choosing one length scale over another.

Appendix 8   Variables with insignificant effect on d_{32}

Several experimental setup variables were investigated. For each variable, multiple series were plotted on graphs of d_{32} vs pressure drop; each series for a different value of the variable. Where multiple series formed distinct curves of d_{32} vs pressure drop, the variable was judged to have significant effect on droplet size; conversely when multiple series overlapped the variable was judged to be insignificant. The latter cases of insignificant variables are presented in this section; the former case of significant variables, in the next section.

Five different variables were found insignificant in affecting d_{32}; evidence for this is presented below. Note – only data for SLES at 0.5 wt% is used in this section. This is so that surfactant is always well in excess of both CMC and saturation of droplet interfaces with surfactant.

Effect of Oil weight fraction upon d_{32}

Increased oil weight fraction might be expected to affect emulsion droplet size distribution via several means. Firstly, coalescence would be increased before newly formed droplets became coated with surfactant, increasing final droplet size. Secondly, increased volume fraction would increase emulsion viscosity and possibly affect droplet size directly, or via a change in amount of energy available per droplet for droplet breakage.

$$t_{\text{ads}} = 10^{-6}\, \rho^{1/5}\, \gamma^{-1/5}\, \varepsilon^{-1/5} \qquad \text{Eq. (7.27)}$$

(Adapted from Walstra and Smulders (1998) changing units of ε to W kg^{-1})

Calculations were carried out regarding coalescence. Surfactant adsorption time t_{ads} for convective transport of surfactant in turbulent inertial emulsification regime (see

Chapter 6) was given by Walstra and Smulders (1998) as Eq. (7.27) above. Using the following order of magnitude values: density (ρ) of 1000 kg·m^{-3}, interfacial tension (γ) of 0.01 N·m^{-1}, ε of 100 000 W·kg^{-1}; t_{ads} was 1 μs. Walstra and Smulders (1998) stated that 10 t_{ads} droplets should be fully coated with surfactant, preventing coalescence. Therefore, coalescence in this system would typically only be possible within 10 μs of the original droplets splitting.

Walstra and Smulders (1998) also calculated that for volume (or weight) fractions of up to 10% dispersed phase, with droplets larger than 1 μm (both applicable in experiments presented in this chapter) the collision timescale was larger than the adsorption timescale. Therefore coalescence was unlikely due to split droplets being quickly coated with surfactant before collisions would occur. Hence this model emulsion system was suitable to characterise droplet breakage in the Sonolator, preserving the droplet size distributions originally present upon emulsification. This had already proved to be the case when characterising a Silverson rotor-stator mixer, as reported by Hall, Cooke, El-Hamouz and Kowalski (2011) and Hall (2012).

Nonetheless, in order to gain clarity about the effect of weight fraction of silicone oil, this variable was varied between 0.5 wt% and 10 wt%. The effect upon d_{32} was observed.
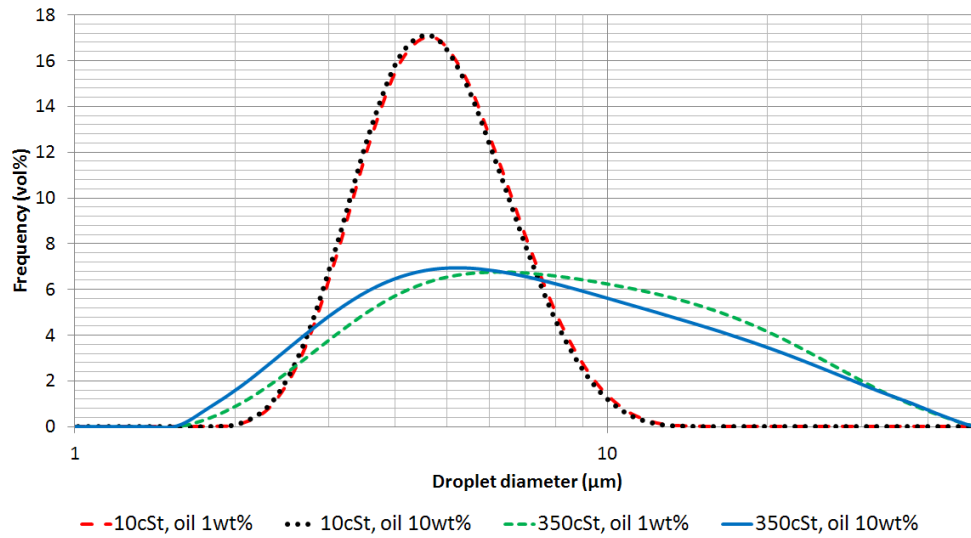
Figure 7.23: Droplet size distributions for 10 cSt and 350 cSt oil emulsified at 1 wt% and 10 wt%. Fixed orifice size (0025), mass flow rate 0.067 kg·s⁻¹, SLES concentration 0.5 wt%.

In Figure 7.23 it was observed that there was no significant change in droplet size distribution for 10 cSt oil emulsified at 1 wt% and 10 wt%. For 350 cSt a small change was observed. To determine how significant this effect was, six further experiments were performed were constructed for these two oil viscosities at three mass flow rates, for fixed SLES concentration of 0.5 wt% and fixed orifice size (0025). These series are displayed in Figure 7.24:
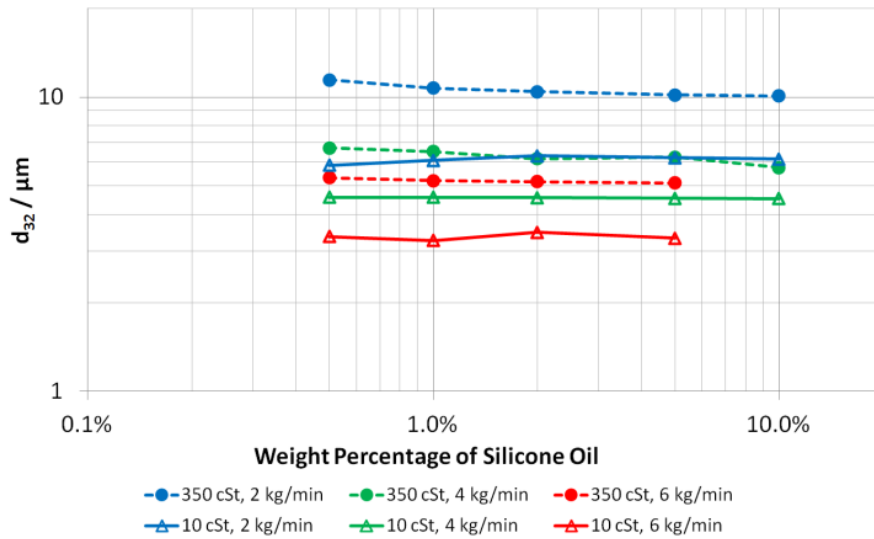
Figure 7.24: Graph of d_{32} value vs oil weight fraction for 10 cSt and 350 cSt silicone oil, for mass flow rates of 0.033 kg·s^{-1}, 0.067 kg·s^{-1}, 0.100 kg·s^{-1}; orifice size 0025.

The data series show that oil concentration in the range 0.5 wt% to 10 wt% has a barely significant effect upon d_{32}. No consistent significant effect was seen for other combinations of flow rate, orifice size or other experimental configuration. This mirrors the finding of Hall (2012) who observed that dispersed phase volume fractions of up to 50% had minimal effect on the droplet size of emulsions produced on a Silverson in line rotor stator mixer.

Walstra & Smulders (1998) give six main effects of high dispersed phase concentration upon emulsification, so it was expected that if oil concentration was increased up to 50 wt% oil some significant effect would occur. Extra factors could include: faster coalescence and more turbulence depression which could result in larger droplets, and increased emulsion viscosity which could change the turbulence breakage regime and affect droplet size.

Subsequent to this finding in the first "week" of experimental runs, data points with experimental conditions which only varied by oil weight fraction were either

combined into the same data set or averaged together to give a combined d_{32} value. In later runs, oil weight fractions of 2 wt% and 5 wt% were carried out, and droplet size distributions directly compared again. The distributions were always very close, validating that d_{32} could be averaged across experiments which only varied by weight fraction in the range 0.5 wt% to 10 wt%.

Effect of experimental rig used

Two different experimental rigs were available: "Hair" and "Muscle". These were very similar Sonolator rigs. The main differences were that "Muscle" was rated to process flammable fluids and had smaller orifice sizes, and that "Hair" had bigger orifice sizes and was not flammable rated.
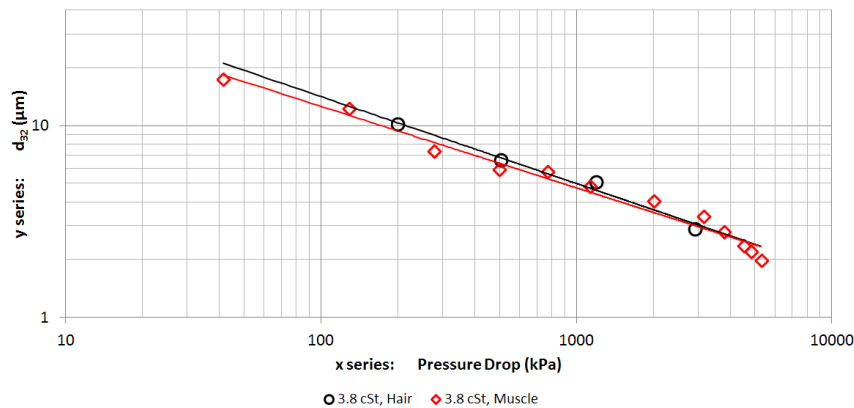
Figure 7.25: Graph of d_{32} vs pressure drop for 3.8 cSt oil, for the two different experimental rigs "Hair" and "Muscle" at Unilever Research & Development, Port Sunlight.
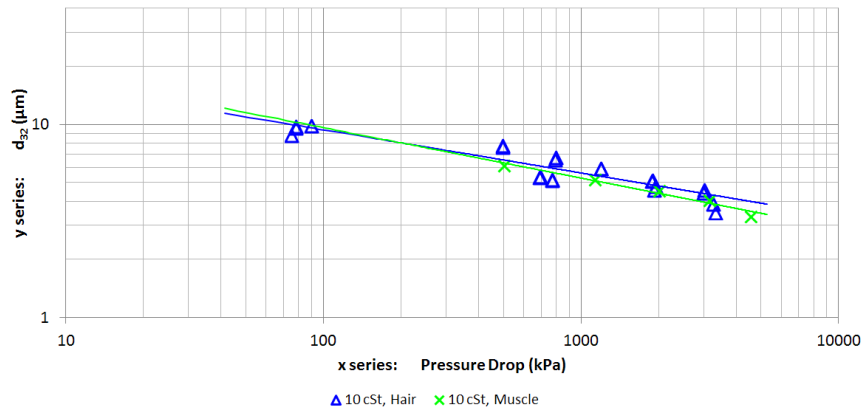
Figure 7.26: Graph of d_{32} vs pressure drop for 10 cSt oil, for "Hair" and "Muscle" rigs.
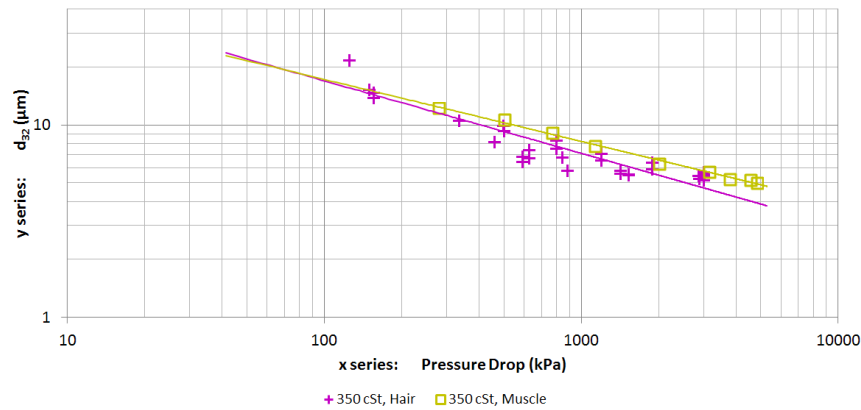
Figure 7.27: Graph of d_{32} vs pressure drop for 350 cSt oil, for "Hair" and "Muscle" rigs.

The pairs of trendlines in each Figure 7.21, Figure 7.22 and Figure 7.25 above show that droplet sizes were comparable between the two rigs for both low and high viscosity oils. It is expected that future results are therefore reproducible across different Sonolator rigs.

Effect of Back-pressure valve position

The back-pressure valve was located on the outlet pipe of the Sonolator, about 100 mm to 200 mm downstream of the orifice. It could be either fully opened, to leave a large gap for the product to travel through, or fully closed which left only a small circular gap between the cone and the cylinder for the fluid to travel to. This contributed

a small amount of extra pressure drop, but only of a few percent of the entire pressure drop.
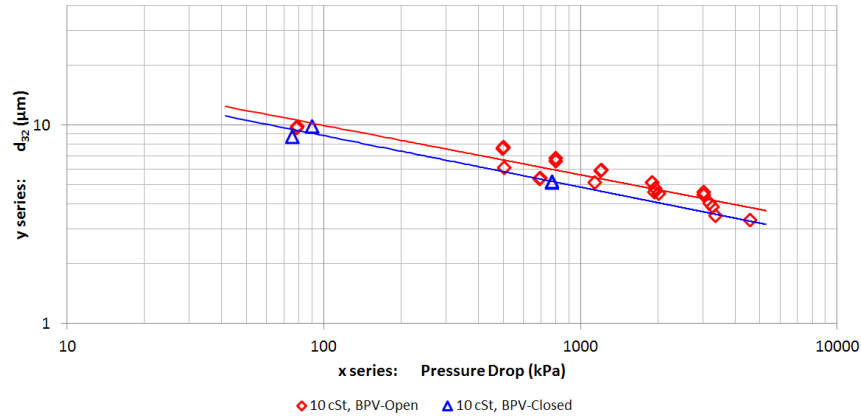
Figure 7.28: Graph of d_{32} vs pressure drop for 10 cSt oil, with the back pressure valve open or shut.
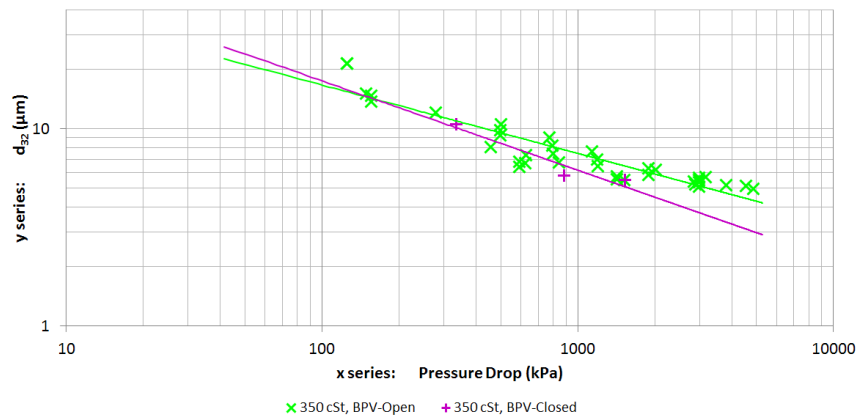
Figure 7.29: Graph of d_{32} vs pressure drop for 350 cSt oil, with the back pressure valve open or shut.

In Figure 7.28 for 10 cSt oil although some of the data points give a smaller d_{32} for the same pressure drop, there is no clear separation between the two data sets. In Figure 7.29 for high viscosity oil no significant effect is found by closing the backpressure valve. Therefore, the back-pressure valve does not significantly contribute to emulsification, over and above the effect of its pressure drop (which is already factored into the pressure drop variable). An increase in backpressure may, however, reduce cavitation near the orifice, see Appendix 1 on cavitation in the Sonolator.

Effect of Oil inlet condition (PE, INJ, TMIX)

During these experiments the oil was introduced in three distinct ways: as a pre-emulsion with SLES (0.5 wt%) in a stirred tank; injected as a separate stream directly into the orifice using an injector; mixed into the aqueous stream at a T-junction upstream of the Sonolator. These were denoted PE, INJ and TMIX respectively.
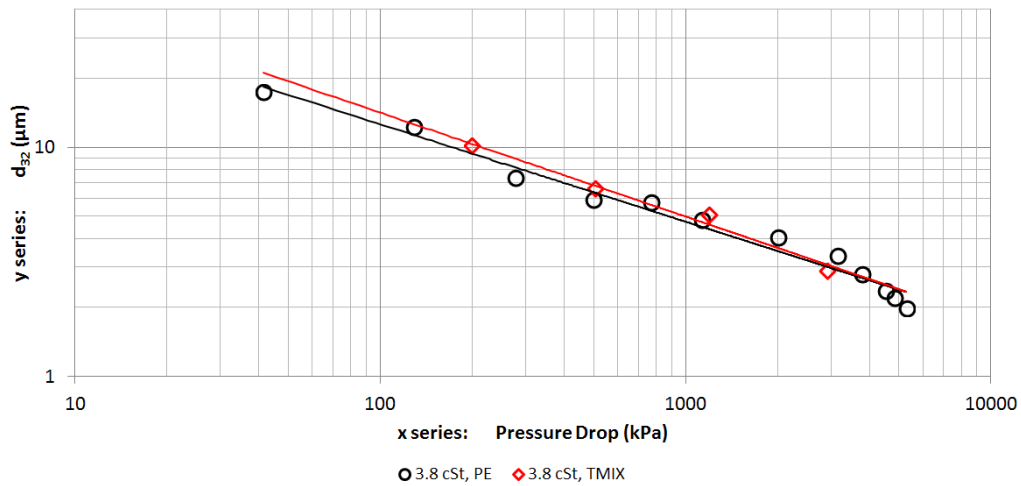
Figure 7.30: Graph of d_{32} vs pressure drop for 3.8 cSt oil, for inlet conditions PE and TMIX.

In Figure 7.30 the inlet conditions PE and TMIX were compared for DC245 (3.8 cSt). The two data sets were overlapping; their respective trendlines were very close together. No significant difference resulting from the difference inlet regimes was found.
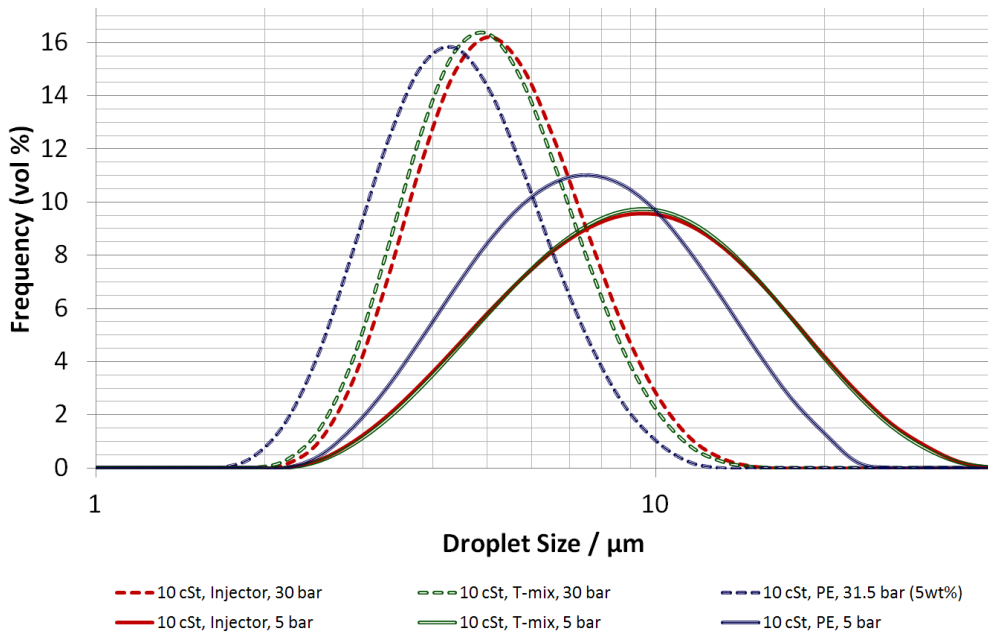
Figure 7.31: Droplet size distributions for 10 cSt oil emulsified at 500 kPa
and 3000 kPa (5 bar, 30 bar) using INJ, PE and TMIX.

In Figure 7.31 the droplet size distributions were plotted for 10 cSt oil between PE (blue), TMIX (green) and INJ (red) inlet regimes, for two different pressure drops. TMIX and INJ were indistinguishable, whereas PE had marginally lower drop sizes. (Note that data for an exact match in pressure drop was not available for 10 cSt, PE; the best match has been used.)
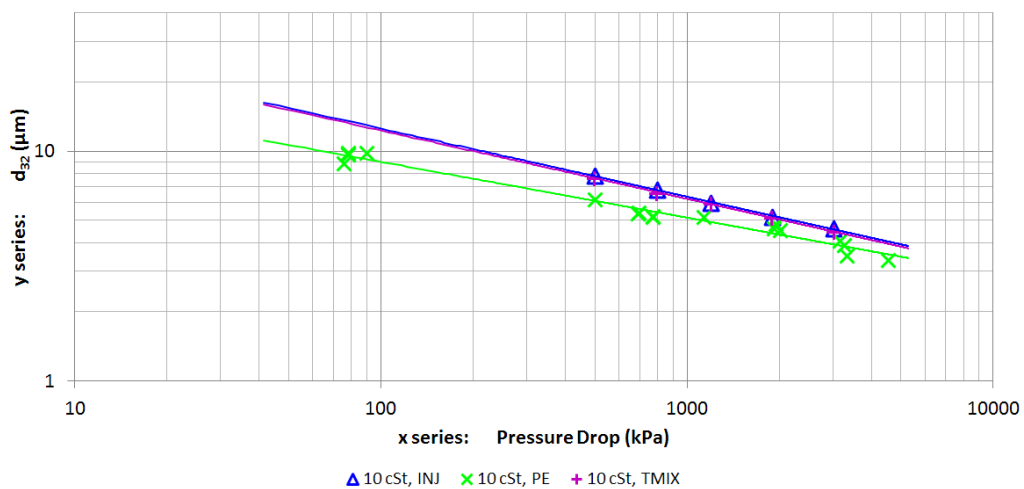
Figure 7.32: Graph of d_{32} vs pressure drop for 10 cSt oil, for inlet conditions
INJ, PE and TMIX.

In Figure 7.32 the corresponding 10 cSt data for many pressure drops for all three regimes was plotted, showing PE overall gave slightly smaller drop sizes than INJ or TMIX, whose data sets almost coincided.
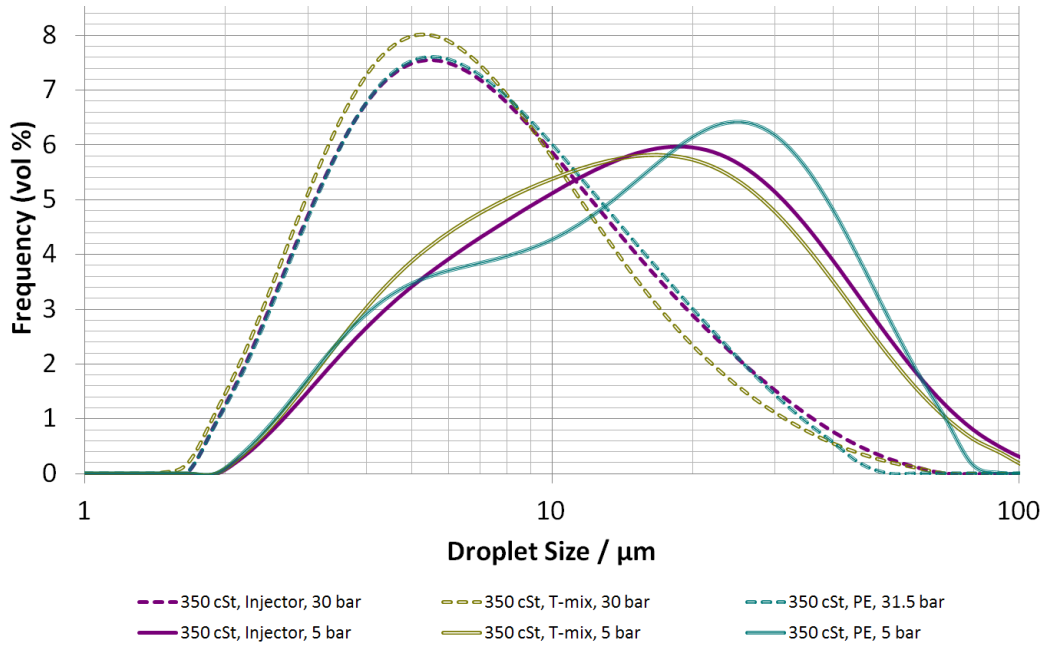
Figure 7.33: Droplet size distributions for 350 cSt oil emulsified at 500 kPa and 3000 kPa (5 bar, 30 bar) using INJ, PE and TMIX.

In Figure 7.33 droplet size distributions are plotted for the three inlet regimes, this time for 350 cSt oil. At each pressure drop the DSDs overlapped considerably. Although at the lower pressure drop there was more variation in DSD, the variation was still not very large.
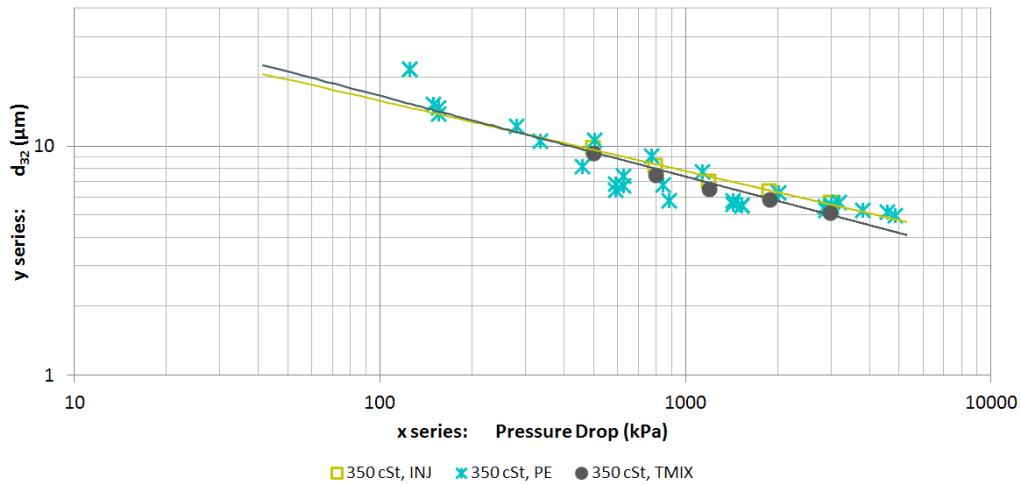
Figure 7.34: Graph of d_{32} vs pressure drop for 350 cSt oil, for inlet conditions INJ, PE and TMIX.

In Figure 7.34 the data points for INJ and TMIX are seen to lie in the middle of the mass of PE data. Hence no significant difference was seen between the three inlet regimes for 350 cSt oil.

Comparing the three oil viscosities: no effect from oil inlet condition was noted from the DSDs or the d_{32} vs pressure drop trends for 3.8 cSt or 350 cSt oils, and only a small difference in d_{32} (12% to 25%) was seen at 10 cSt between the PE data set and the TMIX/INJ data sets. Since these 10 cSt experiments (PE vs TMIX/INJ) were carried out on different rigs, orifices and times; it was judged more likely that a small systematic error between the results sets was present for the 10 cSt oil, and overall there was in fact no significant effect from oil inlet condition for any viscosity, as evidenced by the 3.8 cSt and 350 cSt data sets.

Effect of Orifice size

Orifice size had a large effect on the size of emulsion droplets produced, for fixed mass flow rate; however as shown in Figure 7.17 earlier when d_{32} was plotted against pressure drop there was low scatter for each dispersed phase viscosity. This indicated

that the pressure drop variable already factored in a large proportion of the effect of changing orifice orifice size. This section was to identify whether altering the orifice size affected d_{32} above and beyond the effect due to changed pressure drop.
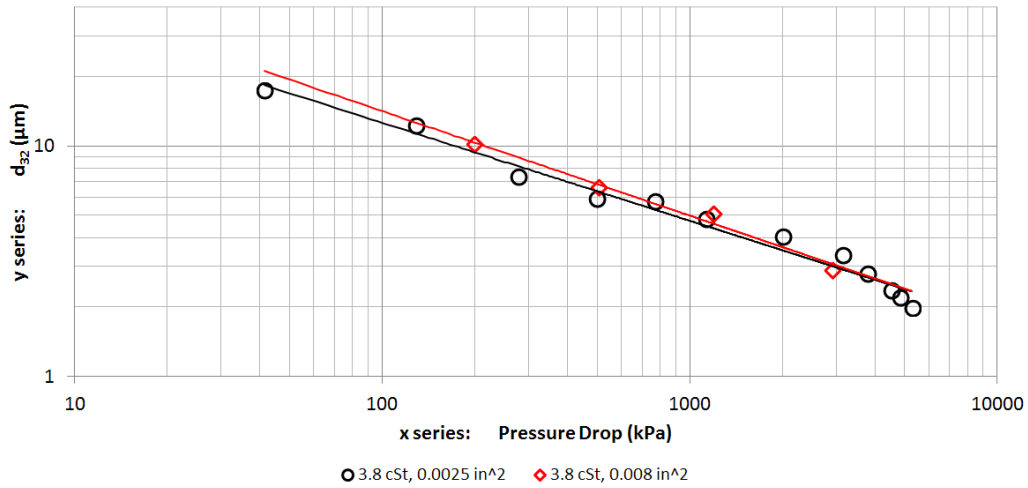
Figure 7.35: Graph of d_{32} vs pressure drop for 3.8 cSt oil, for orifices of size 0025 and 0080.

In Figure 7.35 for 3.8 cSt oil the two series for 0025 and 0080 orifices were close together. No effect of changing orifice size on the d_{32} vs pressure drop graph was noted.
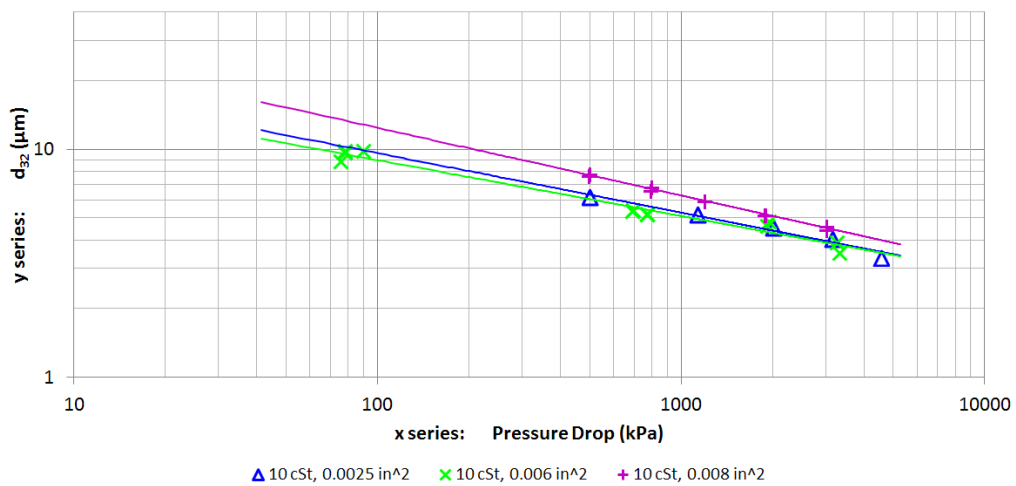
Figure 7.36: Graph of d_{32} vs pressure drop for 10 cSt oil, for 0025. 0060 and 0080 orifices.

In Figure 7.36 for 10 cSt oil three orifices (0025, 0060 and 0080) were compared. The two lower orifice sizes coincided, the larger orifice size had larger drop sizes. (Note that the inlet condition was not constant between these experiments.) Since to change from orifice size 0025 to 0060 had a larger ratio (than for 0060 to 0080), and no discernible difference was found in the d_{32} vs pressure drop trendline, orifice size was seen to be an insignificant variable here as it had been factored out by pressure drop.
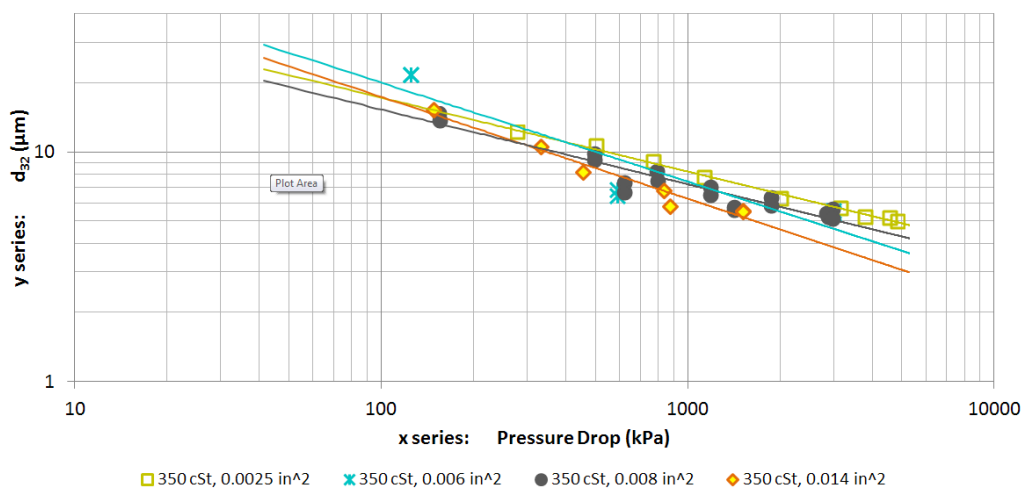
Figure 7.37: Graph of d_{32} vs pressure drop for 350 cSt oil, for orifices of types 0025, 0060, 0080 and 0140.

In Figure 7.37 for 350 cSt oil no clear difference in trend line was seen between the four different data sets from different orifice sizes.

Between these three results sets, the overall conclusion was: when predicting a value for d_{32}, given the Sonolator pressure drop, no extra "orifice size" related term was necessary. This was since the data sets for different orifice sizes were not significantly different from each other as measured by d_{32} vs pressure drop correlations.

Appendix 9   MATLAB code for removing dead pixels in PIV

Script: "deadPixelRemover"

```
%deadPixelRemover
%
%Remove dead pixels (set to zero) according to an existing dead pixel mask
%Live pixels are represented by 1, dead pixels by zero
%This script will open both image and mask, multiply them together
%(componentwise) and output the result to overwrite the original image.
%
%BE VERY CAREFUL! Check on a subset, and check that PIV analysis still works...
%
%IMPORTANT NOTE: This script wipes the "Delta Time" image information.
%It is not yet known how to prevent this from happening.
%TIFF image info can be read in in MATLAB, however DeltaTime attribute is missing
%so it is unknown how to set it again.
%Therefore, when analysing in INSIGHT-4G it will be necessary to
%set Delta-T value by hand, and apply to images before processing.
%It also means that sets of images with multiple delta-T values can no
%longer be processed in INSIGHT-4G after this script has been run
%on the images.
%
%by David Ryan, UK, 2012 (davidryan1998@hotmail.com)

clc;
tic;
originalDirectory=cd;
disp('Script to remove dead pixels from a directory of 12-bit .tif images');
disp(' ');

%% Get a target directory from user
pathName=uigetdir('','Select directory with .tif files to remove dead pixels from');
cd(pathName);

%% Get a list of files in target directory
fileType='\*.tif';
fileList=dir([pathName,fileType]);
N=size(fileList,1);

%% Limit on number of files analysed
fileLimit=20000;
N0=min(N,fileLimit);
fileIndices=getRandomSubsetOfValues(N0,N,1);      %Get list of N0 numbers from 1:N.
Format 1=only included numbers.
disp(['Directory is ',pathName]);
disp(['It contains ',num2str(N),' ',fileType(3:end),' files, of which ',num2str(N0),'
will be processed for dead pixels']);
disp(' ');

%% Get a mask file for the dead pixels (containing 1s and 0s) from user
deadPixelMaskFile=uigetfile('*.bmp','Select dead pixel mask file');
deadPixelFileAndPath=[pathName,'\',deadPixelMaskFile];

if exist(deadPixelFileAndPath,'file')
    [deadPixelImage,deadPixelColourMap]=imread(deadPixelFileAndPath);
```

```
    deadPixelImageInfo=imfinfo(deadPixelFileAndPath);
    disp(['Dead pixel file ',deadPixelMaskFile,' opened successfully']);
else
    error('Dead pixel file not found');
end
disp(' ');


%% Convert dead pixel image from 0, 255 to 0, 1 if necessary
%This wasn't done on some of my experiments, and leads to an error message
%in PIV software (Insight 4G) that minimum pixel value is not equal to 1!
%It still seemed to cross-correlate OK though, without this step.
uniqueVals=unique(deadPixelImage);
if length(uniqueVals)==2 && uniqueVals(1)==0 && uniqueVals(2)==255
    %Change to 0,1
    deadPixelImage=round(deadPixelImage./255);
end

getUserVerificationToProceed;

%% Open each file in turn
tic;
%Each image is greyscale, 0 to 4095
for k=1:N0

    k0=fileIndices(k);      %This has chosen a file at random, if N0<N, or
                            %cycles through 1:N0, if N0=N

    % Extract filename of a 12-bit TIFF file to edit
    fileName=fileList(k0).name;
    inputFileAndPath=[pathName,'\',fileName];

    % Open the file for inspection
    if exist(inputFileAndPath,'file')
        [inputImage,inputImageColourMap]=imread(inputFileAndPath);
        inputImageInfo=imfinfo(inputFileAndPath);

        %deadPixelImage should be 1 for live pixel, 0 for dead pixel
        %Multiplying these two images by components should simply
        %mask the dead pixels in thisImage, resulting in the desired image.
        %
        %NB - imwrite on a bmp by default is 8-bit, 0 to 255
        %Multiplying file by 255 will not compromise image, but will make
        %a 12-bit file into 16-bit... :)
        %
        outputImage=inputImage.*uint16(deadPixelImage);         %One line to do a
complete image mask!

        outputFileAndPath=inputFileAndPath;
        %May need to make file read/write, it may be read-only.
        imwrite(outputImage,outputFileAndPath,'Compression','none');
        %Check format?
        outputImageInfo=imfinfo(outputFileAndPath);

        disp(['Processed file ',num2str(k),' of ',num2str(N0),': ',fileName]);
    else
        disp(['File ',num2str(k),' of ',num2str(N0),': ',fileName,' could not be
found']);
    end
```

```
end

%% Tell the user what has happened
disp(' ');
disp('Batch file to remove dead pixels has completed successfully');

displayTimeTextScript;

cd(originalDirectory);
```

Appendix 10 MATLAB code for processing PIV data

Script: "processPIVvecFiles"

```
%processPIVvecFiles
%Provide input: 'inputDir' to be absolute path of directory to work on
%This script processes one directory of '*.vec' files from Insight4G
%and produces output files in 3 stages inside a 'Processed' subfolder
%USE AN OUTER SCRIPT
%
%by David Ryan, UK, 2012 (davidryan1998@hotmail.com)

%% Stage 01: Trim a whole directory of vector files
%Change to directory supplied previously
%Directory name (if accessed through uigetdir) is absolute, so this step should always
work
originalDirectory=cd;
cd(inputDir);

%% Get a data tag for all summary files
%In the folder there should be a 'metadata.csv'
%file with suitable columns, see function for details

filename='Metadata.csv';
getDataTags;
dataTag=output;


%% Make a 'trim' directory
newDirectory='Processed\01Trim';
%Improvement: put an "exist" if statement in here
mkdir(newDirectory);

%% Get a list of all '.vec' files in current directory to loop through
fileExtension0='.vec';
fileList=dir(['*',fileExtension0]);
n=size(fileList,1);

disp(' ');
disp(['Trimming ',num2str(n),' files in directory']);
disp(cd);
disp(['and putting them in ',newDirectory]);

%% Run the loop on each file in old directory, and move it to new directory
fileExtension1='.csv';
for k=1:n
    % get the file name:
    oldFilename=fileList(k).name;
    newFilename=[oldFilename(1:length(oldFilename)-4),fileExtension1];  %Change file
type
    disp([num2str(k),' of ',num2str(n),': ',newFilename]);
    trimVecFile(oldFilename,[newDirectory,'\',newFilename]);
end

%% Tell the user that the operation has completed successfully
disp(' ');
disp(['Directory ',newDirectory,' created,']);
disp([num2str(n),' trimmed files created there.']);
```

```
%% Stage 02: Replace x and y vectors with integer positions

%Need to go to the new directory to pick up trimmed files
cd(newDirectory);

%% Get unique x and y values out of files
fileList=dir(['*',fileExtension1]);
n=size(fileList,1);
x0=[];
y0=[];
for k=1:n
    %Open each file in turn
    %Extract all x and y values into temporary vectors
    %Save unique values found into x0, y0
    filename=fileList(k).name;
    xTemp=getUniqueValsFromColumn(filename,'',1);
    yTemp=getUniqueValsFromColumn(filename,'',2);
    x0=unique([x0;xTemp]);
    y0=unique([y0;yTemp]);
end
outputFile=['..\uniqueX_',dataTag,'.csv'];      %Write x values to file
outputHeaders='Unique x(mm)';
headerAndMatrix2file(outputFile,outputHeaders,x0);
outputFile=['..\uniqueY_',dataTag,'.csv'];      %Write y values to file
outputHeaders='Unique y(mm)';
headerAndMatrix2file(outputFile,outputHeaders,y0);
disp(' ');
disp('Found unique X and Y values, written to files');

%% Extract multiplier for all x and y values
%When this number is divided out of all x and y values,
%they will become integers. Then subtract (minimum integer -1) to get
%x in 1..X, y in 1..Y format.

%Need to get each vector component minus its predecessor.
xLen=length(x0);
xDiff=x0(2:xLen)-x0(1:xLen-1);

yLen=length(y0);
yDiff=y0(2:yLen)-y0(1:yLen-1);

%Find the minimum value of all of these
%Can't be 0, since original vectors were unique,
%and the diff vector components are therefore non-zero.
diffs=unique([abs(xDiff);abs(yDiff)]);

divisor=min(diffs);
minX=min(x0);
maxX=max(x0);
minY=min(y0);
maxY=max(y0);

%Write this data to file.
%Will use it next to change x and y components to integers

vecFileStats=[divisor minX maxX minY maxY];
outputFile=['..\scalingData_',dataTag,'.csv'];       %Write data just calculated to file
```

```
outputHeaders='Divisor(mm),min x(mm),max x(mm),min y(mm),max y(mm)';
headerAndMatrix2file(outputFile,outputHeaders,vecFileStats);

disp(' ');
disp('Successfully written out vector file statistics');
disp('Vector [divisor minX maxX minY maxY] is');
disp(vecFileStats);


%% Stage 03: Process the vector files to have grid integer X and Y components
% Make a 'grid' directory
% We should already be in Processed\01Trim directory
% Need to go back to Processed, then make new dir in there
newDirectory='..\02Grid';
mkdir(newDirectory);

%% Get a list of all '.csv' files in current directory to loop through
% fileExtension1 should be csv from earlier
% we should be in 01Trim directory
fileList=dir(['*',fileExtension1]);
n=size(fileList,1);

disp(' ');
disp(['Gridding ',num2str(n),' files in directory']);
disp(cd);
disp(['and putting them in ',newDirectory]);

%% Run the loop on each file in old directory, and move it to new directory
for k=1:n
    % get the file name:
    oldFilename=fileList(k).name;
    newFilename=oldFilename;  %Don't change file type here
    disp([num2str(k),' of ',num2str(n),': ',newFilename]);
    gridVecFile(oldFilename,vecFileStats,[newDirectory,'\',newFilename]);
end
disp(' ');
disp(['Directory ',newDirectory,' created,']);
disp([num2str(n),' gridded files created there.']);


%% Stage 04: Work out all 0th to 4th moments of velocity components  in files

%Want to loop through the files just created
cd(newDirectory);

%Calculate array sizes to pass through to script
maxXgrid=int32(round(1+(maxX-minX)/divisor));
maxYgrid=int32(round(1+(maxY-minY)/divisor));
%Inner script below requires these variables to have unchanged names...
%... if this is a problem, replace with a function.

%% Run separate script to find moments and gradients
%subscriptFindMoments;    This was previous script
subscriptFindMomentsAndGradients

%% Run separate script to create graphs and save them to file
cd('..');     %Go to "Processed" directory to save graphs
subscriptCreateGraphs;
```

```
%% End
%Return to original directory
cd(originalDirectory);
disp(' ');
```

Script: "subscriptFindMomentsAndGradients"

```
%subscriptFindMomentsAndGradients
%This script takes over from batchProcessPIVvecFiles and processed stage 02 output
%to produce an average flow file from a whole input directory
%
%Gradients have been added, which take it from a 1 stage process (look at
%file, add moments up) to a 4 stage process (look at file, make grid of 1,
%u, v; add these to moments at each point; make a gradient field; add
%results to gradient moments)
%
%by David Ryan, UK, 2012 (davidryan1998@hotmail.com)

%% Setup constants
smagConst=0.17;        %See Gabriele 2009 for explanation of Smagorinsky Constant for
calculating epsilon from sub grid.

%% Get a list of all '.csv' files in current directory to loop through
% we should be in 02Grid directory
fileExtension2='.csv';
fileList=dir(['*',fileExtension2]);
n=size(fileList,1);

disp(' ');
disp(['Finding moments for ',num2str(n),' files in directory']);
disp(cd);

%% Setup results tables
%maxXgrid and maxYgrid (maximum values) set in outer script
%Data tables for sums at each (integer) x, y
%Previous decimal x, y are now grid x, y in range 1..maxXgrid, 1..maxYgrid

%Set up a zero matrix to be used to repeatedly zero other matrices
z=zeros(maxXgrid,maxYgrid);

s1=z;    %0th moments

s1x=z;   %0th moment: points exist on either side
s1y=z;   %points exist above and below
s1xy=z;  %points exist on all four sides

su=z;    %1st moments
sv=z;

ubar=z;  %Mean Velocities, derived from 1st and 0th moments
vbar=z;

suu=z;   %2nd moments
suv=z;
svv=z;

sdudx2=z;  %2nd moments for spatial gradients and epsilon calc later
```

```
sdvdx2=z;
sdudy2=z;
sdvdy2=z;
scross=z;

%During existing PIV experiments, the room temperature was approximately 22'C, give or
take 3'C.
dynvisc=0.955*10^-3;        %dynamic viscosity of water (Pa.s)
density=997.85;             %density of water (kg/m^3)
kinvisc=dynvisc/density;    %kinematic viscosity of water (m^2/s)

epsilonDE=z;   %#ok<NASGU> %Power per unit mass, calculated from  kinvisc and from the
gradient 2nd moments / 0th moments
epsilonSGS=z;  %#ok<NASGU> %An epsilon corrected for sub grid scale effects, see
Gabriele 2009 for both of these.

suuu=z;  %3rd moments
suuv=z;
suvv=z;
svvv=z;

suuuu=z; %4th moments
suuuv=z;
suuvv=z;
suvvv=z;
svvvv=z;

suuuuu=z; %5th moments
suuuuv=z;
suuuvv=z;
suuvvv=z;
suvvvv=z;
svvvvv=z;

suuuuuu=z; %6th moments
suuuuuv=z;
suuuuvv=z;
suuuvvv=z;
suuvvvv=z;
suvvvvv=z;
svvvvvv=z;

%% Run the loop on each file in directory
for k=1:n
    % get the file name:
    filename=fileList(k).name;
    disp(['Moments: ',num2str(k),' of ',num2str(n),': ',filename]);

    inputData=openFileWithHeaders(filename,',',1);
    headers=inputData{1};
    data=inputData{2};

    [rows columns]=size(data);
    for row=1:rows
        x=round(data(row,1));        %These components have been gridded from (1,1) to
(MAX_X,MAX_Y)
        y=round(data(row,2));        %earlier on, and so can be used as array indices
below.
        u=data(row,3);
```

```
        v=data(row,4);
        %column 5 is the check code - can ignore this.

        s1(x,y)=s1(x,y)+1;
        su(x,y)=su(x,y)+u;
        sv(x,y)=sv(x,y)+v;
        suu(x,y)=suu(x,y)+u*u;
        suv(x,y)=suv(x,y)+u*v;
        svv(x,y)=svv(x,y)+v*v;
        suuu(x,y)=suuu(x,y)+u*u*u;
        suuv(x,y)=suuv(x,y)+u*u*v;
        suvv(x,y)=suvv(x,y)+u*v*v;
        svvv(x,y)=svvv(x,y)+v*v*v;
        suuuu(x,y)=suuuu(x,y)+u*u*u*u;
        suuuv(x,y)=suuuv(x,y)+u*u*u*v;
        suuvv(x,y)=suuvv(x,y)+u*u*v*v;
        suvvv(x,y)=suvvv(x,y)+u*v*v*v;
        svvvv(x,y)=svvvv(x,y)+v*v*v*v;
        suuuuu(x,y)=suuuuu(x,y)+u*u*u*u*u;
        suuuuv(x,y)=suuuuv(x,y)+u*u*u*u*v;
        suuuvv(x,y)=suuuvv(x,y)+u*u*u*v*v;
        suuvvv(x,y)=suuvvv(x,y)+u*u*v*v*v;
        suvvvv(x,y)=suvvvv(x,y)+u*v*v*v*v;
        svvvvv(x,y)=svvvvv(x,y)+v*v*v*v*v;
        suuuuuu(x,y)=suuuuuu(x,y)+u*u*u*u*u*u;
        suuuuuv(x,y)=suuuuuv(x,y)+u*u*u*u*u*v;
        suuuuvv(x,y)=suuuuvv(x,y)+u*u*u*u*v*v;
        suuuvvv(x,y)=suuuvvv(x,y)+u*u*u*v*v*v;
        suuvvvv(x,y)=suuvvvv(x,y)+u*u*v*v*v*v;
        suvvvvv(x,y)=suvvvvv(x,y)+u*v*v*v*v*v;
        svvvvvv(x,y)=svvvvvv(x,y)+v*v*v*v*v*v;

    end
end

disp(' ');
disp('Moments added up across all files');
disp(' ');


%% Calculate steady-state (mean) velocities
%This could probably be vectorised, but would need to deal with zero denominator
%This has to be done before calculating fluctuating velocity gradients,
%hence needing to open each file twice
for x=1:maxXgrid
    for y=1:maxYgrid
        if s1(x,y)~=0
            ubar(x,y)=su(x,y)/s1(x,y);   %mean u velocity component
            vbar(x,y)=sv(x,y)/s1(x,y);   %mean v velocity component
        else
            ubar(x,y)=0;
            vbar(x,y)=0;
        end
    end
end


%% Extract fluctuating velocities for each file, and calculate gradients, which are then
stored
```

```
for k=1:n
    filename=fileList(k).name;
    disp(['Gradients: ',num2str(k),' of ',num2str(n),': ',filename]);

    inputData=openFileWithHeaders(filename,',',1);
    headers=inputData{1};
    data=inputData{2};

    [rows columns]=size(data);

    %Zero all the fluctuating variables
    fluct_u=z;   %Fluctuating Velocities (temporary holders for spatial information)
    fluct_v=z;
    fluct_1p=z;  %Fluctuating existence of velocity at single point
    fluct_1x=z;  %Fluctuating existence of velocity at surrounding pair of points in x
direction
    fluct_1y=z;  %Fluctuating existence of velocity at surrounding pair of points in y
direction
    fluct_1xy=z;  %#ok<NASGU> %Fluctuating existence of velocity at 2 surrounding pairs
of points in x and y direction

    for row=1:rows
        x=round(data(row,1));
        y=round(data(row,2));
        u=data(row,3);
        v=data(row,4);

        %Create a temporary map of points for this file only, and calculate fluctuating
velocities at points
        fluct_1p(x,y)=1;
        fluct_u(x,y)=u-ubar(x,y);
        fluct_v(x,y)=v-vbar(x,y);
    end

    %Vector operations on temporary grid just set up
    %fluct_1x is 1 where fluct_1p is 1 _on either side_
    %Likewise for fluct_1y / _above/below_
    %fluct_1xy requires all four directions to exist, i.e. the previous 2 derived
quantities to both exist at that point.
    fluct_1x(2:maxXgrid-1,1:maxYgrid)=fluct_1p(1:maxXgrid-
2,1:maxYgrid).*fluct_1p(3:maxXgrid,1:maxYgrid);
    fluct_1y(1:maxXgrid,2:maxYgrid-1)=fluct_1p(1:maxXgrid,1:maxYgrid-
2).*fluct_1p(1:maxXgrid,3:maxYgrid);
    fluct_1xy=fluct_1x.*fluct_1y;

    %Keep track of the sums of these
    %Different to s1
    %Will be used to calculate epsilon
    s1x=s1x+fluct_1x;
    s1y=s1y+fluct_1y;
    s1xy=s1xy+fluct_1xy;

    %Check temporary gradient matrices are empty (probably unnecessary, but better safe
than sorry)
    dudx=z;
    dvdx=z;
    dudy=z;
    dvdy=z;
```

```
    %Calculate temporary gradients. DeltaX=DeltaY=divisor from previous script
    %Need to multiply by fluct_1NN inside vector since this will zero any u-u parts
where only one u value exists
    divisor_m=divisor/1000;    %divisor is in mm! This caused some initial problems
    dudx(2:maxXgrid-1,1:maxYgrid)=(fluct_u(3:maxXgrid,1:maxYgrid)-fluct_u(1:maxXgrid-
2,1:maxYgrid)).*fluct_1x(2:maxXgrid-1,1:maxYgrid)./(2*divisor_m);
    dvdx(2:maxXgrid-1,1:maxYgrid)=(fluct_v(3:maxXgrid,1:maxYgrid)-fluct_v(1:maxXgrid-
2,1:maxYgrid)).*fluct_1x(2:maxXgrid-1,1:maxYgrid)./(2*divisor_m);
    dudy(1:maxXgrid,2:maxYgrid-1)=(fluct_u(1:maxXgrid,3:maxYgrid)-
fluct_u(1:maxXgrid,1:maxYgrid-2)).*fluct_1y(1:maxXgrid,2:maxYgrid-1)./(2*divisor_m);
    dvdy(1:maxXgrid,2:maxYgrid-1)=(fluct_v(1:maxXgrid,3:maxYgrid)-
fluct_v(1:maxXgrid,1:maxYgrid-2)).*fluct_1y(1:maxXgrid,2:maxYgrid-1)./(2*divisor_m);

    %Calculate sums of products of gradients for epsilon calc
    sdudx2=sdudx2+dudx.^2;
    sdvdx2=sdvdx2+dvdx.^2;
    sdudy2=sdudy2+dudy.^2;
    sdvdy2=sdvdy2+dvdy.^2;
    scross=scross+dudx.*dvdx;

end

disp(' ');
disp('Gradients calculated for epsilon across all files');
disp(' ');


%% Calculate epsilon using average kinematic viscosity of experiment, and all gradient
data calculated earlier.
%Reference: Gabriele (2009 + erratum 2009) contains all major epsilon equations.

%Reference: Khan(2005) p187 for when some of the 3D components are missing
epsilonDE=kinvisc.*(2*sdudx2./s1x + 2*sdvdy2./s1y + 3*sdudy2./s1y + 3*sdvdx2./s1x +
2*scross./s1xy);
%This version misses all evidence of turbulence at smaller length scales than the IA
grid.

%Reference: Gabriele (2009)
epsilonSGS=((smagConst.*divisor_m).^2).*(4*sdudx2./s1x + 4*sdvdy2./s1y + 2*sdudy2./s1y +
2*sdvdx2./s1x).^(3/2);
%This version is supposed to add in an estimate of turbulence at smaller length scales.
%Although I'm not yet sure how that works
%and the figures for this version did not seem to be right order of magnitude - FIX?
%Jun 2013 - this seems to be OK actually...

%Choose one of these to be used in the upper levels
epsilon=epsilonSGS;

disp('Turbulent statistics calculated');
disp(' ');


%% Concatenate all moments into one data table
rows=maxXgrid*maxYgrid;
output=zeros(rows,49);
for x=1:maxXgrid
    for y=1:maxYgrid
        k=x+maxXgrid*(y-1);
```

```
        xmm=minX+divisor*double(x-1);    %xmin, ymin, divisor set in outer script
        ymm=minY+divisor*double(y-1);

        output(k,1)=x;
        output(k,2)=y;
        output(k,3)=xmm;
        output(k,4)=ymm;

        %Zero some variables defined inside loop
        uVar=0;
        vVar=0;
        tkeEstimate=0;
        if s1(x,y)~=0         %Avoid dividing by zero here
            output(k,5)=ubar(x,y);   %mean u velocity component. (Avoid writing NaN to
    file)
            output(k,6)=vbar(x,y);   %mean v velocity component
            output(k,7)=sqrt(output(k,5)^2+output(k,6)^2);   %mean velocity magnitude

            uVar=suu(x,y)/s1(x,y)-(su(x,y)/s1(x,y))^2;    %variance of u velocity
            vVar=svv(x,y)/s1(x,y)-(sv(x,y)/s1(x,y))^2;       %variance of v velocity

            output(k,8)=sqrt(uVar);   %standard deviation u velocity component
            output(k,9)=sqrt(vVar);   %standard deviation v velocity component

            output(k,10)=sqrt(uVar+vVar);          %standard deviation magnitude

            %Turbulent kinetic energy is 0.5*variance(velocity) =
            %0.5*(var(u)+var(v)+var(w)) = 0.75*(var(u)+var(v)) with
            %isotropic assumption.
            %Note - assumption here that velocity variation is due to
            %turbulence only, and not periodic fluctuations. If periodic
            %fluctuations can be isolated, ought to deduct those from the
            %TKE definition below.
            tkeEstimate=0.75*(uVar+vVar);
        end

        output(k,11)=s1(x,y);  %0th moment (count of data points)
        output(k,12)=su(x,y);  %1st moments
        output(k,13)=sv(x,y);
        output(k,14)=suu(x,y); %2nd moments
        output(k,15)=suv(x,y);
        output(k,16)=svv(x,y);
        output(k,17)=suuu(x,y); %3rd moments
        output(k,18)=suuv(x,y);
        output(k,19)=suvv(x,y);
        output(k,20)=svvv(x,y);
        output(k,21)=suuuu(x,y); %4th moments
        output(k,22)=suuuv(x,y);
        output(k,23)=suuvv(x,y);
        output(k,24)=suvvv(x,y);
        output(k,25)=svvvv(x,y);
        output(k,26)=suuuuu(x,y); %5th moments
        output(k,27)=suuuuv(x,y);
        output(k,28)=suuuvv(x,y);
        output(k,29)=suuvvv(x,y);
        output(k,30)=suvvvv(x,y);
        output(k,31)=svvvvv(x,y);
        output(k,32)=suuuuuu(x,y); %6th moments
        output(k,33)=suuuuuv(x,y);
```

```
        output(k,34)=suuuuvv(x,y);
        output(k,35)=suuuvvv(x,y);
        output(k,36)=suuvvvv(x,y);
        output(k,37)=suvvvvv(x,y);
        output(k,38)=svvvvvv(x,y);

        output(k,39)=s1x(x,y);
        output(k,40)=s1y(x,y);
        output(k,41)=s1xy(x,y);

        output(k,42)=sdudx2(x,y)/s1x(x,y);
        output(k,43)=sdvdx2(x,y)/s1x(x,y);
        output(k,44)=sdudy2(x,y)/s1y(x,y);
        output(k,45)=sdvdy2(x,y)/s1y(x,y);
        output(k,46)=scross(x,y)/s1xy(x,y);

        output(k,47)=epsilonDE(x,y);
        output(k,48)=epsilonSGS(x,y);

        %Defined earlier in this loop.
        output(k,49)=tkeEstimate;

    end
end

disp('Moment and gradient data table collated');
disp('Please wait a moment while this table is written to file:');

% Note - may want to suppress output whever s1(x,y) is too low compared
% with the total number of files, say whenever the count is less than 15%
% of the average count.
% This is so that regions with bad data are not estimated.

%% Send output to a file
outputFile=['..\averageFlows_',dataTag,'.csv'];         %Put it in directory above: the
Processed directory
outputHeaders=['x(grid),y(grid),x(mm),y(mm),ubar(m/s),vbar(m/s),',...
    'av.velocity(m/s),sd.ubar(m/s),sd.vbar(m/s),sd.av.velocity(m/s),',...
    's1,su,sv,suu,suv,svv,suuu,suuv,suvv,svvv,suuuu,suuuv,suvv,suvvv,',...
    'svvvv,suuuuu,suuuuv,suuuvv,suuvvv,suvvvv,svvvvv,suuuuuu,suuuuuv,',...
    'suuuuvv,suuuvvv,suuvvvv,suvvvvv,svvvvvv,s1x,s1y,s1xy,sdudx2,sdvdx2,',...
    'sdudy2,sdvdy2,scross,epsilonDE(W/kg),epsilonSGS(W/kg),k_iso(J/kg)'];
headerAndMatrix2file(outputFile,outputHeaders,output);

disp(['File ',outputFile,' created with moments and gradients of flow fields.']);
```

Appendix 11 MATLAB code for Droplet Breakage Simulations

Script: "scriptRunSim"

```
%scriptRunSim
%Run a simulation of droplets being broken in the Sonolator
%
%by David Ryan, 2012 (davidryan1998@hotmail.com)


%% FRESH START
clear;


%% SETUP SIM
tic;
clc;


%% SETUP VARIABLES
%major variables
numberOfDroplets=4000;
dropletStartingDiameterMicrons=35; %um
dynViscDispCP=350;                 %mPa.s, or cP. This is for oil (dispersed) phase.
interfacialTensionMN=10;        %mN/m
breakageRangeMin=0.01;             %e.g. 0.4 for [0.4, 0.6] or 0.2 for [0.2,0.8]

%minor variables
timeToBreakDroplet_Constant=1;     %This is the constant to use in proportionality given
by Walstra (1998) for breakage time
densityCts=1000;            %kg/m^3  (SI)
densityDisp=1000;           %kg/m^3  (SI)
dynViscCtsCP=1;             %mPa.s, or cP. This is for water (continuous) phase.
minStressExcess=1;          %This should be small, e.g. 1(Pa)

%calc variables
breakageRangeMax=1-max(0,min(0.5,breakageRangeMin));
breakageRangeMult=breakageRangeMax-breakageRangeMin;
maxDaughterDroplets=100;     %This should be large, e.g. 100
%breakageInhomogeneity=1.1;   %Could be used for multiple daughter drops later. BI>=1.
Value of 1 is totally homogeneous, e.g. droplet sizes identical. Value of 10 means
droplets can vary by factor of 10. etc.

%epsilon function
%NOT IMPLEMENTED YET (its hard coded in later)
epsFun='epsilon_0060_8kgpmin_alt';

%background variables
dropStorageSize=1000000;     %This should be large, e.g. 1,000,000
graphBinsPerFactor10=500;
graphMinMicrons=1;                 %um
graphMaxMicrons=100;               %um


%% SETUP INITIAL CALCS
%breakageInhomogeneity=max(1,breakageInhomogeneity);
```

```
interfacialTension=interfacialTensionMN/1000; %N/m (SI)
dynViscDisp=dynViscDispCP/1000;       %Pa.s (SI)
kinViscDisp=dynViscDisp/densityDisp;   %m^2/s (SI)
kinViscDispCST=kinViscDisp*10^6; %mm^2/s, or cSt

dynViscCts=dynViscCtsCP/1000;       %Pa.s (SI)
kinViscCts=dynViscCts/densityCts;   %m^2/s (SI)
kinViscCtsCST=kinViscCts*10^6; %mm^2/s, or cSt


%% CREATE STORAGE SPACE
dropletVolumeMicrons3=zeros(1,dropStorageSize);
dropletTimeMicroseconds=zeros(1,dropStorageSize);
dropletDiameters=zeros(1,dropStorageSize);
dropletKolmoLengths=zeros(1,dropStorageSize);
dropletProcessedFlags=zeros(1,dropStorageSize);

%dropletProcessedFlags format:
%
%0 empty (nothing more to process. Default setting for most of storage array)
%1 unprocessed droplet (execute main loop continuously on these)
%2 processed droplet (was split)
%3 processed droplet in TI regime (final size, OK)
%4 processed droplet in TV regime (final size, error since TV not implemented yet)
%
%At end of loop, all the final droplets will be marked as 3 or 4.


%% INITIALISE STORAGE SPACE
tempRange=1:numberOfDroplets;
tempCell=generateSampleDroplets(dropletStartingDiameterMicrons,numberOfDroplets);
dropletVolumeMicrons3(tempRange)=tempCell{1};
dropletTimeMicroseconds(tempRange)=tempCell{2};
dropletProcessedFlags(tempRange)=tempCell{3};
originalVolumeMicrons3=sum(dropletVolumeMicrons3);


%% MAIN LOOP
dropletToProcess=1;
dropletToCreate=1+numberOfDroplets;
while dropletToProcess<dropStorageSize-maxDaughterDroplets ...   %We've got spare space
left
    && dropletToCreate<dropStorageSize-maxDaughterDroplets ...   %for new droplets
    && dropletProcessedFlags(dropletToProcess)==1                %Looking at an
unprocessed droplet

    %Extract current droplet size and time data
    currentVolume=dropletVolumeMicrons3(dropletToProcess)/10^18;        %m^3 (SI)
    currentTime=dropletTimeMicroseconds(dropletToProcess)/10^6;         %s (SI)
    currentDiameter=2*(3*currentVolume/(4*pi))^(1/3);           %m (SI)

    %Get environmental data
    %epsilon is encapsulated as a function since the times needed are unknown at start
of sim
    currentEpsilon=epsilon_0060_8kgpmin_alt(currentTime);          %m^2/s^3 (SI)
    current_d_max=0.725*interfacialTension^(3/5)*densityCts^(-3/5)*currentEpsilon^(-
2/5);   %Hinze 1955

    %Calculate Kolmogorov microscales
```

```
    kolmo_length=(kinViscCts^3/currentEpsilon)^(1/4);
    %kolmo_time=(kinViscCts/currentEpsilon)^(1/2);
    %kolmo_veloc=(kinViscCts*currentEpsilon)^(1/4);
    %http://en.wikipedia.org/wiki/Kolmogorov_microscales

    %Store diameter and kolmo length data for this droplet
    dropletDiameters(dropletToProcess)=currentDiameter;
    dropletKolmoLengths(dropletToProcess)=kolmo_length;

    %Work out if droplet will break by comparing its diameter to d_max from epsilon
    currentDiamRatio=currentDiameter./current_d_max;
    currentBreakageProb=breakageProbability(currentDiamRatio);
    willDropletBreak=(rand<currentBreakageProb);      %Random factor here

    %Calculate disruptive and cohesive stresses
    stressDisruptiveTI=densityCts*currentEpsilon^(2/3)*currentDiameter^(2/3);
%Walstra 1998 (note his epsilon in W/m3, ours in W/kg)
    stressCohesiveInterface=interfacialTension/currentDiameter;
    stressCohesiveViscous=dynViscDisp*currentDiameter^(-
2/3)*densityCts^(1/2)*densityCts^(-1/2)*currentEpsilon^(1/3);
    stressMaxCohesive=max(stressCohesiveInterface,stressCohesiveViscous);
    stressDisruptiveExcess=stressDisruptiveTI-stressMaxCohesive;

    if currentDiameter>kolmo_length
        %In turbulent inertial (TI) regime. This is OK.

        if ~willDropletBreak  %|| stressDisruptiveExcess<minStressExcess
            %Not enough stress to break droplet. Mark droplet as unbroken and go to next
drop.
            %Mark droplet as processed and final, since it has not split (assuming it
won't in future)
            %NOTE this will only work if epsilon curve is decreasing in
            %time. If not, need to reprogram this to wait a certain length
            %of time then try to break the droplet again. Disadvantage of
            %that is the extra overhead from recalculating droplet breakage
            %statistics over and over... simpler just to have a decreasing
            %epsilon.
            dropletProcessedFlags(dropletToProcess)=3;
        else
            %BREAK DROPLET in TI flow

            %Times for new droplets

timeToBreakDroplet=timeToBreakDroplet_Constant*kinViscDisp*(currentDiameter*currentEpsil
on)^(-2/3);
            newTime=currentTime+timeToBreakDroplet;      %s

            %DROPS SPLITTING INTO MULTIPLE DROPS
            %Number of daughter droplets

%daughterDropsCount=floor(1+sqrt(stressDisruptiveTI/stressCohesiveInterface));
            %Deliberately dependent on interface stress
            %so that for high viscosity a breakage event
            %always gives many daughter droplets.

            %Work out volume fractions
            %Drop is splitting into many small pieces more or less evenly,
            %depending on how inhomogeneous the break-up is.
            %volumeFractions=1+(breakageInhomogeneity-1).*rand(1,daughterDropsCount);
```

```
            %Need to normalise - this step is the one which preserves volume.
            %sumVF=sum(volumeFractions);
            %volumeFractions=volumeFractions./sumVF;

            %BINARY BREAKAGE
            daughterDropsCount=2;
            tempRand=breakageRangeMin+breakageRangeMult*rand;
            volumeFractions=[tempRand,1-tempRand];

            %Store array of new droplets
            rangeToCreate=dropletToCreate:dropletToCreate+(daughterDropsCount-1);

            dropletVolumeMicrons3(rangeToCreate)=currentVolume*10^18.*volumeFractions;
%(um)^3
            dropletTimeMicroseconds(rangeToCreate)=newTime*10^6;
%us
            dropletProcessedFlags(rangeToCreate)=1;

            %Increment count
            dropletToCreate=dropletToCreate+daughterDropsCount;

            %Mark current droplet as processed and split (so no longer exists, its
volume is part of the daughter droplets)
            dropletProcessedFlags(dropletToProcess)=2;
        end

    else
        %Droplet has got small and is in TV regime.
        %Breakage not implemented yet, so no breakage, drop is at final size.
        dropletProcessedFlags(dropletToProcess)=4;
    end

    %Prepare for next loop
    dropletToProcess=dropletToProcess+1;
end

processedTypes=hist(dropletProcessedFlags,[0,1,2,3,4]);
if processedTypes(2)>0
    warning('Some droplets remain unprocessed. Increase array size'); %#ok<WNTAG>
end
storageUsed=round(100*(dropStorageSize-processedTypes(1))/dropStorageSize);
disp([num2str(storageUsed),'% of storage used']);

%dropletData=[dropletVolumeMicrons3;dropletTimeMicroseconds;dropletProcessedFlags;drople
tEpsilons;dropletDiameters;dropletHinzeLengths;dropletKolmoLengths]';
rowsToSelect=dropletProcessedFlags>2;    %only droplets which have gone below Hinze or
Kolgomorov length scales

diamToKolmoRatio=10^mean(log10(dropletDiameters(rowsToSelect)./dropletKolmoLengths(rowsT
oSelect)));
disp([num2str(diamToKolmoRatio),' is average ratio between Final Droplet Diameter and
Kolmogorov Length Scale at that time. (>1 for TI flow regime)']);

dropletVolumeMicrons3_final=dropletVolumeMicrons3(rowsToSelect);
dropletDiameterMicrons_final=2*(3*dropletVolumeMicrons3_final/(4*pi)).^(1/3);
finalVolumeMicrons3=sum(dropletVolumeMicrons3_final);
dropletSizeBinsMicronsLog10=log10(graphMinMicrons):(1/graphBinsPerFactor10):log10(graphM
axMicrons);
[sizeDn,bins]=hist(log10(dropletDiameterMicrons_final),dropletSizeBinsMicronsLog10);
```

```
%Exclude first and final bins since they could contain too much stuff from the tails
volSizeDn=sizeDn.*(bins.^3);
volSizeDnNorm=graphBinsPerFactor10.*volSizeDn./sum(volSizeDn);
%plot(bins(2:end-1),sizeDn(2:end-1));    %NUMBER WEIGHTED
plot(bins(2:end-1),volSizeDnNorm(2:end-1));    %VOLUME WEIGHTED
%loglog(bins,sizeDn);

volumeConsRatio=finalVolumeMicrons3/originalVolumeMicrons3;
volumeConsRatioRound=round(volumeConsRatio*100)/100;
if volumeConsRatioRound==1
    disp(['Original and final total droplet volume in mm^3:
',num2str(originalVolumeMicrons3/10^9)]);
else
    warning(['Original, final total droplet volumes in mm^3:
',num2str(originalVolumeMicrons3/10^9),', ',num2str(finalVolumeMicrons3/10^9)]);
%#ok<WNTAG>
end

%DEBUG
%processedTypes %#ok<NOPTS>

toc
```

Function: "breakageProbability"

```
function output=breakageProbability(parameter)
%Returns zero if parameter is 0.5 or less, 1 if parameter is 1 or more,
%linear interpolation inbetween
%by David Ryan, UK, 2012 (davidryan1998@hotmail.com)
output=max(0,min(1,parameter*2-1));
```

Function: "epsilon_0060_8kgpmin_alt"

```
function output=epsilon_0060_8kgpmin_alt(measTime)
%A sample epsilon curve for use in population balance equations
%Altered to be at the highest value until the peak
%%epsilon_0060_8kgpmin(measTime)
%%measTime: the time at which the epsilon result is needed
%%by David Ryan, UK, 2012 (davidryan1998@hotmail.com)

%Get the time within selected window
measTime=min(1,measTime);
measTime=max(0.00000001,measTime);
%Calculated the upswing and downswing parts of epsilon model
%e1=9e13.*measTime.^1.9117;
e2=0.2741.*measTime.^-1.459;
%Return the one which is smaller. Minimum return is 1 W/kg.
output=max(1,min(526374,e2));
```

Appendix 12 Conference paper – AJK2011

(Included as inserted sheets, pages not numbered.)

Appendix 13 Conference paper – ICMF2013

(Included as inserted sheets, pages not numbered.)

Appendix 14 CD with videos of CFD flows

The CD contains videos created in CFD-Post which animate typical flow velocities and conditions in the Sonolator, to gain a better understanding of the types of transient flow structures encountered.